UNIVERSITY OF THE
WITWATERSRAND,
JOHANNESBURG

THE EXTRACTION AND RECOVERY OF RARE EARTH ELEMENTS, ALUMINIUM, TITANIUM, AND IRON FROM SOUTH AFRICAN COAL FLY ASH

Amanda Qinisile Vilakazi

A thesis submitted to the Faculty of Engineering and the Built Environment, University of the Witwatersrand, Johannesburg in fulfillment of the requirements for the degree of Doctor of Philosophy

January, 2025

DECLARATION

I hereby declare that this thesis is my unaided work. It is being submitted for the degree of Doctor of Philosophy in Materials and Metallurgical Engineering to the University of the Witwatersrand, Johannesburg, South Africa. It has not been submitted before for any other degree or examination to any other University.

.....

25th January 2025

Amanda Qinisile Vilakazi

School of Chemical and Metallurgical Engineering

University of the Witwatersrand, Johannesburg, South Africa

ABSTRACT

Coal fly ash (CFA) is a waste material with the potential for high-value and high-volume utilisation in wastewater treatment and alumina production. The sinter-H_2SO_4 leach process can extract over 80 wt.% of aluminium, which can be commercially processed to generate smelter-grade Al_2O_3. However, due to the high costs involved in the pre-treatment and downstream purification steps, the process has proved neither feasible nor sustainable. This study reports on a holistic approach to adding value in alumina processing by extracting aluminium (Al), rare earth elements (REEs), titanium (Ti), and iron (Fe) as saleable products. The overall aim is to produce a rare-earth concentrate, smelter-grade alumina, high-purity titanium dioxide, and iron-based coagulants. The potential application of the generated secondary solid residue as an adsorbent for wastewater treatment is also evaluated.

In the first experimental stage, CFA was characterised for its composition. XRD analysis revealed an amorphous component with crystalline mullite, quartz, and magnetite/haematite. SEM-EDS and TIMA analyses showed that Al-Si-rich grains are the predominant phase, with discrete REE-bearing grains (phosphates and silicates) and Fe-oxide (magnetite/haematite) grains. Traces of REEs, Ti, Ca, Si, and Fe were also found in the Al-Si-rich grains. Discrete Fe-oxide grains were further recovered using dry magnetic separation to reduce downstream purification costs. The results showed that up to 65.9% Fe-oxides could be recovered at 1.05 T (magnetic field strength). However, the magnetic fraction (CFA-MF) also contained mullite and quartz impurities. The non-magnetic fraction (non-MF) was further processed for the extraction of the selected REEs (Sc, Y, La, Ce, and Nd), Al, Fe, and Ti.

In the preliminary leaching tests, the effects of leaching parameters were investigated using direct H_2SO_4 leach and sinter-H_2SO_4 leach processes. The former resulted in poor metal extraction due to the phase composition of CFA, while the latter showed a much higher extraction efficiency. In the sinter-H_2SO_4 leach process, a maximum of 72% Al, 63% Fe, and 40% Ti were extracted in 6 M H_2SO_4 by leaching at 70°C in a 1:4 S/L ratio for 10 hours. Under the same experimental conditions, less than 20% of the selected REEs were extracted, except for Sc which had 35% extraction. Further investigation was conducted using the sinter-HCl leach process, and the extraction efficiency was significantly improved, with over 50% REEs recovered in 4 M HCl by leaching for 6 hours at 70°C. The lower extraction

efficiency of REEs in the sinter-H_2SO_4 leach process was ascribed to calcium sulphate precipitation and the complex phase composition. Nonetheless, the sinter-H_2SO_4 leach process was optimised using a Design of Experiments (DOE) for alumina production. Consequently, a CFA leach liquor and a solid residue (sintered CFA residue) were generated for further processing.

The CFA leach liquor was concentrated with Al(III), Fe(II/III), and Ti(IV). It was processed by integrating solvent extraction (SX), crystallisation, and oxidation-precipitation processes. All Fe(III) in solution was first reduced to Fe(II), and Ti(IV) was selectively extracted using Primene JM-T/Shellsol D70, followed by stripping in NH_4OH and calcination to produce TiO_2. The synthesised TiO_2 showed lower purity (95.03 wt.%) and BET surface area (10.05 m^2/g) for application as a photocatalyst in wastewater treatment. However, it was classified as a type II pigment grade. Aluminium in the raffinate was directly crystallised and calcined to produce smelter-grade Al_2O_3. The remaining Fe(II)-rich solution was processed at pH 5.0, using an oxidation-precipitation process. Due to the gelatinous Fe(III) precipitate, which was difficult to filter, the recovered CFA-MF was recycled as seeding material to improve the precipitation process. Seeding significantly improved the filtration process for all concentration levels (Cs = 0.5, 1.0, and 2.0). The seeded Fe(III) precipitate at Cs = 1.0 was further used to produce polyferric sulphate (PFS) coagulants by dissolution in dilute sulphuric acid. The generated CFA-PFS was mainly concentrated with Fe(III) and contained minor amounts of Al(III), Mg(II), Mn(II), and Ca(II). The synthesised CFA-PFS coagulant was tested on brewery wastewater and found compatible with commercial PFS. Throughout the purification processes, REEs which were dissolved in the sinter-H_2SO_4 leach process, mostly remained in solution.

The sintered CFA solid residue (CFA-SR) was characterised as a silica and calcium component with significant concentrations of REEs. Phase composition analysis revealed an amorphous material with a Si-Ca-S-rich phase and a Si-rich phase. Traces of Al, Fe, Ti, and REEs were mostly distributed in the Si-Ca-S-rich phase. To minimise the formation of silica gel, the dry digestion-water leach process was carried out in a sulphates and chloride system for REE extraction. The obtained results indicated that the solubility of calcium sulphates and the complex phase composition might be limiting factors for efficient REE extraction. Nevertheless, an REE concentrate was generated with low purity. As a result, the REE-concentrated solution was set as the final product. Overall, combining the sinter-H_2SO_4 leach

process with the dry digestion-water leach process was considered a promising alternative for concentrating and selectively extracting REEs from CFA.

A CFA secondary solid residue (CFA-SSR) was generated after the two-step leaching process for disposal. The material was characterised for potential recycling in wastewater treatment as an adsorbent. Characterisation showed an amorphous and crystalline component with mesopores measuring 11.7 nm. The average particle size was 44.76 µm, while the S_{BET} was 29.236 m^2/g (surface area). Batch tests showed that CFA-SSR has the capacity to adsorb heavy metals (i.e. Ni, Zn, and Fe) in acid mine drainage (AMD). The overall findings indicated that the adsorption capacity could be enhanced by functionalising CFA-SSR to improve selectivity and surface properties.

A process flowsheet was designed for the proposed CFA processing using magnetic separation, a two-step leaching process, and an integrated purification process. The economic evaluation showed that more than one value-added recovery could be an alternative to generate revenue and offset some of the operational costs in alumina processing from CFA.

PUBLICATIONS AND CONFERENCES

Journal Publications

1. Vilakazi, A.Q., Ndlovu, S., Shemi, A., 2025. Dry Magnetic Separation and the Leaching Behaviour of Aluminium, Iron, Titanium, and Selected Rare Earth Elements (REEs) from Coal Fly Ash. *Minerals* 15(2), 119.
2. Vilakazi, A.Q., Ndlovu, S., Chipise, L., Shemi, A., 2022. The recycling of coal fly ash: A review on sustainable developments and economic considerations. *Sustainability* 14(4), 1958.

Conference Publication

1. Amanda Vilakazi, Liberty Chipise, Sehliselo Ndlovu, 2023. Seeded iron recovery from coal fly ash leach liquor to prepare poly ferric sulphate coagulant. 14th *International Conference on Process Hydrometallurgy,* Hydroprocess 2023. Santiago, Chile. 7-9 November 2023.

Oral Conference Presentations

1. Amanda Vilakazi, Liberty Chipise, Sehliselo Ndlovu, 2023. Extraction of selected rare earth elements from CFA using the sinter-H_2SO_4 leach process. *6th Young Professionals Conference,* South African Institute of Mining and Metallurgy, HATCH, South Africa. 16-17 November 2023.
2. Amanda Vilakazi, Sehliselo Ndlovu, Liberty Chipise, 2023. Seeded iron recovery from coal fly ash leach liquor to prepare poly ferric sulphate coagulant *Inaugural Research Seminar, Faculty of Engineering and the Built Environment,* University of the Witwatersrand, South Africa. 25-26 October 2023.
3. Amanda Vilakazi, Sehliselo Ndlovu, Liberty Chipise, 2023. Extractions of rare earth elements from CFA using the sinter-H_2SO_4 leach process. *CRM REE in Coal Research Symposium,* DSI-NRF CIMERA, University of Johannesburg, South Africa. 25 August 2023.

Manuscripts Under Preparation

1. Vilakazi, A.Q., Ndlovu, S. Optimisation of the sinter-H_2SO_4 leach process for alumina production and the processing of the generated by-products.
2. Vilakazi, A.Q., Ndlovu, S. The potential application of the sinter-H_2SO_4 by-products as adsorbents and coagulants for wastewater treatment.

DEDICATION

This thesis is dedicated to my mother, M.M. Vilakazi for her unwavering support and involvement in every milestone of my academic journey.

"Ngiyabonga Binda, Mphephethe"

Amanda Qinisile Vilakazi

ACKNOWLEDGEMENTS

I hereby wish to thank several people who made this research a success.

- My supervisor, Prof. Sehliselo Ndlovu, for the guidance and dedication throughout the research project. Your expertise is highly acknowledged with gratitude. Dr. Alan Shemi and Dr. Liberty Chipise, thank you for the technical inputs and knowledge sharing towards the success of this research.
- DSI/NRF SARChI: Hydrometallurgy and Sustainable Development for financial support.
- University of the Witwatersrand, School of Chemical and Metallurgical Engineering (CHMT) for administrative and technical assistance.
- The Metal Extraction and Recovery Group (Hydrometallurgy group) for your valuable research inputs and providing a conducive environment to study.
- The Center of Microscopy and Microanalysis Unit (MMU WITS) and University of Johannesburg, Extractive Metallurgy Group for making their facilities available and providing training.
- My gratitude also goes to Lijo Mona, Sibongile Xaba, Dr. Motlalepula Nete and Dr. Manish Kumar Sinha. Thank you for the consultations and motivation to complete this project.
- Finally, I would like to express my gratitude to my family for the prayers and countless motivation; "*Ngiyabonga Binda, Mphephethe*".

I am grateful to God, who has sustained me through this quest: "**Faith is a Pace of Grace**"

Amanda Qinisile Vilakazi

TABLE OF CONTENTS

DECLARATION ..... **i**

ABSTRACT ..... **ii**

PUBLICATIONS AND CONFERENCES ..... **v**

DEDICATION ..... **vi**

ACKNOWLEDGEMENTS ..... **vii**

TABLE OF CONTENTS ..... **viii**

LIST OF FIGURES ..... **xiv**

LIST OF TABLES ..... **xx**

ACRONYMS AND SYMBOLS ..... **xxiii**

GLOSSARY ..... **xxv**

1 INTRODUCTION **1**

1.1 Background 1

1.1.1 Potential utilisation of CFA 2

1.1.2 Motivation of the study 6

1.2 Problem Statement 9

1.3 Research Aim and Objectives 9

1.4 Research Hypothesis and Questions 10

1.5 Significance of the Study 11

1.6 Deliverables 12

1.7 Research Methodology 12

1.7.1 Literature review 12

1.7.2 Experimental design 13

1.7.3 Data analysis 13

1.7.4 Conclusions and recommendations 13

1.8 Thesis Layout 14

1.9 Summary 16

References 16

2 LITERATURE REVIEW 20
2.1 Introduction 20
2.2 Occurrence and Distribution of REEs 21
2.2.1 Mineralogy of REE ores 22
2.2.2 REEs in secondary sources 23
2.2.2.1 Coal Combustion Process (CCP) 24
2.2.2.2 CFA mineralogy 26
2.2.2.3 REEs in CFA 27
2.3 Chemistry of REEs 29
2.3.1 Aqueous chemistry 30
2.3.2 Coordination chemistry 31
2.4 Conventional Processing of REEs 33
2.4.1 Physical beneficiation 34
2.4.1.1 Flotation and gravity separation 34
2.4.1.2 Magnetic separation (MS) 34
2.4.2 Hydrometallurgical beneficiation 35
2.4.2.1 Alkaline decomposition 36
2.4.2.2 Acid decomposition 37
2.5 Recovery of Valuable Metals from CFA 38
2.5.1 Magnetic separation 39
2.5.2 Recovery of Al, Fe and Ti 41
2.5.2.1 Direct acid leaching 43
2.5.2.2 Indirect acid leaching 44
2.5.3 Recovery of REEs 46
2.5.3.1 Direct acid leaching 48
2.5.3.2 Indirect acid leaching 48
2.5.3.3 Effect of calcium sulphate 49
2.5.3.4 Silica management 51
2.6 Purification and Separation of Impurities 54
2.6.1 Chemical precipitation 54
2.6.1.1 Hydroxide precipitation 57
2.6.1.2 Oxalate and carbonates precipitation 60
2.6.1.3 Double sulphate precipitation 62

2.6.2 Solvent extraction 62
2.6.2.1 Extraction 64
2.6.2.2 Purification of leach liquor by solvent extraction 66
2.7 Utilisation of CFA in Wastewater Treatment 71
2.7.1 Coagulation 73
2.7.1.1 Destabilisation and aggregation of colloidal particles 74
2.7.1.2 Coagulation with CFA 76
2.7.1.3 Iron-based coagulants 77
2.7.2 Adsorption 82
2.7.2.1 Adsorption using CFA 83
2.7.2.2 Titanium dioxide in wastewater treatment 86
2.8 Summary 90
References 92
3 MATERIALS AND METHODS 113
3.1 Introduction 113
3.2 Reagents and Equipment 113
3.2.1 Chemicals and reagents 113
3.2.2 General analytical techniques 115
3.2.2.1 Particle size distribution (PSD) 115
3.2.2.2 Proximate analysis 116
3.2.2.3 Chemical composition analysis 116
3.2.2.4 Phase composition analysis 116
3.2.2.5 Morphological analysis 118
3.2.2.6 Determination of functional groups 118
3.2.2.7 Brunauer-Emmett-Teller (BET) and Barrett-Joyner-Halenda (BJH) 118
3.2.3 Water quality analysis 119
3.3 Experimental Methodology 119
3.3.1 Material characterisation 119
3.3.2 Dry magnetic separation 119
3.3.3 Leaching experiments 121
3.3.3.1 Direct acid leaching 122
3.3.3.2 Indirect acid leaching 123
3.3.3.3 Dry digestion – water leach 125

3.3.3.4 Design of Experiments 126
3.3.3.5 Experimental Design 128
3.3.4 Purification of CFA leach liquor 128
3.3.4.1 Fe reduction and Ti extraction 129
3.3.4.2 Aluminium crystallisation 130
3.3.4.3 Seeded – Fe(III) precipitation 130
3.3.4.4 Precipitation of rare earth oxalates 132
3.3.5 Coagulation and adsorption in wastewater treatment 132
3.3.5.1 Coagulation experimental procedure 132
3.3.5.2 Adsorption experimental procedure 134
3.4 Data analysis 134
References 135
4 MATERIAL CHARACTERISATION AND PRELIMINARY STUDIES 138
4.1 Hypothesis and Objectives 138
4.2 Results and Discussion 139
4.2.1 Raw CFA characterisation 139
4.2.1.1 Particle size distribution analysis 139
4.2.1.2 Chemical composition analysis 140
4.2.1.3 Phase composition analysis 141
4.2.2 Iron recovery from raw CFA by dry magnetic separation 148
4.2.2.1 Effect of magnetic field intensity 149
4.2.2.2 Magnetic fraction characterisation 150
4.2.3 Pelletisation and sintering 155
4.2.3.1 Surface morphology and particle size distribution analysis 156
4.2.3.2 Chemical composition analysis 158
4.2.3.3 Phase composition analysis 159
4.2.4 Preliminary acid leaching 163
4.2.4.1 Effect of H_2SO_4 leaching 163
4.2.4.2 Effect of HCl leaching 171
4.2.4.3 Comparison of the sinter – HCl and sinter – H_2SO_4 leaching 172
4.3 Conclusion 176
References 177

5 OPTIMISATION OF THE SINTER – H_2SO_4 LEACH FOR ALUMINA PRODUCTION AND THE EXTRACTION OF REEs BY DRY DIGESTION – WATER LEACH FROM THE RESIDUE 183

5.1 Hypothesis and Objectives 183

5.2 Results and Discussion 184

5.2.1 Optimisation of sinter – H_2SO_4 process 184

5.2.1.1 Significant variables 184

5.2.1.1 Optimisation of significant factors variables 188

5.2.2 Purification of CFA leach liquor 192

5.2.2.1 Titanium extraction 193

5.2.2.2 Aluminium crystallisation 195

5.2.2.3 Composition of CFA leach liquor before and after Al and Ti recovery 196

5.2.2.4 Characterisation of potential saleable products 198

5.2.3 Characterisation and processing of the generated sintered CFA – SR 203

5.2.3.1 Particle size distribution analysis 203

5.2.3.2 Chemical composition analysis 204

5.2.3.3 Phase composition analysis 205

5.2.3.4 Dry digestion – water leach process 209

5.2.3.5 Production of REE concentrate 214

5.3 Conclusion 216

References 218

6 POTENTIAL COAGULANT AND ADSORBENT FROM CFA PROCESSING 222

6.1 Hypothesis and Objectives 222

6.2 Results and Discussion 223

6.2.1 Recovery of Fe – based coagulants 223

6.2.1.1 Fe(II) oxidation and precipitation 223

6.2.1.2 Characterisation of Fe(III) precipitates 227

6.2.1.3 Solubility of the precipitate and coagulant production 234

6.2.1.4 Performance of CFA – PFS coagulant on wastewater 235

6.2.2 Characterisation of CFA – SSR as a potential adsorbent 237

6.2.2.1 Physicochemical properties 238

6.2.2.2 Surface morphology 240

6.2.2.3 Phase composition analysis 241

6.2.2.4 Functional group analysis....242
6.2.2.5 Chemical composition analysis....243
6.2.2.6 Point of Zero Charge (pH_{PZC})....245
6.2.2.7 Batch adsorption studies....245
6.3 Conclusion....252
References....253
7 PROCESS FLOWSHEET AND ECONOMIC ANALYSIS....259
7.1 Introduction....259
7.2 Process Flowsheet....259
7.3 Estimated Costs Analysis....262
7.4 Summary....265
References....266
8 CONCLUSIONS AND RECOMMENDATIONS....267
8.1 Conclusions....267
8.2 Recommendations....273
APPENDICES....274
Appendix A: General Equipment....274
Appendix B: Material Characterisation....275
Appendix C: Design of Experiments....282

LIST OF FIGURES

Figure 1.1: A schematic presentation of CCW management and beneficiation alternatives. ..2

Figure 1.2: Treatment of AMD with lime and CFA. 3

Figure 1.3: A thesis layout. 15

Figure 2.1: The LREEs, HREEs and Scandium (Generalic, 2019). 20

Figure 2.2: A general coal processing and combustion unit at Eskom Holdings (Eskom, 2016). 25

Figure 2.3: a) SEM analysis of CFA showing a solid aluminosilicate sphere with needle-like mullite crystals (Dai et al., 2010) and b) QEMSCAN analysis of CFA showing different phases (Ma et al., 2021). 26

Figure 2.4: The general REE mode of occurrence in coal (Fu et al., 2022). 27

Figure 2.5: The lanthanides contraction (De Decker, 2017).....30

Figure 2.6: A representation of trinitrobis (bipyrdyl) lanthanum (III) (Cotton, 2005). 31

Figure 2.7: Common organic ligands used in REE complexation (Dehnicke and Greiner, 2003; Xaba, 2015).....32

Figure 2.8: The REEs beneficiation stages in processing primary ore deposits. 33

Figure 2.9: The conventional hydrometallurgical treatment of REE concentrates **(**adapted from Chegwidden and Kingsnorth, 2002). 36

Figure 2.10: A schematic magnetite spinel structure (Hashimoto et al., 2019). 40

Figure 2.11: A schematic presentation of alumina processing by the Hall-Heroult electrolytic process (Kvande and Drabløs, 2014). 42

Figure 2.12: A schematic presentation of the Bayer process (Adopted from Ndlovu et al., 2017). 42

Figure 2.13: A process flowsheet for a two-step H_2SO_4 leach process and an integrated purification (Adopted from Shemi (2013) and Rampou (2018)). 45

Figure 2.14: The solubility of amorphous silica at ambient temperature (Terry, 1983a). 52

Figure 2.15: A schematic flowsheet of the dry digestion process (Borra et al., 2016). 53

Figure 2.16: Precipitation kinetic processes (Söhnel et al., 1992). 55

Figure 2.17: Hydroxide precipitation diagram of different metal ions at 25℃ (Judge and Azimi, 2020). 58

Figure 2.18: Stability regions of different compounds in the Fe-S-O system (Babcan, 1971). 59

Figure 2.19: Ferrioxalate complex. 61

Figure 2.20: Structure of alkyl amines used as basic extractants (Desouky, 2006). 65

Figure 2.21: Fe(III)-sulphate-pH diagram (Gil et al., 1995). 67

Figure 2.22: Distribution of titanium species in a sulphate system (Sole, 1999). 68

Figure 2.23: Distribution of yttrium sulphate species as a function of sulphate ions concentration at 25℃ (Hiskey and Copp, 2018b). 71

Figure 2.24: Mine wastewater from the Witwatersrand basin, South Africa (Masindi et al., 2022). 72

Figure 2.25: A schematic diagram illustrating various methods of CFA utilisation in wastewater treatment (Mushtaq et al., 2019). 73

Figure 2.26: A conventional coagulation/flocculation unit process (Teh et al., 2016). 74

Figure 2.27: Double layer around a negatively charged colloid (Suopajärvi, 2015). 75

Figure 2.28: The rate Fe oxidation as a function of pH (Morgan and Lahav, 2007). 78

Figure 2.29: The solubility of ferrous hydroxide at 25℃ (Hove, 2008). 79

Figure 2.30: Schematic pathways for common iron oxides and oxyhydroxides (Barrón and Torrent, 2013). 80

Figure 2.31: A schematic photocatalysis process using TiO_2 (Chong et al., 2010). 87

Figure 2.32: A representation of a unit cell for rutile and anatase (Sørensen, 2014). 89

Figure 3.1: Material characterisation techniques through various analytical approaches. ... 115

Figure 3.2: The induced roller magnetic separator (Model: IMR roll, supplied by Eziez, South Africa). 120

Figure 3.3: Leaching test equipment: A scientific shaking incubator (Lenton furnace model 353). 122

Figure 3.4: (a) Pelletiser equipment (Model: R02, H. Birkenmayer (Pty) Ltd), (b) A Lenton muffle furnace (Model: LLC 13/42-PA), and (c) CFA pellets before and after sintering. 124

Figure 3.5: Solvent extraction set-up for Ti(IV) using Primene JM-T/Shellson D70. 129

Figure 3.6: The direct aluminium crystallisation set-up in the raffinate. 130

Figure 3.7: Experimental set-up for seeded Fe(II) oxidation and precipitation (adopted from Mwewa et al. (2019)). 131

Figure 3.8: Jar tester for coagulation. 133

Figure 4.1: Particle size distribution of CFA: (a) sieve analysis and (b) histogram distribution curve by laser particle sizer (LD).....139

Figure 4.2: ICP-MS analysis of REEs in raw CFA. 141

Figure 4.3: SEM micrographs of raw CFA at high resolution and a semi-quantitative EDS analysis of the specific marked points. 143

Figure 4.4: Major phase composition and particle count in raw CFA. 144

Figure 4.5: BSE images of raw CFA and a semi-quantitative phase chemistry of selected grains showing Ti and Fe distribution. 146

Figure 4.6: Elemental maps showing the distribution of REE-bearing grains from raw CFA and a semi-quantitative phase chemistry of selected grians in micrograph C. 147

Figure 4.7: Raw CFA and the recovered fractions (MF and non-MF, 1: 100) after magnetic separation. 148

Figure 4.8: The effect of magnetic field intensity on Fe recovery from raw CFA. 149

Figure 4.9: XRD patterns of raw CFA and CFA magnetic fractions (MF and non-MF). 150

Figure 4.10: Morphological analysis of (a-b) raw CFA and (c-e) CFA-MF showing spherical particles with (f) EDS analysis of CFA-MF. 154

Figure 4.11: SEM images with corresponding PSD analysis for (a) raw CFA and (b) CFA-MF. 155

Figure 4.12: Particle size distribution of (a) CFA non-MF and (b) sintered CFA with SEM images of (c) CFA non-MF and (d) sintered CFA. 157

Figure 4.13: SEM micrographs of sintered CFA and a semi-quantitative EDS analysis of the specific marked points. 161

Figure 4.14: BSE images and elemental maps showing the distribution of REEs in sintered CFA. 162

Figure 4.15: Effect of leaching temperature on the extraction of (a) major elements and (b) selected REEs from CFA at 6 M H_2SO_4, 1:4 S/L ratio leaching for 10 hours. 164

Figure 4.16: Effect of sulphuric acid concentration on the extraction of (a) major elements and (b) selected REEs from CFA at 70℃, 1:4 S/L ratio leaching for 10 hours. 165

Figure 4.17: Effect of leaching time on the extraction of (a) major elements and (b) selected REEs from CFA at 6 M H_2SO_4, 1:4 S/L ratio leaching at 70℃. 166

Figure 4.18: Effect of sulphuric acid concentration on the extraction of (a) major elements and (b) selected REEs from sintered CFA at 70℃, 1:4 S/L ratio leaching for 10 hours. 168

Figure 4.19: Effect of leaching temperature on the extraction of (a) major elements and (b) selected REEs from sintered CFA at 6 M H_2SO_4, 1:4 S/L ratio leaching for 10 hours. 169

Figure 4.20: Effect of leaching time on the extraction of (a) major elements and (b) selected REEs from sintered CFA at 6 M H_2SO_4, 1:4 S/L ratio leaching at 70℃. 170

Figure 4.21: Effect of (a) acid concentration and (b) leaching temperature on the extraction of REEs from sintered CFA using HCl. 172

Figure 4.22: Leaching efficiency of sintered CFA using 6 M H_2SO_4 at 70℃ for 10 hours and 4 M HCl at 70℃ for 6 hours. 173

Figure 4.23: XRD patterns of sintered CFA solid residues after HCl and H_2SO_4 leaching. 174

Figure 4.24: Surface morphology of sintered CFA solid residue leached in (a)-(b) 4 M HCl and (c)-(d) 6 M H_2SO_4. 175

Figure 5.1: A bar graph showing significant variables in the Al extraction process. 186

Figure 5.2: Effect of experimental variables (A: H_2SO_4 concentration, B: time, C: temperature, and D: S/L ratio) on the extraction of Al from sintered CFA. 187

Figure 5.3: The interaction between H_2SO_4 concentration and leaching temperature in the Al extraction from sintered CFA. 188

Figure 5.4: A 3D response surface for the percentage extraction of Al as a function of temperature and H_2SO_4 concentration from sintered CFA. 191

Figure 5.5: Elemental analysis of REEs in a CFA leach liquor. 192

Figure 5.6: FT-IR spectrum of TiO_2 calcined at 500℃. 195

Figure 5.7: FT-IR spectroscopic results for $(NH_4)_2SO_4$, $Al(NH_4)_2SO_4$, and Al_2O_3 196

Figure 5.8: Synthesised aluminium oxide and titanium dioxide. 198

Figure 5.9: XRD pattern of Al_2O_3 calcined at 800℃. 199

Figure 5.10: (a) XRD pattern of TiO_2 calcined at 500℃ and (b)-(c) SEM images showing spherical grain-like nanoparticles. 201

Figure 5.11: N_2 adsorption-desorption isotherm and the respective pore diameter distribution curves for TiO_2 calcined at 500℃. 202

Figure 5.12: The images of sintered CFA and sintered CFA residue (CFA-SR). 203

Figure 5.13: Particle size distribution of the sintered CFA-SR. 203

Figure 5.14: The concentration of REEs in sintered CFA-SR. 204

Figure 5.15: XRD analysis of sintered CFA-SR. 205

Figure 5.16: SEM analysis of the sintered CFA-SR and EDS analysis of selected marked points. 207

Figure 5.17: Elemental maps showing the distribution of REEs in sintered CFA-SR and their association with the Si-rich and Ca-rich components. 208

Figure 5.18: Effect of sulphate baking temperature on the extraction of (a) major elements and (b) selected REEs from sintered CFA-SR by baking for 12 hours followed by water leaching at 25℃ for 24 hours. 210

Figure 5.19: Effect of sulphate baking time on the extraction of (a) major elements and (b) selected REEs from sintered CFA-SR by baking at 300℃ followed by water leaching for at 25℃ for 24 hours. 211

Figure 5.20: Effect of baking time on the extraction of (a) major elements and (b) selected REEs from sintered CFA-SR by baking at 70℃ followed by water leaching for at 25℃ for 24 hours. 212

Figure 5.21: SEM micrograph analysis of sintered CFA-SR (a) before treatment and (b-c) after dry digestion in H_2SO_4 and HCl. 214

Figure 5.22: The generated concentrate after oxalate precipitation. 215

Figure 5.23: FT-IR spectrum of the generated concentrate after oxalate precipitation. 216

Figure 6.1: Standard acid base titration curve with 2 M NaOH. 224

Figure 6.2: Plot of Fe(II) oxidation over time at pH 5 and 25℃. 225

Figure 6.3: The effect of seeding on the Fe(III) recovery at pH 5 and 25℃. 226

Figure 6.4: Reddish-brown Fe(III) precipitates generated by NaOH precipitation at pH 227

Figure 6.5: XRD analysis of the Fe(III) precipitates before and after seeding at pH 5, 25 ℃. 228

Figure 6.6: The FT-IR spectra of the Fe(III) precipitates before and after seeding and CFA-MF at pH 5, 25 ℃. 229

Figure 6.7: SEM micrographs of (a)-(b) CFA-MF and (c)-(f) Fe(III) precipitates formed at pH 5, 25℃ (Cs=0, 1.0, 0.5). 231

Figure 6.8: N_2 adsorption-desorption isotherm and the respective pore diameter distribution curves for the (a) Seed material (MF) and (b)-(d) Fe(III) precipitates. 233

Figure 6.9: Solubility of the seeded Fe(III) precipitate dissolved in sulphuric acid. 234

Figure 6.10: Synthesised CFA-PFS coagulant. 235

Figure 6.11: Performance of CFA-PFS during the treatment of brewery wastewater. 237

Figure 6.12: The generated CFA secondary solid residue (CFA-SSR). 237

Figure 6.13: Particle size distribution of CFA-SSR. 238

Figure 6.14: N_2 adsorption-desorption isotherms for (a) raw CFA and (b) CFA-SSR. 240

Figure 6.15: Surface morphology of CFA-SSR showing amorphous nanoparticles and the calcium sulphates rhombohedral-like component. 241

Figure 6.16: XRD analysis of the generated CFA-SSR.....242

Figure 6.17: FT-IR spectrum for raw CFA, sintered CFA and CFA-SSR. 243

Figure 6.18: Effect of initial solution pH on the adsorption of heavy metals: Adsorbent dosage: 5 g, Agitation speed= 150 rpm, Contact time = 6 hours. 248

Figure 6.19: Effect of adsorbent dosage on metal ions using AMD effluent at pH 7, 150 rpm, ~25℃, for 6 hours. 249

Figure 6.20: Effect of contact time on the adsorption of (a) metal ions including (b) sulphate ions and solution pH in AMD effluent: pH 7, 150 rpm, ~25℃. 250

Figure 7.1: Process flowsheet for the extraction of valuable resources from CFA. 260

Figure 7.2: Annual operating cost summary of the itemised costs. 265

LIST OF TABLES

Table 1.1: A typical chemical composition of Eskom CFA, Bauxite and smelter-grade alumina....4

Table 1.2: Typical REE concentrations (mg/kg) in different CFA materials from various power plants....7

Table 2.1: Common ore deposits and minerals containing REEs (Krishnamurthy and Gupta, 2005; Castor and Hedrick, 2006)....22

Table 2.2: Industrial waste products containing REEs....24

Table 2.3: The phase composition of Eskom CFA (Shemi, 2013)....27

Table 2.4: A summary of the extraction of rare earth elements from CFA....47

Table 2.5: Solubility products of different iron oxides and oxyhyroxide (Schwertmann and Cornell, 2008)....80

Table 2.6: Common synthesised zeolites and their characteristics (Bindhu and Sugunan, 1998; Querol et al., 2002)....85

Table 2.7: Selective properties of CFA and activated CFA used in adsorption processes....86

Table 3.1: A list of reagents with their purities and suppliers....114

Table 3.2: Various parameters of the induced roller magnetic separator....121

Table 3.3: Leaching parameters and conditions for the preliminary tests using HCl and H_2SO_4....123

Table 3.4: The experimental test parameters for dry digestion-water leaching....126

Table 3.5: Leaching experimental design....128

Table 3.6: The experimental conditions for Fe(II) oxidation and precipitation....131

Table 3.7: Coagulation experimental parameters....133

Table 4.1: XRF analysis of the major chemical compositions in raw CFA....140

Table 4.2: XRD analysis of the phase compositions in raw CFA....142

Table 4.3: XRF analysis of the major chemical compositions in raw CFA, non-MF and MF....151

Table 4.4: The REE concentrations and enrichment factors after magnetic separation 152

Table 4.5: Phase composition analysis of CFA and sintered CFA at different ratios.....156

Table 4.6: ICP-MS analysis of REEs in coal and sintered CFA.....158

Table 4.7: The major chemical compositions in coal and sintered CFA at 4:4:2.....159

Table 5.1: Experimental variables and their coded levels 184

Table 5.2: The percentage extraction of Al using 2^4 full factorial designs.....185

Table 5.3: Analysis of variance for selected factorial model.....186

Table 5.4: Observed percentage extraction of Al using CCRD.....189

Table 5.5: Analysis of variance for the re-fitted quadratic model 190

Table 5.6: Aluminium extraction at optimum leaching conditions from sintered CFA 191

Table 5.7: Elemental analysis of the major components in a CFA leach liquor.....192

Table 5.8: Extraction of Ti with Primene/Shellsol D70 in a sulphate system 194

Table 5.9: CFA leach liquor before and after Al and Ti extraction.....197

Table 5.10: Concentration of selected REEs in CFA leach liquor during purification 198

Table 5.11: XRF analysis of synthesised Al_2O_3 and the required smelter-grade 199

Table 5.12: XRF analysis of the synthesised TiO_2 compared with pigment grade and Degussa P25 quality 200

Table 5.13: Textural properties of TiO_2 calcined at 500℃ 202

Table 5.14: Chemical composition of major elements in sintered CFA-SR.....204

Table 5.15: Bulk chemical composition of the oxalate precipitate.....215

Table 6.1: Composition of CFA leach liquor before and after Fe(III) precipitation 226

Table 6.2: Textural properties of CFA-MF and Fe(III) precipitates before and after seeding 232

Table 6.3: Chemical composition of CFA-PFS 235

Table 6.4: Characteristics of brewery wastewater 236

Table 6.5: Texture properties of the generated CFA-SSR, commercial adsorbent and industrial by-products 239

Table 6.6: Assignments of infrared wavenumbers for raw CFA, sintered CFA and CFA-SSR 243

Table 6.7: Chemical composition of the generated CFA-SSR and industrial by-products ..244

Table 6.8: The pH_{PZC} value for raw CFA and CFA-SSR 245

Table 6.9: Chemical composition of raw AMD and AMD-effluent.....246

Table 6.10: Comparison of maximum adsorption efficiency in wastewater by CFA-SSR and industrial by-produtcs 251

Table 7.1: Operation parameters and the equipment used in the process flowsheet 261

Table 7.2: Stream summary for processing CFA.....262

Table 7.3: Material requirements and costs 263

Table 7.4: Economic evaluation parameters.....264

Table 7.5: Executive Summary for the analysed process 264

Table 8.1: Evaluation of various steps in the extraction and recovery of REEs and other values from CFA.....268

ACRONYMS AND SYMBOLS

LIST OF ACRONYMS

ASTM	American Society for Testing and Materials
ANOVA	Analysis of variance
AMD	Acid mine drainage
BET	Brunauer-Emmett-Teller
BSE	Backschattered electron
COD	Chemical oxygen demand
CCRD	Central composite rotatable design
CFA	Coal fly ash
CFA-MF	Coal fly ash-magnetic fraction
CFA-PFS	Coal fly ash-polyferic sulphate
CFA-SR	Coal fly ash-solid residue
CFA-SSR	Coal fly ash-secondary solid residue
DOE	Design of Experiments
EC	Electrical conductivity
EF	Enrichment factor
FT-IR	Fourier transform- infrared spectroscopy
HREEs	Heavy rare earth elements
ICP-OES/MS	Inductively coupled plasma-optical emission spectroscopy/ mass spectroscopy
L.O.I	Loss on ignition
LREEs	Light rare earth elements
TDS	Total dissolved solids
IRMS	Induced roller magnetic separator
MF	Magnetic fraction
MS	Magnetic separation
Non-MF	Non-magnetic fraction
PSD	Particle size distribution
PZC	Point of zero charge
REEs	Rare earth elements
RSM	Response surface methodology

SX	Solvent extraction
S/L	Solid to liquid ratio
SEM-EDS	Scanning electron microscopy-energy dispersive spectroscopy
TIMA	TESCAN Integrated Mineral Analyser
UV	Ultra violet
XRD	X-ray diffraction
XRF	X-ray fluoresence

LIST OF SYMBOLS

Symbol	Unit	Definition
m	kg or g	mass
M	mol/L or ppm	Molar concentration
T	℃	Temperature
T	hr or min	Time
T	--	Magnetic field strength (Tesla)
P	Pa	Pressure
P_{O2}	Pa	Oxygen partial pressure
V	L or mL	Volume
pH	--	Potential hydrogen
pH_{pzc}	--	pH at which the surface of the adsorbent has a net-charge of zero
rmp	r/min	Agitation rate
wt.%	%	Weight percentage
%	--	Percentage
q	mg/g	Adsorption capacity
Q_{max}	mg/g	Maximum adsorption capacity at equilibrium
K_{sp}	mol/L	Solubility product
S_{BET}	m^2/g	BET surface area
V_p	cm^3/g	Pore volume
D_p	nm	Pore diameter
d	μm	Particle size diameter
NTU	--	Nephelometric turbidity units

GLOSSARY

CFA	Material generated during the coal combustion process and disposed of in landfills and ash ponds as solid waste.
Sintered CFA	Material generated by mixing CFA with lime and coal, followed by pelletisation and heating at high temperatures (>1000℃) to produce a pulverised product.
CFA-SR	A solid material generated after leaching CFA or sintered CFA.
CFA-SSR	A solid material generated as waste for disposal after a two-step leaching process.
CFA-MF	Fe-oxide (magnetite/haematite) material that contains mullite and quartz as impurities. It is recovered as the magnetic fraction during magnetic separation and further utilised as a solid seed in wastewater treatment.
CFA-PFS	Synthesised coagulants using the generated CFA Fe(III) rich solution and and CFA-MF as seeding material.
Non-MF	The non-magnetic fraction obtained after recovering Fe-oxide by magnetic separation. The material contains mullite, quartz, and amorphous components.
AMD	Mine waste solution that is acidic and has high concentrations of heavy metals (i.e. Al, Fe, Mg, Mn, Zn, and Ni).
AMD effluent	Mine waste solution that is alkaline and has high concentrations of heavy metals except Al and Fe.

1 INTRODUCTION

1.1 Background

Coal is a primary energy resource that is generally regarded as the cheapest compared to oil and natural gas. Due to the impact of global warming, coal-based resources are being revised to mitigate the large CO_2 emissions from coal power plants. In line with the Paris climate goals, High-Efficiency, Low-Emission (HELE) coal combustion has been identified as a "clean" potential technology and is considered a key aspect of energy transformation (Nicol, 2013; Harris et al., 2019; Ali et al., 2021). However, such a transition requires the reconstruction and upgrading of old power plants, which rely heavily on a sound policy framework and strong financial support (Ali et al., 2021). In addition to coal, "green" energy solutions, such as hydropower and nuclear energy, are considered alternatives with the potential to achieve net-zero emissions (Winkler, 2005). In South Africa, over 80% of the energy mix comes from coal (Eskom, 2016). Therefore, energy transformation remains a mammoth task.

Eskom Holdings is the main power utility in South Africa, with 15 coal-based power plants in the country. In the coal combustion process, 34 million tonnes of coal combustion waste (CCW) are generated annually, with approximately 7% recycled, while the remaining waste is dumped in landfills (Eskom, 2016; SACAA, 2021). The disposal of CCW as a primary management technique is a major concern, resulting in environmental pollution, limited land storage, and water shortages during ash slurry disposal (Zhang, 2014; Reynolds-Clausen and Singh, 2017; Harris et al., 2019). The alternative strategy to alleviate these disposal concerns is beneficiation. **Figure 1.1** shows a summary of CCW management and alternative beneficiation methods.

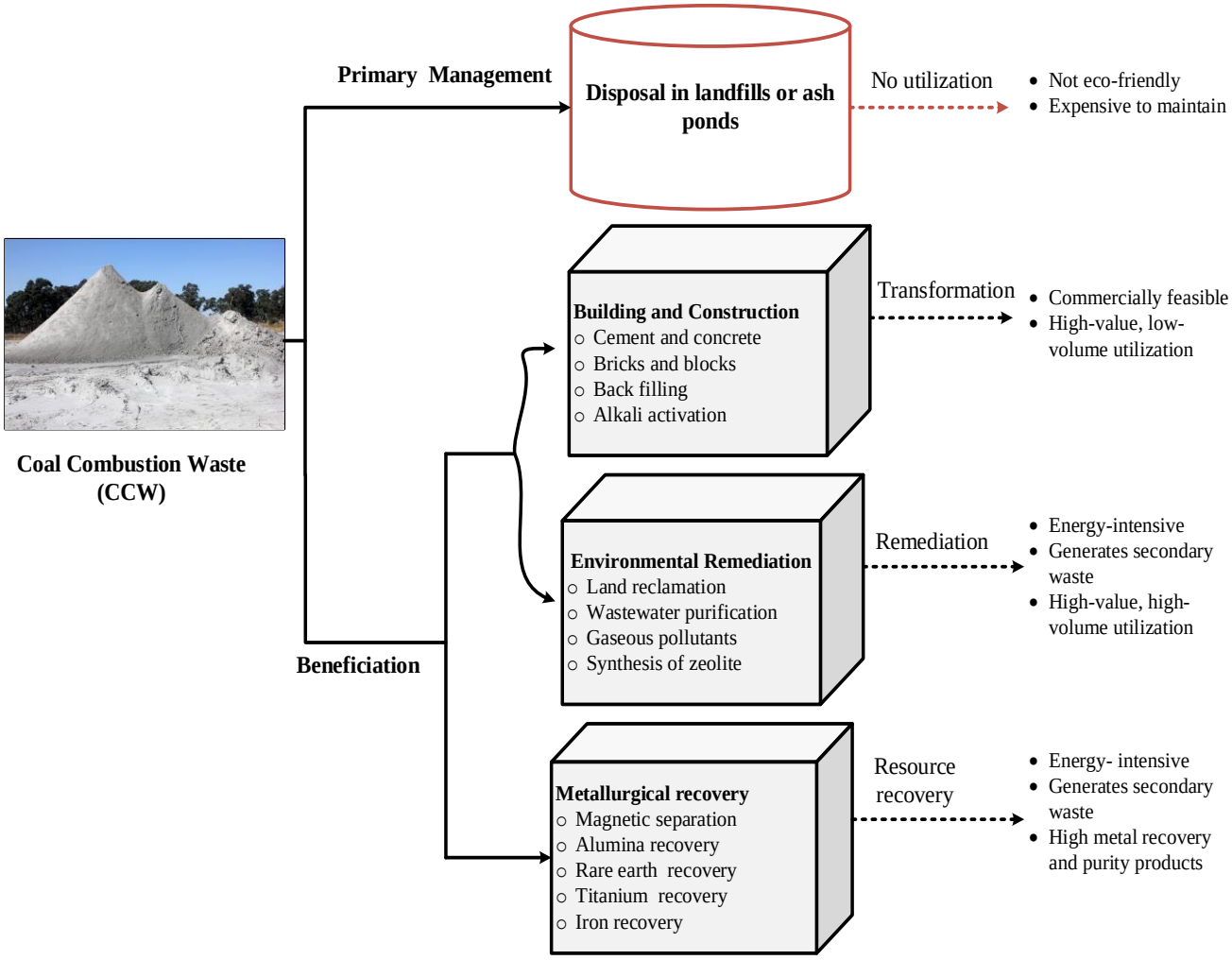

Figure 1.1: A schematic presentation of CCW management and beneficiation alternatives.

1.1.1 Potential utilisation of CFA

A significant part of CCW is coal fly ash (CFA). The South African CFA is defined as an aluminosilicate material that contains hollow cenosphere particles, has a fine texture, and alkaline pH (8-11) (Sakamoto et al., 2003; Tishmack and Burns, 2004). It is commercially utilised in the construction industry and is regulated by the South African National Standards (SANS) 50197-1:2000. In this sector, it can be applied as a raw feed or added as a supplementary material, with the amount ranging from 5-35% (Afrisam, 2009; Arp et al., 2018). While the application of CFA is feasible in the construction industry (i.e. cement and concrete), large quantities are still disposed of, resulting in environmental concerns as described in the section above. Therefore, the application of CFA in this sector offers high-value, but a low-volume utilisation rate. To increase the utilisation of CFA in the construction

industry, alternatives such as high-volume fly ash concrete (HVFC, 50% CFA) and geopolymers (100% CFA) are extensively researched (Aggarwal et al., 2010; Meesala et al., 2020). However, these high proportions of CFA have not yet been regulated or commercialised. Nonetheless, CFA has also found value as a resource in wastewater treatment and alumina production. As can be inferred from the following subsections, both alternatives have high-value and high-volume utilisation of CFA.

Wastewater treatment

Coal power plants are the major water consumers and polluters by generating acidic to neutral wastewater. The conventional remediation of wastewater on a commercial scale involves active chemical neutralisation, as illustrated in **Figure 1.2**. In this process, lime (CaO) is typically added to wastewater to neutralise, precipitate, and adsorb impurities such as SO_4^{2-} and heavy metals (i.e. Al and Fe) (Johnson and Hallberg, 2005). The substitution of lime with CFA is among the most innovative and efficient alternatives. Such a process has been patented and accepted by the South African Water Research Commission (WRC Report No. 2129/1/18). The process is developed to treat neutral mine water (NMW, pH 8) and acid mine drainage (AMD, pH 2) (Madzivire et al., 2015; Kalombe et al., 2020). During pilot plant commissioning, it was also noted that small quantities of CaO and $Al(OH)_3$ (seeding materials) are necessary to improve the purification capacity of AMD (Kalombe et al., 2020).

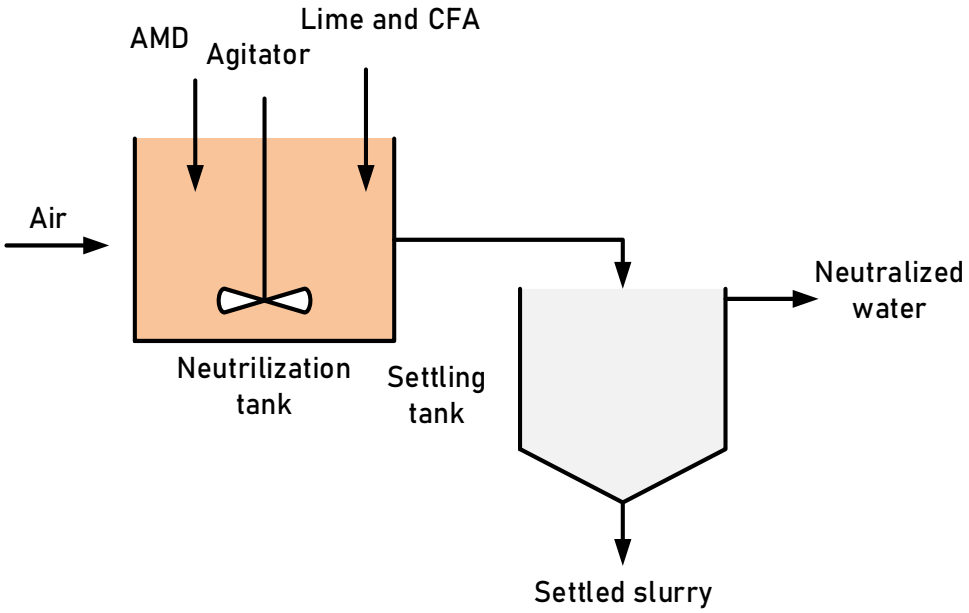

Figure 1.2: Treatment of AMD with lime and CFA.

The treatment of mine water with CFA can enable coal power plants to comply with waste treatment regulations and achieve zero-liquid discharge (Kruger and Krueger, 2005). However, in the treatment process, the settled slurry has been identified as a secondary solid waste (SSW) that could potentially pollute the environment. Thus far, the possible application of SSW as a starting material in zeolite synthesis and geopolymers has been investigated (Petrik et al., 2003; Vadapalli et al., 2008; Somerset et al., 2008; Madzivire et al., 2015; Kalombe et al., 2020).

Alumina production

The abundance of aluminium in CFA has resulted in the extensive research on its utilisation as an alternative source of alumina, apart from bauxite deposits (Yao et al., 2014; Sibanda et al., 2016). The South African CFA contains 25-30 wt.% Al_2O_3, which is a competitive source of alumina after bauxite (30-60 wt.% Al_2O_3). The extraction of alumina from CFA could also be beneficial for South Africa. Despite having a well-established smelter industry that imports and refines alumina on a commercial scale, there are no known exploitable deposits in the country. A typical chemical composition of Eskom CFA and bauxite is presented in **Table 1.1**, along with the grade required for smelter processing (Authier-Martin et al., 2001; Sibanda et al., 2016).

Table 1.1: A typical chemical composition of Eskom CFA, Bauxite and smelter-grade alumina

Components	Eskom CFA, wt. %	Bauxite, wt. %	Smelter-grade, wt. %
SiO_2	45 - 60	<0.5 - 10	0.005-0.025
Al_2O_3	25 - 30	30 - 60	99.3-99.7
Fe_2O_3	4 - 6	1 - 30	0.005-0.020
TiO_2	1.3 - 1.7	<0.5 - 10	0.001-0.008
CaO	3 - 11	0.1 - 2.0	<0.005-0.020
P_2O_5	0.3 - 1.1	0.02 - 1.1	<0.0001-0.0015
A:S	> 9	1-2	--

--Not available

The most technical and economical process for bauxite processing is the Bayer process (Authier-Martin et al., 2001; Shemi et al., 2015). During processing, bauxite is leached in sodium hydroxide at elevated temperature and pressure to form sodium aluminate, as shown in **Equation 1.1**. The aluminate solution is then directly crystallised to produce aluminium

hydroxide, as shown in **Equation 1.2**, and calcined to obtain smelter-grade alumina, as shown in **Equation 1.3**. This process is selective for impurities such as Fe and Ti. However, it is only feasible for materials with an alumina-to-silica (A/S) mass ratio above 9 (Hollapa and Wijk, 2014; Ndlovu et al., 2017).

$$Al_2O_{3(s)} + 2NaOH_{(aq)} \rightarrow 2NaAlO_{2(aq)} + 3H_2O \quad \textbf{1.1}$$

$$2NaAlO_{2(aq)} + 4H_2O \rightarrow 2Al(OH)_{3(s)} + 2NaOH_{(aq)} \quad \textbf{1.2}$$

$$2Al(OH)_{3(s)} \rightarrow Al_2O_{3(s)} + 3H_2O \quad \textbf{1.3}$$

Due to the low solubility of silica in acidic solutions, acid leaching has been extensively studied as an ideal option for alumina processing. However, CFA is a challenging material to process. The silica content can range from 40-60 wt.%, which can result in silica gel that is difficult to manage. Additionally, the refractory mullite ($Al_6Si_2O_{13}$) contains approximately 70 wt.% Al_2O_3, which can only be treated by pyrometallurgical processes (Kelmers et al., 1982; Matjie et al., 2005; Shemi et al., 2015). Nevertheless, the lime-sinter and lime-sulfur-carbon-sinter methods have successfully processed CFA for alumina extraction of up to 90 wt.% (Yao et al., 2014; Sibanda et al., 2016). For example, in the sinter-H_2SO_4 leach process, CFA is thermally treated at 1000-1100℃ by mixing it with lime or soda to alter the mullite crystal structure into a more soluble form such as anorthite or plagioclase, as shown in **Equation 1.4**. This transformation is then followed by acid leaching, as shown in **Equation 1.5** (Kelmers et al., 1982; Matjie et al., 2005; Shemi et al., 2015).

$$3Al_2O_3 \cdot 2SiO_{2(s)} + 3CaO_{(s)} + 4SiO_{2(s)} \rightarrow 3(CaO \cdot Al_2O_3 \cdot 2SiO_2)_{(s)} \quad \textbf{1.4}$$

$$CaO \cdot Al_2O_3 \cdot 2SiO_{2(s)} + 4H_2SO_{4(aq)} \rightarrow Al_2(SO_4)_{3(aq)} + CaSO_{4(s)} + 2SiO_{2(s)} + 4H_2O \quad \textbf{1.5}$$

Pilot plants based on the sinter-leach processes were commissioned in China for alumina processing using CFA. However, recovering only alumina as a saleable product proved to be

neither economical nor sustainable (Yao et al., 2014; Sibanda et al., 2016; Luo et al., 2020). One challenge encountered during the sinter-alkaline leach process was the limited applications of the residual silicate, which could not contribute to profit. In the sinter-H_2SO_4 leach process, high quantities of Fe and Ti were co-extracted with Al, which consequently required downstream purification, adding to the processing costs (Sibanda et al., 2016; Luo et al., 2020).

A sustainable process was defined by Sibanda et al. (2016) as a process that can generate more than one saleable product and minimise waste disposal. As a result, the process will generate revenue and offset the processing costs.

1.1.2 Motivation of the study

Rare earth elements (REEs) are considered "strategic and critical" due to their unique properties. Minable deposits are found in China, South Africa, Australia, India, and the United States. However, the REE production remains a small-scale enterprise, as only a few countries can beneficiate them up to the refining stage. For instance, apart from China, Molycorp Mountain Pass (USA) and Lynas Mount Weld (Australia) possess the capability to separate and refine REEs. According to the US Geological Survey report of 2020, China accounts for nearly 95% of the REE production, while consuming 75% within its borders (Cordier, 2022). This dominance resulted in a Chinese monopoly in 2010, as evidenced by the limited export quotas and price volatility (Golev et al., 2014; De Lima and Leal Filho, 2015). To mitigate the potential risks associated with an inadequate REE supply, extensive research is being conducted to identify alternative potential resources outside primary deposits. Thus, the extraction of REEs from secondary resources is mainly for a sustainable supply rather than seeking a cost-effective alternative. Secondary resources such as electronic waste, bauxite residue (red mud), phosphogypsum waste, and CFA are being extensively investigated for the extraction and recovery of REEs (Kumari et al., 2018; De Lima and Leal Filho, 2015). In South Africa, CFA is a potential alternative that also offers a solution for reducing environmental pollution. Typical concentrations of REEs found in CFA from various power plants are presented in **Table 1.2**.

Table 1.2: Typical REE concentrations (mg/kg) in different CFA materials from various power plants

Element, ppm	Tutuka power station, SA[1]	Polish power plant, Poland[2]	Junga power plant, China[3]	Power plant in Kentucky, USA[4]
Scandium-Sc	26.50	30.00	23.0	42.39
Yttrium-Y	64.87	48.50	54.2	107.64
Lanthanum-La	91.36	59.60	104.3	108.25
Cerium-Ce	182.42	123.20	178.0	212.20
Preseodymium-Pr	19.72	13.74	21.5	--
Neodymium-Nd	71.76	53.50	72.5	88.13
Samarium-Sm	14.38	11.10	13.5	18.68
Europeium-Eu	6.65	2.40	2.39	3.88
Gadolium-Gd	12.62	8.93	11.7	18.81
Terbium-Tb	2.68	1.50	1.83	2.95
Dyspresium-Dy	11.91	8.34	10.76	17.46
Holmium-Ho	2.35	1.77	2.13	3.54
Erbium-Er	6.65	4.53	6.17	9.88
Tholium-Tm	0.95	0.75	0.56	1.40
Ytterbium-Yb	6.5	4.55	3.93	8.82
Lutetium-Lu	0.93	0.68	0.55	1.31
Total (REEs)	**522.25**	**373.90**	**507.05**	**645.34**

[1]Akinyemi et al., 2012; [2]Franus et al., 2015; [3]Dai et al., 2010; [4]Hower et al., 2019

The South African National Mineral Research Organisation (Mintek) launched the South African Centralised Refinery (SACREF) for REEs in 2016. This project aims to develop a complete mining value chain for the separation and refining of REEs in South Africa. Potential deposits that have already been identified include the phosphogypsum waste dump, Steenkampskraal monazite-apatite-quartz, Zandkopsdrift, and Phalaborwa carbonatite deposits (MINTEK, 2019; MINTEK, 2020). CFA could potentially also be used as feed concentrate in the SACREF process.

The main challenge in processing REEs, either from primary or secondary resources, is their low concentrations and dispersed distribution (Krishnamurthy and Gupta, 2005; Mukaba et al., 2021). Therefore, the extraction of REEs along with Al, Fe, and Ti could potentially make CFA processing sustainable. The sinter-H_2SO_4 leach process provides such an alternative due to the high co-extraction of Fe and Ti, which can be recovered as saleable products (Shemi et al., 2015; Rampou et al., 2017; Rushwaya and Ndlovu, 2017). However, the extraction of REEs using H_2SO_4 in CFA has been reported to yield low recoveries (Kashiwakura et al., 2013; Świnder et al., 2017). As an alternative, HCl is successfully used as a lixiviant to extract REEs from CFA (Cao et al., 2018; King et al., 2018). However, large quantities of HCl are not economically viable. The boiling point of HCl decreases when the molarity is high. For example, at 3 M HCl, the boiling point is ~103°C, while at 12 M HCl, it is ~48°C. Consequently, it forms a corrosive mist and requires expensive equipment (Perry, 1984; Shemi et al., 2015; Ndlovu et al., 2017).

This study sought to develop a comprehensive method for recovering REEs, Al, Fe, and Ti as saleable products. Dry magnetic separation is first utilised to recover Fe-oxide (magnetite/haematite). Sulphuric acid is used as a leaching reagent for selective metal extraction through a two-step leaching process. In the first stage, the sinter-H_2SO_4 leach process is utilised for the extraction of Al, Fe, and Ti. The second leaching stage involves the extraction of REEs from the sintered CFA solid residue (CFA-SR) using the dry digestion-water leach process. A combined solvent extraction, crystallisation, and precipitation process is further utilised to produce Fe-based coagulants, high-purity TiO_2, smelter-grade Al_2O_3, and REE concentrate. The resulting CFA secondary solid residue (CFA-SSR) is further characterised as a potential adsorbent for wastewater treatment to minimise waste disposal.

1.2 Problem Statement

Although the application of CFA is feasible in the construction sector, large quantities are still being disposed of, creating an environmental problem. CFA can also be a valuable resource for extracting alumina on a commercial scale. The biggest drawback thus far is the relatively high costs associated with processing alumina as the sole product.

1.3 Research Aim and Objectives

More than one resource recovery from the processing of CFA could potentially offer sustainable solutions by generating revenue and reducing environmental pollution. Therefore, the aim of this study is to explore the extraction and recovery of the following:

1. Al_2O_3 for smelter-grade production
2. Poly-ferric sulphate coagulants for wastewater treatment
3. TiO_2 (anatase or rutile) for wastewater treatment
4. REE concentrate for the production of individual oxides
5. Silica-rich material for wastewater treatment

The specific objectives of the study are as follows:

i. Identify the phase distribution of Al, Fe, Ti, and REEs in CFA.
ii. Investigate the extraction of Fe-oxide (magnetite/haematite) using magnetic separation.
iii. Investigate the optimum leaching conditions for the extraction of Al, Fe, Ti, and REEs from CFA.
iv. Investigate the possibility of using an acid baking/dry digestion technique to recover REEs in CFA-SR (sintered residue).
v. Investigate the feasibility of purifying CFA leach solutions using a combination of solvent extraction (SX), precipitation, and crystallisation.
vi. Analyse the purity of the generated CFA-SSR (silica-rich material) and determine its feasibility for wastewater treatment.

vii. Develop a process flow sheet based on the work done and conduct an economic analysis.

1.4 Research Hypothesis and Questions

It is hypothesised that a shift from extracting a single product (alumina) to extracting multiple products may result in an economically feasible process. Therefore, the extraction and recovery of REEs, Fe, and Ti, in addition to Al, are evaluated using the sinter-H_2SO_4 leach process and an integrated purification process.

The research study will also attempt to answer the following questions:

1. What is the mineralogical distribution of REEs, Fe, and Ti in CFA (i.e. raw CFA, sintered CFA, and sintered CFA-SR), and how are these elements associated with the major phase compositions?
2. What is the effect of calcium sulphate on metal extraction when using H_2SO_4 as a lixiviant, and can REEs be extracted using the sinter-H_2SO_4 leaching process?
3. Can the dry digestion technique be used as an alternative method to the sinter-H_2SO_4 leach process for the extraction of REEs which are precipitated with calcium sulphate in CFA-SR (sintered residue)?
4. Can REEs be selectively separated from Al, Fe, Ti, and Si?
5. Can Fe be recovered by oxidation and precipitation processes and further used to generate Fe-based coagulants for wastewater treatment?
6. What are the physicochemical characteristics of the generated CFA-SSR, and can the material be proposed to add value in wastewater treatment?
7. Can more than one valuable resource be economically generated from CFA processing?

1.5 Significance of the Study

The economic benefits and practical recovery of multiple resources in alumina processing from CFA have not been widely explored. This work presents an opportunity to expand on current knowledge by including the extraction of REEs. The study further contributes to waste disposal management by repurposing the generated by-products into coagulants and adsorbents:

1. In addition to alumina, the extraction of the REEs using the sinter-H_2SO_4 leach process is significant. The extraction efficiency of alumina can reach up to 88 wt.% at high acid concentrations (>3 M H_2SO_4) and temperature conditions (>70°C) (Shemi et al., 2015). Under these leaching conditions, the REEs are also commercially recovered as double salts (Krishnamurthy and Gupta, 2005). Therefore, the solubility difference between these metals is a fundamental conceptual theory for selective leaching. In addition, the mineralogical distribution of REEs significantly contributes to their solubility. As a result, the study also provides insights into the distribution of REEs in CFA and therefore, the influence on their leaching behaviour.
2. The production of Fe-based coagulants from the CFA leached liquor can be easily incorporated into mine water treatment processes, generating revenue and subsidising treatment costs. The contribution to scientific knowledge includes:
    i. Recycling the magnetic fraction (Fe-oxide) as seeding material to improve filtration in Fe(III) recovery through oxidation and precipitation processes.
    ii. Generating coagulants and evaluating their potential application for commercial consideration.
3. The generated CFA-SSR after the leaching processes can be recycled to minimise waste disposal. Therefore, a detailed characterisation of CFA-SSR is presented for its potential contribution to wastewater treatment.
4. A preliminary cost analysis of the proposed process flowsheet is also presented to indicate the feasibility of extracting multiple valuable resources from CFA. This evaluation will provide an opportunity to assess and improve on scaling up.

1.6 Deliverables

The following are the deliverables of the study:

i. A literature review on the chemistry of REEs, occurrence, extraction and recovery from primary deposits and silica-rich materials such as CFA.
ii. A literature review on the utilisation of CFA as an adsorbent and coagulant in wastewater treatment.
iii. A two-step sulphate leach process for selective REEs extraction from Al, Fe, Ti, and Si.
iv. Synthesis of smelter-grade alumina, high-purity titania, and REE concentrate.
v. Production of Fe-based coagulants from CFA leach liquor using the magnetic fraction as seeding material for ferrihydrite precipitation.
vi. Characterisation of CFA materials for REEs recovery and wastewater treatment.
vii. A designed process flowsheet and preliminary cost analysis.

1.7 Research Methodology

The primary tasks involved in the research approach included the following:

1.7.1 Literature review

A literature review was conducted to understand the chemistry of REEs, their production using conventional hydrometallurgical processes, and current progress on metal extraction from CFA. Furthermore, the review was extended to include the utilisation of CFA as an adsorbent and coagulant in wastewater treatment, thus the implications on the generated CFA-SSR and Fe-based coagulants.

1.7.2 Experimental design

Based on the literature survey, an experimental design was formulated for the extraction and recovery of Al, Fe, Ti, and REEs. The experimental test work involved the following:

1. Material characterisation
2. Fe reduction from CFA by magnetic separation
3. Dissolution behaviour of REEs in H_2SO_4 and HCl
4. Identification and optimisation of the sinter-H_2SO_4 for alumina production
5. Extraction and recovery of REEs from sintered CFA-SR using a dry-digestion technique and precipitation
6. Production of alumina, titania and Fe-based coagulants from sintered CFA leach liquor by integrated SX, crystallisation and oxidation-precipitation
7. Characterisation of CFA-SSR for potential wastewater treatment
8. Testing the CFA-SSR and Fe-base coagulants for wastewater treatment

1.7.3 Data analysis

A series of laboratory tests were conducted under various experimental conditions in line with the experimental design. The output data were used to determine the efficient selective extraction parameters for Al, Fe, Ti, and REEs. In addition, the tests measured the efficiency of producing Fe-based coagulants and evaluated their effectiveness. The output data were also used to recommend a feasible application of the generated CFA-SSR.

1.7.4 Conclusions and recommendations

The evaluation of the study follows data analysis to conclude and make recommendations. The conclusions present significant findings regarding the set objectives, while the recommendations highlight some of the limitations and provide suggestions for subsequent studies.

1.8 Thesis Layout

This section provides a preview of the chapters in this thesis. A thesis layout is also presented in **Figure 1.3**.

Chapter 1 *Introduction***:** A general introduction to the research study is presented in this chapter. This includes the background of the study, problem statement, research objectives, and the overall scope of the research.

Chapter 2 *Literature Review***:** A comprehensive survey on the extraction and recovery of REEs and other valuable resources from CFA is presented in this chapter. It covers various aspects, such as the chemistry of REEs, their occurrence, and conventional processing techniques. The survey also extends to the extraction and recovery of Al, Fe, Ti, and REEs from CFA. Furthermore, the chapter also reviews the utilisation of CFA as a coagulant and adsorbent in wastewater treatment.

Chapter 3 *Material and Methods***:** The reagents and techniques used for material characterisation are described in detail. The experimental procedures and typical setups are also detailed.

Chapter 4 – 6 *Results and Discussion***:** These chapters present the laboratory findings and discussions thereof. The chapters are divided as illustrated in **Figure 1.3**.

Chapter 7 – 8 *Evaluation of the Study***: Chapter 7** presents the suggested process flowsheet and the preliminary economic analysis. **Chapter 8** follows with the main conclusions of the research findings, including recommendations for future studies.

Each chapter includes a summary or conclusion to provide comprehension of the content and guide the reader towards subsequent chapters. All references used in this study are presented at the end of each chapter. The appendices, which contain the supplementary data for this study, follow the conclusions and recommendations.

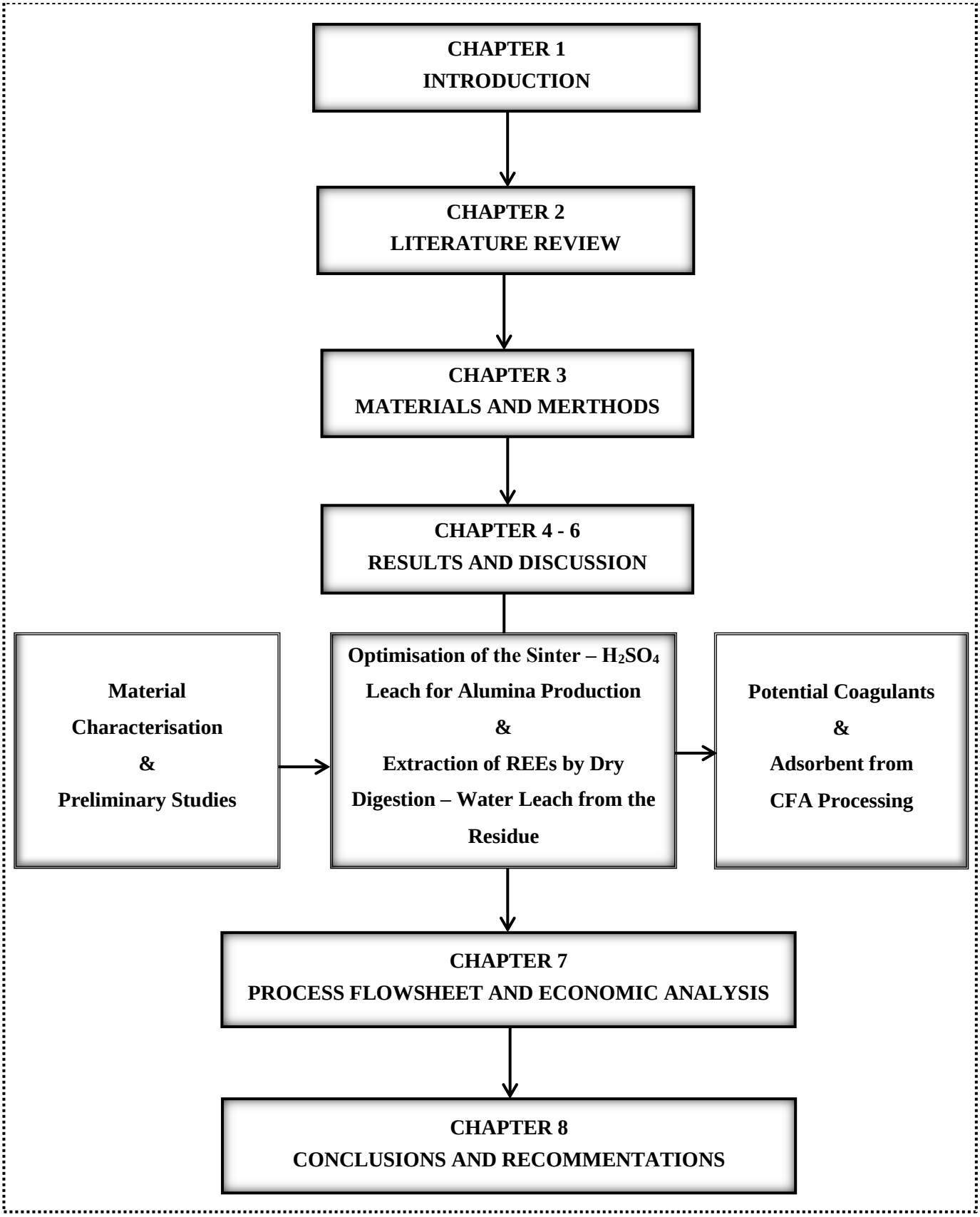

Figure 1.3: A thesis layout.

1.9 Summary

Chapter 1 gives a general introduction to the research work, including specific study objectives and the overall scope. The significance of the study, which is to expand the current knowledge base on CFA processing, is also detailed. The chapter also concludes with a brief discussion of the research methodology and thesis layout. The next chapter will discuss the literature that has been reviewed.

References

Afrisam Institute, Cement & Concrete. Available online: https://www.afrisam.co.za/uploads/documents/Cementitious_materials_for_concrete.pdf (Accessed on 06-03-2021).

Akinyemi, S., Gitari, W., Akinlua, A., Petrik, L., 2012. Mineralogy and geochemistry of sub-bituminous coal and its combustion products from mpumalanga province, South Africa. Analytical Chemistry, Krull, I.S., (Editor), InTechOpen, Rijeka, Croatia, 47-70.

Aggarwal, V., Gupta, S.M. and Sachdeva, S.N., 2010. Concrete durability through high volume fly ash concrete (HVFC) a literature review. *International Journal of Engineering Science and Technology* 2(9), 4473-4477.

Ali, H., Phoumin, H., Weller, S.R. and Suryadi, B., 2021. Cost-Benefit Analysis of HELE and Subcritical Coal-Fired Electricity Generation Technologies in Southeast Asia. *Sustainability* 13(3), 1591.

Arp, R., Bole-Rentel, T. and Jakuja, N. Greenhouse Gas Emissions Reductions for the South African Cement Sector. Available online: https://www.wwf.org.za (Accessed on 12-06-2021).

Authier-Martin, M., Forte, G., Ostap, S. and See, J., 2001. The mineralogy of bauxite for producing smelter-grade alumina. *JOM* 53, 36-40.

Cao, S., Zhou, C., Pan, J., Liu, C., Tang, M., Ji, W., Hu, T. and Zhang, N., 2018. Study on influence factors of leaching of rare earth elements from coal fly ash. *Energy and Fuels* 32(7), 8000-8005.

Cordier, D.J, 2022. Rare Earth Mineral Commodity summaries 2022. U.S Geological Survey. Available online: https://pubs.usgs.gov/periodicals/mcs2022/mcs2022.pdf (Accessed on 29-07-2023).

Dai, S., Zhao, L., Peng, S., Chou, C.-L., Wang, X., Zhang, Y., Li, D., Sun, Y., 2010. Abundances and distribution of minerals and elements in high-alumina coal fly ash from the Jungar Power Plant, Inner Mongolia, China. *International Journal of Coal Geology* 81(4), 320-332.

De Lima, I.B. and Leal Filho, W., 2015. Rare earths industry: Technological, economic, and environmental implications. Elsevier. ISBN: 978-0-12-802328-0.

Eskom, 2016. Eskom and Ash Management. Available online: https://www.eskom.co.za/Pages/Landing.aspx (Accessed on 07-03-2021).

Franus, W., Wiatros-Motyka, M.M., Wdowin, M., 2015. Coal fly ash as a resource for rare earth elements. Environ. *Environmental Science and Pollution Research* 22, 9464-9474.

Golev, A., Scott, M., Erskine, P.D., Ali, S.H. and Ballantyne, G.R., 2014. Rare earths supply chains: Current status, constraints and opportunities. *Resources Policy* 41, 52-59.

Harris, D., Heidrich, C., Feuerborn, J., 2019. Global Aspects on Coal Combustion Products. Available online: https://www.coaltrans.com/insights/article/global-aspects-on-coal-combustion-products (Accessed on 05-07-2020).

Hollapa, L. and Wijk, O., 2014. Treatise on Process Metallurgy Vol 3-Industrial Processes: Part A Ferrous Process Metallurgy. Elsevier. ISBN: 978-0-08-100000-7.

Hower, J.C., Qian, D., Briot, N.J., Santillan-Jimenez, E., Hood, M.M., Taggart, R.K., Hsu-Kim, H., 2019. Nano-scale rare earth distribution in fly ash derived from the combustion of the fire clay coal, Kentucky. *Minerals* 9(4), 206.

Johnson, D.B. and Hallberg, K.B., 2005. Acid mine drainage remediation options: a review. *Science of the Total Environment* 338(1-2), 3-14.

Kalombe, R.M., Ojumu, T.V., Katambwe, V.N., Nzadi, M., Bent, D., Nieuwouldt, G., Madzivire, G., Kevern, J. and Petrik, L.F., 2020. Treatment of acid mine drainage with coal fly ash in a jet loop reactor pilot plant. *Minerals Engineering* 159, 106611.

Kashiwakura, S., Kumagai, Y., Kubo, H. and Wagatsuma, K., 2013. Dissolution of rare earth elements from coal fly ash particles in a dilute H_2SO_4 solvent. *Open Journal of Physical Chemistry* 3(2), 69-75.

Kelmers, A., Canon, R., Egan, B., Felker, L., Gilliam, T., Jones, G., Owen, G., Seeley, F. and Watson, J., 1982. Chemistry of the direct acid leach, calsinter, and pressure digestion-acid leach methods for the recovery of alumina from fly ash. *Resources and Conservation* 9, 271-279.

King, J.F., Taggart, R.K., Smith, R.C., Hower, J.C. and Hsu-Kim, H., 2018. Aqueous acid and alkaline extraction of rare earth elements from coal combustion ash. *International Journal of Coal Geology* 195, 75-83.

Krishnamurthy, N. and Gupta, C.K., 2005. Extractive metallurgy of rare earths. CRC press, New York. ISBN: 0-415-33340-7.

Kruger, R.A. and Krueger, J.E., 2005. Historical development of coal ash utilization in South Africa. In Proceedings of the World Coal Ash (WOCA), 11-15 April 2005. Lexington, KY, USA. Available online: https://p2infohouse.org/ref/45/44905.pdf (Accessed on 03-04-2021).

Kumari, A., Jha, M.K. and Pathak, D., 2018. Review on the processes for the recovery of rare earth metals (REMs) from secondary resources. Presented at the TMS Annual Meeting & Exhibition, Springer, 53-65.

Luo, Y., Wu, Y., Ma, S., Zheng, S., Zhang, Y. and Chu, P.K., 2020. Utilization of coal fly ash in China: a mini-review on challenges and future directions. *Environmental Science and Pollution Research* 28, 1-14.

Madzivire, G., Gitari, W., Vadapalli, V. and Petrik, L., 2015. Jet loop reactor application for mine water treatment using fly ash, lime and aluminium hydroxide. *International Journal of Environmental Science and Technology* 12, 173-182.

Matjie, R., Bunt, J. and Van Heerden, J., 2005. Extraction of alumina from coal fly ash generated from a selected low rank bituminous South African coal. *Minerals Engineering* 18(3), 299-310.

Meesala, C.R., Verma, N.K. and Kumar, S., 2020. Critical review on fly-ash based geopolymer concrete. *Structural Concrete* 21(3), 1013-1028.

Mintek Annual Integrated Report, 2019. Available online: https://mintek.co.za/media/annual-report/annual-report-2019.pdf (Accessed on 03-04-2021).

Mintek Annual Integrated Report, 2019/2020. Available online: https://mintek.co.za/media/annual-report/annual-report-2020.pdf (Accessed on 18-01-2024).

Mukaba, J.L., Eze, C.P., Pereao, O. and Petrik, L.F., 2021. Rare earths' recovery from phosphogypsum: An overview on direct and indirect leaching techniques. *Minerals* 11(10), 1051.

Ndlovu, S., Simate, G.S. and Matinde, E., 2017. Waste Production and Utilization in the Metal Extraction Industry; CRC Press: Boca Raton. ISBN-13: 978-1-4987-6729-3.

Nicol, K., 2013. Status of Advanced Ultra-Supercritical Pulverised Coal Technology; IEA Clean Coal Centre: London, UK. ISBN: 978-92-9029-549-5.

Perry, R., 1984. Perry's Chemical Engineers' Handbook; McGraw. ISBN: 0-07-049841-5.

Petrik, L.F., White, R.A., Klink, M.J., Somerset, V.S., Burgers, C.L. and Fey, M.V., 2003. Utilization of South African fly ash to treat acid coal mine drainage, and production of high-quality zeolites from the residual solids. Proceedings of the International Ash Utilization Symposium, 20-23 October 2003, Lexington, KY, USA.

Rampou, M., Ndlovu, S. and Shemi, A., 2017. Purification of coal fly ash leach liquor for alumina recovery using an integrated precipitation and solvent extraction process. *Journal of Sustainable Metallurgy* 3, 782-792.

Reynolds-Clausen, K. and Singh, N., 2019. South Africa's power producer's revised coal ash strategy and implementation progress. *Coal Combustion Gasification Products* 11, 9-11.

Rushwaya, M.J. and Ndlovu, S., 2017. Purification of coal fly ash leach liquor by solvent extraction: Identification of influential factors using Design of Experiments. *International Journal of Mineral Processing* 164, 11-20.

South African Coal Fly Ash Association (SACAA) 2021. Available online: https://www.sacaa.co.za (Accessed on 21-10-2021).

Sakamoto, T., Shibata, K., Takanashi, K., Owari, M. and Nihei, Y., 2003. Analysis of surface composition and internal structure of fly ash particles using an ion and electron multibeam microanalyzer. *Applied Surface Science* 203-204, 762-766.

Shemi, A., Ndlovu, S., Sibanda, V. and Van Dyk, L.D., 2015. Extraction of alumina from coal fly ash using an acid leach-sinter-acid leach technique. *Hydrometallurgy* 157, 348-355.

Sibanda, V., Ndlovu, S., Dombo, G., Shemi, A. and Rampou, M., 2016. Towards the utilization of fly ash as a feedstock for smelter grade alumina production: A review of the developments. *Journal of Sustainable Metallurgy* 2, 167-184.

Somerset, V., Petrik, L. and Iwuoha, E., 2008. Alkaline hydrothermal conversion of fly ash precipitates into zeolites 3: the removal of mercury and lead ions from wastewater. *Journal of Environmental Management* 87(1), 125-131.

Świnder, H., Białecka, B. and Jarosiński, A., 2017. Recovery of rare earth elements from coal combustion fly ashes. 17th International Multidisciplinary Scientific GeoConference (SGEM) 29 June-5 July 2017, Sofia, Bulgaria. 11(1.1). DOI:10.5593/sgem2017/11.

Tishmack, J.K. and Burns, P.E., 2004. The chemistry and mineralogy of coal and coal combustion products. *Geological Society, London, Special Publications* 236, 223-246.

Vadapalli, V., Klink, M., Etchebers, O., Petrik, L., Gitari, W., White, R., Key, D. and Iwuoha, E., 2008. Neutralization of acid mine drainage using fly ash, and strength development of the resulting solid residues. *South African Journal of Science* 104(7), 317-322.

Winkler, H., 2005. Renewable Energy Policy in South Africa: Policy Options for Renewable Electricity. *Energy Policy* 33(1), 27-38.

Yao, Z., Xia, M., Sarker, P. and Chen, T., 2014. A Review of the alumina recovery from coal fly ash, with a focus in China. *Fuel* 120, 74-85.

Zhang, X., 2014. Management of Coal Combustion Wastes; IEA Clean Coal Centre: London, UK. ISBN: 978-92-9029-551-8.

2 LITERATURE REVIEW

2.1 Introduction

The rare earth elements (REEs) are a group of 17 elements, which comprise the lanthanide series (La-Lu), as well as yttrium (Y) and scandium (Sc). They are further divided into heavy-REEs (HREEs, Eu-Lu, and Y) and light-REEs (LREEs, La-Sm) as presented in **Figure 2.1**. Scandium and yttrium are frequently classified as REEs due to their occurrence in the same mineral resources and their comparable chemical characteristics (Stevenson and Nervik, 1961; Habashi, 1997; Krishnamurthy and Gupta, 2005).

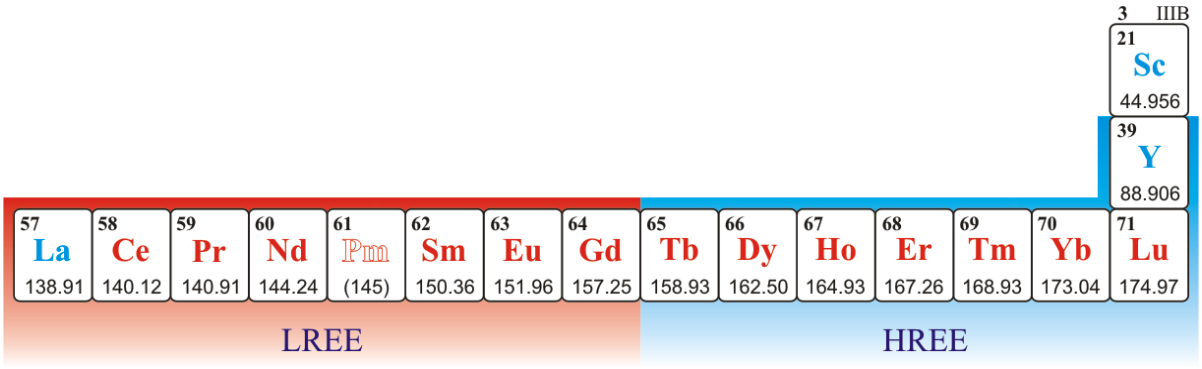

Figure 2.1: The LREEs, HREEs and Scandium (Generalic, 2019).

The emerging modern technologies, emphasising renewables and low-carbon footprint materials, heavily rely on REEs due to their value-added characteristics such as low energy consumption, miniaturisation, and high-speed performance (Balaram, 2019; Serpell et al., 2021). More than 60% of REEs are consumed as catalysts and permanent magnets (Serpell et al., 2021). In catalysis, they can mitigate the effects of greenhouse gas emissions; thus, they are used as oxidants to help convert and purify CO, NO_x, hydrocarbons, and volatile organic compounds (VOCs) (Charalampides et al., 2015). As permanent magnets, they offer a robust spin-orbit coupling, which ensures considerable magnetic hysteresis. This property makes them critical components in power generators, electric cars, and wind turbines (Skokov and Gutfleisch, 2018). The neodymium-iron-boron (Nd-Fe-B) and samarium-cobalt (Sm-Co) magnets are common REE magnets (Charalampides et al., 2015).

According to the Minerals Commodity Summary published by the United States Geological Survey (USGS), China governs the REE market, holding ~37% of the global REE reserves and consuming over 50% (Cordier, 2022; Cordier, 2023). Due to this geopolitical supply dominance, the monopoly on REE pricing and export markets has compelled consumers to explore alternative sources (Shen et al., 2020). The recycling of end-of-life products and industrial waste has, therefore, been extensively considered and researched as secondary resources for REEs (Binnemans et al., 2013; Akcil, 2019; Mukaba et al., 2021). End-of-life products can be defined as consumer goods containing REEs such as magnets, fluorescent lamps, and power batteries that end up in scrap yards. These consumer scraps can be reclaimed and further processed to manufacture new REE products (Binnemans et al., 2013; Tunsu et al., 2015). On the other hand, industrial waste products are the waste materials generated in the processing of primary ores and consequently, end up in landfills or ash ponds. Such materials have been found to contain valuable elements such as REEs, and they include coal fly ash (CFA), bauxite residue, and phosphogypsum waste (Akcil, 2019; Mukaba et al., 2021).

In this research study, CFA which is generated from the coal combustion process (CCP), is the alternative secondary source of interest. Therefore, the study aims to extract REEs and other potential values that could make CFA processing attractive. Within the context of this research project, this literature review will cover the basic chemistry of REEs, their occurrence, and conventional processing techniques. The survey will also explore the current knowledge on the recovery of value-added elements (i.e. REEs, Al, Fe, and Ti) from CFA and their potential utilisation in metal production and wastewater treatment.

2.2 Occurrence and Distribution of REEs

The REEs do not occur as native elements since they readily react with halogens and non-metals (i.e. C, H, S, O, N, and P). As a result, they occur in numerous ores as minor or major constituents. It is also noteworthy that, although they are referred to as “rare,” they are abundant in the Earth’s crust and occur in trace concentrations. As a result, the economic processing of REEs is challenging (Stevenson and Nervik, 1961; Krishnamurthy and Gupta, 2005).

2.2.1 Mineralogy of REE ores

More than 200 REE-bearing minerals have been discovered from different types of deposits, and the most economical are those associated with bastnäsite, xenotime, and monazite. Bastnäsite, $LnCO_3F$, is a primary fluoro-carbonate mineral exploited for LREEs. Monazite, $(Ln,Th)PO_4$, and xenotime, YPO_4, are the phosphate minerals. The latter is abundant in HREEs (i.e. yttrium), while monazite is mostly exploited for LREEs such as cerium and lanthanum (Habashi, 1997; Krishnamurthy and Gupta, 2005). Some of the common REE deposits and minerals are listed in **Table 2.1**.

Table 2.1: Common ore deposits and minerals containing REEs (Krishnamurthy and Gupta, 2005; Castor and Hedrick, 2006)

Ore deposits	Minerals	Typical compound
Phosphates	Apatite	$(Ca,Ln)_5(PO_4)_3(Cl,F,OH)$
	Xenotime	**YPO_4**
	Kolbeckite	$ScPO_4 \cdot H_2O$
	Monazite	**$(Ln,Th)PO_4$**
	Florencite	$(Ln)Al_3(PO_4)_2(OH)_6$
Carbonatite	Synchysite	$Ca(Ln)(CO_3)_2F$
	Bastnäsite	**$LnCO_3F$**
Silicate	Thortveitite	$(Sc,Y)_3Si_2O_7$
	Titanite	$CaTiSiO_5$
	Zircon	$ZrSiO_4$
	Grossular	$Ca_3Al_2(SiO_4)_3$
	Allanite	$(Ca,Ce)_2(Al, Fe^{3+})_2(SiO_4)_3(OH)$
	Eudialyte	$Na_4(Ca,Ln)_2(Fe,Mn,Y)_3ZrSi_8O_{22}(OH,Cl)_2$
Complex oxides	Perovskite	$(Ca,Ln)TiO_3$
	Columbite	$(Mg,Fe,Mn)(Nb,Ta)_2O_6$
	Wolframite	$(Fe,Mn)WO_4$
	Fergusonite	$(REE)NbO_4$

Ln - Lanthanide series

The largest REE deposits are found in China, the USA, and Australia. The Bayan Obo mine in China and Molycorp Mountain Pass in the USA are the largest carbonatite complexes that contain 6% REO and 7.68% REO, respectively. Lynas Mount Weld, Australia, is a phosphate deposit that contains 17% REO (Krishnamurthy and Gupta, 2005). The REEs in these deposits are commercially exploited on a full scale, from mining up to the refining stage (see **Figure 2.8**). South Africa also hosts large REE deposits in Steenkampskraal and Zandkopsdrift (ZKD). The Steenkampskraal deposit is a monazite-apatite-quartz vein with 75% monazite and is estimated to contain 26.2 kg/t REO. The Zandkopsdrift deposit is a complex carbonatite with xenotime and monazite as the major REE-bearing minerals and contains approximately 950-kilo tonnes of REO (Jepson, 2012). These deposits will contribute significantly to the South African Centralised Refinery (SACREF) project, which aims to process the available South African REE deposits by generating a uniform feed concentrate to be refined using the yet-to-be-developed centralised facility (MINTEK, 2019).

2.2.2 REEs in secondary sources

Industrial waste products such as phosphogypsum, CFA, bauxite residue, and mine tailings are alternative secondary resources for the extraction of REEs (see **Table 2.2**). It is also noted that the concentration of REEs in these products is lower than that of primary ores. Therefore, their extraction should be done strategically to be cost-effective, efficient, and sustainable (Sibanda et al., 2016; Bisaka et al., 2017). Mintek has several research projects on the extraction of REEs from phosphogypsum for the SACREF project (MINTEK, 2019; Yahorava et al., 2016; Yahorava et al., 2018). The advantages of extracting REEs from this waste product are pollution reduction in the phosphate plants and land reclamation from disposal sites (Akcil, 2019; Mukaba et al., 2021). Consequently, CFA can also be processed for the SACREF project and alleviate some of the waste management concerns described in **Section 1.1**, **Chapter 1**. However, to add value to CFA processing at full capacity, it is important to understand the CCP and CFA mineralogy.

Table 2.2: Industrial waste products containing REEs

Waste product	Location	ΣREEs	Reference
Acid mine drainage (AMD)	Sitai coal mine, Shanxi Province, North China	61.21 µg/L	(Zhao et al., 2007)
Mine tailings	Baotou, Mongolia China	6.48 wt.%	(Wang and Liang, 2015)
Phosphogypsum	Phalaborwa, South Africa	*0.5-1.0 wt.%	(Preston et al., 1996)
Bauxite residue	Aluminium of Greece, Agios Nikolaos, Greece.	0.1 wt.%	(Borra et al., 2016)
Coal fly ash (CFA)	Eskom, South Africa	522.2 mg/Kg	(Akinyemi et al., 2012)

* Ln_2O_3

2.2.2.1 Coal Combustion Process (CCP)

Coal is a combustible and heterogeneous rock that contains both organic and inorganic materials. It originates from ancient vegetation compacted between layers of other rocks and modified by various factors, such as microbial activity, pressure, and heat over a long period (Eskom, 2016). The carbon component in coal is the major source used for energy supply. In CCP, coal is transported to a coal crusher, pulverised, and fed into a boiler furnace unit to generate electricity. The furnace combustion temperature is usually >1500°C; therefore, the mineral content in coal, such as kaolinite, calcite, and pyrite are fused, oxidised, and decomposed into secondary phase compositions quantified in CFA (Vassilev and Vassileva, 1996; McLennan et al., 2000; Tomeczek and Palugniok, 2002; Kutchko and Kim, 2006). For example, kaolinite is proposed by Shcherban et al. (1995) to decompose into mullite and quartz, as shown in **Equation 2.1**.

$$3Al_2Si_2O_5(OH)_{4(s)} \xrightarrow{>1500℃} 3Al_2O_3 \cdot 2SiO_{2(s)} + 4SiO_{2(s)} + 6H_2O \qquad \textbf{2.1}$$

As coal burns, molten ash particles form and are forced up the furnace stack by pressure, gravity, and surface tension. The lighter ash particles mix with the flue gases and move into the post-combustion zone. In this zone, the temperature is relatively low (<200°C). Once the flue gases pass through the electromagnetic precipitator, the ash particles rapidly cool and solidify into ash particles known as fly ash (CFA). Depending on the power plant design, the

flue gases are often treated to minimise air pollution. In some power plants, they are captured and stored (Vassilev and Vassileva, 1996; McLennan et al., 2000; Tomeczek and Palugniok, 2002; Kutchko and Kim, 2006). A general combustion unit at Eskom is illustrated in **Figure 2.2.**

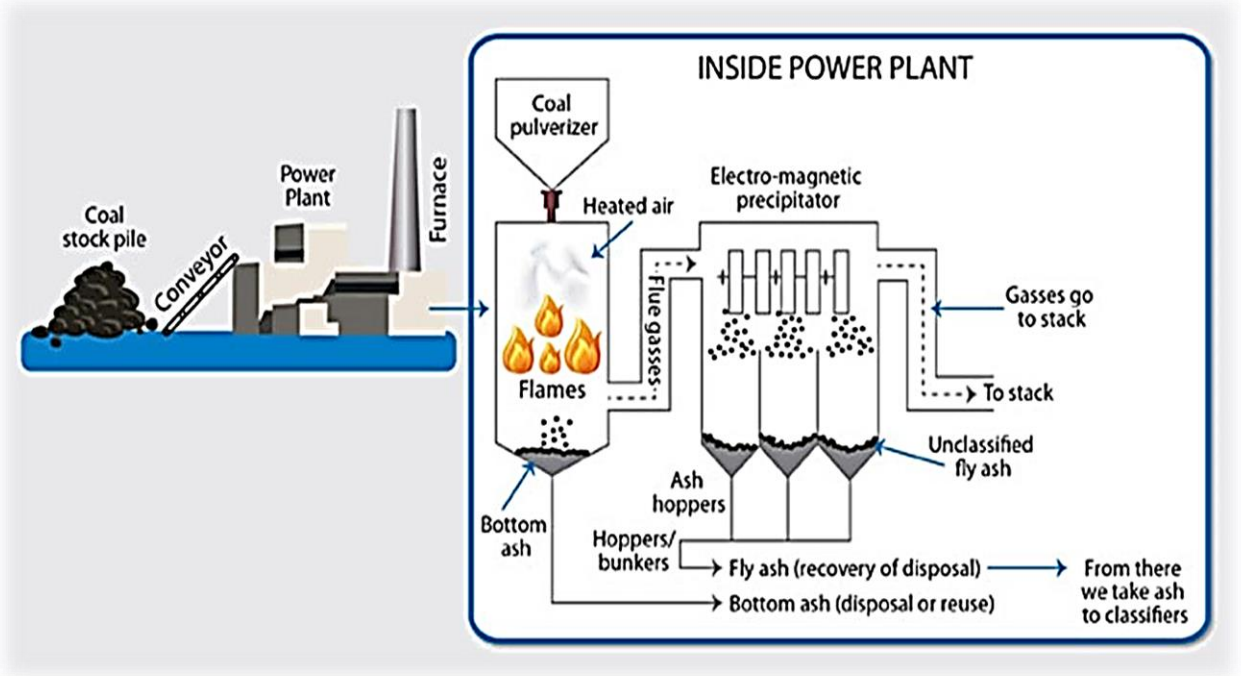

Figure 2.2: A general coal processing and combustion unit at Eskom Holdings (Eskom, 2016).

The composition of CFA is a function of the parent coal source, combustion conditions (i.e. temperature), and post-combustion conditions (i.e. cooling rate) (Campbell, 1999; Tishmack and Burns, 2004). Although Eskom runs several power plants in South Africa, over 80% of the coal is outsourced from various coal mining companies (i.e. Exxaro and Seriti) to maximise energy efficiency (Eskom, 2016). In addition, there are 19 coalfields across South Africa with the quality of coal ranging from bituminous to sub-bituminous. Therefore, the parent coal source may not always be consistent. Nonetheless, according to the South African Coal Fly Ash Association (SACAA), South Africa mostly produces Class F CFA which is pozzolanic (SACAA, 2021).

2.2.2.2 CFA mineralogy

CFA can be cenospheric and have spherical and irregular grains as shown in **Figure 2.3 (a)** and **(b)**. Due to rapid cooling in the post-combustion zone, it is also noted that CFA can be predominantly amorphous with a few common crystalline phases such as mullite, quartz, magnetite, haematite, and calcite (Tishmack and Burns, 2004; Landman, 2005; Loubser and Verryn, 2008; Shemi, 2013; Dai et al., 2014). Other minor crystalline phases have been quantified, including rutile and zircon, as presented in **Figure 2.3 (b)** (Ma et al., 2021; Van Alphen et al., 2007).

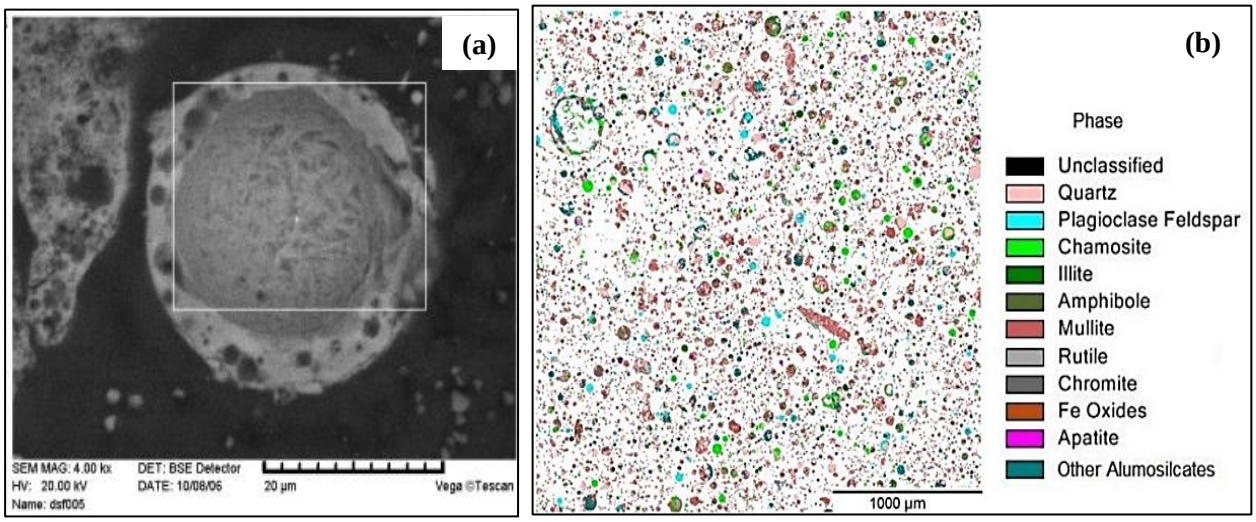

Figure 2.3: a) SEM analysis of CFA showing a solid aluminosilicate sphere with needle-like mullite crystals (Dai et al., 2010) and b) QEMSCAN analysis of CFA showing different phases (Ma et al., 2021).

In general, South African CFA can be classified as a crystalline and non-crystalline component as presented in **Table 2.3** (Kelmers et al., 1982; Ward and French, 2005; Shemi, 2013). The non-crystalline phase, also known as the amorphous phase, constitutes more than 50% of CFA and contains oxides such as SiO_2, Al_2O_3, Fe_2O_3, TiO_2, MgO, and CaO (Loubser and Verryn, 2008). The amorphous phase has shown some solubility for Al_2O_3 and Fe_2O_3 in mineral acids and alkaline solutions (for aluminium) (Kelmers et al., 1982; Shemi, 2013; Sedres, 2016). On the other hand, crystalline components such as mullite ($Al_6Si_2O_{13}$) and quartz (SiO_2) are non-reactive during direct leaching processes (with either alkaline or acid solutions) but tend to require high temperatures or high pressures to decompose (Kelmers et al., 1982; Shemi, 2013; Sedres, 2016). A typical phase composition of Eskom CFA is shown in **Table 2.3**.

Table 2.3: The phase composition of Eskom CFA (Shemi, 2013)

Phase composition	Phase, wt.%	Al_2O_3, wt.%
Amorphous	52.9	27.8
Quartz - SiO_2	13.97	--
Haematite - Fe_2O_3	0.8	--
Magnetite - Fe_3O_4	1.65	--
Mullite - $Al_6Si_2O_{13}$	30.68	72.2

--Not available

2.2.2.3 REEs in CFA

There have been several studies conducted over the years to quantify REE-bearing minerals in coal and coal waste products (i.e. CFA). In coal, REEs have been reported in organic and inorganic matter (Zhang et al., 2015; Eterigho-Ikelegbe et al., 2021). The primary REE-bearing minerals that have been quantified are monazite, xenotime, allanite, zircon, and apatite. However, REEs have also been found dispersed in major coal minerals such as kaolinite and pyrite (Roth et al., 2017; Zhang et al., 2015; Eterigho-Ikelegbe et al., 2021). Fu et al. (2022) summarised the possible occurrence of REEs in coal as presented in **Figure 2.4**.

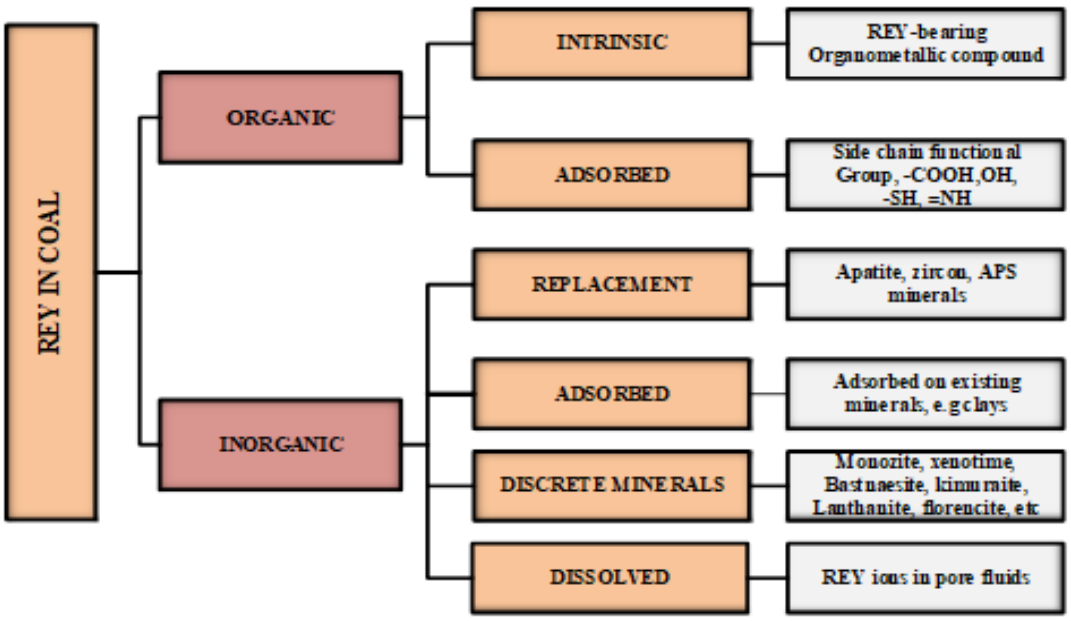

Figure 2.4: The general REE mode of occurrence in coal (Fu et al., 2022).

In coal combustion, REEs can be altered and concentrated in CFA since they are hardly volatile. Liu et al. (2019) hypothesised that in the boiler system, the REE-bearing minerals/hosts in coal are fragmented, incorporated into silica, or thermally decomposed into oxides. As the flue gas transports them, they remain in the glass or occur as individual minerals and react with SO_2 and CO_2 to transform into silicate and carbonate upon cooling. Due to this complex mechanism of occurrence, the speciation of REEs has been of interest to many researchers to understand their occurrence and distribution pattern (Kolker et al., 2017; Hood et al., 2017; Stuckman et al., 2018; Wang et al., 2019; Pan et al., 2019; Hower et al., 2020). The main components associated with REEs in CFA are as follows:

i. Organic matter

ii. Glass phase

iii. Discrete phase

Coal is known to contain both organic and inorganic matter, as briefly discussed in the above subsection. Therefore, organic compounds such as unburned carbon (residual carbon), which remain concentrated in CFA after CCP, have also been associated with REEs (Fu et al., 2022). In a study by Hower et al. (2020), CFA was pre-treated using froth flotation. The concentration of REEs in the CFA feed was increased from 464 to 512 ppm in the carbon froth concentrate. Kolker et al. (2017) and Hood et al. (2017) also observed a similar association of REEs with nanosized carbon.

The glass phase (non-crystalline) is a significant component of CFA, and as a result, many researchers have been interested in this phase (Kolker et al., 2017; Wang et al., 2019; Pan et al., 2019). A study conducted by Kolker et al. (2017) used a SHRIMP-RG ion microprobe to observe the distribution of REEs in aluminosilicate (Al-Si) glass. Similarly, Stuckman et al. (2018) used near-edge absorption spectroscopy (μ-XANES) and micro-X-ray fluorescence (μ-XRF) to map REEs in the aluminosilicate glass. In their study, they observed that REEs had large grains measuring over 40 μm and also irregular shapes. Thompson et al. (2018) used a combination of SEM-EDS and LA-ICP-MS to study REEs in the glass phase. Small grains of zircon and monazite were found in the Al-Si glass sphere. Liu et al. (2019) observed similar behaviour. In their study, LREEs were more enriched in monazite/rhabdophane, and HREEs in xenotime/churchite, lime, and zircon.

Based on different studies on the speciation of REEs, Fu and colleagues (2022) reviewed the possible mechanisms of incorporation as follows:

1. Physical encapsulation - Individual REE phases are incorporated into the glass as inclusions.

2. Physiochemical diffusion - REE phases are diffused throughout the Al-Si glass during the melting process.

There are also independent minerals referred to as ‘discrete phases’ that are not associated with the glass phase (similar to magnetite/haematite) and have been found to contain the REEs. Typical discrete phases associated with REEs include REE-carbonates, REE-oxides, REE-silicates, and REE-phosphates (Montross et al., 2018; Taggart et al., 2018; Liu et al., 2019).

Although several studies have linked REEs in CFA to various phases, it is widely agreed that they are predominantly associated with the glass phase. Consequently, economic extraction should aim to target the phase (Liu et al., 2019; Wu et al., 2022; Xu et al., 2022; Fu et al., 2022).

2.3 Chemistry of REEs

According to the International Union of Pure and Applied Chemistry (IUPAC), transition elements are defined as “elements having a *d* subshell that is partially filled with electrons, or an element that can form stable cations with an incompletely filled *d*-orbital” (Stevenson and Nervik, 1961). Scandium and yttrium conform to the $(n-1)d^1(n)s^2$ pattern. Therefore, they are characterised by the gradual filling of the 3d(Sc → Cu) and 4d(Y → Ag) orbitals. These *d*-electrons act as valence electrons and participate in chemical interactions. Scandium has an electron configuration of $[Ar]3d^14s^2$. Due to its inability to form an ion with an incomplete 3*d* subshell, it is not considered a "true" transition element. The lanthanides are defined by the progressive filling of the *f*-orbitals ($[Xe]4f^05d^16s^2$), except La. Therefore, according to the IUPAC system, they are not considered transition elements. Cerium (Ce), for instance, has the electron configuration of $[Xe]4f^15d^16s^2$. Interestingly, the 4*f* orbital is filled before the 5*d* orbitals. This unique feature implies that the electrons in the 4*f* subshell cannot effectively

shield the outer electrons (5*s* and 5*p*) from the increasing nuclear charge. As a result, the ionic radii of cerium and its neighbouring elements exhibit a gradual decrease with an increase in atomic number (i.e. La^{+3} = 1.216 Å and Lu^{+3} = 1.032 Å). This pattern is unique among the lanthanides, and it is referred to as the Lanthanide Contraction (see **Figure 2.5**) (Stevenson and Nervik, 1961; De Decker, 2017).

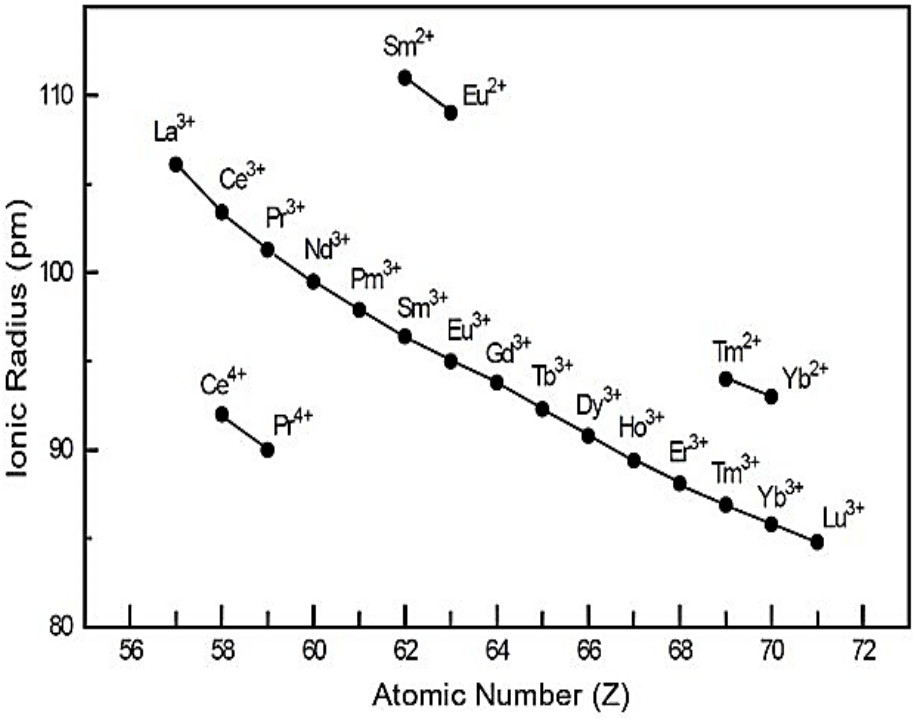

Figure 2.5: The lanthanides contraction (De Decker, 2017).

The exceptional chemical and physical properties of REEs, such as elevated coordination number, substantial unpaired magnetic moments, and enhanced photoluminescence, are a result of the shielded 4*f*-orbital. These properties have made REEs attractive for application in advanced emerging modern technologies (Stevenson and Nervik, 1961; Balaram, 2019).

2.3.1 Aqueous chemistry

The fundamental chemistry of REEs is characterised by their trivalent oxidation state (REE^{3+}). Cerium (Ce) exhibits stability in both aqueous solutions and solid compositions in its tetravalent state (Ce^{4+}). Generally, the lanthanides are reduced to Ln_2O_3 when exposed to air at room temperature. However, cerium will form Ceria, CeO_3 under the same conditions.

The only other binary solid compounds for Ce^{4+} are hydrous ceric oxide, $CeO_2 \cdot nH_2O$, and ceric fluoride, CeF_4. The divalent Sm, Eu, and Yb are also stable in aqueous solution and solid composition. These cations are strong reducing agents in acidic solutions and will be reduced in the order $Sm^{2+} >> Yb^{2+} >> Eu^{2+}$. Nonetheless, in an aqueous acidic solution, they are rapidly oxidized by oxygen into REE^{3+} (Stevenson and Nervik, 1961; Habashi, 1997; Krishnamurthy and Gupta, 2005).

2.3.2 Coordination chemistry

The lanthanides are considered hard Lewis acids and will form stable complexes with oxygen and nitrogen-containing ligands ($Ln^{4+} >> Ln^{3+} >> Ln^{2+}$). Due to size constraints (atomic number), the anhydrous Ln^{+3} ions will form stable complexes from Lu^{3+} to La^{3+}. The complexes formed will generally have higher coordination numbers (6-12). Therefore, the coordination geometry can range from octahedral, cubic, tricapped, trigonal prismatic, and more complex geometries. This behaviour of the lanthanides is extended to Y and La. However, scandium (Sc^{3+}, $3[Ar]3d^0$) cannot form stable complexes with a coordination greater than 6 (Stevenson and Nervik, 1961; Cotton et al., 1999; Dehnicke and Greiner, 2003). Nonetheless, a typical 10-coordination complexation of lanthanum with bipyridyl is shown in **Figure 2.6**.

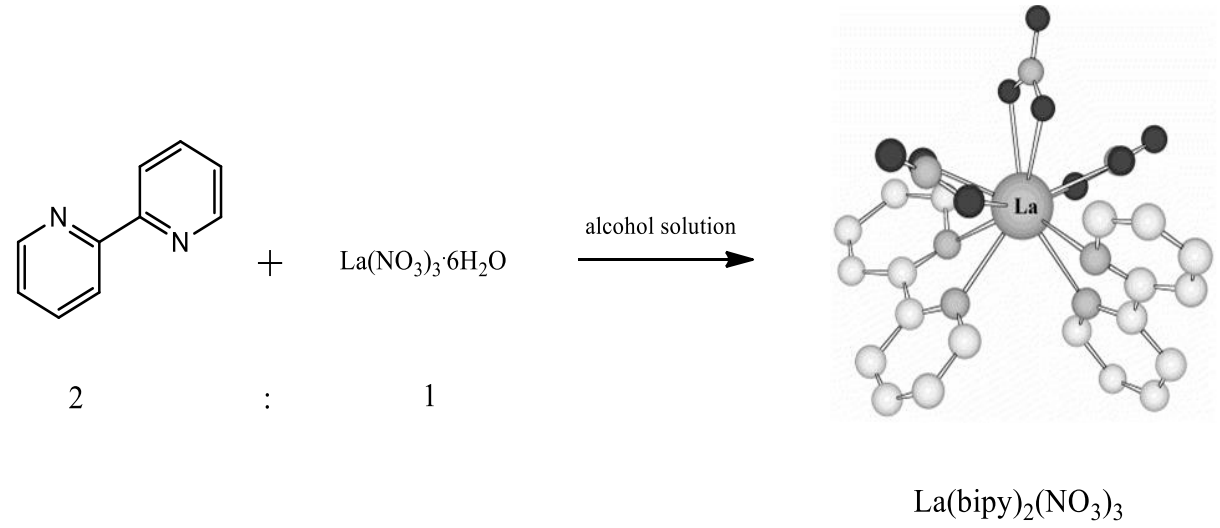

Figure 2.6: A representation of trinitrobis (bipyrdyl) lanthanum (III) (Cotton, 2005).

Research has also demonstrated that the most stable complexes of REEs are those derived from polyaminopolycarboxylic acids, including citric acid (2-Hydroxypropane-1,2,3-tricarboxylic acid) and EDTA (ethylene diamine tetraacetic acid). The anions of these ligands can form multiple bonds using O_2 and N_2 donors available in the ligand system. In general, ligands with a large charge, small size, and chelating abilities will mostly yield complexes with REE^{3+} (Dehnicke and Greiner, 2003; Xaba, 2015). The most common organic ligands that can form complexes with REEs are presented in **Figure 2.7**.

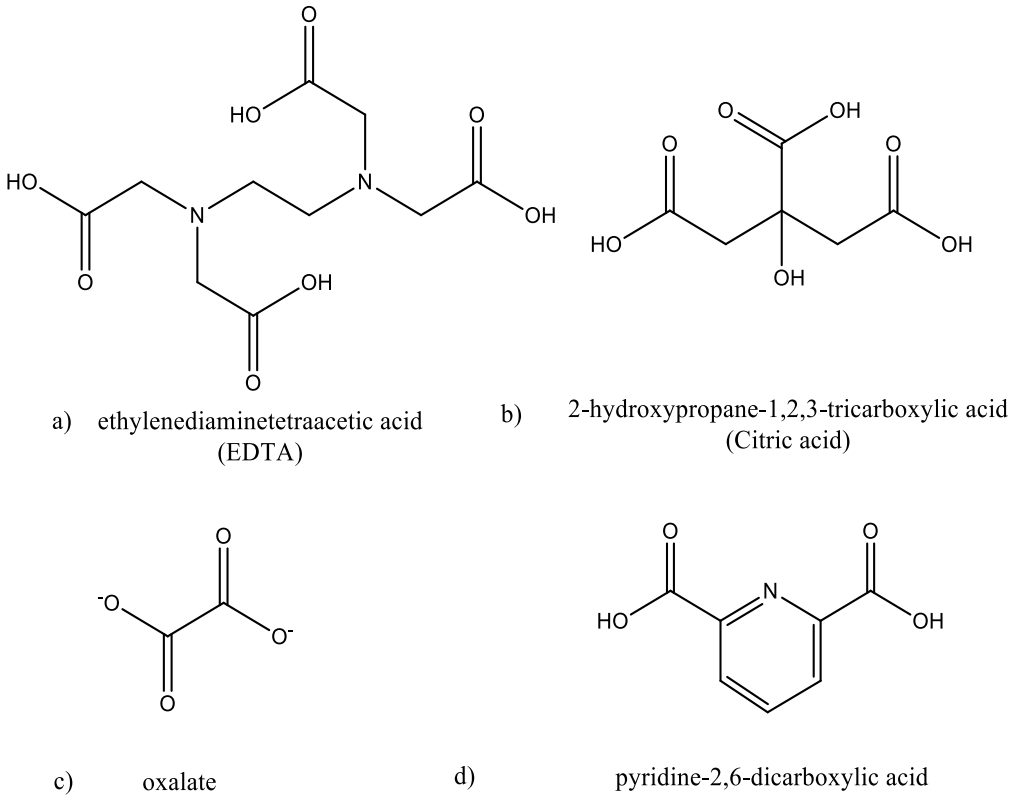

Figure 2.7: Common organic ligands used in REE complexation (Dehnicke and Greiner, 2003; Xaba, 2015).

The basic chemistry of REEs discussed in these sections is commercially utilised to separate REEs from impurities and into individual elements. This enables separation based on complex species formation, ion hydrolysis, and salt solubility. Consequently, it is for these reasons that the separation and purification of REEs through selective leaching, ion exchange, adsorption, and solvent extraction have been successful.

2.4 Conventional Processing of REEs

The conventional beneficiation steps in processing REEs from primary ores begin with mining and then proceed to the refining stage as shown in **Figure 2.8**. The processing stages selected will be determined by the type of ore being processed (i.e. gangues and mineralogy) and the economics of the operational conditions (Habashi, 1997; Krishnamurthy and Gupta, 2005). In the context of this study, the main focus will be on physical separation and hydrometallurgical beneficiation stages.

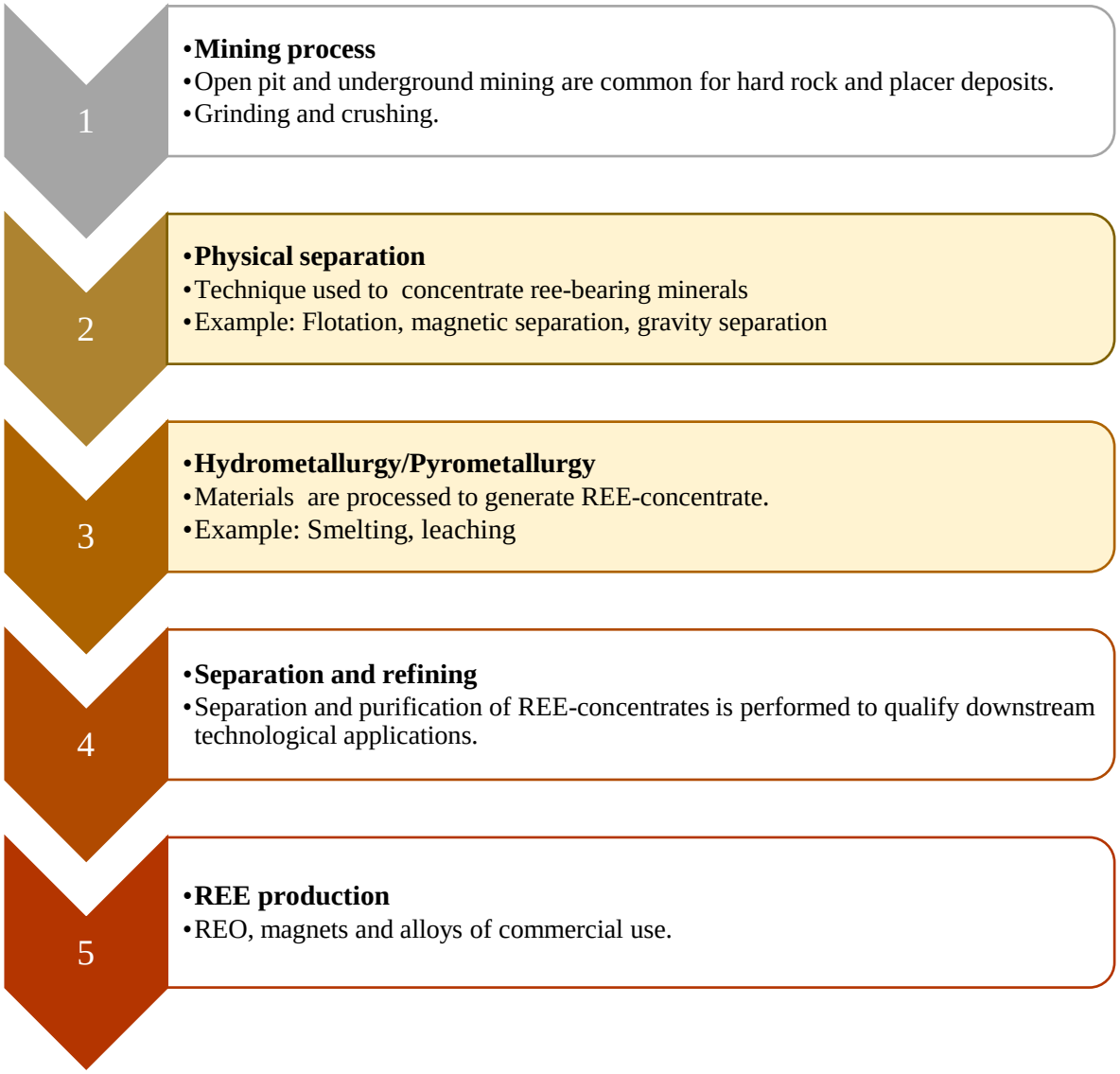

Figure 2.8: The REEs beneficiation stages in processing primary ore deposits.

2.4.1 Physical beneficiation

The physical separation process often follows the mining and comminution stages. In this process, REEs are liberated from the host and concentrated without altering the chemical composition (Wills and Finch, 2015; Abaka-Wood et al., 2016). The most common physical beneficiation techniques are gravity separation, flotation, and magnetic separation (MS).

2.4.1.1 Flotation and gravity separation

Flotation is based on the hydrophobicity (i.e. repelling water) of minerals, causing them to rise to the surface of the froth cell after chemical modification, thus physically separating them from the gangue materials (Jordens et al., 2014). In this process, collectors, which are surface-active reagents, selectively bind to REE-bearing minerals, making them hydrophobic for recovery. The most common collectors used for REEs are phosphoric acid esters, hydroxamates, and fatty acids. The Bayan Obo and Mountain Pass mines use flotation to process monazite and bastnäsite, respectively. In monazite processing, zircon and rutile are the most common REE gangue minerals with similar chemical and physical behaviours, resulting in poor flotation. Depressants such as sodium oxalate, sodium sulphide, and sodium silicate are added to reject the gangue minerals (De Lima and Leal Filho, 2015).

The REE-bearing minerals are also processed by gravity separation since they have a higher specific gravity (4-7 g/cm^3) compared to most gangue minerals (i.e. quartz, calcite, and dolomite, <3 g/cm^3) (Jordens et al., 2013). At the Bayan Obo mine, gravity separation is employed to separate monazite and bastnäsite from the iron and silicate gangue materials. This process takes place between the rougher and cleaner flotation circuits (Jordens et al., 2014; De Lima and Leal Filho, 2015).

2.4.1.2 Magnetic separation (MS)

In MS, magnetic minerals are separated from non-magnetic components according to their magnetic susceptibility by applying an external magnetic field (Fears, 2018). There are typically three different types of magnetism (Svoboda and Fujita, 2003; Jordens et al., 2014; Fears, 2018):

1. **Paramagnetism:** Although paramagnetic minerals are not strongly attracted to magnetic fields, they do exhibit magnetic characteristics when exposed to a magnetic field. The characteristics of these components result from the unpaired electrons and the realignment of the electron paths in the direction of an externally applied field. Typical examples of these minerals include haematite, ilmenite, and REE-bearing minerals (i.e. xenotime and bastnäsite).

2. **Ferromagnetism:** These minerals have a strong attraction to magnetic fields and can maintain their magnetic properties even when the external field is no longer present. Magnetite, in particular, is known for its exceptional ability to align magnetically.

3. **Diamagnetism:** Minerals that are weakly repelled by magnetic fields include calcite, quartz, and plagioclase. Consequently, when a magnetic field is present, they acquire a magnetic moment that opposes the field. These minerals are widely referred to as diamagnetic minerals.

MS can be used to concentrate REE-bearing minerals or reject gangue (Krishnamurthy and Gupta, 2005). In the Bayan Obo mine, Fe-containing minerals such as magnetite are recovered by MS, while REEs are concentrated and further processed by flotation (De Lima and Leal Filho, 2015). In placer deposits, monazite responds well to MS, and it is separated from non-magnetic gangues such as rutile and zircon. It is also noted that the integration of physical separation techniques is the most efficient alternative to concentrate the REE-bearing minerals (Wills and Finch, 2015).

2.4.2 Hydrometallurgical beneficiation

In hydrometallurgy-based processes, the REE-bearing minerals are decomposed and extracted to produce a rare earth concentrate for further separation of individual elements. The alkaline and acid decomposition methods are commercially used to process bastnäsite, xenotime, and monazite for the LREEs and HREEs, while scandium is almost exclusively recovered as a by-product (Shaoquan and Suqing, 1996; Habashi, 1997; Krishnamurthy and Gupta, 2005). The conventional alkaline and acid treatment processes are shown in **Figure 2.9** and are discussed in detail.

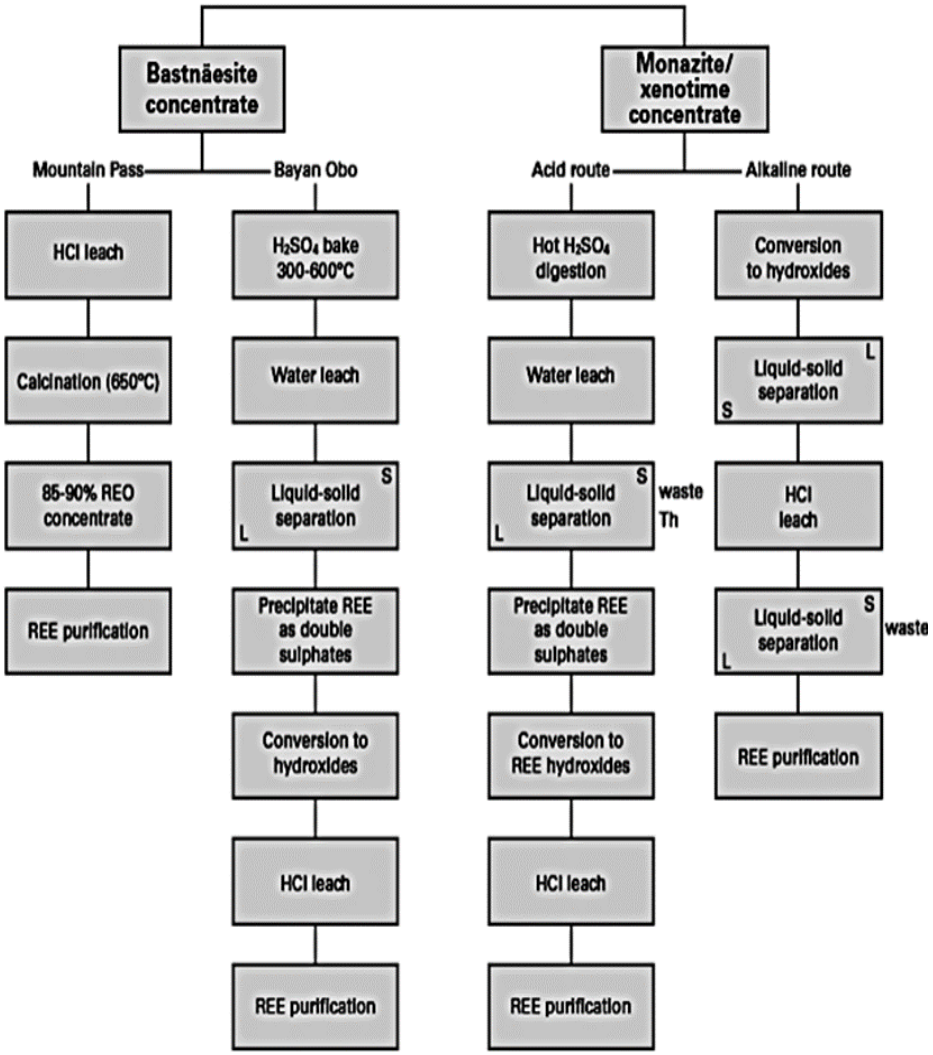

Figure 2.9: The conventional hydrometallurgical treatment of REE concentrates **(**adapted from Chegwidden and Kingsnorth, 2002).

2.4.2.1 Alkaline decomposition

Alkaline decomposition, also known as caustic decomposition, is commonly applied to phosphate minerals such as monazite and xenotime at high temperatures (~120-150°C) in an autoclave or at a lower temperature (~120°C) at normal pressures using a more concentrated alkaline solution (Habashi, 1997; Kim and Osseo-Asare, 2012). In monazite processing, the concentrate is mixed with a hot-caustic solution (50-70 wt.% NaOH) and decomposed to form the insoluble REE-hydroxide as shown in **Equation 2.2**. In this process, thorium is also decomposed as shown in **Equation 2.3**. A soluble trisodium phosphate (Na_3PO_4) is recovered as a saleable product and sold to the fertiliser industry (Kim and Osseo-Asare, 2012).

$$\mathrm{REPO_{4(s)} + 3NaOH_{(aq)} \rightarrow RE(OH)_{3(s)} + Na_3PO_{4(aq)}} \quad \textbf{2.2}$$

$$\mathrm{Th_3(PO_4)_{4(s)} + 12NaOH_{(aq)} \rightarrow 3Th(OH)_{4(s)} + 4Na_3PO_{4(aq)}} \quad \textbf{2.3}$$

The resulting REE-hydroxide cake can be leached with HCl or HNO_3 (Krishnamurthy and Gupta, 2005). In monazite processing, the cake is leached in dilute HCl at 70-80°C, as shown in **Equation 2.4**, and crystallised to produce $RECl_3 \cdot 6H_2O$. In this process, thorium hydroxide in **Equation 2.5** remains undissolved and, therefore, is selectively separated from REEs (Sadri et al., 2017).

$$\mathrm{RE(OH)_{3(s)} + 3HCl_{aq} \rightarrow RECl_{3(aq)} + 3H_2O} \quad \textbf{2.4}$$

$$\mathrm{Th(OH)_{4(s)} + 4HCl_{aq} \rightarrow ThCl_{4(s)} + 4H_2O} \quad \textbf{2.5}$$

The alkaline treatment process has the added advantage of cracking and pre-concentrating REEs due to their low solubility in alkaline solutions, as discussed in **Section 2.3**. This process is often preferred in monazite due to the simultaneous recovery of the phosphates, which are recovered as saleable products (Sadri et al., 2017). It is also noted that if the concentrate is complex and contains several REE-bearing minerals, decomposition is limited (Chi and Wang, 1996).

2.4.2.2 Acid decomposition

Sulphuric acid baking, or acid decomposition, is a cheaper alternative compared to alkaline decomposition and has been used to process REE-phosphate and carbonate minerals. During processing, the concentrate is mixed with H_2SO_4 (93-98 wt.%) to form a paste and reacted in an acid-resistant furnace at 200-500°C to decompose the REE-phosphate/carbonate, followed by water leaching to recover the water-soluble REE-sulphates (Demol et al., 2019; Peiravi et al., 2021). An example of REE-phosphate processing is shown in **Equation 2.6** and **2.7**.

$$2\mathrm{REPO_4} + 3\mathrm{H_2SO_{4(aq)}} \rightarrow (\mathrm{RE})_2(\mathrm{SO_4})_{3(s)} + 6\mathrm{H^+} + 2\mathrm{PO_4^{3-}} \quad \textbf{2.6}$$

$$(\mathrm{RE})_2(\mathrm{SO_4})_3 \cdot \mathrm{nH_2O_{(s)}} \rightarrow 2\mathrm{RE^{3+}} + 3\mathrm{SO_4^{2-}} + \mathrm{nH_2O} \quad \textbf{2.7}$$

In monazite concentrates, the LREEs have low solubility in this system due to the formation of double sulphates as shown in **Equation 2.8** (discussed in detail in **Section 2.6.1**). As a result, caustification discussed in **Section 2.4.2.1** can be used to convert the insoluble double sulphates into REE-hydroxides, followed by HCl or HNO_3 leaching (Krishnamurthy and Gupta, 2005; Sadri et al., 2017).

$$\mathrm{LRE_2(SO_4)_{3(aq)}} + \mathrm{Na_2SO_{4(aq)}} + 2\mathrm{H_2O} \rightarrow \mathrm{Na_2SO_4 \cdot LRE_2(SO_4)_3 \cdot 2H_2O_{(s)}} \quad \textbf{2.8}$$

Similar to alkaline decomposition, acid decomposition is also effective in producing high REE recoveries. However, the disadvantage of this process is that REEs will co-extract with high levels of impurities such as U, Th, Al, and Fe, which require further downstream removal (Krishnamurthy and Gupta, 2005; Sadri et al., 2017). In addition, it is also noted that during baking, a high-strength solid paste forms on the baking equipment, which reduces mass transfer, consequently resulting in technical issues (Nayak and Panda, 2010).

2.5 Recovery of Valuable Metals from CFA

The conventional processing of REEs has been discussed in **Section 2.4**, and this section will focus on CFA processing. Liu and Li (2015) proposed that the extraction of metals from secondary sources must be economical and practically achievable to ensure sustainability. Therefore, according to Sibanda et al. (2016), a sustainable process can extract more than one saleable product and minimise waste production and disposal. As a result, in addition to the extraction of REEs, metals of value such as Al, Fe, and Ti, which are quantified in CFA, are also considered in this study.

2.5.1 Magnetic separation

In **Section 2.2.2.2**, it is mentioned that Fe-bearing minerals (i.e. magnetite/haematite), can occur as discrete phases in CFA. As a result, both dry MS and wet MS have been utilised since the 1970s (Rao et al., 1970; Murtha and Burnet, 1978; Brown, 1980; Aldrich, 1984). Murtha and Burnet (1978) first used a low-gradient electromagnetic separator to recover Fe-oxide (magnetite/haematite) from CFA. The procedure was repeated three times, resulting in 85% recovery of Fe-oxide, with impurities of SiO_2 and Al_2O_3 being less than 10%. In the 1980s, Brown (1980) and Aldrich (1984) patented processes for recovering Fe-oxide using both dry and wet separators. MS has since been widely adopted.

In later studies, it was reported that magnetite will co-extract with diamagnetic components such as mullite and quartz in the magnetic fraction due to the agglomerative particles in CFA. Thus, SiO_2 and Al_2O_3 are the major impurities quantified with Fe-oxide recovery (Valeev et al., 2019; Cornelius et al., 2021; Strzałkowska, 2021). Shoumkova (2011) found that a spinel magnetite structure in **Figure 2.10** also affects the purity of the extracted magnetic fraction in both wet and dry MS. Magnetite has a general formula of AB_2O_4 with a cubic crystal structure containing 32 face-centred cubic (fcc) oxygen atoms coordinated to non-equivalent 8 tetrahedral (*A*) and 16 octahedral *(B*) sites (Bragg, 1915). In the general formula, *B* can accommodate divalent metals such as Mg, Fe, Zn, or Mn, and *A* the trivalent metals such as Fe, Cr, and Al. Thus, these elemental impurities are often quantified in the magnetic fraction (Bragg, 1915; Hashimoto et al., 2019). This magnetite effect has also been reported by Valeev et al. (2019) and Strzałkowska (2021). In general, the magnetic fraction can be defined as Fe-oxide component that is spherical, dense and has very fine particles (1-32 μm) with impurities (i.e. Al_2O_3 and SiO_2) due to the complex CFA phase composition (Murtha and Burnet, 1978; Valeev et al., 2019; Strzałkowska, 2021).

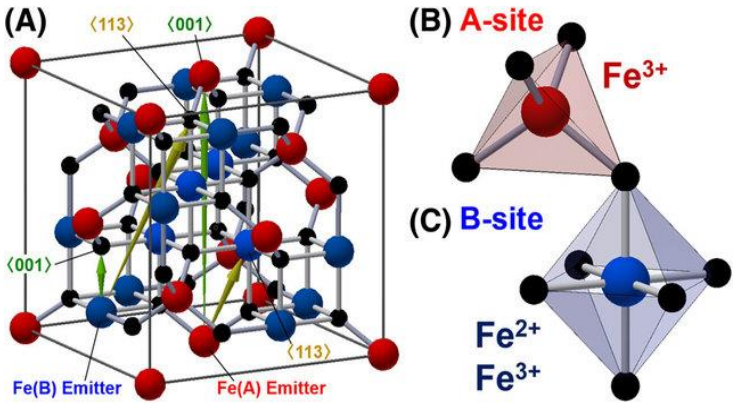

Figure 2.10: A schematic magnetite spinel structure (Hashimoto et al., 2019).

Shoumkova (2011) and Strzałkowska (2021) reported that Fe-oxide can be recovered from CFA using different MS techniques. Therefore, the choice of technique depends on the required final product and its application. As such, the magnetic fraction has been reported as a potential resource for iron ore processing, a Fenton-like catalyst for wastewater treatment, and a dense medium separator for coal cleaning (Murtha and Burnet, 1978; Shoumkova, 2011; Strzałkowska, 2021). The non-magnetic fraction containing mullite and quartz (including an amorphous component) has been reported as a suitable material for the metallurgical recovery of alumina, zeolite synthesis, and as a feed/additive in the construction industry (Rao et al., 1970; Hill and Raistrick, 1981; Lisowyj, 1986; Cornelius et al., 2021).

In the extraction of REEs from CFA, MS has also been reported as a pre-concentration method. In **Section 2.4.1**, it is reviewed that REE-bearing minerals like monazite and xenotime possess magnetic properties. However, in CFA processing, REEs have been reported in the non-magnetic fraction due to their association with the aluminosilicate glass (Lin et al., 2017; Lanzerstorfer, 2018; Nugroho et al., 2019; Rosita et al., 2020; Pan et al., 2020; Cornelius et al., 2021). In a study by Cornelius et al. (2021), wet magnetic separation was used to recover Fe and concentrate REEs. In their study, REEs were reported in the non-magnetic fraction with the mullite, quartz, and amorphous components. The EF value was also calculated between 0.6 and 1.0. Abaka-Wood et al. (2022) also used a laboratory-scale wet high-intensity magnetic separator (WHIMS) to recover REEs from CFA. In their study, Fe recovery increased with an increase in the magnetic field intensity and at optimum conditions, ~60% of REEs were reported in the non-magnetic fraction (Abaka-Wood et al., 2022). Due to the complex distribution of REEs in CFA, it was proposed that future studies

focus on detailed mineralogical analysis of REEs in the magnetic fraction for a more detailed mineral association and liberation characteristics.

According to a review by Rybak and Rybak (2021), concentrating REEs through a "multi-stage" procedure could be an ideal approach, as the EF value is significantly low in MS alone. Such a multistage process can include MS and acid-alkaline leaching processes. Cornelius et al. (2021) used a combination of wet MS and zeolitisation to concentrate REEs in CFA. After Fe recovery by MS, the non-magnetic fraction was further processed by zeolitisation in 8 M NaOH solution at 150℃ for 24 hours. The recovered zeolite was a hydroxysodalite compound that contained amorphous silica and sodium sulphate (thernadite). The remaining residue was amorphous with mullite and quartz components and concentrated with REEs (EF 0.8-1.6) slightly higher than MS alone (Cornelius et al., 2021).

It can be presumed that MS is effective for Fe-oxide recovery and concentrating REEs. Therefore, for this study, MS will be considered for recovering Fe-oxide as a value-added material (discussed in **Section 2.7.1**) and as a pre-concentration step for REEs.

2.5.2 Recovery of Al, Fe and Ti

Early research on the extraction of metals from CFA focused extensively on Al due to its relative abundance (20-30% Al_2O_3) (Yao et al., 2014; Sibanda et al., 2016; Valeev et al., 2022). Aluminium is a lightweight, corrosion-resistant metal that has high thermal and electrical conductivity. These properties make Al applicable in diverse industries, such as construction, electrical, mechanical, and transportation (Ndlovu et al., 2017). South Africa operates the largest alumina smelter in Africa, which is a subsidiary of South 32 situated in Richards Bay, KwaZulu-Natal. The Hillside Aluminium plant imports smelter-grade alumina (>90% Al_2O_3) from Worsley Alumina in Australia and further processes it using the Hall-Heroult electrolytic process (see **Figure 2.11**) to produce high-quality alumina products for domestic applications and exports (Mioche, 2019). With no alumina resource in South Africa, there is an opportunity to beneficiate Al from alumina to pure metal production.

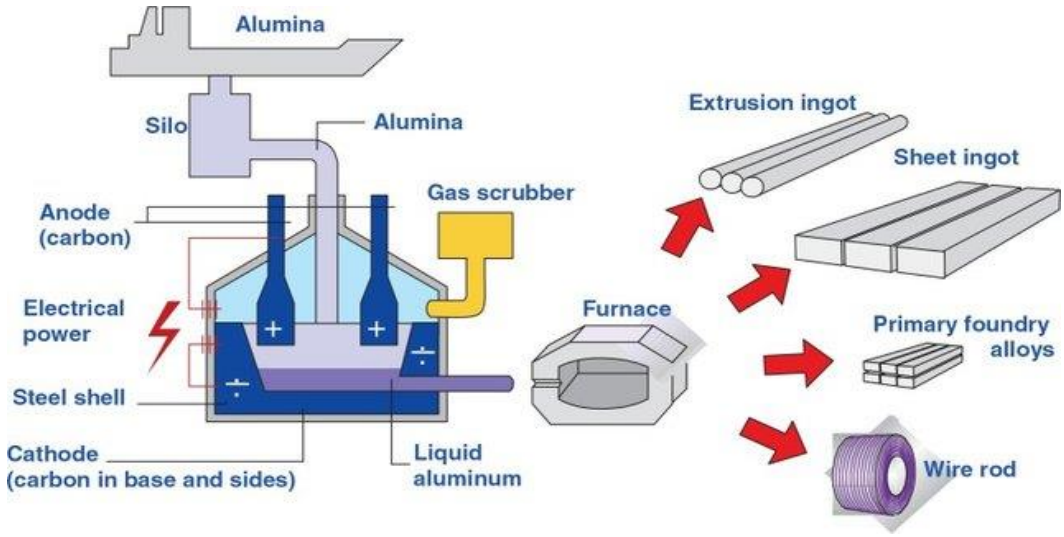

Figure 2.11: A schematic presentation of alumina processing by the Hall-Heroult electrolytic process (Kvande and Drabløs, 2014).

The Bayer process shown in **Figure 2.12** is commercially utilised to treat the primary aluminium deposit bauxite for smelter-grade production. This process uses caustic leaching at high pressure and temperature to leach $Al(OH)_3$, which is directly precipitated and further calcined at >1000℃ to produce smelter-grade alumina (Shcherban et al., 1995; Ndlovu et al., 2017). The primary benefit of this process is the selectivity for elements such as Fe and Ti, which often require downstream purification.

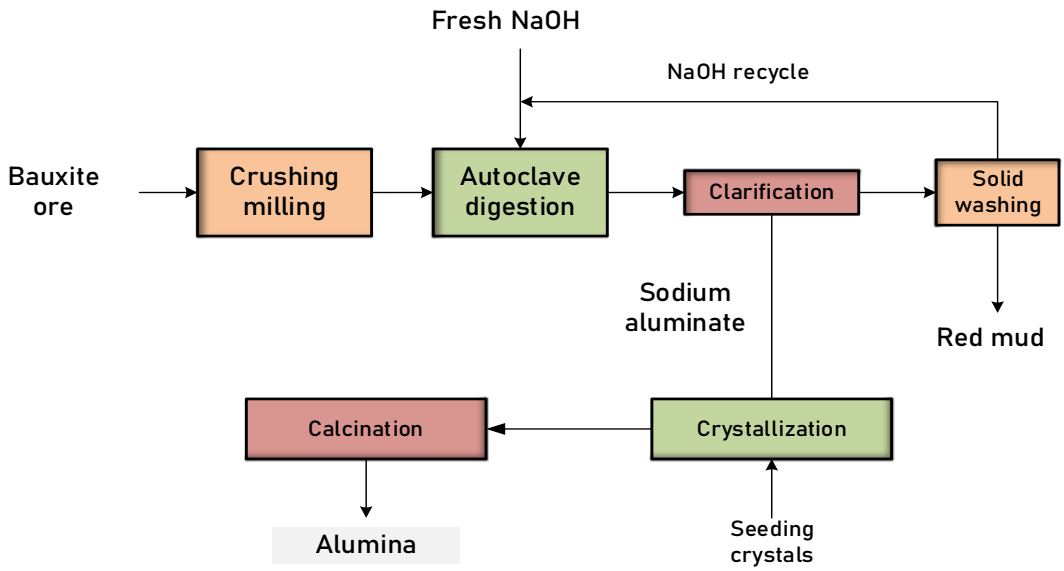

Figure 2.12: A schematic presentation of the Bayer process (Adopted from Ndlovu et al., 2017).

Direct application of the Bayer process in CFA has been observed to be ineffective due to the high silica content (40-60% SiO_2) (Authier-Martin et al., 2001; Liu and Li, 2015; Sibanda et al., 2016). The Bayer process is feasible for bauxite with an alumina-to-silica mass ratio (A:S) >9. In CFA, the A:S ratio is <2, which makes processing challenging due to the formation of a sodium aluminium hydro-silicate that is difficult to manage (Su et al., 2011; Liu and Li, 2015). Nonetheless, progress has been made in CFA processing using direct and indirect acid leaching processes (Yao et al., 2014; Sibanda et al., 2016; Valeev et al., 2022).

2.5.2.1 Direct acid leaching

The direct acid leaching of CFA has been investigated by several researchers using H_2SO_4 due to its efficient alumina extraction and cost-efficiency (Seidel and Zimmels, 1998; Matjie et al., 2005; Nayak and Panda, 2010; Shemi, 2013). In a study by Seidel and Zimmels (1998), CFA was leached in a concentrated H_2SO_4 solution (pH 0.8) for 100 days at atmospheric pressure and temperature. Their results showed only 30% Al extraction from CFA. They also observed that in the leaching process, calcium sulphate forms a barrier on the surface and within the pores of the CFA particles, thereby affecting the leaching process. To improve the mass transfer on the surface, HCl was used to dissolve calcium as a pre-treatment method. However, no significant improvement was observed with 28% Al extraction (Seidel and Zimmels, 1998). Shemi (2013) found that higher acid concentrations (3-8 M H_2SO_4) and leaching temperatures (45-80℃) led to the co-extraction of Al and Ca, leading to the formation of calcium sulphates and subsequently decreased Al extraction. The optimum extraction of 27.8% Al was reported in 6 M H_2SO_4 at 75℃ after leaching for 10 hours. It was also noted that due to the distribution of alumina in the amorphous and mullite phases (see **Table 2.3**), the latter remained insoluble. Consequently, the 27.8% Al extraction was equivalent to 89.3% Al extraction in the amorphous phase (Shemi, 2013).

Leaching at high temperatures (>100℃) and high acid concentration (~18 M H_2SO_4) has also demonstrated the capacity to extract alumina in both the amorphous and mullite phases (Nayak and Panda, 2010; Valeev et al., 2020). Nayak and Panda (2010) used 18 M H_2SO_4 (acid: CFA ratio = 2) to leach CFA at 200℃ for 8 hours and observed 84.2% Al extraction. Under these conditions, acid fumes due to acid boiling were a major challenge. In addition, the researchers consistently added H_2O to prevent the mixture from solidifying and to sustain the solid-to-liquid ratio for optimum Al extraction (Nayak and Panda, 2010).

2.5.2.2 Indirect acid leaching

Thermal pre-treatment before leaching is also an alternative, despite the energy costs. Sintering is a treatment method that involves the transformation of the mullite phase at >1000℃ by mixing with lime or soda to form calcium aluminate and dicalcium silicate (Murtha and Burnet, 1978; Matjie et al., 2005; Shemi, 2013). This transformation is followed by acid or alkaline leaching according to the desired end product (Shcherban et al., 1995; Shemi, 2013). The sinter alkaline-based processes were commissioned on a pilot scale in China between 2013 and 2015. The Melic Sea Group used this process by first recovering silica from CFA using the desilication method (alkaline leaching). The desilicated CFA was sintered and leached in an alkaline solution, resulting in a 90% Al extraction. The main drawback of this process was its excessive alkaline consumption (Yao et al., 2014; Luo et al., 2020).

The sinter-acid leach process is another alternative that researchers have investigated (Matjie et al., 2005; Shemi 2013). Matjie et al. (2005) pelletised a mixture of CFA, CaO, and coal (5:4:1) and sintered the material at 1000℃. This was followed by leaching in 6.12 M H_2SO_4 for 4 hours at 80℃, resulting in 85.2% Al extraction. Shemi (2013) postulated that alumina in the amorphous and mullite phases could be leached separately to yield higher Al extraction. Therefore, a two-step leaching process was developed. In the first leaching stage, Al in the amorphous phase was directly leached with 6 M H_2SO_4 for 10 hours at 82℃ to extract 89.3% Al. The remaining residue was processed in the second leaching stage using the sinter-acid leaching process. In this stage, the CFA residue was mixed with lime and coal (5:4:1), pelletised, and sintered at ~1100℃. The sintered CFA residue was leached in 6 M H_2SO_4 at 82℃ for 30 minutes at a 1:4 S/L ratio, resulting in 84.3% Al extraction from the mullite phase. The developed acid-leach-sinter-acid leaching process extracted 88.2% Al from both the amorphous and mullite phases (see **Figure 2.13**).

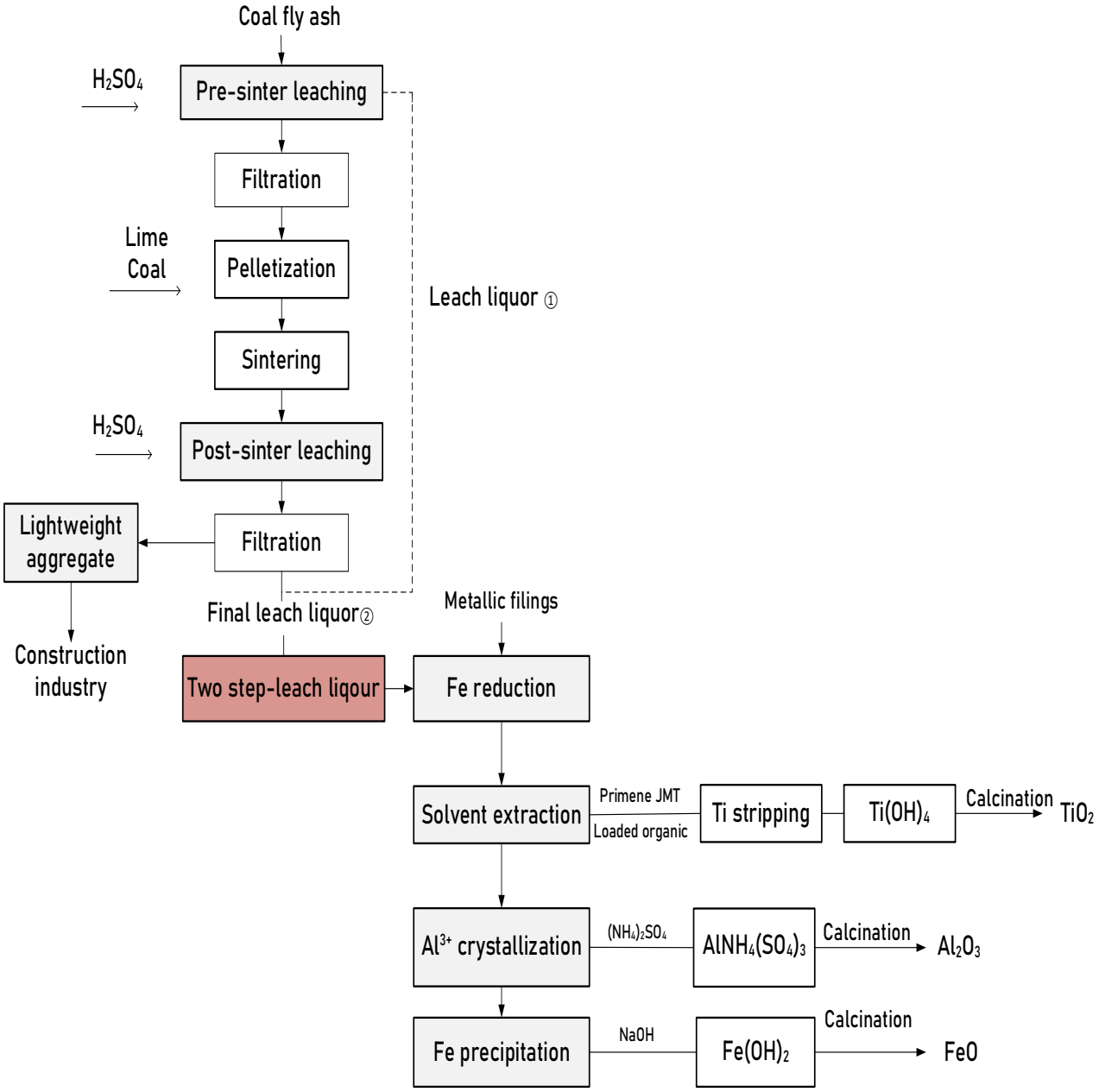

Figure 2.13: A process flowsheet for a two-step H_2SO_4 leach process and an integrated purification (Adopted from Shemi (2013) and Rampou (2018)).

The extracted Al in solution can be directly crystallised and calcined to produce smelter-grade alumina. Alum (aluminium sulphate salt) has a water solubility that is temperature dependent, and at 0°C, it is 2.4 g per 100 g (Poling et al., 2008; Ma et al., 2021). Therefore, at 0°C, alum can be directly crystallised and calcined to produce alumina (**Equation 2.9** and **2.10**). However, in the sinter-H_2SO_4 leaching process, high levels of Ti and Fe impurities were found to lower the purity of smelter-grade alumina (Matjie et al., 2005; Rushwaya, 2016; Rampou, 2018).

$$Al_2(SO_4)_{3(aq)} + (NH_4)_2S0_{4(aq)} + 40H_2O \leftrightarrow 2Al(NH_4)(SO_4)_2 \cdot 20H_2O_{(s)} \quad \textbf{2.9}$$

$$2Al(NH_4)(SO_4)_2 \cdot 20H_2O_{(s)} \xrightarrow{>500℃} Al_2O_{3(s)} + 2NH_{3(g)} + 4SO_{3(g)} + 21H_2O \quad \textbf{2.10}$$

It can be deduced that the primary drawback of the sinter-H_2SO_4 leaching process is the co-extraction of Al with impurities, which requires downstream purification and adds to the processing costs (Yao et al., 2014; Sibanda et al., 2016). Nonetheless, in this study, the sinter-H_2SO_4 leach was considered for alumina extraction. Therefore, Ti and Fe will be purified with the intention to generate saleable products (discussed in **Section 2.7**).

In both the sinter-acid and sinter-alkaline leach processes, large quantities of solid residues (CFA-SR) are also generated as waste material for disposal. Matjie et al. (2005) and Shemi (2013) proposed that the CFA-SR could be used in the building and construction industry as lightweight aggregate since the composition is primarily Si-rich and Ca-rich. In the sinter-alkaline process, the CFA-SR was identified as a useful material in manufacturing cement (Yao et al., 2014; Luo et al., 2020). Ideally, the material should be recycled to minimise waste disposal. Therefore, in this study, the material will be considered as an adsorbent for wastewater treatment (discussed in **Section 2.7**).

2.5.3 Recovery of REEs

The extraction of REEs from CFA is an ongoing research topic. Similar to the processing of alumina, progress has been achieved in both direct and indirect acid leaching methods. Therefore, this section will discuss the methods. A summary of the extraction of REEs from CFA using direct and indirect acid leaching processes is also presented in **Table 2.4**.

Table 2.4: A summary of the extraction of rare earth elements from CFA

Source	Pre-treatment	Leaching Conditions	REE Recovery	References
Guizhou, China	None	2M HCl, 10/1 S/L ratio, 120 min	Around 20% for La, 40% for Ce, 5% for Pr, 20% for Nd, and 10% for Y	Tang et al., 2019
	Na_2CO_3, 1/1 S/L, 860℃	3M HCl, 1:20 S/L (w/v), 400 rpm	72.78% for total REEs	
Guizhou, China	None	3M HCl, 1:10 S/L 10/1 (w/v), 60 ℃, 120 min	71.9% La, 66.0% Ce, 61.9% Nd	Cao et al., 2018
Sichuan, China	None	8M HCl, 1:40 S/L (w/v), 80℃, 6 hrs	32.36% for total REEs	Wang et al., 2019
	40% NaOH, 1:10 S/L (w/v), 150℃, 2 hrs	8M HCl, 1:30 S/L (w/v), 60℃, 2 hrs	88.15% for total REEs	
Powder River Basin, United States	None	12M HCl, 1:100 S/L, 85℃, 4 hrs	Nearly 100% for total REEs	King et al., 2018
Appalachian Basin, United States	None	12M HCl, 1:100 S/L, 85℃, 4 hrs	40-57% for total REEs	
	6.25M NaOH, 1:10 S/L mass ratio, 85℃, 4 hrs	20% HCl	48.8-85.9% for total REEs	
Japan	None	9.5% H_2SO_4, 1:100 S/L (w/v), 80 ℃, 2 hrs	Around 10-45% of La was extracted	Kashiwakura et al., 2013
Eskom CFA, South Africa	CFA was firstly roasted at 400℃ (1:1)	3M HCl.	47.78% HREEs, 46.78% MREEs and 33.93% LREEs	Mokoena et al., 2022
Eskom CFA, South Africa	None	5-18.2M H_2SO_4, 85-100℃	None	Sedres (2016)
--	5M NaOH at 100℃ for 120 min	5M HCl solution at 50℃ after 120 min	> 90% of REEs	Trinh et al., 2022

-- Not available

2.5.3.1 Direct acid leaching

The extraction of REEs from CFA has been investigated using HCl and H_2SO_4 with different extraction efficiencies (Kashiwakura et al., 2013; Sedres, 2016; King et al., 2018). In a study by Kashiwakura et al. (2013), dilute sulphuric acid was used to extract REEs at 80℃. After leaching for 120 min, a maximum of 45% of REEs were extracted. Their findings supported the unreacted core concept, implying that REEs are relatively dispersed both on the surface and in the aluminosilicate. However, the mineralogical data was not reported. Sedres (2016) investigated the extraction of REEs at various acidic concentrations (5-18.2 M H_2SO_4) and leaching temperatures (85-100℃). The phase composition of CFA was predominantly quartz, mullite, magnetite, and lime. Throughout the study, the extraction of REEs was not observed (Sedres 2016). Rosita et al. (2020) proposed that the extraction of REEs from CFA using H_2SO_4 could be attained at a lower sulphuric acid concentration. In their study, silica was first reduced with 8 M NaOH at 90℃ for 20 minutes. The desilicated residue was reported as quartz and mullite-rich material and ~75% REEs were leached with 1 M H_2SO_4. While desilication was effective in reducing silica, Zhang et al. (2018) and Wang et al. (2019) have reported the loss of HREEs during the filtration process due to their high solubility in alkaline solutions compared to LREEs.

Cao et al. (2018) used HCl to investigate the extraction of REEs from CFA containing lime, anhydrite, and haematite as the major crystalline phases. The optimum leaching conditions were observed at 3 M HCl, 60℃, and 200 rpm by leaching for 120 minutes. Under these leaching conditions, 70% of the REEs were extracted (Cao et al., 2018). King et al. (2018) observed different extraction efficiencies of REEs under the same experimental conditions. The Powder River Basin (PRB) CFA showed nearly 100% REE extraction in 6 M HCl at 85℃ by leaching for 4 hours. However, Illinois Basin (IL) CFA showed 43% REE extraction. The mineralogical distribution of REEs in the two CFA samples was not clearly distinguished; however, they both contained the amorphous phase, quartz, mullite, magnetite, and haematite components (King et al., 2018).

2.5.3.2 Indirect acid leaching

The sodium peroxide-sinter method, developed by the U.S. Geological Survey, was designed for processing silicate minerals (Meier Allen et al., 1996; Meier et al., 2002). Due to the

complex composition of CFA, this method has been utilised and modified by many researchers as a pre-treatment method for processing aluminosilicate associated REEs. King et al. (2018) used alkaline roasting as a pre-treatment method to enhance the REE extraction from IL-CFA. In their experiments, roasting at 450℃ using NaOH, followed by HCl leaching, resulted in good recoveries. However, their study did not provide clear information on the distribution of REEs among quartz, mullite, magnetite, and haematite. In a study by Tang et al. (2019), CFA with quartz, aluminum oxide, haematite, indialite ($Mg_2Al_4Si_5O_{18}$), and mayenite ($Ca_{12}Al_{14}O_{33}$) was used for the extraction of REEs. CFA was mixed with Na_2CO_3 in a 1:1 ratio, roasted at 860℃ to activate the aluminosilicates, and leached in 3 M HCl for 2 hours. The leaching efficiency of REEs reached a maximum of 72.78%. Quartz and halide were quantified as the main composition of the residue after leaching, suggesting that the residue may contain the insoluble fraction of REEs. Similarly, in a study by Mokoena et al. (2022), the low REE extraction efficiency after pre-treatment was considered a result of the presence of quartz and the incomplete transformation of the mullite. In their study, CFA was roasted at 400℃ with NaOH (1:1 ratio) and leached in 3 M HCl for 120 minutes. A maximum extraction efficiency of 47.78% HREEs, 46.78% MREEs, and 33.93% LREEs was observed. In their study, it was proposed that a higher roasting temperature may be adequate to decompose mullite and quartz, where REEs are largely associated. In addition, the formation of silica gel at low acid concentrations was reported to be a major concern in the leaching process (Mokoena et al., 2022).

It can be assumed that pre-treatment of CFA before acid leaching is beneficial for the extraction of REEs associated with the aluminosilicates. Therefore, in this study, sintering will be considered as a mullite transformation process for Al extraction and the REE-liberation process.

2.5.3.3 Effect of calcium sulphate

While sulphuric acid is efficient for alumina extraction (see **Section 2.5.2**), limited research is available on the efficient extraction of REEs. Therefore, hydrochloric acid is often reported as a suitable lixiviant for REEs (see **Table 2.4**). Similar to Al extraction, the formation of calcium sulphate has also been established in the extraction of REEs. In apatite processing, sulphuric acid is used as a leaching reagent to produce phosphoric acid or phosphate-based fertilisers (Roux, 1989; Preston et al., 1996). In this process, a calcium sulphate waste stream

known as phosphogypsum is produced as a secondary solid residue concentrated with 2-8 wt.% Ln_2O_3 (lanthanides). Research conducted by Preston et al. (1996) showed that 85% of REEs could be recovered from gypsum by using dilute HNO_3 and $Ca(NO_3)_2$ as leaching reagents (Preston et al., 1996). In a study by Ariuntuya (2018), the apatite concentrate was extracted at various sulphuric acid concentrations (1-6 M H_2SO_4). Above 2 M H_2SO_4, the extraction of REEs (LREEs and HREEs) declined from 60% to 20% due to the formation of calcium sulphates. The maximum REE extraction of ~80% was obtained by leaching with 1 M H_2SO_4 at 20℃ for 1 hour.

According to the literature, it has been reported that HREEs and LREEs can precipitate together with gypsum ($CaSO_4 \cdot nH_2O$) and phosphates under highly acidic conditions and temperatures. Hemihydrates ($CaSO_4 \cdot 1/2H_2O$) will precipitate with over 95% of REEs at temperatures ranging from 90 to 110℃. At 70 to 83℃, dihydrates ($CaSO_4 \cdot 2H_2O$) can precipitate with 70-80% of REEs (Binnemans et al., 2015; Yahorava et al., 2016). Consequently, these REEs (LREEs and HREEs) can precipitate with phosphogypsum in three forms:

i. Independent soluble phases (double sulphate, phosphates)

ii. Adsorbed on the surface of gypsum crystals

iii. Integrated into the crystal lattice of gypsum

The REE phases, such as independent soluble phases and those adsorbed on the surface, can dissolve when the solid-liquid ratio is high (S/L, 1:10), the temperature is low (<20℃), and the acid concentration is also low (<30% H_2SO_4) (Binnemans et al., 2015; Yahorava et al., 2016; Wu et al., 2018; Yahorava et al., 2018). Nevertheless, operation at low acid concentrations in silica-rich materials can result in silica gel formation, which makes the filtration process difficult. Alternative techniques in which the crystal structure of calcium sulphates is disintegrated (i.e. recrystallised) to liberate REEs have also been established. These methods of recrystallisation include mechanoactivation and hydrothermal treatment (Todorovsky et al., 1997; Hammas-Nasri et al., 2016; Wu et al., 2018; Yahorava et al., 2018). In hydrothermal treatment, a sample is dried in an oven (>90-100℃) for 24 hours to enable the dehydration of gypsum into β-hemihydrate (Hammas-Nasri et al., 2016; Yahorava et al., 2018). Yahorava et al. (2018) adopted the process from the construction industry, where the

dehydration process recrystallises to liberate phosphorus oxide (P_2O_5), which is then stabilised by lime (Kurdowski and Sorrentino, 1996; Roszczynialski et al., 1996). Alternatively, α-hemihydrate is generated in an autoclave using high-pressure steam (Karni and Karni, 1995). Mechanoactivation is performed using a centrifugal ball mill in air and the solvent of choice (i.e. HCl, H_2SO_4, or H_2O) (Todorovsky et al., 1997).

Considering the low solubility of REEs in a sulphate system, the effect of calcium sulphates on the REE extraction will be considered in the sinter-H_2SO_4 leach process.

2.5.3.4 Silica management

This review has highlighted that silica management is also important for preventing silica gel formation. In CFA, silica can occur in mullite, quartz, and the amorphous phase. The mullite and quartz are the inert phases; thus, their solubility in an aqueous system can be regarded as negligible (except when HF is present) (Terry, 1983a; Terry, 1983b). However, the amorphous silica is easily soluble in an aqueous system with possible silica gel formation (Queneau and Berthold, 1986). The solubility of amorphous silica at ambient temperature and pH less than 9 is ~100 mg/L. In alkaline settings (pH >9), it rises with the production of silicate ions, as illustrated in **Figure 2.14**. The dissolution of silica may result in a higher concentration of silica in the solution, which could subsequently lead to an increase in the silicon supersaturation index. This index is regarded as the driving force behind silica polymerisation. In the processing of eudialyte and bauxite residues, it has been observed that under acidic conditions, below the isoelectric point for silica in solution (i.e. pH 1.7-2.2), the hydrolysis of silica happens rapidly, resulting in the production of silica monomers, H_4SiO_4 and H_3SiO_4 according to **Equation 2.11** and **2.12**. The gel network in **Equation 2.13** eventually results in the formation of silica gel in acidic solutions (Marin Rivera, 2019; Wang et al., 2019). Parameters such as temperature, the concentration of divalent cations in solution, and the concentration of silica can affect the rate of silica gel polymerisation (Terry, 1983a; Terry, 1983b).

$$M_2SiO_{4(s)} + 2H_2SO_{(4)} + H_2O_{(l)} \rightarrow 2MSO_{4(aq)} + H_2O_{(l)} + H_4SiO_{4(aq)} \qquad \textbf{2.11}$$

$$H_4SiO_{4(aq)} + H_2O_{(l)} \rightarrow H_3SiO_4^- + H_3O^+ \quad \textbf{2.12}$$

$$Si_xO_yOH + H_4SiO_{4(aq)} \rightarrow Si_{(x+1)}O_{(y+2)}OH_{(\text{silica gel})} + 2H_2O \quad \textbf{2.13}$$

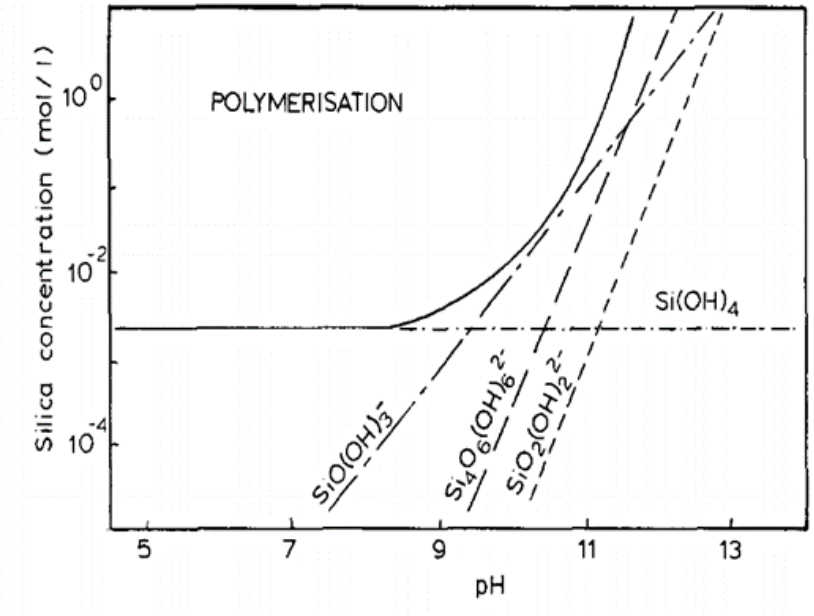

Figure 2.14: The solubility of amorphous silica at ambient temperature (Terry, 1983a).

Silica gel formation can be managed using a "water-starve" technique (Terry, 1983b; Terry, 1983a; Iler, 1955). For example, acid leaching of silicate minerals with H_2SO_4 and an excess of water can result in the formation of silica gel, as illustrated in **Equation 2.11** to **2.13**. However, if the water is restricted, the reaction will proceed as shown in **Equation 2.14** to **2.16** (Kazadi et al., 2016). The dry digestion technique, referred to as acid baking/acid fuming, is such a technique for silica management (Terry, 1983b; Terry, 1983a; Iler, 1955**;** Kazadi et al., 2016). In this process (see **Figure 2.15**), the feed is mixed with concentrated sulphuric acid (200-500℃) or hydrochloric acid (<100℃) to allow decomposition, followed by water leaching. The technique has been explored on a pilot scale, laboratory scale, and commercially to treat silicate minerals such as zinc ores (Terry, 1983b; Musadaidzwa and Tshiningayamwe, 2009) and eudialyte concentrates (Borra et al., 2016; Voßenkaul et al., 2017; Davris et al., 2017; Marin Rivera, 2019). For example, the extraction of REEs from eudialyte concentrate was piloted by Ma et al. (2019) using the dry digestion technique. In

their process, eudialyte concentrate was mixed with concentrated HCl (1:1) for 60 minutes at 70-80℃. The paste formed was then water leached at 50℃ for 1 hour to recover 84.2-85.4% REEs. Marin Rivera (2019) also investigated the extraction of selected REEs from bauxite residue using an HCl-based dry digestion method. In this study, the extraction of Sc was reported to co-extract with iron. Borra et al. (2016) used a sulphate-based dry digestion technique to decompose bauxite residue followed by water leach. Under optimum conditions, ~60% Sc and >90% REEs were extracted into solution. The leached residue was concentrated with Fe_2O_3, Al_2O_3, SiO_2, and calcium sulphate (Borra et al., 2016).

$$M_2SiO_{4(s)} + 2H_2SO_{(4)} + nH_2O_{(l)} \rightarrow 2MSO_{4(aq)} + nH_2O_{(l)} + Si(OH)_4 \quad \textbf{2.14}$$

$$2MSO_4 \cdot nH_2O + Si(OH)_4 \rightarrow 2MSO_4 \cdot (n+2)H_2O + SiO_{2(\text{filterable})} \quad \textbf{2.15}$$

$$M_2SiO_{4(s)} + 2H_2SO_{(4)} + nH_2O_{(l)} \rightarrow 2MSO_{4(aq)} + (n+2)H_2O_{(l)} + SiO_{2(\text{filterable})} \quad \textbf{2.16}$$

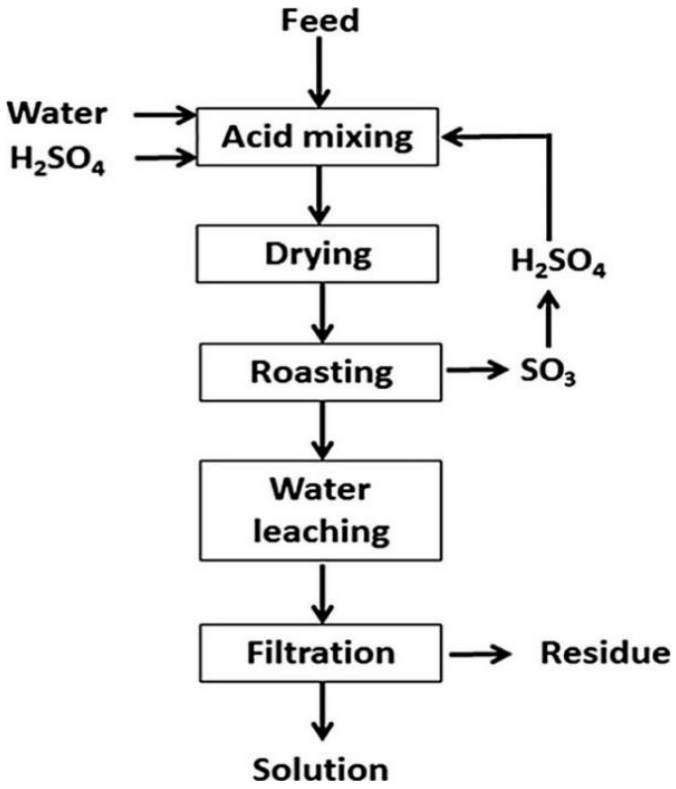

Figure 2.15: A schematic flowsheet of the dry digestion process (Borra et al., 2016).

The dry digestion technique is effective in managing silica and calcium, and results in a high extraction of REEs (Borra et al., 2016; Marin Rivera, 2019). Therefore, in this study, it will be considered as an alternative leaching method for REEs. While the process is effective, it is also noted that high co-extraction of metal impurities, such as Ti and Al can occur.

2.6 Purification and Separation of Impurities

Chemical precipitation and solvent extraction are commonly used commercial techniques in the purification processes. In the context of this study, the objective of purifying the REE-containing solution is to produce a concentrate rather than to separate individual elements. Therefore, chemical precipitation will be considered. It is also stated in **Section 2.5.2** that Ti and Fe are co-extracted as major impurities during the production of smelter-grade alumina. Therefore, solvent extraction is also discussed as an option for their recovery.

2.6.1 Chemical precipitation

In chemical precipitation, ions in solution react with suitable counter-ions to form insoluble compounds. This process typically includes supersaturation, nucleation, and crystal growth. Nucleation occurs when a certain number of particles combine to form a nuclei solid-phase (Söhnel et al., 1992; Christian, 1994). This process is carried out through primary and secondary nucleation mechanisms presented in **Figure 2.16**. Primary nucleation, also known as homogeneous nucleation, takes place when there is a lack of crystalline material. If the formation of a new solid phase is caused by the presence of a foreign solid phase, this process is known as secondary nucleation or heterogeneous nucleation (Söhnel et al., 1992).

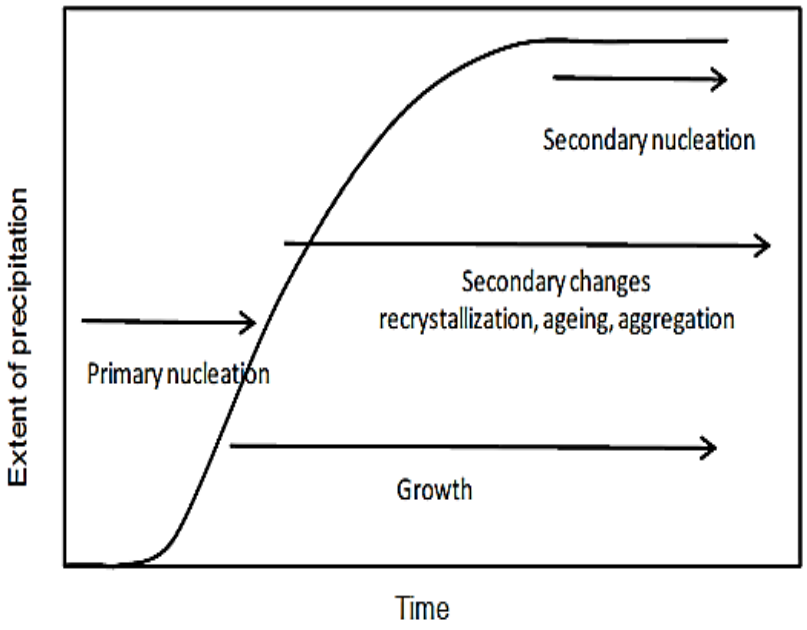

Figure 2.16: Precipitation kinetic processes (Söhnel et al., 1992).

The fundamental equation that summarises the precipitation process is known as the Von Weimarn ratio and is presented in **Equation 2.17** (Christian, 1994). The relative supersaturation (RSS) of the precipitation process is characterised by the relationship between Q, which represents the actual concentration of the solute, and S, which signifies the equilibrium concentration of the solute. A high RSS ratio indicates the formation of precipitate with small colloidal particles and a high rate of nucleation. Since particle growth and nucleation are important in precipitation, a low RSS ratio with particle growth as a crystalline solid is essentially desired (Christian, 1994).

$$\mathrm{RSS} = \frac{(\mathrm{Q} - \mathrm{S})}{\mathrm{S}} \qquad \textbf{2.17}$$

In the precipitation process, particle sizes may be regulated by variables such as reagent concentration, pH, and temperature (Christian, 1994; Skoog et al., 2004). Crystalline particles are usually desired since they are easy to filter and thus, separate from the solution. The introduction of seed crystals can also induce the growth of larger crystals (Hove, 2008). Solid Seeds are crystals that are added to induce nucleation at constant experimental parameters such as temperature or concentration. They are also used to enhance the surface area and drive the reaction kinetics in favour of crystal growth. In addition, they can also have

different properties such as mass, shape, and polymorphic form. The surface area of the seed material should be large enough to consume the supersaturation, thereby suppressing homogeneous nucleation (Hove, 2008; Javed, 2017; Mwewa, 2020).

The solubility of a product is often facilitated by controlling the conditions of a reaction leading to precipitation. The ionic compound in solution will dissolve to a point of saturation and can be expressed by a general formula in **Equation 2.18**. The newly formed solid compound will become insoluble once the solubility product has been reached or surpassed (**Equation 2.19**). Ksp can be expressed in terms of concentrations and in the precipitation process, it is used to determine the precipitation of a compound from an aqueous solution (Christian, 1994; Skoog et al., 2004).

$$MA_{(s)} \leftrightarrow M^{+}_{(aq)} + A^{-}_{(aq)} \qquad \textbf{2.18}$$

$$K_{sp} = [M^{+}][A^{-}] \qquad \textbf{2.19}$$

where M^+ is the cation and A^- is the anion

The separation or isolation of the analyte from a solution can result in the precipitation of more than one element of interest by three mechanisms (Christian, 1994; Kolthoff, 2002):

1. **Inclusion:** Impurities are adsorbed/trapped within the crystal lattice
2. **Occlusion:** Impurities are placed/trapped in the crystal instead of the analyte
3. **Surface adsorption:** Impurities are adsorbed on the crystal surface

Inclusions and occlusions are often difficult to remove; thus, sample digestion and re-dissolution in a fresh or different solvent are most effective. Alternatively, the addition of a masking agent before precipitation may help to minimise co-precipitation (Kolthoff, 2002; Skoog et al., 2004). In REEs, organic compounds such as EDTA and HEDTA shown in **Figure 2.7** are common masking agents.

Chemical precipitation can be attained through the use of both organic and inorganic reagents. The organic reagents are mainly chelating and offer the benefit of producing a

precipitate with low water solubility (Christian, 1994). However, the reagent should be selective for the analyte (target metal). So far, selective precipitation in REE chemistry is complex due to the presence of impurities that tend to co-precipitate. Nonetheless, hydroxides, oxalates, carbonates, and double salts are commercially available.

2.6.1.1 Hydroxide precipitation

Hydroxide precipitation is widely employed as a means of purifying solutions. The process involves adding a suitable counter ion (i.e. OH^-) to form insoluble compounds with the metal ions present in the solution (Cotton et al., 1995). For instance, NaOH and $Ca(OH)_2$ can react with REE^{3+} to produce $REE(OH)_3$. When the pH of aqueous solutions is more than 7, the lanthanides can be precipitated, and the resultant precipitate is largely soluble in acidic solutions. Scandium will precipitate at a significantly lower pH (~5) relative to the lanthanides. Therefore, Sc can be separated from the lanthanides (Stevenson and Nervik, 1961; Monhemius, 1977; Habashi, 1997; Krishnamurthy and Gupta, 2005). It is also noteworthy that at pH >7, the lanthanides will precipitate with Fe^{2+}, whereas at pH <6, Sc^{3+} will precipitate with Y^{3+}, Al^{3+}, Ti^{4+}, and Fe^{3+}. Nevertheless, **Figure 2.17** illustrates the hydroxide precipitation of common metal ions as a function of pH and metal ion concentration.

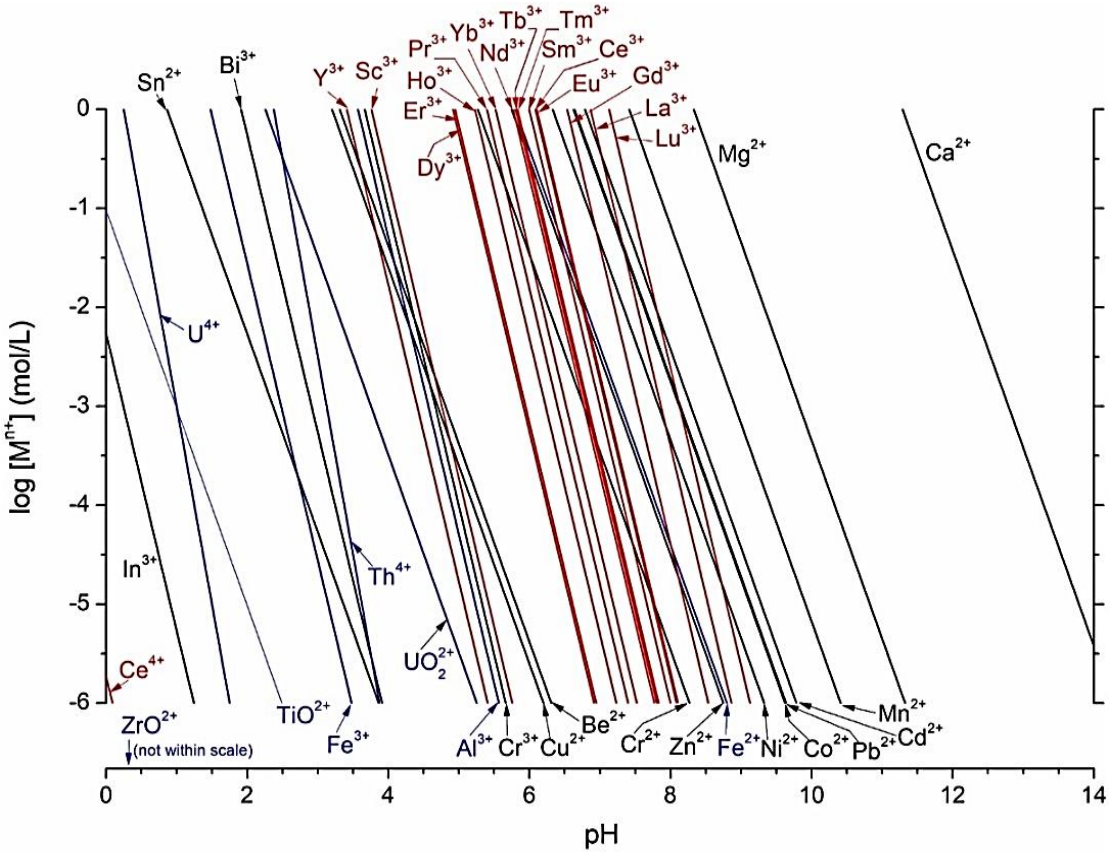

Figure 2.17: Hydroxide precipitation diagram of different metal ions at 25°C (Judge and Azimi, 2020).

In an aqueous solution, iron hydrolysis is a function of temperature and pH. Babcan (1971) studied the iron phases formed during the hydrolysis of a 0.5 M ferric sulphate solution, and the graphical relationship between pH, temperature, and the main equilibrium phases are presented in **Figure 2.18**. At low pH (<2), the increase in temperature can decrease the solubility of iron hydroxide to a more crystalline compound such as jarosite. However, at higher pH values, the metastable ferrihydrite (discussed in **Section 2.7.1.3**) is formed and can be transformed into haematite and/or goethite.

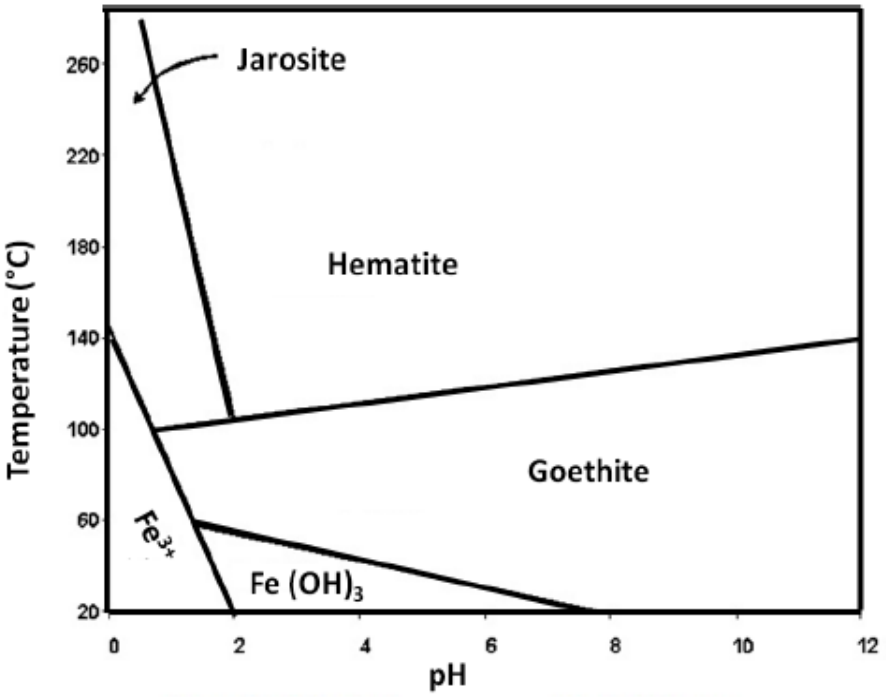

Figure 2.18: Stability regions of different compounds in the Fe-S-O system (Babcan, 1971).

Oxidative iron precipitation is often conducted to minimise co-precipitation with lanthanides. Diatomic oxygen in **Equation 2.20** is dissolved in an aqueous solution, followed by Fe(II) oxidation as presented in **Equation 2.21** (Haber and Weiss, 1934).

$$O_{2(g)} \longrightarrow O_{2(aq)} \qquad \textbf{2.20}$$

$$4Fe^{2+} + O_{2(aq)} + 4H^{+} \longrightarrow 4Fe^{3+} + 2H_2O_{(l)} \qquad \textbf{2.21}$$

Aeration is often sufficient for Fe(II) oxidation; however, other oxidants such as H_2O_2, MnO_2, and $KMnO_4$ are also widely used. Iron precipitation as jarosite at elevated temperatures has also been used. In an acidic sulphate solution, Fe^{3+} may form jarosite in the presence of sodium or potassium cations at 80-90°C (see **Equation 2.22**). However, at these elevated temperatures, co-precipitation with REEs is reported (Dutrizac, 2004; Dutrizac and Chen, 2009; Riley and Dutrizac, 2017).

$$M_2SO_{4(aq)} + 3Fe_2(SO_4)_{3(aq)} + 12H_2O \rightarrow 2MFe_3(S0_4)_2(OH)_{6(s)} + 6H_2SO_{4(aq)} \quad \textbf{2.22}$$

where M = Na^+ or K^+

Dutrizac (2004) studied the behaviour of REEs (La-Lu) in a synthetic sulphate solution. The morphology analysis showed that REE^{3+} do not extensively substitute with Fe^{3+} in the jarosite structure. However, it was observed that an increase in sodium-jarosite and potassium-jarosite in solution results in an increase in co-precipitation with the REE^{3+}. In a different study, scandium was also observed as a substitute for Fe^{3+} in the jarosite structure (Dutrizac and Chen, 2009).

For the purpose of this study, it can be deduced that the hydroxide precipitation of REEs is complex due to the high concentrations of Fe, Ti, and Al in CFA compared to REEs. Therefore, the hydroxide precipitation of the REE concentrate will not be considered.

2.6.1.2 Oxalate and carbonates precipitation

Precipitation using oxalates is known as the effective "intermediate" REE precipitation method. REEs are highly attracted to oxalate ions, and they will react to form REE-oxalates as demonstrated in **Equation 2.23** (Stevenson and Nervik, 1961; Habashi, 1997). The REE-oxalates can further be calcined into oxides as shown in **Equation 2.24**. Josso et al. (2018) reported that REE-oxalates can be formed in the order of MREEs>LREEs>HREEs.

$$2REE^{3+} + 3{C_2O_4}^{2-} + nH_2O \rightarrow 2REE_2(C_2O_4)_3 \cdot nH_2O_{(s)} \quad \textbf{2.23}$$

$$2REE_2(C_2O_4)_3 \cdot 8H_2O_{(s)} \xrightarrow{600-800℃} 2REE_2O_{3(s)} + 6CO_{2(g)} + 8H_2O \quad \textbf{2.24}$$

The concentration of REEs and potential interfering elements in the solution (i.e. Al and Fe) has a major influence on the choice of precipitating reagent. Oxalate precipitation is reported as efficient for the selective precipitation of REEs with low concentrations in solution (Chi and Xu, 1999; Qi, 2018). Josso et al. (2018) used a low-grade REE ferromanganese ore to

study the precipitation of REEs with ammonium oxalate from a chloride leach liquor with low REE concentrations (~0.1 g/L). At pH 1-2, >96% of REEs were selectively precipitated with less than 2% impurities (i.e. Ca, Ti, Fe, and Al). Yang et al. (2016) also observed that the selective precipitation of REE-oxalate can be achieved at pH <3 to minimise co-precipitation with Al and Fe. Therefore, it can be deduced that the oxalate precipitation process is pH-dependent (Chi and Xu, 1999; Qi, 2018). Archambo and Kawatra (2022) recovered REE-oxalate from a chloride-leached solution containing 170 g/ton REEs. In their study, REE recovery was between 30 and 50%. A possible reason for the low recovery was related to stoichiometry. It is noteworthy that when the concentration of REEs is low in the solution, excess oxalate is necessary for adequate complexation. Therefore, although oxalic acid is effective in selective precipitation from impurities such as Al and Fe, they also form oxalate complexes (i.e. ferrioxalate, shown in **Figure 2.19**) in the solution, resulting in high reagent consumption (Xia, 2013). Nonetheless, in this research study, oxalate precipitation will be considered for the production of high-purity REE concentrate.

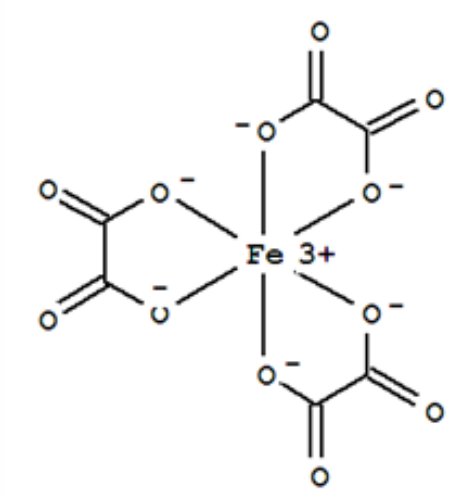

Figure 2.19: Ferrioxalate complex.

Carbonate precipitation is also an alternative. However, the precipitate that forms is less crystalline than that of oxalates. Consequently, the process requires seed crystallisation or surfactants, thus increasing the overall processing costs (Xia, 2013; Ma et al., 2019).

2.6.1.3 Double sulphate precipitation

The REEs can also be precipitated as double sulphates with reagents such as Na_2SO_4 and $(NH_4)_2SO_4$. In this method, a leach liquor is reacted with a sulphate salt at a high temperature (50-100℃) and precipitated as a sulphate compound called a double sulphate. High temperatures are necessary since the solubility of the sulphate salt decreases with an increase in temperature. This method is commercially used to separate the LREEs from the HREEs as shown in **Equation 2.25** (Krishnamurthy and Gupta, 2005). In an earlier study by Xu (1995), a leach solution containing 35 g/L REEs, 21 g/L Fe, and 1.5 M H^+ was directly precipitated with a sulphate salt. This process was selective for REEs with minimal Fe co-precipitation (~0.2%). Kul et al. (2008) precipitated REEs at 50℃ using a Na_2SO_4 solution. More than 90% of REEs were recovered with less than 1.0% impurities.

$$M^+ + LRE^{3+} + 2SO_4^{2-} + nH_2O \rightarrow LRE(SO_4)_3 \cdot nH_2O_{(s)} \qquad \textbf{2.25}$$

where M = NH_4^+, Na^+, and K^+

While double sulphate precipitation is effective, the main challenges reported are the excessive reagents required and the energy cost for precipitation (Kul et al., 2008; Silva et al., 2019). Nonetheless, as discussed in **Section 2.5.3**, the precipitation of REE-sulphates is reported at elevated temperatures and acid concentrations in the leaching process. Consequently, it is anticipated that during the sulphuric acid leaching process, the extraction efficiency of REEs will remain low due to the double sulphate effect.

2.6.2 Solvent extraction

Solvent extraction (SX) is a commercially preferred technique that has a strong scientific foundation in REE chemistry and the separation of elements such as Ti, Fe, and Al (Krishnamurthy and Gupta, 2005; Wang and Cheng, 2011). Industrial processes make use of a counter-current mixer settler continuous process to achieve metal extraction. In this study, batch extraction, which is a small-scale laboratory set-up, will be used to achieve the set objectives.

In SX, a solute is distributed between two immiscible liquid phases until equilibrium is attained. The distribution of solute A, equilibrated between an aqueous phase and an organic phase, may be described by **Equation 2.26**. This process is quite simple as two immiscible solvents are mixed, shaken vigorously, and left to separate (Christian, 1994; Rydberg, 2004).

$$A_{aq} \leftrightarrow A_{org} \qquad \textbf{2.26}$$

To evaluate the efficiency of an extraction process, the concentration of the solute between the two immiscible solvents can be calculated. This is defined as the distribution ratio, D, and is formulated in **Equation 2.27** (Christian, 1994; Rydberg, 2004).

$$D = \frac{[A]_{org}}{[A]_{aq}} \qquad \textbf{2.27}$$

A separation factor (α) can also be used to define the efficiency of the separation process. It is defined as a measure of the system's ability to separate solute A from solute B, which is the ratio of the distribution coefficient of A to the distribution coefficient of B. For example, the separation factor between Ti and Fe can be calculated using **Equation 2.28**. Therefore, if α >1, the separation of Ti and Fe is considered feasible. A higher α-value leads to improved separation and requires a minimum number of steps to attain the extraction (Christian, 1994).

$$\propto_{Ti,Fe} = \frac{D_{(Ti)}}{D_{(Fe)}} \qquad \textbf{2.28}$$

Selective extraction can be accomplished by targeting a metal of interest (i.e. Ti) in the solution and then stripping the organic phase under various experimental conditions (Christian, 1994). The stripping/selective stripping of metal ions in the organic phase can be accomplished using acids such as H_2SO_4, HCl, and HNO_3 or alkaline solutions of NaOH and NH_4OH. The stripping reagent is selected according to the chemistry of the organic phase and the type of salt being considered (Krishnamurthy and Gupta, 2005; Desouky, 2006).

2.6.2.1 Extraction

In SX, the selected complexing reagent (extractants) and the extracting solvent are important variables. The latter is affected by the stability and solubility of the analyte complex (Christian, 1994). Organic solvents containing long-chain alcohols, aromatic compounds, and aliphatic compounds are common. Typical solvents used in metal extraction include xylene, 2-octanol, hexane, and kerosene (Stevenson and Nervik, 1961; Habashi, 1997). Emulsion is also possible between the aqueous and organic phases during the extraction process, and it is mostly challenging to disintegrate. Alcohol-modifying reagents are commonly utilised, and they include decanol, n-octanol, and p-nonyl phenol (Xie et al., 2014; Zhu et al., 2015; Jha et al., 2016). Consequently, a few fundamental criteria can be considered when selecting the extracting solvent, and they include; (i) the density difference between the liquid and aqueous phases, (ii) low viscosity and boiling point for easy removal, and (iii) high selectivity and loading capacity for either the analyte or impurities.

In a sulphate system, selectivity is mostly attained by complexation with a suitable extractant. Certain extractants have great separation efficiency in a single system, whereas others may be utilised in several systems. The three basic extractants are:

i. Neutral extractants
ii. Acid extractants
iii. Anionic extractants

Neutral Extractants

The organic compounds containing C=O and P=O groups (i.e. phosphates and ketones) are common neutral extractants. Typical extractants include tri-n-butyl- phosphate (TBP) and tri-n-octylphosphine oxide (TOPO) (Xie et al., 2014; Jha et al., 2016). These extractants are regarded as “basic” and will complex with neutral metal complexes by replacing waters of hydration, thus forming an organo-metal complex that becomes soluble in the organic phase (Ferdowsi and Yoozbashizadeh, 2017).

Acid Extractants

The extraction through acidic extractants (HL) is observed through a cation exchange mechanism where the extractant proton (H^+) is replaced by the metal (M^{3+}), as demonstrated

in **Equation 2.29**. In this process, the extractant employed will "self-associate", generating dimers and polymers to minimise the polarity in non-polar solvents. Consequently, it is often observed that during SX, solvent properties such as density and solubility in water have a greater impact on the acidic extractants (Xie et al., 2014; Jha et al., 2016). The carboxylic acids (Versatic acids, Naphthenic acids) and organophosphorus acids (D2EHPA, PC88A, and Cyanex 272) are typical acidic extractants that utilise functional groups such as –POOH, –COOH, and $–SO_3H$ (Xie et al., 2014; Jha et al., 2016).

$$M^{3+}_{(aq)} + 3HL_{(org)} \longrightarrow ML_{3(org)} + 3H^{+}_{(aq)} \qquad \textbf{2.29}$$

where M = REE^{3+} or Fe^{3+}

Anionic Extractants

To achieve anionic exchange, a strong anionic ligand will react with metal ions to form a strong anionic metal complex that is easily extracted into the organic phase. Usually, long-chain alkyl or aryl amines, as demonstrated in **Figure 2.20**, work efficiently as strong anionic ligands due to their properties, such as high molecular weight (250-600 g/mol) (Xie et al., 2014). In acidic solutions, amines are known to produce stable salts, and they have anion exchange capacity in the order $ClO_4^- > NO_3^- > HSO_4^- > F^-$. Complexing reagents such as EDTA and DTPA can be added to the system to improve the selectivity of REEs when using primary and secondary amines (Desouky, 2006; Xie et al., 2014). These organic compounds will form a metal complex that can be selectively extracted in the organic phase or masked in the aqueous phase (Scal et al., 2020).

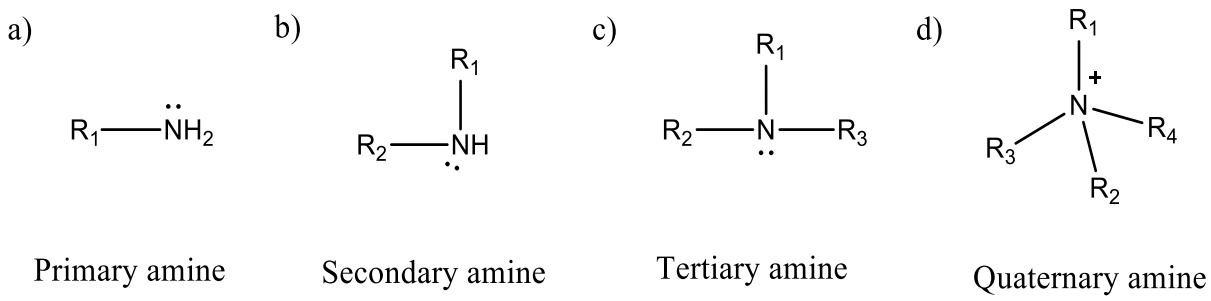

Figure 2.20: Structure of alkyl amines used as basic extractants (Desouky, 2006).

The primary amines for example, will first protonate into sulphate (or bisulphate) ion-pairs as shown in **Equation 2.30** to allow easy exchange with complex ions. This will be followed by the extraction of an anionic complex species into the organic phase, as presented in **Equation 2.31** (Desouky, 2006).

$$2RNH_{2(org)} + H_2SO_{4(aq)} \longrightarrow (RNH_3)_2SO_{4(org)} \qquad \textbf{2.30}$$

$$2M(SO_4)^{3-}_{(aq)} + 3(RNH_3)_2SO_{4(org)} \longrightarrow 2(RNH_3)_2M(SO_4)_{3\,(org)} + 3SO^{2-}_{4(aq)} \qquad \textbf{2.31}$$

where M = Fe or REEs, RNH_2 = Primary amines, and R = $(CH_3)_3C(CH)_2C(CH_3)_2)_4$

The pH level and the aqueous solution system also affect the extraction performance. In a sulphate system, the dibasic nature of sulphuric acid results in the sulphate-bisulphate equilibria as demonstrated in **Equation 2.32** and **2.33**. As a result, the main anionic species at elevated acid concentrations (low pH) are bisulphate, and when the acid concentration drops, the common species will be the sulphate ion (Desouky, 2006). Considering amines in this research study, the hydrogen ions in the CFA leach liquor will be essential in determining the optimum extraction of the analyte (i.e. Ti and Fe).

$$H_2SO_{4\,(aq)} \longrightarrow H^+ + HSO_4^- \qquad K_2 = 1 \times 10^3 \qquad \textbf{2.32}$$

$$HSO_4^- \longrightarrow H^+ + SO_4^{2-} \qquad K_3 = 1.27 \times 10^{-2} \qquad \textbf{2.33}$$

2.6.2.2 Purification of leach liquor by solvent extraction

The general principles of SX have been discussed. Therefore, to produce smelter-grade alumina after the sinter-H_2SO_4 leach process, solvent extraction will be considered as a purification technique. As such, it is crucial to consider the distribution of REEs, Al, Fe, and Ti during the extraction process.

Solvent Extraction of Al, Ti, and Fe

Direct crystallisation of alumina after the sinter-H_2SO_4 leach process is desired. However, Ti^{4+} and Fe^{3+} are the major Al^{3+} impurities reported, which consequently affect the purity of the generated alumina (Li et al., 2011; Matjie et al., 2005; Rushwaya, 2016; Rampou, 2018; Ma et al., 2021). Therefore, SX has been studied to purify the CFA leach liquor. Specifically, primary amines have displayed great selectivity for Fe^{3+} and Ti^{4+} extraction in the organic phase, whereas Al^{3+} remains in solution (Matjie et al., 2005; Li et al., 2011; Rushwaya, 2016; Rampou, 2018). Nevertheless, it has been noted that in very acidic solutions (pH 0.1), Fe^{3+} has a low loading capacity compared to a less acidic solution (pH >1) (Aglietti et al., 1990; Rushwaya, 2016). Li et al. (2011) demonstrated that Fe(III) can be extracted in its hydrolysed state as shown in **Equation 2.34**. Therefore, at high acid concentrations (<0), $FeHSO_4^{2+}$ is the major iron (III) species; thus, in its hydrolysed form, it mostly remains in the raffinate (Alguacil et al., 1987; Li et al., 2011). **Figure 2.21** also demonstrates that species such as $FeSO_4^+$ and $Fe(SO_4)_2^-$ are hydrolysed to $FeHSO_4^{2+}$ as the dominant Fe species in acidic sulphates (Li et al., 2011; Rushwaya, 2016).

$$Fe^{3+} + H_2O + SO_4^{2-} \rightarrow Fe(OH)SO_{4(aq)} + H^+ \qquad \textbf{2.34}$$

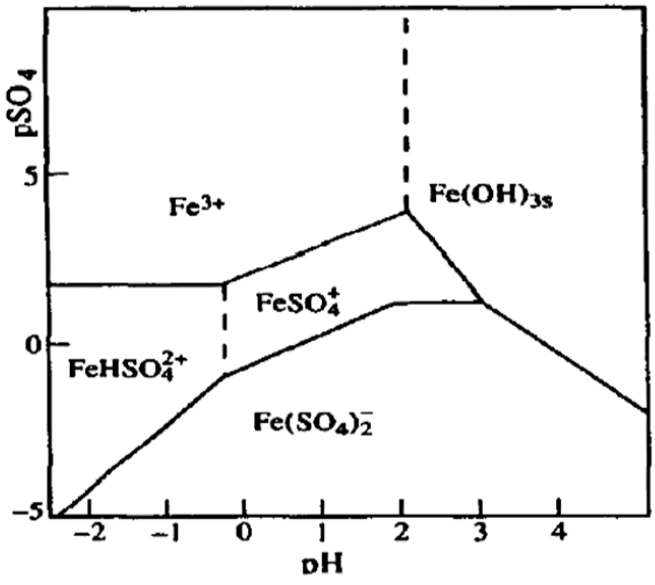

Figure 2.21: Fe(III)-sulphate-pH diagram (Gil et al., 1995).

In a preliminary study by Rushwaya (2016), it was demonstrated that at 0.28 M H^+, 88% Fe^{3+}, and 99% Ti^{4+} are extracted using Primene JM-T/Shellsol D70, while at 4.67 M H^+, 36.9% Fe^{3+} and 99% Ti^{4+} are extracted (Rushwaya, 2016). Therefore, it was concluded that Fe^{3+} has a low loading capacity at acidic sulphate concentrations. Sole (1999) illustrated the speciation of titanium in a sulphuric acid system and showed that the dominant species at all concentration levels is the bisulphate complex $Ti(OH)_3HSO_4$ (see **Figure 2.22**). Thus, the high extraction of Ti^{4+} was observed by Rushwaya (2016) at 0.28 M H^+ and 4.67 M H^+. Rampou (2018) used a two-step leaching process developed by Shemi (2013) to generate a leach solution for further purification using an integrated SX and precipitation process (see **Figure 2.13**). In this process, Fe^{3+} was first reduced to Fe^{2+}, followed by Ti^{4+} extraction using Primene JM-T (10%)/kerosene in A/O:1:1 for 15 minutes. The extracted Ti was stripped using a 1 M NH_4OH solution to selectively recover $Ti(OH)_4$, which was then calcined to produce 93.3% TiO_2. This TiO_2 was classified as type II quality according to the standard set by the American Society for Testing and Materials (ASTM). The Al in the raffinate was directly crystallised as alum (**Equation 2.9**) and calcined to produce 96% alumina of smelter quality. The remaining solution was processed to precipitate $Fe(OH)_2$, which was subsequently calcined at ~1000°C to produce haematite (79.29% Fe_2O_3) with the capacity to be used as a source of iron ore (Rampou, 2018).

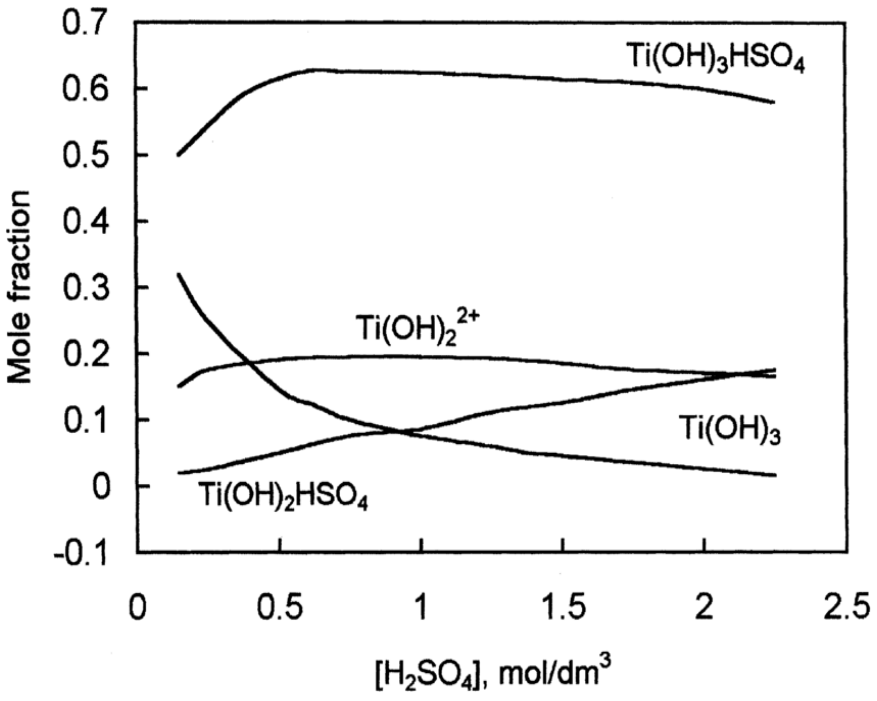

Figure 2.22: Distribution of titanium species in a sulphate system (Sole, 1999).

From the above discussion, it can be concluded that the integrated purification technique is the most effective for producing high-purity products in the acidic sulphate system. Therefore, high-purity TiO_2 can be generated from SX followed by precipitation and calcination. Similarly, iron oxide (i.e. haematite) can be recovered to add value to iron ore processing. In this research study, Ti and Fe will be considered as value-added materials in wastewater treatment processes since coal power plants are the major water consumers and polluters. Further discussion is presented in **Section 2.7**.

Distribution of REEs in Solvent Extraction

In the early 1970s, AS Megon patented a process to purify and separate REEs from xenotime (Gaudernack et al., 1973). In this process, a leach liquor containing ~20 g/L REEs was obtained from a sulphate acid decomposition step discussed in **Section 2.4.2** and purified by SX using 30% 2-ethylhexyl phosphoric acid (D2EHPA) in Shellsol (Gaudernack et al., 1973; Xie et al., 2014). The HREEs (Nd, Sm, and Y) were selectively extracted into the organic phase while LREEs and Fe^{2+} remained in the raffinate. The extracted HREEs were further selectively separated by dilute HNO_3 and H_2SO_4 solutions, while the LREEs in the raffinate were selectively extracted with NH_4SCN in a different circuit. The application of acidic extractants was later adopted by many researchers to study the extraction from secondary REE resources (Xie et al., 2014; Battsengel et al., 2018; Innocenzi et al., 2018).

Battsengel et al. (2018) investigated the purification of REEs from an apatite sulphate leached solution (1 M H_2SO_4) that has 1.16 g/L REEs, 0.027 g/L Al, and 0.008 g/L Fe. The REEs (HREEs) were extracted using 1.2 M D2EHPA in kerosene, while the LREEs remained in the raffinate. Al and Fe were co-extracted into the organic phase in minor quantities. The loaded HREEs were selectively stripped from the organic phase with 3 M H_2SO_4 and precipitated as REE-oxalates. The LREEs in the raffinate were also directly and selectively precipitated as oxalates. Comparable findings were obtained by Innocenzi et al. (2018) who treated a fluorescent lamp leach solution (sulphate) containing 6290 mg/L REEs and 1270 mg/L impurities. In their study, the extraction of REEs with D2EHPA in kerosene followed the order Y≥Tb>Gd≥Eu>Ce≥La at pH 0.5. At a solution pH >2, it was noted that all the REEs were loaded in the organic phase. Selective stripping was conducted with dilute H_2SO_4 followed by precipitation with oxalic acid.

Acidic extractants are also selective for Sc during SX. However, the main impurity in Sc solutions is Ti (Wang and Li, 1994; Shaoquan and Suqing, 1996; Ju et al., 2022). In a study by Wang and Li (1994), an aqueous feed containing ~14 mg/L Sc, ~100 g/L Ti, 100 g/L Fe, and ~200 g/L H_2SO_4 was treated with Cyanex 923 in kerosene. Selective stripping of Ti was attained by adding H_2O_2 in the organic phase to form a stable complex $[TiO(H_2O_2)]^{2+}$. Approximately 59% Ti(IV) and <4% Sc(III) were scrubbed from the loaded organic phase. The selective Ti scrubbing was followed by Sc stripping using 2 M H_2SO_4. A recent study by Ju and colleagues (2022) investigated the selective precipitation of Ti from Sc before SX using phosphoric acid. Ti(IV) was first directly precipitated from the sulphate leach liquor as titanium phosphate followed by Sc SX from Fe-bearing solution (Ju et al., 2022).

Amines are also attractive for REE extraction from a sulphate solution. Primary amines, such as N1923 and Primene JM-T, are utilised to separate U and Th from REEs. When the solution pH is less than 0, both elements are extracted into the organic phase, leaving the REEs in the aqueous phase. The REEs are further selectively extracted by adjusting the pH to greater than 0, resulting in the production of Fe(II)-rich solution (Desouky, 2006; Xie et al., 2014; Zhu et al., 2015). Secondary amines, such as N235, are also efficient in extracting REEs in the presence of complexing reagents (Rice and Stone, 1962). In a study by Hiskey and Copp (2018a), the behaviour of REEs in a sulphate copper leach solution (pH 1.86) was studied at room temperature using Primene JM-T/Kerosene. The copper pregnant leach solution (PLS) contained 15 ppm Y and 2 ppm Nd. Yttrium and neodymium extractions were 90% and 95%, respectively, using 0.15 M Primene JM-T at an O:A phase ratio of 1:1. In a different study, the behaviour of other REEs was evaluated. At 0.15 M Primene JM-T, Y extraction was 88.4%, whereas the LREEs and HREEs averaged 95% and 92%, respectively (Hiskey and Copp, 2018b). The solution chemistry was modelled by PHREEQC software and at low Primene JM-T concentrations, $REE(SO_4)_3^{3-}$ were the dominant species being extracted. An example of the Y-SO_4^{2-} system is presented in **Figure 2.23**, where at 0.23 M SO_4^{2-}, $Y(SO_4)_3^{3-}$ with significant amounts of $Y(SO_4)^{2-}$ is quantified. As extractant concentrations increase, the reaction appears to favour $REE(SO_4)^{2-}$. Similar extraction behaviour was also observed in Sc extraction using Primene JM-T in kerosene (Schack, 1965).

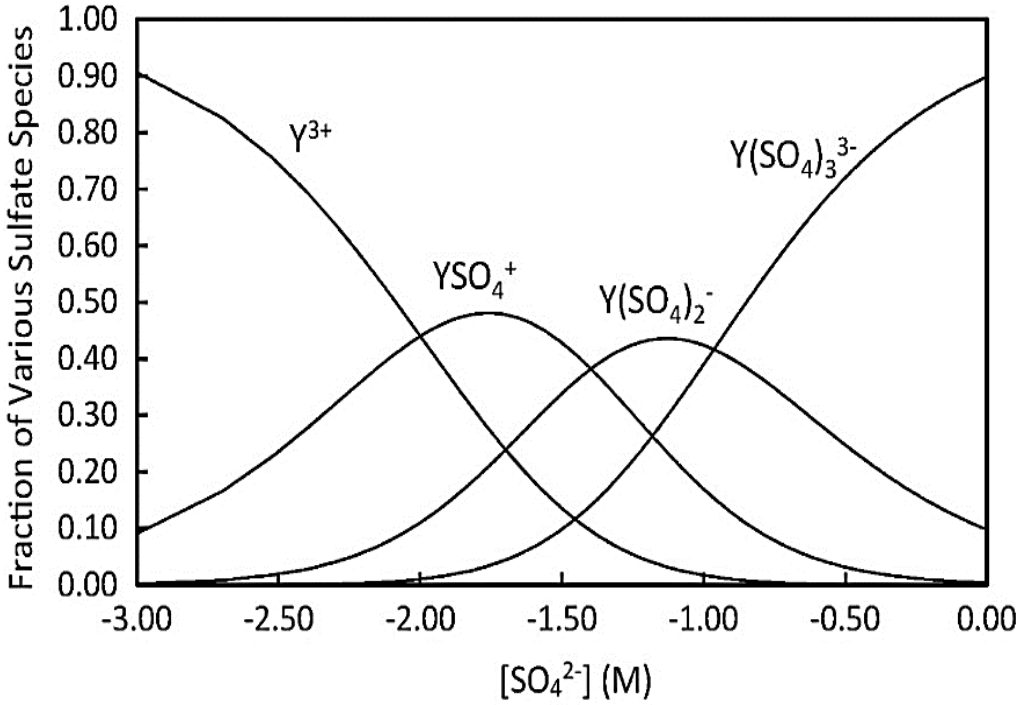

Figure 2.23: Distribution of yttrium sulphate species as a function of sulphate ions concentration at 25°C (Hiskey and Copp, 2018b).

To summarise, REEs are also extracted by amines in an acidic sulphate system. Thus, in this research study, their extraction behaviour will be monitored during the purification of Ti and Fe from a sulphate CFA leach liquor for the production of smelter-grade alumina.

2.7 Utilisation of CFA in Wastewater Treatment

The most cost-effective and feasible approach for recycling CFA is its direct use as an additive or starting material. The building and construction industry has made significant contributions by utilising CFA in the manufacturing of bricks and blocks, as well as in the production of concrete and cement (Kruger and Krueger, 2005). Notable construction projects that have incorporated CFA include the Maputo-Katembe Bridge in Mozambique, the Katse Dam in Lesotho, and the Burj Khalifa in Dubai (Eskom, 2016). However, due to commercial regulations on CFA utilisation, only a limited dosage of 5-35% is allowed, which restricts its large-scale utilisation (Afrisam, 2009; Arp et al., 2018). Another potential application for direct use of CFA is in wastewater treatment. Acid mine drainage (AMD), shown in **Figure 2.24**, is the greatest environmental threat and has proven challenging to prevent at the source. Therefore, remediation using industrial waste products such as CFA to

adjust the water pH, oxidise, adsorb, and precipitate metal ions as hydroxides has been recognised as the cheapest and most innovative alternative (Singh et al., 2018; Mushtaq et al., 2019).

Figure 2.24: Mine wastewater from the Witwatersrand basin, South Africa (Masindi et al., 2022).

CFA can also be indirectly applied in wastewater treatment by extracting Fe, Ti, Al, and Si, which are commonly used for adsorption, coagulation, and catalysis, as shown in **Figure 2.25** (Mushtaq et al., 2019). However, the cost implications of indirect utilisation (i.e. leaching and synthesis) have not been proven to be economical; thus, commercial scaling is not yet feasible. In the alumina (Al_2O_3) production in **Section 2.5.2**, Ti, Fe, and CFA-SR (Si-rich residue) are generated as by-products for downstream purification or disposal. Therefore, in this study, value addition is considered through adsorption and coagulation.

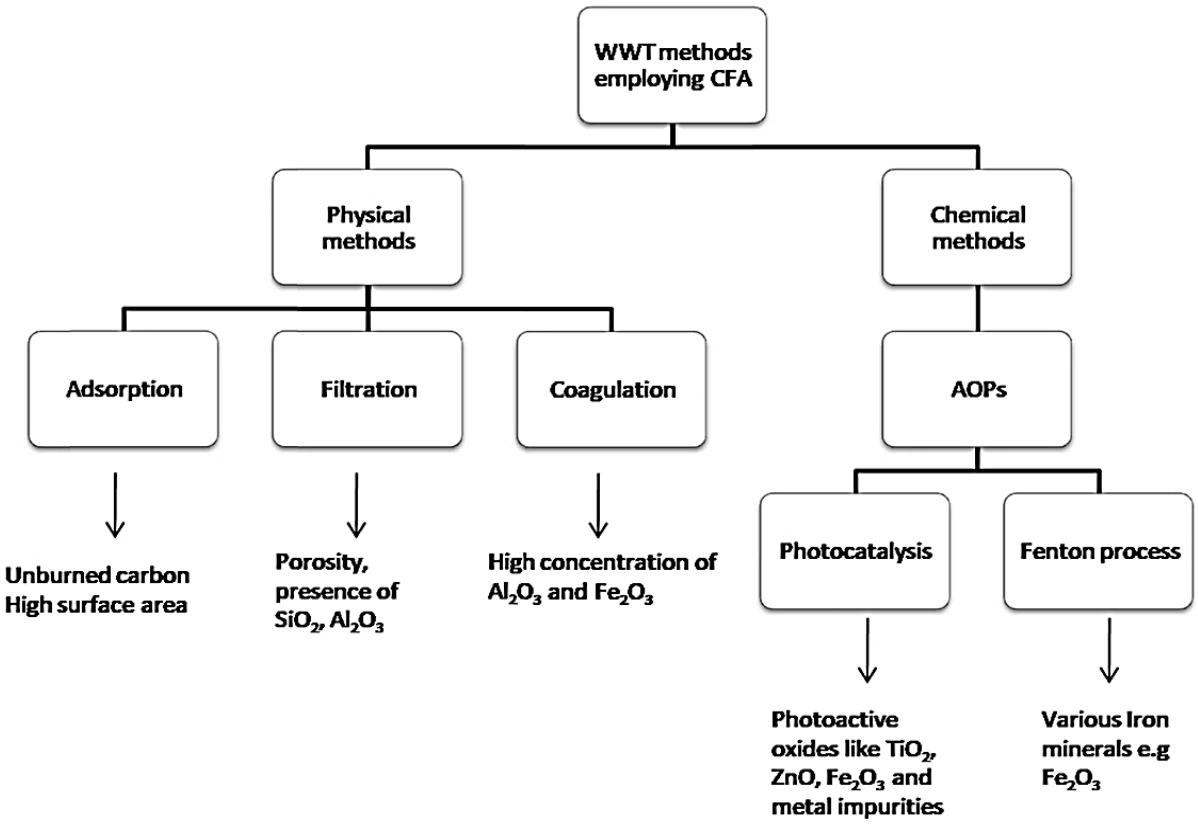

Figure 2.25: A schematic diagram illustrating various methods of CFA utilisation in wastewater treatment (Mushtaq et al., 2019).

2.7.1 Coagulation

Coagulation is a popular water treatment method used to remove colloidal impurities. Colloids are insoluble particles that carry a negative charge in surface water and cannot aggregate unless their charge is neutralised (due to zeta potential force). Therefore, coagulants, which are positive ions, are added to neutralise the negative charges. This eventually leads to the formation of aggregates called flocs, which can be precipitated and filtered. Generally, the coagulation process involves flash mixing, coagulation/flocculation, sedimentation, and filtration, as demonstrated in **Figure 2.26** (Saunders and Saunders, 1991; Ebeling et al., 2003).

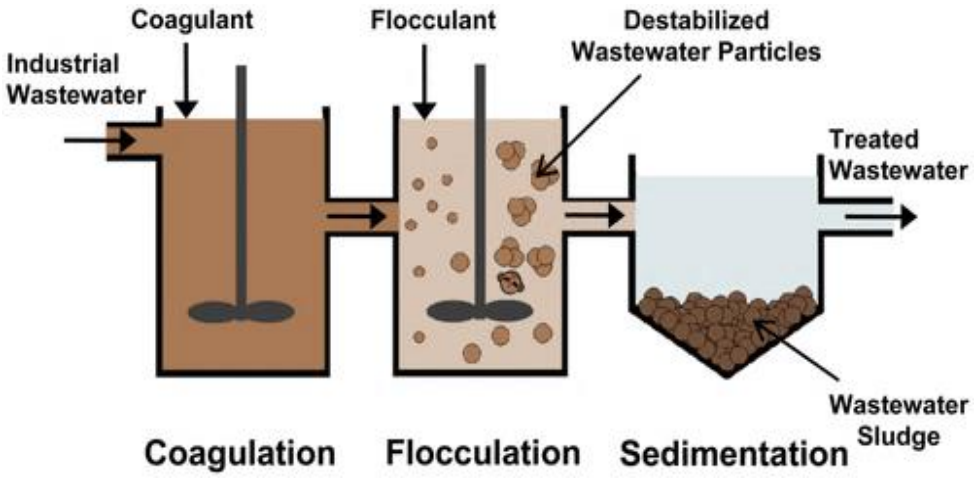

Figure 2.26: A conventional coagulation/flocculation unit process (Teh et al., 2016).

Several coagulants are available on a commercial scale to aid in coagulation, and they vary from metal-based to polymer-based coagulants (Matilainen et al., 2010). The metal salts of aluminium ($Al_2(SO_4)_3 \cdot 18H_2O$ and $AlCl_3$) and iron ($FeCl_3 \cdot 6H_2O$, $Fe_2(SO_4)_3$ and $FeSO_4 \cdot 7H_2O$) are common, and CFA is abundant in both metals.

2.7.1.1 Destabilisation and aggregation of colloidal particles

When coagulants are added to wastewater, they dissociate into their respective ions, such as Al^{3+} and Fe^{3+}, and associate to form $Al(H_2O)_6^{3+}$ and $Fe(H_2O)_6^{3+}$. This hydrolytic reaction produces a series of monomeric to polymeric complexes. Polymeric species of Fe and Al include $Fe_2(OH)_2^{4+}$, $Fe_3(OH)_4^{5+}$, $Al_2(OH)_2^{4+}$, and $Al_3(OH)_4^{5+}$, respectively (Gregory and Duan, 2001). Coagulants are therefore used to change the physical properties of the suspended and dissolved particles. In general, when added to wastewater, they will destabilise, agglomerate, and subsequently remove suspended solids from the water (Saunders and Saunders, 1991; Ebeling et al., 2003).

The essential mechanisms involved in coagulation include the following:

i. Ionic layer compression

ii. Adsorption and charge neutralisation

iii. Sweep coagulation

Ionic layer compression involves the addition of charged ions that accumulate at the particle surface and are held by attractive and electrostatic forces. On the surface, ions of opposite charge will result in electrostatic attractions and repulsions; thus, an electrical double layer will form as presented in **Figure 2.27**. In wastewater treatment, this phenomenon is not feasible. However, the adsorption of counter ions to neutralise the particle charge is important (O'Melia, 1987; Saunders and Saunders, 1991; Suopajärvi, 2015).

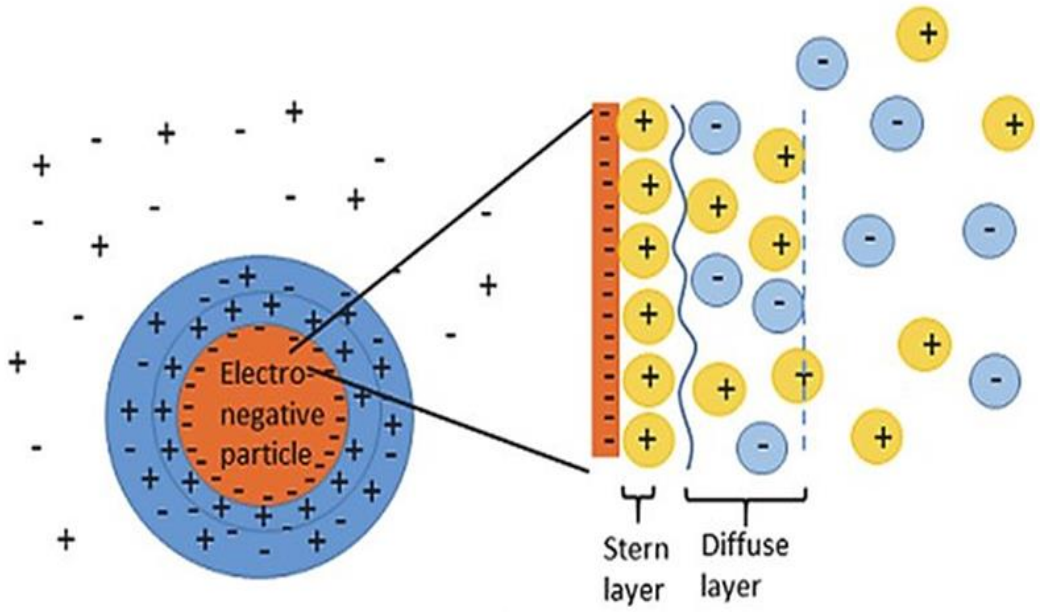

Figure 2.27: Double layer around a negatively charged colloid (Suopajärvi, 2015).

Charge neutralisation is achieved by the adsorption of particles on the surface. The trivalent Al and Fe ions are multiprotic acids that will hydrolyse producing monomeric and polymeric species in an aqueous solution. Thus, the negative surface charge is neutralised, resulting in a decrease in the repulsion energy barrier and rapid coagulation. This can occur through electrostatic force or a form of surface complex formation (Kang, 1994; Gregory and Duan, 2001). For practical water treatment operations, it is favourable to add metal coagulants at a dosage higher than the solubility of the amorphous hydroxide precipitates to ensure optimal removal of colloidal particles, as these particles can collide and become entangled in the precipitates (Amitharajah and O'Melia, 1990). This process also facilitates sweep flocculation. The excess amorphous hydroxide can act as a "sweeping agent" that adsorbs impurities and fine particles (Gregory and Duan, 2001).

Coagulation can be influenced by many variables that are either controlled or uncontrolled. Controlled variables include coagulant dose, reaction time, and coagulation mixing intensity. Variables that cannot be controlled include the source of water being treated, such as pH and turbidity (Hu et al., 2016; Mwewa, 2020).

2.7.1.2 Coagulation with CFA

CFA contains both Al and Fe, which are the resources for metal-based coagulants. Therefore, several researchers have explored the extraction of both metals in acid and alkaline solutions to produce coagulants (Fan et al., 2005; Li et al., 2009; Sun et al., 2011; Hu et al., 2016). Fan and colleagues produced a sulphate-based complex coagulant. In their study, ferric and aluminium sulphates in **Equation 2.35** and **2.36** were extracted using 3 M H_2SO_4, by leaching at 120℃ for 4 hours. The extraction efficiency was 84.8% for Fe and 55.1% for Al. The low Al extraction was attributed to the mullite phase. From the leached solution, a sulphate-based complex coagulant was produced and tested on the arsenic-prepared stock solution, and more than 97% As was recovered (Fan et al., 2005). Hu et al. (2016) prepared the sulphate-based coagulant and compared its efficiency with the commercial coagulant. At a coagulant dosage of 3.2 mL/L and pH >5, 92% of the suspended solids (SS), 65% of the chemical oxygen demand (COD), and 98% PO_4^{3-} were efficiently removed from domestic wastewater.

$$Fe_2O_{3(s)} + 3H_2SO_{4(aq)} \rightarrow Fe_2(SO_4)_{3(aq)} + 3H_2O \qquad \textbf{2.35}$$

$$Al_2O_{3(s)} + 3H_2SO_{4(aq)} \rightarrow Al_2(SO_4)_{3(aq)} + 3H_2O \qquad \textbf{2.36}$$

In research conducted by Sun et al. (2011), the production of CFA-coagulant was extended to include the preparation of polyferric-aluminum-silicate-sulphate (PFASS) coagulants. The process included alkaline leaching, polymerisation, and acid leaching. The study aimed to treat oily wastewater for the removal of turbidity and COD. The optimal mole ratios for turbidity and COD removal were 12:1 and 16:1, respectively.

Compared to commercial coagulants that require primary resources as starting materials, CFA-based coagulants are both inexpensive and efficient. In this research study, aluminium is identified as a smelter-grade resource. Therefore, only iron (extracted as a by-product) will be considered as a potential coagulant.

2.7.1.3 Iron-based coagulants

Ferrous oxidation and precipitation are important concepts in water treatment processes. The chemistry of iron in solution involves a continuous cycle of ferrous (Fe(II)) and ferric (Fe(III)) oxidation states. Therefore, the oxidation of Fe(II) in solution affects the level of supersaturation during precipitation (Hove, 2008). This section will review ferrous oxidation and precipitation in acidic sulphate solution at a pH range relevant to this study.

Ferrous Oxidation

The oxidation of ferrous iron by molecular oxygen (see **Equation 2.21** and **2.20**) is affected by many parameters, including solution pH and ions in the solution (Morgan and Lahav, 2007; Stumm and Lee, 1961). Morgan and Lahav (2007) studied the Fe(II) oxidation rate versus pH (see **Figure 2.28**) and observed that below pH 4, the rate of oxidation is very low. As the pH increases above 4, the oxidation rate accelerates, and they concluded that in this region (pH 4-7), the oxidation rate is dependent on pH. Similar results were observed by Stumm and Lee (1961). The Fe(II) oxidation reaction was found to increase by 100-fold as pH increased from 6-8. Mwewa (2020) studied the rate of ferrous oxidation at pH 5-7. The findings of the study showed that the rate of oxidation increases with pH, and therefore, the reaction rate is of the first-order relative to ferrous iron for all pH levels.

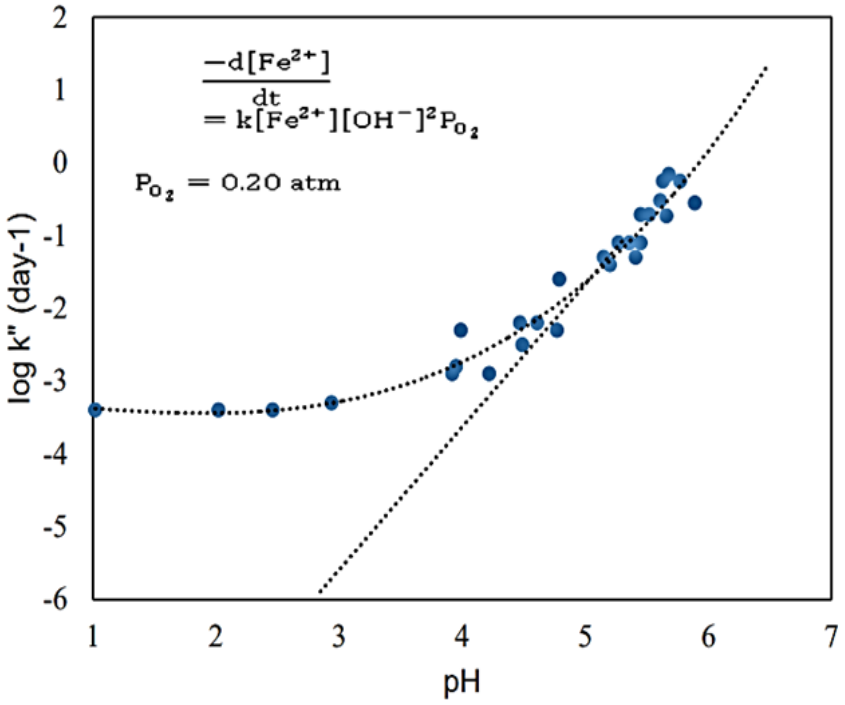

Figure 2.28: The rate Fe oxidation as a function of pH (Morgan and Lahav, 2007).

A change in Fe speciation as pH increases has also been reported (Lowson, 1982; Millero, 1985; Morgan and Lahav, 2007; Jones et al., 2014). Jones et al. (2014) used electrochemical studies to explain this phenomenon. At pH 2.5, the Fe(III)/Fe(II) redox couple was 0.77 V, and as the pH increased, a more negative reduction potential of -0.02 V was observed. The Fe species in solution changed from Fe^{2+} to $Fe(OH)^{+2}$ and $Fe(OH)_0^{2+}$. Therefore, it was concluded that the negative potential was a result of Fe(II) becoming a better-reducing agent and more readily oxidised (Jones et al., 2014). Lowson (1982) and Millero (1985) showed that the rate constant for the oxidation of $Fe(OH)_2^0$ is higher than the rate constant for $FeOH^+$ which, in turn, is greater than the rate constant of Fe^{2+}. The reactivity of these species was also observed by Morgan and Lahav (2007), who showed that the hydrolysed Fe(II) species are more readily oxidised than non-hydrolysed ferrous species in the order $Fe(OH)_2^0{}_{(aq)} >> Fe(OH)^+ >> Fe^{2+}$.

Iron Hydrolysis and Precipitation

In an aqueous solution, ferrous iron (Fe^{2+}) and ferric iron (Fe^{3+}) form hexa-coordinated complexes in which hydroxylation results in polymerisation reactions when deprotonation occurs (Hove, 2008). Since hydrolysis is dependent on acid-base reactions, the dominant

hydroxyl species in the solution will depend on the prevailing pH (Hove, 2008; Mwewa, 2020). Hove (2008) constructed a ferrous solubility diagram (see **Figure 2.29**) based on literature to elucidate that ferrous hydroxides are formed at high pH levels, forming both crystalline hydroxide and amorphous hydrous oxide. Both forms of ferrous suspension are unstable and prone to oxidation when exposed to air.

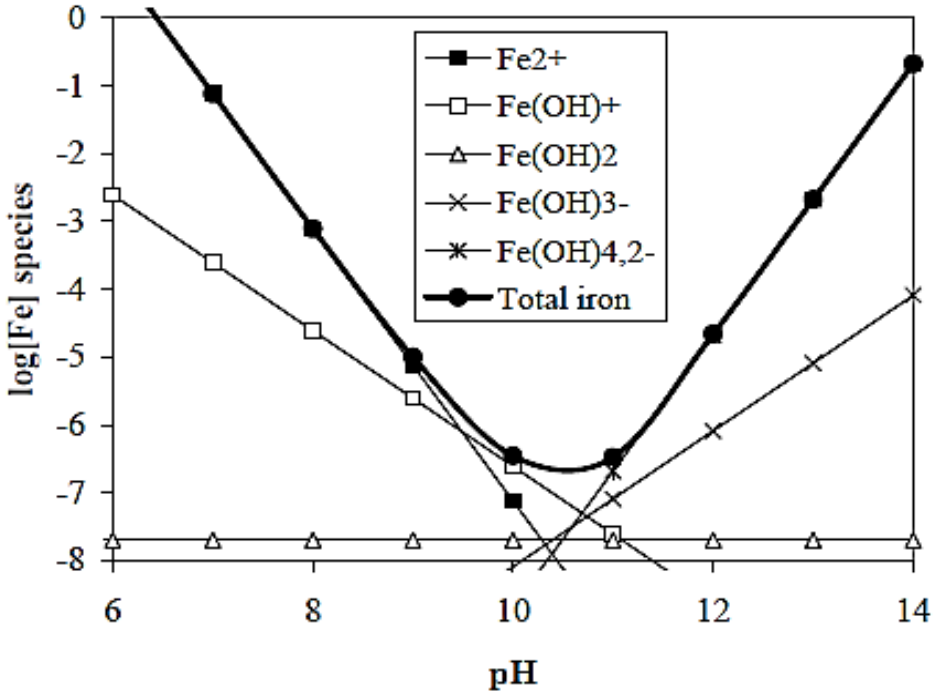

Figure 2.29: The solubility of ferrous hydroxide at 25°C (Hove, 2008).

In Fe(III) hydrolysis, the hexa-aqua ferric complexes will deprotonate to form monomeric complexes in a wide pH range. Similar to ferrous chemistry, the solubility of ferric hydroxide is a function of pH. Fe(III) hydrolysis and subsequent polymerisation and precipitation are the major formation pathways of the iron oxides as shown in **Figure 2.30**. The solubility of ferric oxides/hydroxides is presented in **Table 2.5**, and ferrihydrite is a common phase. The formation of oxide/hydroxide phases has been reported to depend on the OH^-:Fe(III) molar ratio (Cornell et al., 1989; Hove, 2008; Schwertmann and Cornell, 2008; Mwewa, 2020).

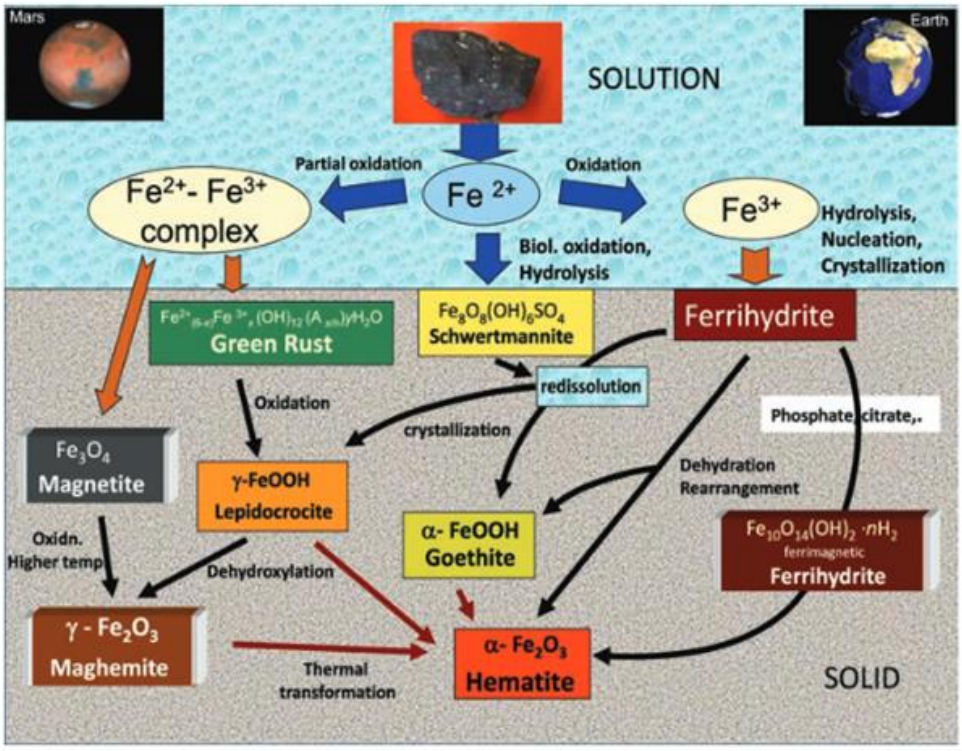

Figure 2.30: Schematic pathways for common iron oxides and oxyhydroxides (Barrón and Torrent, 2013).

Table 2.5: Solubility products of different iron oxides and oxyhyroxide (Schwertmann and Cornell, 2008)

Mineral phase	Formula	Solubility product as $pFe^{3+} + 3pOH^-$
Ferrihydrite	$Fe_5HO_8 \cdot 4H_2O$	37-39.4
Haematite	α-Fe_2O_3	42.2-43.3
Lepidocrocite	γ-FeOOH	40.6-42.5
Goethite	α-FeOOH	43.3-44
Magnetite	Fe_3O_4	--

--Not available

Notably, the precipitation of Fe(III) is often defined by fast kinetics, resulting in very small particles (~1 µm). This rapid precipitation leads to the production of metastable or poorly crystalline phases (i.e. ferrihydrite or schwertmannite) (Karapinar, 2003; Hove, 2008; Han et al., 2015; Kefeni et al., 2017; Mwewa, 2020). Ferrihydrite is defined by the general formula

$5Fe_2O_3 \cdot 9H_2O$ and is a poorly crystalline iron oxide/hydroxide phase (Murad and Schwertmann, 1980). Other formulas have been suggested for ferrihydrite, such as $Fe_5HO_8 \cdot 4H_2O$ and $2FeOOH_2 \cdot 6H_2O$ (Jambor and Dutrizac, 1998). Schwertmannite is a complex hydroxy ferric sulphate with the formula $Fe_8O_8(OH)_6SO_4$. Similar to ferrihydrite, it is metastable. According to Loan et al. (2002), schwertmannite can be differentiated (at most qualitatively) by its hedgehog morphology. However, according to Claassen and Sandenbergh (2006), schwertmannite is essentially ferrihydrite with a high sulphate content. Consequently, both phases have been identified in the treatment of iron-containing solutions such as AMD and effluent solutions.

Seeding is also an important concept in precipitation since it provides a large surface area, and consequently achieves supersaturation, thereby suppressing homogeneous nucleation (discussed in **Section 2.6.1**). Seeding with magnetite, haematite, and goethite has been reported to be effective in AMD treatment and effluent solutions (Karapinar, 2003; Hove, 2008; Han et al., 2015; Kefeni et al., 2017). In a study by Karapinar (2003), Fe(III) in solution was precipitated as ferrihydrite at pH >5. For efficient ferrihydrite removal, magnetite (2 g/L) was used as the seed material in high-gradient magnetic separation at 6900 G and 0.57 L/min. In a study by Kefeni et al. (2017), copper-magnetite and magnetite nanoparticles were synthesised and used as seed materials for AMD treatment. At pH ~7, more than 90% of Al, Mg, Mn, Fe, Ni, and Zn were recovered by the precipitation method. The removal mechanism was described as adsorption and partial incorporation into the nanoparticles.

Hove (2008) used a synthesised goethite and haematite as seed materials in an oxidative and precipitation process to recover Fe(III). Seeding reduced the BET surface area (S_{BET}) from 325 m^2/g for unseeded material to ~90 and ~120 m^2/g for goethite and haematite seeding respectively. The particle size increased from ~250 µm to 300 µm and ~270 µm for goethite and haematite seeding (Hove, 2008). The results confirmed that seeding does improve the dewaterability of the precipitates. Coetzee et al. (2017) used goethite (130 m^2/g) as seeding material for iron recovery in a precious metal sulphate leach solution. The unseeded precipitate was mainly ferrihydrite with 215.8 m^2/g. The seeded precipitate at pH 2.5 had low BET due to aggregation and molecular growth inside micropores. The precipitate produced at a higher pH (~4) had a higher S_{BET} (156.5 m^2/g) than goethite (seed), with an increase in the external surface area being responsible for the increase in the total surface area. The higher

S_{BET} was a result of rapid precipitation which forms a poorly ordered crystal structure and a more amorphous surface structure (Coetzee et al., 2017).

In this research study, the production of iron-based coagulants from a CFA leach liquor will be evaluated. Thus, to improve the solid-liquid separation, the magnetic fraction to be recovered by MS as described in **Section 2.5.1** will be utilised as seeding material. Consequently, the coagulants generated in this study could be a cost-effective alternative to assist power plants in meeting effluent discharge limits, thereby complying with waste management policies.

2.7.2 Adsorption

Adsorption is a widely used industrial process for purifying organic and inorganic pollutants (Ahmaruzzaman, 2011; Singh et al., 2018; Yao et al., 2015; Mushtaq et al., 2019). It involves the transfer of a solute (adsorbate) from the fluid phase to the surface of a solid phase (adsorbent) through physisorption or chemisorption. Physisorption is a reversible process where the adsorbate molecules or ions are held on the adsorbent surface by weak intermolecular forces. On the other hand, chemisorption is often irreversible and difficult to desorb, as the adsorbent is strongly bonded to the surface through chemical bonds formed due to chemical specificity (Bagwell et al., 2001; Manchisi et al., 2020). Different adsorbates are adsorbed onto different adsorbents in various ways. Four essential steps are observed in the adsorption process:

i. Bulk solution transport
ii. Film diffusion transport
iii. Pore transport
iv. Adsorption

The adsorbate is carried from the bulk solution to the reaction sites on the surface through advection and dispersion. As it is transported, the adsorbate diffuses across the stationary liquid film and eventually reaches the surface. Pore transport takes place through the pores on the surface of the adsorbent, where the adsorbate moves by a combination of molecular

diffusion and surface diffusion. Lastly, during the adsorption step, the adsorbate attaches to an available adsorption site on the adsorbent (Tchobanoglus et al., 2003).

Adsorbents such as zeolite, activated carbon, and mesoporous silica are readily available for commercial use. However, these adsorbents are expensive, limiting their practical application (Dotto and McKay, 2020; Manchisi et al., 2020). When evaluating their performance, it has been observed that alternative adsorbents must possess the following basic characteristics:

1. Mechanical and chemical stability
2. Good physicochemical properties
3. High adsorption capacity and efficiency
4. Fast kinetics
5. Regenerability and reuse

Consequently, industrial by-products such as CFA should ideally possess these characteristics for commercial consideration.

2.7.2.1 Adsorption using CFA

Comprehension of the chemical, physical, and phase composition of the adsorbent is essential since these properties largely control the adsorption capacity of the adsorbent material (Xu and McKay, 2017; Manchisi et al., 2020). Physicochemical properties such as BET surface area (S_{BET}), pore diameter (D_p), and pore volume (Vp) are commonly evaluated. Ideally, a high surface area with a large microstructure is essential for high adsorption efficiency. The adsorbent properties can also be modified to improve the adsorption performance. In CFA processing, zeolitisation is a common activation method (Querol et al., 2002; Ahmaruzzaman, 2010; Yao et al., 2015; Mushtaq et al., 2019).

In this section, a detailed adsorption process using CFA is discussed, including the possible mechanisms involved and activation through zeolite synthesis. Additionally, several variables that affect the adsorption process are discussed, such as solution pH, adsorbent dosage, and adsorption temperature.

Neutralisation and Precipitation

Lime (CaO) is typically used to neutralise and precipitate metal ions in AMD. However, liming is costly and results in a sludge that is difficult to dispose of. Therefore, CFA has been used to treat AMD (Prasad and Mortimer, 2011; Kalombe et al., 2020). CFA contains a mixture of basic oxides such as SiO_2, CaO, Fe_2O_3, and Al_2O_3, with the capacity to undergo hydration reactions in an aqueous solution, resulting in an alkaline system that can precipitate and adsorb metal ions (Kalombe et al., 2020). The adsorption mechanism has been proposed by Gitari et al. (2006) and (2008), Vadapalli et al. (2008), and Madzivire et al. (2011). Calcium oxide in CFA will dissolve in the solution and precipitate the sulphates as calcium sulphates (see **Equation 2.37**). The metal ions such as Fe, Al, and Mg precipitate as hydroxide and oxyhydroxides as shown in **Equation 2.38** and **2.39**. Consequently, this creates a large surface area that subsequently adsorbs the sulphate ions. The precipitation of these metal ions will mostly occur at the pH corresponding to their minimum solubility.

$$Ca^{2+} + SO_4^{2-} + 2H_2O \rightarrow CaSO_4 \cdot 2H_2O_{(s)} \qquad \textbf{2.37}$$

$$M^{3+} + 3H_2O \rightarrow M(OH)_{3(s)} + 3H^+ \qquad \textbf{2.38}$$

$$X^+ + M^{3+} + 2SO_4^{2-} + 6OH^- \rightarrow XM_3(SO_4)_2(OH)_{6(s)} + H^+ \qquad \textbf{2.39}$$

where X = Ca or Na and M = Al or Fe

Adsorption Capacity of CFA

Mohan and Gandhimathi (2009) studied the adsorption of heavy metals from municipal wastewater with an alkaline pH (~8.1). From the point of zero charge in CFA (pH_{ZPC} 6.9), the silica, alumina, and iron content of CFA were negatively charged above pH 6.9. The removal efficiencies of heavy metals were 39% Cu, 28% Mn, 74% Pb, 42% Zn, and 71% Cd, respectively. However, the total dissolved solids (TDS) and chemical oxygen demand (COD) had lower removal efficiency with 5.5% and 28%, respectively. In a study by Alinnor (2007), the pH of the solution was observed to control the adsorption efficiency. Therefore, the pH level greatly affects how metal ions are absorbed since it regulates the surface charge of the adsorbent. At pH 4, 74.8% Cu^{2+} was removed while at pH 12, the removal increased to 98.1% Cu^{2+}. Similar results were observed for Pb. The effect of temperature was also studied

at pH 6.4. In this study, an increase in temperature from 30-40℃ increased adsorption (70-80% Pb^{2+}). However, beyond 60℃, the adsorption dropped.

Madzivire et al. (2010) also studied the adsorption of acid mine water (AMD) and neutral mine water (NMW). In their study, the effect of pH was also observed, and thus, seeding was introduced for efficient adsorption. Treatment of NMW was successful at pH >11 for sulphate removal, followed by seeding with gypsum and amorphous $Al(OH)_3$ subsequently precipitating the sulphates as ettringite. The sulphates were reduced from 1043 to 213 ppm, which is well below the South African Department of Water Affairs and Sanitation (DWAS) effluent limit of 500 ppm.

CFA Activation

The physicochemical properties of an adsorbent material are commonly improved through chemical activation. In CFA, alkaline activation by zeolite synthesis is popular. In this process, zeolite is synthesised in the presence of an alkaline solution (NaOH or KOH) at 50-100℃ for 2-14 days (Murayama et al., 2002). The zeolitisation process occurs through the dissolution of Al and Si, condensation/gelation, nucleation, and crystallisation. The process can be achieved by direct leaching, hydrothermal leaching, sonication, and microwave-assisted leaching (Bindhu and Sugunan, 1998; Querol et al., 2002). Nonetheless, the most common zeolites synthesised from CFA are classified in **Table 2.6**. Zeolite type X is known for having the highest cation exchange capacity (CEC) due to its large pore sizes, which can measure up to 7.3Å.

Table 2.6: Common synthesised zeolites and their characteristics (Bindhu and Sugunan, 1998; Querol et al., 2002)

Zeolite class	Zeolite type	Si/Al ratio	Pore size (Å)
Silica molecular sieves	Silicalite	>100	<1
High silica	ZSM-5, EU-1	>10	2.3
Intermediate silica	Zeolite Y, P	1.7-8	4.1
Low silica	Zeolite A, X	1-1.5	7.3

Hydrothermal synthesis is commonly used to produce zeolites with large pores and surface areas (Bindhu and Sugunan, 1998; Querol et al., 2002; Ahmaruzzaman, 2010). In a study by Chigondo and Nyamunda (2013), zeolite was directly synthesised from CFA with NaOH at 100℃ for 24 hours. The composition of the zeolite was primarily mullite and quartz with zeolite A and X as the new phases. The BET analysis showed an increase in surface area from raw CFA (5.22 m^2/g) to zeolite (67.65 m^2/g). Comparable findings were also reported by Liu et al. (2018). In their study, they synthesised zeolite P and the S_{BET} was 42.006 m^2/g. Some of the selective properties of CFA and activated CFA (zeolite) used in the adsorption of wastewater are presented in **Table 2.7**.

Table 2.7: Selective properties of CFA and activated CFA used in adsorption processes

Material	Synthesis method	CEC value (meg/100g)	$S_{BET}(m^2/g)$	References
Raw CFA	None	16.2	11	(Franus, 2012)
Zeolite-NaX	Hydrothermal	332.5	40	
Raw CFA	None	8.35	5.27	(Kurniawati et al., 2021)
Zeolite-NaX	Hydrothermal	18.353	26.79	
Raw CFA	None	--	5.92	(Sivalingam and Sen, 2018)
Zeolite-NaX	Hydrothermal	--	648.42	

--Not available

It is noteworthy that the synthesis of zeolite primarily aims to improve the surface properties of CFA, thus enhancing the adsorption efficiency. Therefore, in this study, a secondary solid residue (SSR) will be generated after the extraction process. The characterisation of this material will, therefore, be considered for potential application as an adsorbent in wastewater treatment.

2.7.2.2 Titanium dioxide in wastewater treatment

Titanium is a transition metal typically applied in aircraft due to its high strength, corrosion resistance, and thermal stability in alloys. It is naturally sourced as titanium dioxide (TiO_2) from ilmenite (>54% TiO_2) and rutile (>95% TiO_2) deposits. In South Africa, ilmenite is the primary source of Ti from heavy mineral sands along the coastal regions of the Namakwa Sands and Richards Bay (Dworzanowski, 2013). It is further processed by smelting to

produce titanium slag (80-95% TiO_2) for export (Kotzé, 2006; Dworzanowski, 2013). Since the titanium market is small and competitive, titanium feedstock is primarily beneficiated for specialised products such as titanium metals and pigments (Kotzé, 2006; Gambogi, 2023). Pigment-grade TiO_2 is produced on a small scale in South Africa, with no titanium metal production. Nevertheless, the Titanium Centre of Competence (TiCOC), hosted by the Council for Scientific and Industrial Research (CSIR), is currently involved in process innovations to stimulate and develop the titanium market in South Africa (Sehoana and Fazluddin, 2019).

Titanium dioxide is also a useful catalyst and adsorbent for organic and inorganic pollutants in wastewater treatment processes. Khan et al. (2015) defined a photocatalyst as a material that can absorb light to produce electron-hole pairs that enable a chemical reaction. Electron pairs are powerful oxidising and reducing agents that are useful in chemical reactions (Sørensen, 2014; Khan et al., 2015). Titanium dioxide is among the catalysts used in photocatalysis due to its wide band gap, morphology, high surface area, stability, and reusability (Khan et al., 2015). A typical catalytic activity of TiO_2 is presented in **Figure 2.31** where its electrons are excited by UV radiation energy, resulting in the formation of electron-hole pairs that help decompose organic compounds (Chong et al., 2010). As an adsorbent, TiO_2 has also found application in wastewater treatment to recover heavy metals such as arsenic and organics such as phenols. However, the application is not common (Bekkouche et al., 2004; Bang et al., 2005).

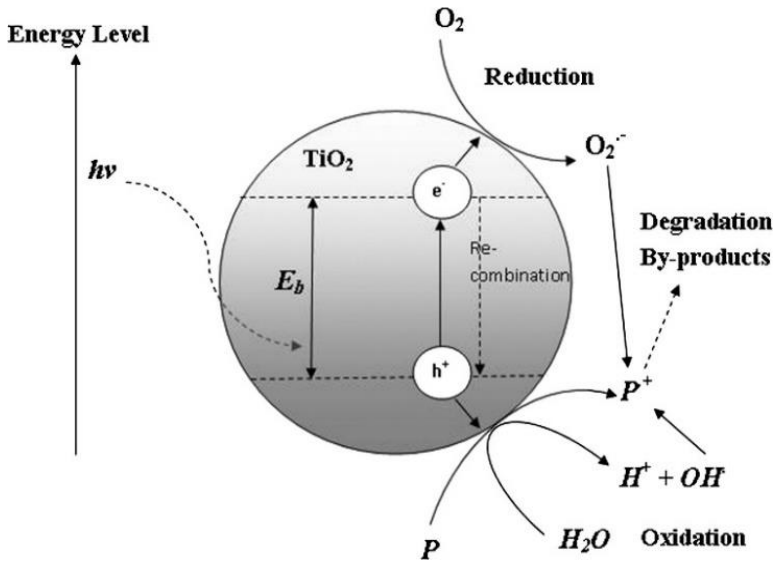

Figure 2.31: A schematic photocatalysis process using TiO_2 (Chong et al., 2010).

A titanium by-product of alumina processing could add value to wastewater treatment. In this section, some of the methods used to synthesise TiO_2 are discussed, including the common physicochemical properties of TiO_2 used for wastewater treatment.

Synthesis of TiO_2 Nanoparticles

Various titanium compounds, such as titanium (III/IV) chloride ($TiCl_3$ or $TiCl_4$) and titanium alkoxides (i.e. titanium isopropoxide), are sold on the market and used as a source of titanium (IV) for the synthesis of TiO_2 in wastewater treatment. The commonly reported synthesis methods are precipitation, sol-gel and solvothermal methods (Kumar and Pandey, 2018; Gázquez et al., 2014; Wang et al., 2022):

1. **Sol-gel method:** The sol-gel is commonly used to prepare crystalline TiO_2 through hydrolysis and polymerisation of a metal precursor. In this process, the titanium alkoxides are reacted with an organic solvent (isopropanol or methanol) to create a gel-metal complex. This process is commonly used due to its high purity, low synthesis temperature (<100°C), and simple experimental operation.

2. **The solvothermal (hydrothermal) method:** Hydrothermal and solvo-thermal processes are often regarded as similar processes since they require high temperatures (>100°C) and pressure conditions; thus, they are often conducted in autoclaves. In the solvo-thermal process, the solvent is non-aqueous, while in the hydrothermal process, the solvent is an aqueous solution.

3. **Precipitation method:** In the precipitation process, titanium in solution (i.e. $TiCl_4$ or $Ti(SO_4)_2$) is directly precipitated using alkaline reagents such as NaOH and NH_4OH to form titanium hydroxide which is further calcined to form TiO_2.

Nadeem et al. (2018) and Irshad et al. (2021) reported that the major disadvantage in the mass production of TiO_2 using these methods is the high cost of buying titanium compounds as starting materials for synthesis. Therefore, an opportunity arises in this rsearch study to produce titanium dioxide that can be used as an adsorbent or catalyst in wastewater treatment. The precipitation method will be considered, and the basic principles of precipitation are discussed in **Section 2.6.1**.

Physicochemical Properties of TiO_2

The most common TiO_2 polymorphs are anatase and rutile crystals presented in **Figure 2.32**. Rutile is a more thermodynamically stable tetragonal crystal, while anatase is metastable. Both polymorphs are widely used in wastewater treatment and are obtained after synthesis by calcination at 400-800°C (Hlekelele, 2017; Nadeem et al., 2018; Irshad et al., 2021). The American Society for Testing and Materials (ASTM, 1988) standard classifies the quality of TiO_2 (min rutile) as type I (>94% TiO_2) to type IV (>80% TiO_2), and this classification can assist in quantifying the purity and quality of TiO_2 produced (Gázquez et al., 2014).

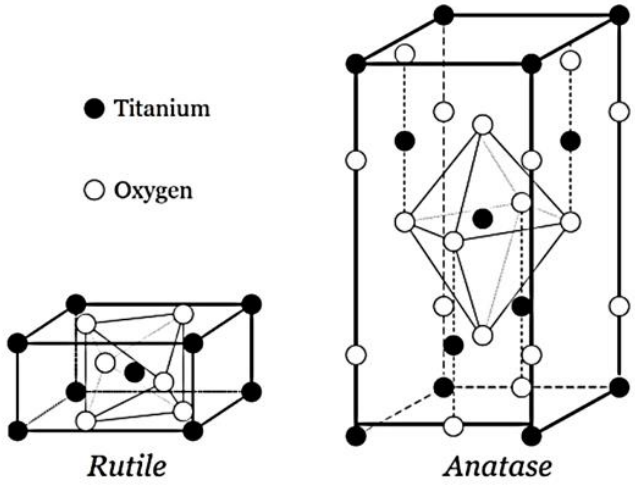

Figure 2.32: A representation of a unit cell for rutile and anatase (Sørensen, 2014).

The synthesis method used can determine the physicochemical properties of TiO_2, and consequently, its performance in water treatment. Therefore, attributes such as morphology, particle size, and chemical composition are important. Zeng et al. (2019) defined the TiO_2 produced by precipitation as a polycrystalline spherical granular structure with S_{BET} of 105-140 m^2/g (surface area). Hlekelele (2017) observed a similar characterisation. In the study, TiO_2 was synthesised using titanium isopropoxide as the Ti source in 1 M NH_4OH in a pressure autoclave at 120°C for 24 hours. The morphology of the compound was also spherical with S_{BET} of 82 m^2/g and D_p of 9.2 nm. Wang et al. (2020) used titanium tetrachloride as the starting material by synthesising with 25% NH_4OH at 65°C for 12 hours. The analysis results were also in the range of 48-67 m^2/g and 0.258-0.282 cm^3/g.

The photo-reactivity of titanium dioxide depends on the surface area of the catalyst and the availability of active sites. Therefore, particle size is a significant variable for photocatalytic efficiency. The smaller the particles, the higher the surface-to-weight ratio; hence, the more active sites there are for catalytic activity. Chemical modification, known as doping, has also been extensively investigated to alter the properties of TiO_2 by narrowing its bandgap. Both anions (Cl, P, and F) and cations (REEs, V, Fe, and Zn) have been extensively investigated (El-Bahy et al., 2009; Parida and Sahu, 2008; Hlekelele, 2017).

In this study, a titanium by-product will be synthesised by the precipitation method and characterised to determine the quality and physicochemical properties for consideration in wastewater treatment.

2.8 Summary

The extensive research available on CFA processing has focused on the extraction of alumina for smelter-grade production. This literature is extended to the extraction and recovery of REEs, Ti, and Fe. Therefore, highlights from this chapter can be summarised as follows:

- South African CFA is predominantly amorphous with major crystalline phases such as mullite, quartz, and magnetite/haematite. More than 70% of Al is distributed in the refractory mullite. Thus, although energy-intensive, hydrothermal treatment is recommended for the decomposition of the mullite to a more soluble phase such as plagioclase to extract Al worth scaling. In addition, due to the complex mineralogical distribution of REEs in CFA, hydrothermal treatment is also recommended for the liberation or transformation of REEs. Nonetheless, a preliminary study must also focus on understanding the distribution of REEs in CFA.
- The extraction of REEs from CFA has been conducted using HCl and H_2SO_4. The former is identified as a suitable lixiviant due to its higher extraction efficiency. The latter results in the formation of calcium sulphate at high leaching temperatures and concentrated acidic solution (>3 M H_2SO_4). Consequently, this results in low metal extraction efficiency (i.e. Al and REEs). In addition, dry digestion-water leach is a commercial technique that can manage both calcium and silica parameters which

results in silica gel and calcium sulphate barriers. This technique is an alternative to REE extraction.

- This review has highlighted that the Fe particles in CFA can occur independently as discrete phases; therefore, magnetic separation can be used to reduce and recover magnetite/haematite. It is also reviewed that the material can be recovered by various MS techniques depending on its intended use. Therefore, in this study, dry MS will be considered for the recovery of Fe-oxide, and the material will be recycled as seeds in ferrihydrite precipitation.

- Since acid-leaching processes often have low selectivity, solvent extraction and chemical precipitation are the considered purification techniques. In the sinter-H_2SO_4 leach process, it is noted that Fe and Ti are the major impurities extracted with Al. Therefore, integrated SX and selective precipitation will be utilised to generate smelter-grade alumina while producing Fe and Ti by-products of economic value. In addition, oxalate precipitation will be considered for REE precipitation.

- CFA has also been utilised in wastewater treatment to produce coagulants and adsorbents for toxic heavy metals. In this regard, an opportunity arises to recycle CFA by-products by generating high-purity TiO_2 and Fe-based coagulants for wastewater treatment. In addition, a secondary solid residue will be generated after metal extraction for disposal. Therefore, in this study, the material will be characterised for consideration in wastewater treatment.

This chapter has reviewed and summarised literature based on the extraction and recovery of valuable resources from CFA. The next chapter discusses the materials and methods used in the study.

References

Abaka-Wood, G., Addai-Mensah, J. and Skinner, W., 2022. The concentration of rare earth elements from coal fly ash. *Journal of the Southern African Institute of Mining and Metallurgy* 122(1), 21-28.

Abaka-Wood, G., Addai-Mensah, J. and Skinner, W., 2016. Review of flotation and physical separation of rare earth element minerals. 4th UMaT Biennial International Mining and Mineral Conference, Tarkwa, Ghana, 55-62.

Afrisam, 2009, Institute, Cement & Concrete. Available online: https://www.afrisam.co.za/uploads/documents/Cementitious_materials_for_concrete.pdf (Accessed on 06-03-2021).

Aglietti, E., Tavani, E. and Lopez, J.P., 1990. Acid process for the extraction of aluminium from argentine weathered basalts. *Minerals Engineering* 3(3-4), 331-343.

Ahmaruzzaman, M., 2011. Industrial wastes as low-cost potential adsorbents for the treatment of wastewater laden with heavy metals. *Advances in Colloid and Interface Science* 166(1-2), 36-59.

Ahmaruzzaman, M., 2010. A review on the utilization of fly ash. *Progress in Energy and Combustion Science* 36(3), 327-363.

Akcil, A., 2019. Critical and rare earth elements: recovery from secondary resources. CRC Press, Florida. ISBN: 9780367086473.

Akinyemi, S., Gitari, W., Akinlua, A. and Petrik, L., 2012. Mineralogy and geochemistry of sub-bituminous coal and its combustion products from Mpumalanga Province South Africa. Analytical Chemistry. Ira, S.K (editor). 47-70. ISBN: 978-953-51-0837-5.

Aldrich, R.G., 1984. Separation of high grade magnetite from fly ash. U.S. Patent 4432868.

Alinnor, I., 2007. Adsorption of heavy metal ions from aqueous solution by fly ash. *Fuel* 86(55-6), 853-857.

Alguacil, F.J., Amer, S. and Luis, A., 1987. The application of Primene 81R for the purification of concentrated aluminium sulphate solutions from leaching clay minerals. *Hydrometallurgy* 18(1), 75-92.

Alinnor, I., 2007. Adsorption of heavy metal ions from aqueous solution by fly ash. *Fuel* 86, 853-857.

Amitharajah, A. and O'Melia, C., 1990. Coagulation process: Destabilization, Mixing and flocculation. In: Pontius, F.W., Ed., Water Quality and Treatment, 4th Edition, McGraw-Hill, New York, 269-365.

Archambo, M.S. and Kawatra, S.K., 2022. Extraction of rare earths from red mud iron nugget slags with oxalic acid precipitation. *Mineral Processing and Extractive Metallurgy Review* 43(5), 656-663.

Ariuntuya, B., 2018. Recovery of Rare Earth Elements from Apatite Ores by Hydrometallurgical Process. PhD thesis, Graduate School of Engineering and Resource Science, Akita University, Japan.

Arp, R., Bole-Rentel, T. and Jakuja, N., 2018. Greenhouse Gas Emissions Reductions for the South African Cement Sector. Available online: https://www.wwf.org.za (Accessed on 12-06-2021).

Authier-Martin, M., Forte, G., Ostap, S. and See, J., 2001. The mineralogy of bauxite for producing smelter-grade alumina. *JOM* 53, 36-40.

Babcan, J., 1971. Die synthese von jarosit $KFe_3(SO_4)_2(OH)_6$. *Geol Zbornik Geol Carpath* 22(002), 299-304.

Bagwell, T., Henry, H. and Kenneth, M., 2001. Handbook of public water systems (2nd edition). John Wiley & Sons, New York. ISBN: 978-0-471-29211-1.

Balaram, V., 2019. Rare earth elements: A review of applications, occurrence, exploration, analysis, recycling, and environmental impact. *Geoscience Frontiers* 10(4), 1285-1303.

Bang, S., Patel, M., Lippincott, L. and Meng, X., 2005. Removal of arsenic from groundwater by granular titanium dioxide adsorbent. *Chemosphere* 60(3), 389-397.

Barrón, V. and Torrent, J., 2013. Iron, manganese and aluminium oxides and oxyhydroxides. European Mineralogical Union and the Mineralogical Society of Great Britain & Ireland. 9(14), 297-336.

Battsengel, A., Batnasan, A., Narankhuu, A., Haga, K., Watanabe, Y. and Shibayama, A., 2018. Recovery of light and heavy rare earth elements from apatite ore using sulphuric acid leaching, solvent extraction and precipitation. *Hydrometallurgy* 179, 100-109.

Bekkouche, S., Bouhelassa, M., Salah, N.H. and Meghlaoui, F., 2004. Study of adsorption of phenol on titanium oxide (TiO_2). *Desalination* 166, 355-362.

Bindhu, J., Sugunan, S., 1998. A comparative study of medium and large pore zeolites in Alkylation reactions. PhD thesis, Department of Applied Chemistry, Cochin University of Science and Technology, India.

Binnemans, K., Jones, P.T., Blanpain, B., Van Gerven, T. and Pontikes, Y., 2015. Towards zero-waste valorisation of rare-earth-containing industrial process residues: a critical review. *Journal of Cleaner Production* 99, 17-38.

Binnemans, K., Jones, P.T., Blanpain, B., Van Gerven, T., Yang, Y., Walton, A. and Buchert, M., 2013. Recycling of rare earths: a critical review. *Journal of Cleaner Production* 51, 1-22.

Bisaka, K., Thobadi, I. and Pawlik, C., 2017. Extraction of rare earths from iron-rich rare earth deposits. *Journal of the Southern African Institute of Mining and Metallurgy* 117(8), 731-739.

Borra, C.R., Mermans, J., Blanpain, B., Pontikes, Y., Binnemans, K. and Van Gerven, T., 2016. Selective recovery of rare earths from bauxite residue by combination of sulfation, roasting and leaching. *Minerals Engineering* 92, 151-159.

Bragg, W., 1915. The structure of magnetite and the spinels. *Nature* 95, 561-561.

Brown, J.W., 1980. Process for recovering magnetite from fly ash. U.S. Patent 4191336.

Campbell, A.E., 1999. Chemical, physical and mineralogical properties associated with the hardening of some South African fly ashes. MSc dissertation, Department of Geological Science, University of Cape Town, South Africa.

Cao, S., Zhou, C., Pan, J., Liu, C., Tang, M., Ji, W., Hu, T. and Zhang, N., 2018. Study on influence factors of leaching of rare earth elements from coal fly ash. *Energy and Fuels* 32(7), 8000-8005.

Castor, S.B. and Hedrick, J.B., 2006. Rare earth elements. Industrial Minerals Volume (7th edition). Society for mining, Metallurgy, and Exploration, Littleton, CO. 769-792.

Charalampides, G., Vatalis, K.I., Apostoplos, B. and Ploutarch-Nikolas, B., 2015. Rare earth elements: industrial applications and economic dependency of Europe. *Procedia Economics and Finance* 24, 126-135.

Chegwidden, J., Kingsnorth, D.J., 2002. Rare earths supply and demand. A European market focus. *Industrial Minerals* 415, 52-61.

Chi, R., and Wang, D., 1996. Rare earth ore processing and extraction technology. Science Publishing Company, Beijing, 305-332.

Chi, R., Xu, Z., 1999. A solution chemistry approach to the study of rare earth element precipitation by oxalic acid. *Metallurgical and Materials Transactions B* 30, 189-195.

Chigondo, M. and Nyamunda, B., 2013. Synthesis and characterisation of zeolites from coal fly ash (CFA). *Engineering Science and Technology: An International Journal* 3(4), 714-718

Chong, M.N., Jin, B., Chow, C.W. and Saint, C., 2010. Recent developments in photocatalytic water treatment technology: a review. *Water Research* 44(10), 2997-3027.

Christian, G.D, 1994. Analytical Chemistry (5th edition). John Wiley and sons, New York. ISBN-13: 978-0471597612.

Claassen, J.O. and Sandenbergh, R.F., 2006. Particle growth parameters in the precipitation of metastable iron phases from zinc-rich solutions. *Hydrometallurgy* 84(3-4), 165-174.

Coetzee, R., Dorfling, C., Bradshaw, S., 2017. Characterization of precipitate formed during the removal of iron and precious metals from sulphate leach solutions. *Journal of the Southern African Institute of Mining and Metallurgy* 117, 771-778.

Cordier, D.J., 2023. Rare Earth Mineral commodity summaries 2023. U.S Geological survey. Available online: https://pubs.usgs.gov/periodicals/mcs2023/mcs2023.pdf (Accessed on 29-07-2023).

Cordier, D.J, 2022. Rare Earth Mineral Commodity summaries 2022. U.S Geological survey. Available online: https://pubs.usgs.gov/periodicals/mcs2022/mcs2022.pdf (Accessed on 29-07-2023).

Cornelius, M.-L.U., Ameh, A.E., Eze, C.P., Fatoba, O., Sartbaeva, A. and Petrik, L.F., 2021. The Behaviour of Rare Earth Elements from South African Coal Fly Ash during Enrichment Processes: Wet, Magnetic Separation and Zeolitisation. *Minerals* 11(9), 950.

Cornell, R.M., Giovanoli, R. and Schneider, W., 1989. Review of the hydrolysis of iron (III) and the crystallization of amorphous iron (III) hydroxide hydrate. *Journal of Chemical Technology and Biotechnology* 46(2), 115-134.

Cotton, A.F., Wilkinson, G. and Gaus, P.L., 1995. Basic inorganic chemistry. Wiley. ISBN: 978-0-471-50532-7.

Cotton, F.A., Wilkinson, G., Murillo, C.A. and Bochmann, M., 1999. Advanced inorganic chemistry. John Wiley and Sons, Inc. ISBN: 0-471-17560-9.

Cotton, S.A., 2005. Establishing coordination numbers for the lanthanides in simple complexes. *Comptes Rendus Chimie* 8(2), 129-145.

Dai, S., Zhao, L., Hower, J.C., Johnston, M.N., Song, W., Wang, P. and Zhang, S., 2014. Petrology, mineralogy, and chemistry of size-fractioned fly ash from the Jungar power plant, Inner Mongolia, China, with emphasis on the distribution of rare earth elements. *Energy and Fuels* 28(2), 1502-1514.

Dai, S., Zhao, L., Peng, S., Chou, C.-L., Wang, X., Zhang, Y., Li, D. and Sun, Y., 2010. Abundances and distribution of minerals and elements in high-alumina coal fly ash from the Jungar Power Plant, Inner Mongolia, China. *International Journal of Coal Geology* 81(4), 320-332.

Davris, P., Stopic, S., Balomenos, E., Panias, D., Paspaliaris, I. and Friedrich, B., 2017. Leaching of rare earth elements from eudialyte concentrate by suppressing silica gel formation. *Minerals Engineering* 108, 115-122.

De Decker, J., 2017. Functionalized metal-organic frameworks as selective metal adsorbents. PhD thesis, Department of Materials, Ghent University, Belgium.

De Lima, I.B. and Leal Filho, W., 2015. Rare earths industry: Technological, economic, and environmental implications. Elsevier. ISBN: 978-0-12-802328-0.

Dehnicke, K. and Greiner, A., 2003. Unusual Complex Chemistry of Rare-Earth Elements: Large Ionic Radii-Small Coordination Numbers. *Angewandte Chemie International Edition* 42(12), 1340-1354.

Demol, J., Ho, E., Soldenhoff, K. and Senanayake, G., 2019. The sulphuric acid bake and leach route for processing of rare earth ores and concentrates: A review. *Hydrometallurgy* 188, 123-139.

Desouky, O.A.E.N., 2006. Liquid-liquid extraction of rare earth elements from sulphuric acid. PhD thesis, Department of Chemistry, University of Leeds, England.

Dotto, G.L. and McKay, G., 2020. Current scenario and challenges in adsorption for water treatment. *Journal of Environmental Chemical Engineering* 8(4), 103988.

Dutrizac, J., 2004. The behaviour of the rare earths during the precipitation of sodium, potassium and lead jarosites. *Hydrometallurgy* 73(1-2), 11-30.

Dutrizac, J. and Chen, T., 2009. The behaviour of scandium, yttrium and uranium during jarosite precipitation. *Hydrometallurgy* 98(1-2), 128-135.

Dworzanowski, M., 2013. The role of metallurgy in enhancing beneficiation in the South African mining industry. *Journal of the Southern African Institute of Mining and Metallurgy* 113(11), 677-680.

Ebeling, J.M., Sibrell, P.L., Ogden, S.R. and Summerfelt, S.T., 2003. Evaluation of chemical coagulation-flocculation aids for the removal of suspended solids and phosphorus from intensive recirculating aquaculture effluent discharge. *Aquacultural Engineering* 29(1-2), 23-42.

El-Bahy, Z.M., Ismail, A.A. and Mohamed, R.M., 2009. Enhancement of titania by doping rare earth for photodegradation of organic dye (Direct Blue). *Journal of Hazardous Materials* 166(1), 138-143.

Eskom, 2016. Eskom and Ash Management. Available online: https://www.eskom.co.za/Pages/Landing.aspx (Accessed on 07-03-2021).

Eterigho-Ikelegbe, O., Harrar, H. and Bada, S., 2021. Rare earth elements from coal and coal discard–A review. *Minerals Engineering* 173, 107187.

Fan, M., Brown, R.C., Wheelock, T.D., Cooper, A.T., Nomura, M. and Zhuang, Y., 2005. Production of a complex coagulant from fly ash. *Chemical Engineering Journal* 106(3), 269-277.

Fears, P., 2018. Magnetic Separators for Mineral Processing. Available online: https://www.bunting-redditch.com/magnetic-separators-for-mineral-processing (Accessed on 14-05-2021).

Ferdowsi, A. and Yoozbashizadeh, H., 2017. Solvent extraction of rare earth elements from a nitric acid leach solution of apatite by mixtures of tributyl phosphate and di-(2-ethylhexyl) phosphoric acid. *Metallurgical and Materials Transactions B* 48, 3380-3387.

Franus, W., 2012. Characterization of X-type Zeolite Prepared from Coal Fly Ash. *Polish Journal of Environmental Studies* 21(2), 337-343.

Fu, B., Hower, J.C., Zhang, W., Luo, G., Hu, H. and Yao, H., 2022. A review of rare earth elements and yttrium in coal ash: Content, modes of occurrences, combustion behavior, and extraction methods. *Progress in Energy and Combustion Science* 88, 100954.

Gambogi, J., 2023. Titanium and Titanium dioxide, Mineral commodity summaries 2023. U.S Geological survey. Available online: https://pubs.usgs.gov/periodicals/mcs2023/mcs2023.pdf (Accessed on 29-07-2023).

Gaudernack, B., Hannestad, G. and Hundere, I., 1973. Process for separating yttrium values from the lanthanides. U.S. Patent 3751553.

Gázquez, M.J., Bolívar, J.P., García-Tenorio García-Balmaseda, R. and Vaca, F., 2014. A review of the production cycle of titanium dioxide pigment. *Materials Sciences and Applications* 5(7), 441-458.

Generalic, E., 2019. Periodic table of rare earth elements. Available online: https://www.periodni.com/rare_earth_elements.html (Accessed on 28-07-2023).

Gil, A.F., Salgado, L., Galicia, L. and González, I., 1995. Predominance-zone diagrams of Fe (III) and Fe (II) sulphate complexes in acidic media. Voltammetric and spectrophotometric studies. *Talanta* 42(3), 407-414.

Gitari, M., Petrik, L., Etchebers, O., Key, D., Iwuoha, E. and Okujeni, C., 2006. Treatment of acid mine drainage with fly ash: removal of major contaminants and trace elements. *Journal of Environmental Science and Health, Part A* 41(8), 1729-1747.

Gitari, W., Petrik, L., Etchebers, O., Key, D. and Okujeni, C., 2008. Utilization of fly ash for treatment of coal mines wastewater: Solubility controls on major inorganic contaminants. *Fuel* 87(12), 2450-2462.

Gitari, W.M., Petrik, L.F. and Akinyemi, S.A., 2018. Treatment of acid mine drainage with coal fly ash: exploring the solution chemistry and product water quality. Coal Fly Ash benefitiation: Treatment of Acid Mine Drainage with Coal Fly Ash. Intech, Croatia. ISBN: 978-953-51-3753-5.

Gregory, J. and Duan, J., 2001. Hydrolyzing metal salts as coagulants. *Pure and Applied Chemistry* 73(12), 2017-2026.

Habashi, F., 1997. Handbook of Extractive Metallurgy (Volume I). Weinbeim, New York. ISBN: 3-527-28792-2.

Haber, F. and Weiss, J., 1934. The catalytic decomposition of hydrogen peroxide by iron salts. Proceedings of the Royal Society of London. *Series A-Mathematical and Physical Sciences* 147(861), 332-351.

Hammas-Nasri, I., Horchani-Naifer, K., Férid, M. and Barca, D., 2016. Rare earths concentration from phosphogypsum waste by two-step leaching method. *International Journal of Mineral Processing* 149, 78-83.

Han, H., Sun, W., Hu, Y., Tang, H. and Yue, T., 2015. Magnetic separation of iron precipitate from nickel sulphate solution by magnetic seeding. *Hydrometallurgy* 156, 182-187.

Hashimoto, Y., Taguchi, M., Fukami, S., Momono, H., Matsushita, T., Matsuda, H., Matsui, F. and Daimon, H., 2019. Site-sensitive X-ray photoelectron spectroscopy of Fe_3O_4 by photoelectron diffraction. *Surface and Interface Analysis* 51(1), 115-119.

Hill, R.O. and Raistrick, B., 1981. Process of extraction of aluminum values from coal ash. U.S. Patent 4243640.

Hiskey, J.B. and Copp, R.G., 2018a. Solvent extraction of yttrium and rare earth elements from copper pregnant leach solutions using Primene JM-T. *Minerals Engineering* 125, 265-270.

Hiskey, J.B. and Copp, R.G., 2018b. Recovery of yttrium and neodymium from copper pregnant leach solutions by solvent extraction. *Hydrometallurgy* 177, 21-26.

Hlekelele, L., 2017. Synthesis, Characterization and Photocatalytic Activity of TiO_2 and TiO_2 Based Quaternary Mixed Metal Oxides Supported on Carbon and Fly Ash Based Materials. PhD thesis, Department of Chemistry, University of the Witwatersrand, South Africa.

Hood, M.M., Taggart, R.K., Smith, R.C., Hsu-Kim, H., Henke, K.R., Graham, U., Groppo, J.G., Unrine, J.M. and Hower, J.C., 2017. Rare earth element distribution in fly ash derived from the Fire Clay coal, Kentucky. *Coal Combustion and Gasification Products* 9, 22-33.

Hove, M., 2008. The kinetics and mechanisms of the oxidation and precipitation of iron : the high density sludge (HDS) process. PhD thesis, Department of Chemical Engineering, University of Cape Town, South Africa.

Hower, J.C., Groppo, J.G., Joshi, P., Dai, S., Moecher, D.P. and Johnston, M., 2013. Location of cerium in coal-combustion fly ashes: Implications for recovery of lanthanides. *Coal Combustion and Gasification Products* 5, 73-78.

Hower, J.C., Groppo, J.G., Joshi, P., Preda, D.V., Gamliel, D.P., Mohler, D.T., Wiseman, J.D., Hopps, S.D., Morgan, T.D. and Beers, T., 2020. Distribution of Lanthanides, Yttrium, and Scandium in the pilot-scale beneficiation of fly ashes derived from eastern Kentucky coals. *Minerals* 10(2), 105.

Hu, K., Zhao, Q., Chen, W., Tang, F. and Xu, H., 2016. Preparation and performance of fly ash-based coagulants in chemically enhanced primary treatment of domestic wastewater. *Desalination and Water Treatment* 57(10), 4429-4438.

Iler, R.K., 1955. The Colloid Chemistry of Silica and Silicates, Cornell University Press. Ithaca, New York.

Innocenzi, V., Ippolito, N.M., Pietrelli, L., Centofanti, M., Piga, L. and Vegliò, F., 2018. Application of solvent extraction operation to recover rare earths from fluorescent lamps. *Journal of Cleaner Production* 172, 2840-2852.

Irshad, M.A., Nawaz, R., UR Rehman, M.Z., Adrees, M., Rizwan, M., Ali, S., Ahmad, S. and Tasleem, S., 2021. Synthesis, characterization and advanced sustainable applications of titanium dioxide nanoparticles: A review. *Ecotoxicology and Environmental Safety* 212, 111978.

Jambor, J.L. and Dutrizac, J.E., 1998. Occurrence and constitution of natural and synthetic ferrihydrite, a widespread iron oxyhydroxide. *Chemical Reviews* 98(7), 2549-2586.

Javed, T., 2017. Iron precipitation and associated metal loss from simulated process solutions. PhD thesis, Faculty of Graduate and Postdoctoral Studies, University of British Columbia.

Jepson, N., 2012. A 21st century scramble: South Africa, China and the rare earth metals industry. South African Institute of International Affairs. The Centre for Chinese Studies, Faculty of Arts and Social Sciences, Stellenbosch University, South Africa.

Jha, M.K., Kumari, A., Panda, R., Kumar, J.R., Yoo, K. and Lee, J.Y., 2016. Review on hydrometallurgical recovery of rare earth metals. *Hydrometallurgy* 165(1), 2-26.

Jones, A.M., Griffin, P.J., Collins, R.N., Waite, T.D., 2014. Ferrous iron oxidation under acidic conditions–The effect of ferric oxide surfaces. *Geochimica et Cosmochimica Acta* 145, 1-12.

Jordens, A., Cheng, Y.P. and Waters, K.E., 2013. A review of the beneficiation of rare earth element bearing minerals. *Minerals Engineering* 41, 97-114.

Jordens, A., Sheridan, R.S., Rowson, N.A. and Waters, K.E., 2014. Processing a rare earth mineral deposit using gravity and magnetic separation. *Minerals Engineering* 62, 9-18.

Josso, P., Roberts, S., Teagle, D.A., Pourret, O., Herrington, R. and de Leon Albarran, C.P., 2018. Extraction and separation of rare earth elements from hydrothermal metalliferous sediments. *Minerals Engineering* 118, 106-121.

Ju, J., Feng, Y., Li, H. and Wang, B., 2022. A Novel Approach for Separation and Recovery of Titanium, Scandium, Iron from Acidic Wastewater and Red Gypsum Utilization. *Mining, Metallurgy and Exploration* 39, 1297-1312.

Judge, W. and Azimi, G., 2020. Recent progress in impurity removal during rare earth element processing: A review. *Hydrometallurgy* 196, 105435.

Kalombe, R.M., Ojumu, T.V., Katambwe, V.N., Nzadi, M., Bent, D., Nieuwouldt, G., Madzivire, G., Kevern, J. and Petrik, L.F., 2020. Treatment of acid mine drainage with coal fly ash in a jet loop reactor pilot plant. *Minerals Engineering* 159, 106611.

Kang, L.S., 1994. Flocculation kinetics using iron (III) coagulant in water treatment: The effects of sulphate and temperature. PhD thesis, Civil and Construction Engineering, Iowa State University, USA.

Karapinar, N., 2003. Magnetic separation of ferrihydrite from wastewater by magnetic seeding and high-gradient magnetic separation. *International Journal of Mineral Processing* 71(1-4), 45-54.

Karni, J. and Karni, E.Y., 1995. Gypsum in construction: origin and properties. *Materials and Structures* 28, 92-100.

Kashiwakura, S., Kumagai, Y., Kubo, H. and Wagatsuma, K., 2013. Dissolution of rare earth elements from coal fly ash particles in a dilute H_2SO_4 solvent. *Open Journal of Physical Chemistry* 3(2), 69-75.

Kazadi, D.M., Groot, D.R., Steenkamp, J.D. and Pöllmann, H., 2016. Control of silica polymerisation during ferromanganese slag sulphuric acid digestion and water leaching. *Hydrometallurgy* 166, 214-221.

Kefeni, K.K., Mamba, B.B. and Msagati, T.A., 2017. Magnetite and cobalt ferrite nanoparticles used as seeds for acid mine drainage treatment. *Journal of Hazardous Materials* 333, 308-318.

Kelmers, A., Canon, R., Egan, B., Felker, L., Gilliam, T., Jones, G., Owen, G., Seeley, F. and Watson, J., 1982. Chemistry of the direct acid leach, calsinter, and pressure digestion-acid leach methods for the recovery of alumina from fly ash. *Resources and Conservation* 9, 271-279.

Khan, M.M., Adil, S.F. and Al-Mayouf, A., 2015. Metal oxides as photocatalysts. *Journal of Saudi Chemical Society* 19(5), 462-464.

Kim, E. and Osseo-Asare, K., 2012. Aqueous stability of thorium and rare earth metals in monazite hydrometallurgy: Eh-pH diagrams for the systems Th-, Ce-, La-, Nd-(PO_4)-(SO_4)-H_2O at 25°C. *Hydrometallurgy*, 113-114, 67-78.

King, J.F., Taggart, R.K., Smith, R.C., Hower, J.C. and Hsu-Kim, H., 2018. Aqueous acid and alkaline extraction of rare earth elements from coal combustion ash. *International Journal of Coal Geology* 195, 75-83.

Kolker, A., Scott, C., Hower, J.C., Vazquez, J.A., Lopano, C.L. and Dai, S., 2017. Distribution of rare earth elements in coal combustion fly ash, determined by SHRIMP-RG ion microprobe. *International Journal of Coal Geology* 184, 1-10.

Kolthoff, I., 2002. Theory of coprecipitation. The formation and properties of crystalline precipitates. *The Journal of Physical Chemistry* 36, 860-881.

Kotzé, H., Bessinger, D. and Beukes, J., 2006. Ilmenite smelting at Ticor SA. *Journal of the Southern African Institute of Mining and Metallurgy* 106(3), 165-170.

Krishnamurthy, N. and Gupta, C.K., 2005. Extractive metallurgy of rare earths. CRC press, New York. ISBN: 0-415-33340-7.

Kruger, R.A.; Krueger, J.E., 2005. Historical development of coal ash utilization in South Africa. In Proceedings of the World Coal Ash (WOCA), 11-15 April 2005. Lexington, KY, USA. Available online: https://p2infohouse.org/ref/45/44905.pdf (Accessed on 03-04-2021).

Kul, M., Topkaya, Y.A.V.U.Z. and Karakaya, İ., 2008. Rare earth double sulphates from pre-concentrated bastnasite. *Hydrometallurgy* 93(3-4), 129-135.

Kumar, A., Pandey, G., 2018. Different methods used for the synthesis of TiO_2 based nanomaterials: A review. *American Journal of Nano Research and Applications* 6(1), 1-10.

Kurdowski, W. and Sorrentino, F., 1996. Red mud and phosphogypsum and their fields of application. Waste Materials used in Concrete Manufacturing. Chandra, S. (editors). William Andrew Publishing. 290-351. ISBN: 978-0-8155-1393-3.

Kurniawati, M., Azhari, N., Kadja, G., Mukti, R. and Notodarmojo, S., 2021. Conversion of coal fly ash into advanced crystalline materials. *IOP Conference Series: Earth and Environmental Science* 623, 012040.

Kutchko, B.G. and Kim, A.G., 2006. Fly ash characterization by SEM-EDS. *Fuel* 85(17-18), 2537-2544.

Kvande, H. and Drabløs, P.A., 2014. The aluminum smelting process and innovative alternative technologies. *Journal of Occupational and Environmental Medicine* 56(5), S23-S32.

Landman, A.A., 2005. Aspects of solid-state chemistry of fly ash and ultramarine pigments. PhD thesis, Faculty of Natural and Agricultural Sciences, University of Pretoria, South Africa.

Lanzerstorfer, C., 2018. Pre-processing of coal combustion fly ash by classification for enrichment of rare earth elements. *Energy Reports* 4, 660-663.

Li, L., Fan, M., Brown, R.C., Koziel, J.A. and Van Leeuwen, J.H., 2009. Production of a new wastewater treatment coagulant from fly ash with concomitant flue gas scrubbing. *Journal of Hazardous Materials* 162(2-3), 1430-1437.

Li, L., Wu, Y., Liu, Y. and Zhai, Y., 2011. Extraction of alumina from coal fly ash with sulphuric acid leaching method. *The Chinese Journal of Process Engineering* 11(2), 254-258.

Li, M., He, Z. and Zhou, L., 2011. Removal of iron from industrial grade aluminum sulphate by primary amine extraction system. *Hydrometallurgy* 106(3-4), 170-174.

Lin, R., Howard, B.H., Roth, E.A., Bank, T.L., Granite, E.J. and Soong, Y., 2017. Enrichment of rare earth elements from coal and coal by-products by physical separations. *Fuel* 200, 506-520.

Lisowyj, B., 1986. Method for extraction of iron aluminum and titanium from coal ash. U.S. Patent 45670261986.

Liu, P., Huang, R. and Tang, Y., 2019. Comprehensive understandings of rare earth element (REE) speciation in coal fly ashes and implication for REE extractability *Environmental Science and Technology* 53(9), 5369-5377.

Liu, Y., Luo, Q., Wang, G., Li, X. and Na, P., 2018. Synthesis and characterization of zeolite from coal fly ash. *Materials Research Express* 5(5), 055507.

Liu, Z. and Li, H., 2015. Metallurgical process for valuable elements recovery from red mud-A review. *Hydrometallurgy* 155, 29-43.

Loan, M., Parkinson, G., Newman, M. and Farrow, J., 2002. Iron oxy-hydroxide crystallization in a hydrometallurgical residue. *Journal of Crystal Growth* 235(1-4), 482-488.

Loubser, M. and Verryn, S., 2008. Combining XRF and XRD analyses and sample preparation to solve mineralogical problems. *South African Journal of Geology* 111(2-3), 229-238.

Lowson, R.T., 1982. Aqueous oxidation of pyrite by molecular oxygen. *Chemical Reviews* 82(5), 461-497.

Luo, Y., Wu, Y., Ma, S., Zheng, S., Zhang, Y. and Chu, P.K., 2020. Utilization of coal fly ash in China: a mini-review on challenges and future directions. *Environmental Science and Pollution Research* 28, 18727-18740.

Ma, Y., Stopic, S., Xakalashe, B., Ndlovu, S., Forsberg, K. and Friedrich, B., 2021. A cleaner approach for recovering Al and Ti from coal fly ash via microwave-assisted baking, leaching, and precipitation. *Hydrometallurgy* 206, 105754.

Ma, Y., Stopic, S. and Friedrich, B., 2019. Hydrometallurgical Treatment of an Eudialyte Concentrate for Preparation of Rare Earth Carbonate. *Johnson Matthey Technology Review* 63(1), 2-13.

Madzivire, G., Gitari, W.M., Vadapalli, V.K., Ojumu, T.V. and Petrik, L.F., 2011. Fate of sulphate removed during the treatment of circumneutral mine water and acid mine drainage with coal fly ash: Modelling and experimental approach. *Minerals Engineering* 24(13), 1467-1477.

Madzivire, G., Petrik, L.F., Gitari, W.M., Ojumu, T.V. and Balfour, G., 2010. Application of coal fly ash to circumneutral mine waters for the removal of sulphates as gypsum and ettringite. *Minerals Engineering* 23(3), 252-257.

Manchisi, J., Matinde, E., Rowson, N.A., Simmons, M.J., Simate, G.S., Ndlovu, S. and Mwewa, B., 2020. Ironmaking and steelmaking slags as sustainable adsorbents for industrial effluents and wastewater treatment: a critical review of properties, performance, challenges and opportunities. *Sustainability* 12(5), 2118.

Marin Rivera, R., 2019. Innovative Technologies for Rare Earth Element Recovery from Bauxite Residue. PhD thesis, Department of Chemical Engineering, Katholieke Universiteit Leuven, Belgium.

Masindi, V., Foteinis, S., Renforth, P., Ndiritu, J., Maree, J., Tekere, M. and Chatzisymeon, E., 2022. Challenges and avenues for acid mine drainage treatment, beneficiation, and valorisation in circular economy: A review. *Ecological Engineering* 183, 106740.

Matilainen, A., Vepsäläinen, M. and Sillanpää, M., 2010. Natural organic matter removal by coagulation during drinking water treatment: A review. *Advances in Colloid and Interface Science* 159(2), 189-197.

Matjie, R., Bunt, J. and Van Heerden, J., 2005. Extraction of alumina from coal fly ash generated from a selected low rank bituminous South African coal. *Minerals Engineering* 18(3), 299-310.

McLennan, A., Bryant, G., Stanmore, B. and Wall, T., 2000. Ash formation mechanisms during pf combustion in reducing conditions. *Energy and Fuels* 14(1), 150-159.

Meier, A., Slowik, T. and Taggart, J., 2002. Rare earth elements by inductively coupled plasma-mass spectrometry. Analytical methods manual for the Mineral Resource Surveys Program US Geological Survey 166.

Meier Allen, L., Frederick, E., Briggs Paul, H. and Buullock Jr, J.H., 1996. Coal ash by inductively coupled plasma-mass spectrometry. Analytical Methods for the Mineral Surveys Program: US Geology Survey Open File Report 96-525.

Millero, F.J., 1985. The effect of ionic interactions on the oxidation of metals in natural waters. *Geochimica et Cosmochimica Acta* 49 (2), 547-553.

Mintek Annual Integrated Report, 2019. Available online: https://mintek.co.za/media/annual-report/annual-report-2019.pdf (Accessed on 03-04-2021).

Mioche, P., 2019. A history of aluminium in South Africa. *Cahiers d'histoire de l'aluminium* 62(1), 60-89.

Mohan, S. and Gandhimathi, R., 2009. Removal of heavy metal ions from municipal solid waste leachate using coal fly ash as an adsorbent. *Journal of Hazardous Materials* 169(1-3), 351-359.

Mokoena, K., Mokhahlane, L.S. and Clarke, S., 2022. Effects of acid concentration on the recovery of rare earth elements from coal fly ash. *International Journal of Coal Geology* 259, 104037.

Monhemius, A. and AJ, M., 1977. Precipitation diagrams for metal hydroxides, sulphides, arsenates and phosphates. *Transactions of the Institution of Mining and Metallurgy* 86, C202-C206.

Montross, S.N., Verba, C.A., Chan, H.L. and Lopano, C., 2018. Advanced characterization of rare earth element minerals in coal utilization byproducts using multimodal image analysis. *International Journal of Coal Geology* 195, 362-372.

Morgan, B. and Lahav, O., 2007. The effect of pH on the kinetics of spontaneous Fe(II) oxidation by O_2 in aqueous solution – basic principles and a simple heuristic description. *Chemosphere* 68(11), 2080-2084.

Mukaba, J.L., Eze, C.P., Pereao, O. and Petrik, L.F., 2021. Rare earths' recovery from phosphogypsum: An overview on direct and indirect leaching techniques. *Minerals* 11(10), 1051.

Murad, E. and Schwertmann, U., 1980. The Möessbauer spectrum of ferrihydrite and its relations to those of other iron oxides. *American Mineralogist* 65(9-10), 1044-1049.

Murayama, N., Yamamoto, H. and Shibata, J., 2002. Zeolite synthesis from coal fly ash by hydrothermal reaction using various alkali sources. Journal of Chemical Technology & Biotechnology: International Research in Process, *Environmental & Clean Technology* 77(3), 280-286.

Murtha, M. and Burnet, G., 1978. The magnetic fraction of coal fly ash: its separation, properties, and utilization. *Proceedings of the Iowa Academy of Science* 85(1), 10-13.

Musadaidzwa, J. and Tshiningayamwe, E., 2009. Skorpion Zinc solvent extraction: the upset conditions. *Journal of the Southern African Institute of Mining and Metallurgy* 109(11), 691-695.

Mushtaq, F., Zahid, M., Bhatti, I.A., Nasir, S. and Hussain, T., 2019. Possible applications of coal fly ash in wastewater treatment. *Journal of Environmental Management* 240, 27-46.

Mwewa, B., 2020. Recovery of coagulants from acid mine drainage. PhD thesis, Chemical and Metallurgical Engineering, University of the Witwatersrand, South Africa.

Nadeem, M., Tungmunnithum, D., Hano, C., Abbasi, B.H., Hashmi, S.S., Ahmad, W. and Zahir, A., 2018. The current trends in the green syntheses of titanium oxide nanoparticles and their applications. *Green Chemistry Letters and Reviews* 11(4), 492-502.

Nayak, N. and Panda, C.R., 2010. Aluminium extraction and leaching characteristics of Talcher Thermal Power Station fly ash with sulphuric acid. *Fuel* 89(1), 53-58.

Ndlovu, S., Simate, G.S. and Matinde, E., 2017. Waste production and utilization in the metal extraction industry. CRC Press, Boca Raton. ISBN-13: 978-1-4987-6729-3.

Nugroho, N., Rosita, W., Perdana, I., Bendiyasa, I., Mufakhir, F. and Astuti, W., 2019. Iron bearing oxide minerals separation from rare earth elements (REE) rich coal fly ash. *IOP Conference Series: Materials Science and Engineering* 478, 012026.

O'Melia, C., 1987. Particle-particle interactions. IN: Aquatic Surface Chemistry: Chemical Processes at the Particle-Water Interface. John Wiley and Sons, New York.

Pan, J., Nie, T., Hassas, B.V., Rezaee, M., Wen, Z. and Zhou, C., 2020. Recovery of rare earth elements from coal fly ash by integrated physical separation and acid leaching. *Chemosphere* 248, 126112.

Pan, J., Zhou, C., Tang, M., Cao, S., Liu, C., Zhang, N., Wen, M., Luo, Y., Hu, T. and Ji, W., 2019. Study on the modes of occurrence of rare earth elements in coal fly ash by statistics and a sequential chemical extraction procedure. *Fuel* 237, 555-565.

Parida, K.M. and Sahu, N., 2008. Visible light induced photocatalytic activity of rare earth titania nanocomposites. *Journal of Molecular Catalysis A: Chemical* 287(1-2), 151-158.

Peiravi, M., Dehghani, F., Ackah, L., Baharlouei, A., Godbold, J., Liu, J., Mohanty, M. and Ghosh, T., 2021. A review of rare-earth elements extraction with emphasis on non-conventional sources: Coal and coal byproducts, iron ore tailings, apatite, and phosphate byproducts. *Mining, Metallurgy and Exploration* 38, 1-26.

Poling, B.E., Thomson, G.H., Friend, D.G., Rowley, R.L. and Wilding, W.V., 2008. Physical and chemical data. Perry's chemical engineers' handbook, 2, 156-182.

Prasad, B. and Mortimer, R.J., 2011. Treatment of acid mine drainage using fly ash zeolite. *Water, Air, and Soil Pollution* 218, 667-679.

Preston, J., Cole, P., Craig, W. and Feather, A., 1996. The recovery of rare earth oxides from a phosphoric acid by-product. Part 1: Leaching of rare earth values and recovery of a mixed rare earth oxide by solvent extraction. *Hydrometallurgy* 41(1), 1-19.

Qi, D., 2018. Hydrometallurgy of rare earths: extraction and separation. Elsevier. ISBN: 978 0 12 813920 2.

Queneau, P.B. and Berthold, C.E., 1986. Silica in hydrometallurgy: an overview. *Canadian Metallurgical Quarterly* 25(3), 201-209.

Querol, X., Moreno, N., Umaña, J. t, Alastuey, A., Hernández, E., Lopez-Soler, A. and Plana, F., 2002. Synthesis of zeolites from coal fly ash: an overview. *International Journal of Coal Geology* 50(1-4), 413-423.

Rampou, M., 2018. Purification of coal fly ash leach liquor for alumina recovery. MSc dissertation, Chemical and Metallurgical Engineering, University of the Witwatersrand, South Africa.

Rao, R.B., Chattopadhyay, P. and Banerjee, G., 1970. Removal of iron from fly ash for ceramic and refractory applications. *Magnetic and Electrical Separation* 10, 21-27.

Rice, A. and Stone, C., 1962. Amines in Liquid-Liquid Extraction of Rare-Earth Elements. US Department of the Interior, Bureau of Mines. Report No: BM-RI-5923.

Riley, E. and Dutrizac, J., 2017. The behaviour of the rare earth elements during the precipitation of ferrihydrite from sulphate media. *Hydrometallurgy* 172, 69-78.

Rosita, W., Bendiyasa, I.M., Perdana, I. and Anggara, F., 2020a. Recovery of rare earth elements and Yttrium from Indonesia coal fly ash using sulphuric acid leaching. International Energy Conference Astechnova, 30-31 October 2019, AIP Conference Proceedings. 2223(1), 050004.

Rosita, W., Bendiyasa, I.M., Perdana, I. and Anggara, F., 2020b. Sequential particle-size and magnetic separation for enrichment of rare-earth elements and yttrium in Indonesia coal fly ash. *Journal of Environmental Chemical Engineering* 8(1), 103575.

Roszczynialski, W., Gawlicki, M. and Nocuń-Wczelik, W., 1996. Production and use of by-product gypsum in the construction industry. Waste Materials used in Concrete Manufacturing. Chandra, S. (editors).William Andrew Publishing. 53-141. ISBN: 978-0-8155-1393-3.

Roth, E., Macala, M., Lin, R., Bank, T., Thompson, R., Howard, B., Soong, Y. and Granite, E., 2017. Distributions and extraction of rare earth elements from coal and coal by-products. World of Coal Ash (WOCA), Conference, University of Kentucky Center for Applied Energy Research, Lexington. Available online: https://www.osti.gov/servlets/purl/1812004 (Accessed on 21-10-2021).

Roux, E., De Jager, D.H, Du Plooy, J.H, Nicotra, A., Van der Linde, G.J. and De Waal, P., 1989. Phosphate in South Africa. *Journal of the Southern African Institute of Mining and Metallurgy* 89(5), 129-139.

Rushwaya, M.J., 2016. Purification of Coal Fly Ash Leach Solution by Solvent Extraction. MSc dissertation, Chemical and Metallurgical Engineering, University of the Witwatersrand, South Africa.

Rybak, A. and Rybak, A., 2021. Characteristics of some selected methods of rare earth elements recovery from coal fly ashes. *Metals* 11(1), 142.

Rydberg, J., Cox, M., Musikas, C. and Choppin, D.R., 2004. Solvent Extraction Principles and Practice. Marcel Dekker, New York. ISBN: 0-8247-5063-2.

Sadri, F., Nazari, A.M. and Ghahreman, A., 2017. A review on the cracking, baking and leaching processes of rare earth element concentrates. *Journal of Rare Earths* 35(8), 739-752.

Saunders, F.M. and Saunders, F.M., 1991. Coagulant recovery: A critical assessment. The Foundation. The American Water Works Association Research Foundation, Denver, CO.

Scal, M.L.W., Seruff, L.A. and Vera, Y.M., 2020. Study of the separation of didymium from lanthanum using liquid-liquid extraction: Comparison between saponification of the extractant and use of lactic acid. *Minerals Engineering* 148, 106200.

Schack, C.H., 1965. Recovery of scandium from uranium plant iron sludge and from wolframite concentrates. Report of investigation 6580, U.S Department of the Interior, Bureau of Mines. Washington, United State.

Schwertmann, U. and Cornell, R.M., 2008. Iron oxides in the laboratory: preparation and characterization. Weinheim, New York. ISBN: 3-527-29669-7.

Sedres, G., 2016. Recovery of SiO_2 and Al_2O_3 from coal fly ash. MSc dissertation, Department of Chemistry, University of the Western Cape, South Africa.

Sehoana, M. and Fazluddin, S., 2019. Development of lining materials for reactor vessel used in the CSIR titanium process. *IOP Conference Series: Materials Science and Engineering*, 655, 012007.

Seidel, A. and Zimmels, Y., 1998. Mechanism and kinetics of aluminum and iron leaching from coal fly ash by sulphuric acid. *Chemical Engineering Science* 53(22), 3835-3852.

Serpell, O., Paren, B. and Chu, W., 2021. Rare Earth Elements: A Resource Constraint of the Energy Transition. Kleiman Center for Energy Policy: Philadelphia, PA, USA.

South African Coal Fly Ash Association (SACAA) 2021. Available online: https://www.sacaa.co.za (Accessed on 21-10-2021).

Shaoquan, X. and Suqing, L., 1996. Review of the extractive metallurgy of scandium in China (1978-1991). *Hydrometallurgy* 42(3), 337-343.

Shcherban, S., Raizman, V. and Pevzner, I., 1995. Technologies of coal fly ash processing into metallurgical and silicate chemical products. Proceedings of the American Chemical Society (ACS), 20-25 August 1995, Chicago, IL, USA

Shemi, A., 2013. Extraction of aluminium from coal fly ash using a two-step acid leach process. MSc dissertation, Chemical and Metallurgical Engineering, University of the Witwatersrand, South Africa.

Shen, Y., Moomy, R. and Eggert, R.G., 2020. China's public policies toward rare earths, 1975-2018. *Mineral Economics* 33, 127-151.

Shoumkova, A.S., 2011. Magnetic separation of coal fly ash from Bulgarian power plants. *Waste Management and Research* 29(10), 1078-1089.

Sibanda, V., Ndlovu, S., Dombo, G., Shemi, A. and Rampou, M., 2016. Towards the utilization of fly ash as a feedstock for smelter grade alumina production: a review of the developments. *Journal of Sustainable Metallurgy* 2, 167-184.

Silva, R.G., Morais, C.A. and Oliveira, É.D., 2019. Selective cerium removal by thermal treatment of mixed rare earth oxalates or carbonates obtained from non-purified rare earth sulphate liquor. *Minerals Engineering*, 139, 105865.

Singh, N., Nagpal, G. and Agrawal, S., 2018. Water purification by using adsorbents: a review. *Environmental Technology and Innovation* 11, 187-240.

Sivalingam, S. and Sen, S., 2018. Optimization of synthesis parameters and characterization of coal fly ash derived microporous zeolite X. *Applied Surface Science* 455, 903-910.

Skokov, K. P. and Gutfleisch, O., 2018. Heavy rare earth free, free rare earth and rare earth free magnets-Vision and reality. *Scripta Materialia*, 154, 289-294.

Skoog, D.A., West, D.M., Holler, F.J. and Crouch, S.R., 2004. Fundamentals of analytical chemistry (8th edition). Thomson Brooks/Cole, Australia. ISBN:10:0-03-035523-0.

Söhnel, O., Garside, J. and Principles, P., 1992. Basic Principles and Industrial Applications, Butterworths/Heinemann, Oxford.

Sole, K.C., 1999. Recovery of titanium from the leach liquors of titaniferous magnetites by solvent extraction: Part 1. Review of the literature and aqueous thermodynamics. *Hydrometallurgy* 51(2), 239-253.

Sørensen, G., 2014. Occurrence and effects of nanosized anatase titanium dioxide in consumer products. Danish Environmental Protection Agency. ISBN: 978-87-93283-02-2.

Stevenson, P.C. and Nervik, W.E., 1961. The radiochemistry of the rare earths, scandium, yttrium, and actinium. National Academy of Sciences-National Research Council, Nuclear Science Series, NAS-NS 30-20.

Strzałkowska, E., 2021. Morphology, chemical and mineralogical composition of magnetic fraction of coal fly ash. *International Journal of Coal Geology* 240, 103746.

Stuckman, M.Y., Lopano, C.L. and Granite, E.J., 2018. Distribution and speciation of rare earth elements in coal combustion by-products via synchrotron microscopy and spectroscopy. *International Journal of Coal Geology* 195, 125-138.

Stumm, W. and Lee, G.F., 1961. Oxygenation of Ferrous Iron. *Industrial and Engineering Chemistry* 53(2), 143-146.

Su, S.Q., Yang, J., Ma, H.W., Jiang, F., Liu, Y.Q. and Li, G., 2011. Preparation of ultrafine aluminum hydroxide from coal fly ash by alkali dissolution process. *Integrated Ferroelectrics* 128(1), 155-162.

Sun, T., Sun, C., Zhu, G., Miao, X., Wu, C., Lv, S. and Li, W., 2011. Preparation and coagulation performance of poly-ferric-aluminum-silicate-sulphate from fly ash. *Desalination* 268(1-3), 270-275.

Suopajärvi, T., 2015. Functionalized nanocelluloses in wastewater treatment applications. PhD thesis, Faculty of Technology, University of Oulu, Finland.

Svoboda, J. and Fujita, T., 2003. Recent developments in magnetic methods of material separation. *Minerals Engineering* 16(9), 785-792.

Taggart, R.K., Rivera, N.A., Levard, C., Ambrosi, J.P., Borschneck, D., Hower, J.C. and Hsu-Kim, H., 2018b. Differences in bulk and microscale yttrium speciation in coal combustion fly ash. *Environmental Science: Processes and Impacts* 20, 1390-1403.

Tang, M., Zhou, C., Pan, J., Zhang, N., Liu, C., Cao, S., Hu, T. and Ji, W., 2019. Study on extraction of rare earth elements from coal fly ash through alkali fusion-Acid leaching. *Minerals Engineering* 136, 36-42.

Tchobanoglus, G., Burton, F. and Stensel, H.D., 2003. Wastewater engineering: treatment and reuse. Metcalf & Eddy (4th Edition). McGraw-Hill, New York. ISBN: 0071122508.

Teh, C.Y., Budiman, P.M., Shak, K.P.Y. and Wu, T.Y., 2016. Recent advancement of coagulation–flocculation and its application in wastewater treatment. *Industrial & Engineering Chemistry Research* 55(16), 4363-4389.

Terry, B., 1983a. The acid decomposition of silicate minerals part II. Hydrometallurgical applications. *Hydrometallurgy* 10(2), 151-171.

Terry, B., 1983b. The acid decomposition of silicate minerals part I. Reactivities and modes of dissolution of silicates. *Hydrometallurgy* 10(1), 135-150.

Thompson, R.L., Bank, T., Montross, S., Roth, E., Howard, B., Verba, C. and Granite, E., 2018. Analysis of rare earth elements in coal fly ash using laser ablation inductively coupled plasma mass spectrometry and scanning electron microscopy. *Spectrochimica Acta Part B: Atomic Spectroscopy* 143, 1-11.

Tishmack, J.K. and Burns, P.E, 2004. The chemistry and mineralogy of coal and coal combustion products. *Geological Society* 236, 223-246.

Todorovsky, D., Terziev, A. and Milanova, M., 1997. Influence of mechanoactivation on rare earths leaching from phosphogypsum. *Hydrometallurgy* 45(1-2), 13-19.

Tomeczek, J. and Palugniok, H., 2002. Kinetics of mineral matter transformation during coal combustion. *Fuel* 81(10), 1251-1258.

Trinh, H.B., Kim, S. and Lee, J., 2022. Recovery of rare earth elements from coal fly ash using enrichment by sodium hydroxide leaching and dissolution by hydrochloric acid. *Geosystem Engineering* 25(1-2), 53-62.

Tunsu, C., Petranikova, M., Gergorić, M., Ekberg, C. and Retegan, T., 2015. Reclaiming rare earth elements from end-of-life products: A review of the perspectives for urban mining using hydrometallurgical unit operations. *Hydrometallurgy* 156, 239-258.

Vadapalli, V., Klink, M., Etchebers, O., Petrik, L., Gitari, W., White, R., Key, D. and Iwuoha, E., 2008. Neutralization of acid mine drainage using fly ash, and strength development of the resulting solid residues. *South African Journal of Science* 104(7), 317-322.

Valeev, D., Bobylev, P., Osokin, N., Zolotova, I., Rodionov, I., Salazar-Concha, C. and Verichev, K., 2022. A review of the alumina production from coal fly ash, with a focus in Russia. *Journal of Cleaner Production* 363, 132360.

Valeev, D., Kunilova, I., Alpatov, A., Varnavskaya, A. and Ju, D., 2019. Magnetite and Carbon Extraction from Coal Fly Ash Using Magnetic Separation and Flotation Methods. *Minerals* 9(5), 320.

Valeev, D., Kunilova, I., Shoppert, A., Salazar-Concha, C. and Kondratiev, A., 2020. High-pressure HCl leaching of coal ash to extract Al into a chloride solution with further use as a coagulant for water treatment. *Journal of Cleaner Production* 276, 123206.

Van Alphen, C., Matjie, R.H. and Rajoo, P., 2007. QEMSCAN Analysis of Coal and Fly Ash Formation Model-New Developments. Automated Mineralogy, Minerals Engineering (MEI) Conferences. 1-2 September 2007, Brisbane, Australia.

Vassilev, S.V. and Vassileva, C.G., 1996. Mineralogy of combustion wastes from coal-fired power stations. *Fuel Processing Technology* 47(3), 261-280.

Voßenkaul, D., Birich, A., Müller, N., Stoltz, N. and Friedrich, B., 2017. Hydrometallurgical processing of eudialyte bearing concentrates to recover rare earth elements via low-temperature dry digestion to prevent the silica gel formation. *Journal of Sustainable Metallurgy* 3, 79-89.

Wang, C. and Li, D., 1994. Extraction mechanism of Sc (III) and separation from ThUV). Fe (III) and Lu (III) with bis (2, 4, 4-trimethylpentyl) phos-phinic acid in n-hexane from sulphuric acid solutions. *Solvent Extraction and Ion Exchange* 12(3), 615-631.

Wang, J., Wang, Z., Wang, W., Wang, Y., Hu, X., Liu, J., Gong, X., Miao, W., Ding, L. and Li, X., 2022. Synthesis, modification and application of titanium dioxide nanoparticles: a review. *Nanoscale* 14, 6709-6734.

Wang, L. and Liang, T., 2015. Geochemical fractions of rare earth elements in soil around a mine tailing in Baotou, Scientific Reports 5, 12483.

Wang, W. and Cheng, C.Y., 2011. Separation and purification of scandium by solvent extraction and related technologies: a review. *Journal of Chemical Technology and Biotechnology* 86(10), 1237-1246.

Wang, Z., Dai, S., Zou, J., French, D. and Graham, I.T., 2019. Rare earth elements and yttrium in coal ash from the Luzhou power plant in Sichuan, Southwest China: Concentration, characterization and optimized extraction. *International Journal of Coal Geology* 203, 1-14.

Wang, Z., Liu, S., Cao, X., Wu, S., Liu, C., Li, G., Jiang, W., Wang, H., Wang, N. and Ding, W., 2020. Preparation and characterization of TiO_2 nanoparticles by two different precipitation methods. *Ceramics International* 46(10), 15333-15341.

Ward, C.R. and French, D., 2005. Relation between coal and fly ash mineralogy, based on quantitative X-ray diffraction methods. World Coal Ash WOCA, 11-15 April 25.

Wills, B.A. and Finch, J., 2015. Wills' mineral processing technology: an introduction to the practical aspects of ore treatment and mineral recovery (8^{th} edition). Butterworth-heinemann. ISBN: 978-0-08-097053-0.

Wu, G., Shi, N., Wang, T., Cheng, C.-M., Wang, J., Tian, C. and Pan, W.P., 2022. Enrichment and occurrence form of rare earth elements during coal and coal gangue combustion. *Environmental Science and Pollution Research* 29, 44709-44722.

Wu, S., Wang, L., Zhao, L., Zhang, P., El-Shall, H., Moudgil, B., Huang, X. and Zhang, L., 2018. Recovery of rare earth elements from phosphate rock by hydrometallurgical processes-A critical review. *Chemical Engineering Journal* 335, 774-800.

Xaba, S.M., 2015. Method development for the quantification of selected early rare earth elements. MSc dissertation, Department of Chemistry, University of the Free State, South Africa.

Xia, C., 2013. A review on iron separation in rare earths hydrometallurgy using precipitation and solvent extractions method, Proceedings of the 52nd Conference of Metallurgists (COM 2013), Canadian Institute of Mining, Metallurgy and Petroleum, Montreal, Quebec, Canada volume 1, 255-275.

Xie, F., Zhang, T.A., Dreisinger, D. and Doyle, F., 2014. A critical review on solvent extraction of rare earths from aqueous solutions. *Minerals Engineering* 56, 10-28.

Xu, F., Qin, S., Li, S., Wang, J., Lu, Q. and Xing, J., 2022. Distribution, occurrence mode, and extraction potential of critical elements in coal ashes of the Chongqing Power Plant. *Journal of Cleaner Production* 342, 130910.

Xu, G.X., 1995. Chapter 8: Rare Earths. Metallurgical Industry Press, Beijing.

Xu, M., McKay, G., 2017. Removal of heavy metals, lead, cadmium, and zinc, using adsorption processes by cost-effective adsorbents. *Adsorption Processes for Water Treatment and Purification*, 109-138.

Yahorava, V., Bazhko, V. and Freeman, M., 2016. Viability of phosphogypsum as a secondary resource of rare earth elements. XXVIII International Mineral Processing Congress Proceeding, 11-15 September 2016, Quebec City, Canada. Canadian Institute of Mining Metallurgy & Petroleum (CIM), 1-16.

Yahorava, V., Lakay, E. and Clark, W., 2018. Hydrothermal Pre-Treatment Process of phosphogypsum for enhanced rare earths recovery. Beneficiation of phosphates VIII, 4-29 May-April 2018, Century City Conference Center Cape Town, South Africa. Engineering Conferences International (ECI) Digital Archives. Available online https://dc.engconfintl.org/phosphates_viii (Accessed on 07-08-2022).

Yang, Y., Wang, X., Wang, M., Wang, H. and Xian, P., 2016. Iron recovery from the leached solution of red mud through the application of oxalic acid. *International Journal of Mineral Processing*, 157, 145-151.

Yao, Z., Ji, X., Sarker, P., Tang, J., Ge, L., Xia, M. and Xi, Y., 2015. A comprehensive review on the applications of coal fly ash. *Earth-Science Reviews* 141, 105-121.

Yao, Z., Xia, M., Sarker, P. and Chen, T., 2014. A review of the alumina recovery from coal fly ash, with a focus in China. *Fuel* 120, 74-85.

Zeng, G., Zhang, Q., Liu, Y., Zhang, S. and Guo, J., 2019. Preparation of TiO_2 and Fe-TiO_2 with an impinging stream-rotating packed bed by the precipitation method for the photodegradation of gaseous toluene. *Nanomaterials* 9(8), 1173.

Zhang, W., Rezaee, M., Bhagavatula, A., Li, Y., Groppo, J. and Honaker, R., 2015. A review of the occurrence and promising recovery methods of rare earth elements from coal and coal by-products. *International Journal of Coal Preparation and Utilization* 35(6), 295-330.

Zhang, W., Yang, X. and Honaker, R.Q., 2018. Association characteristic study and preliminary recovery investigation of rare earth elements from Fire Clay seam coal middlings, *Fuel* 215, 551-560.

Zhao, F., Cong, Z., Sun, H. and Ren, D., 2007. The geochemistry of rare earth elements (REE) in acid mine drainage from the Sitai coal mine, Shanxi Province, North China. *International Journal of Coal Geology* 70(1-3), 184-192.

Zhu, Z., Pranolo, Y. and Cheng, C.Y., 2015. Separation of uranium and thorium from rare earths for rare earth production-A review. *Minerals Engineering* 77, 185.

3 MATERIALS AND METHODS

3.1 Introduction

The study sought to develop a comprehensive method to extract and recover REEs and other valuable resources (i.e. Al, Fe, Ti, and Si) from CFA. Therefore, this chapter details the experimental procedures utilised to attain the set objectives in **Section 1.3** of **Chapter 1**. The experimental stages are divided into four major phases:

1. Material characterisation and magnetic separation
2. Acid leaching processes
3. Purification of CFA leach liquor
4. Adsorption and coagulation using CFA by-products

The chapter also highlights different materials and analytical techniques used to achieve the set objectives. The CFA used in the research work was sourced from Matla Power Plant in Mpumalanga, operated by Eskom Power Utility. Since the material was already pulverised, it was used without further comminution. A riffler splitter (see **Figure A.1**) was used to prepare a representative sample for the entire experimental work.

3.2 Reagents and Equipment

3.2.1 Chemicals and reagents

All the reagents used in this study, along with their purities and suppliers, are listed in **Table 3.1**.

Table 3.1: A list of reagents with their purities and suppliers

Chemical	Formula	Purity	Supplier
Coal	--	56% C	Trans-alloys (Pty) Ltd-
Sulphuric acid	H_2SO_4	98%	Merck
Hydrochloric acid	HCl	32%	Merck
Orthophosphoric acid	H_3PO_4	85%	Merck
Sodium diphenylamine	$NaC_{12}H_{10}NO_3S$	--	Sigma - Aldrich
Calcium carbonate	$CaCO_3$	99%	Sigma - Aldrich
Sodium hydroxide	NaOH	--	Sigma - Aldrich
Ammonium acetate	$NC_2H_7O_2$	≥98%	Sigma - Aldrich
Ammonium hydroxide	NH_4OH	25% ammonia	Merck
Ammonium sulphate	$N_2H_8SO_4$	99%	Merck
Ammonium iron sulphate	$FeH_{20}N_2O_{14}S_2$	99%	Sigma Aldrich
Fe powder (fine)	≥99%	--	Sigma Aldrich
Oxalic acid dihydrate	$C_2H_6O_6$	> 99 %	Merck
Potassium dichromate	$K_2Cr_2O_7$	≥99%	CC imelmann
Potassium nitrate	KNO_3	>99%	--
Primary™ JM-T amine	$C_{19}H_{41}N$	80% alkyl amine	Rohm and Haas
Shellsol D70	--	--	Shell Chemicals

-- Not available

Ultra-pure water (conductivity = 0.001 mS/cm) was used to prepare all solutions in the experimental study. The water was prepared with a Direct-Q® 5 UV ultra-water purification system from Merck Millipore. All glassware (i.e. beakers and volumetric flasks) was cleaned by soaking in 55% HNO_3 for approximately 24 hours, followed by a thorough rinsing (2-3 times) with ultra-pure water, and dried before use.

3.2.2 General analytical techniques

Material characterisation can be achieved using various analytical techniques, as shown in **Figure 3.1**. This section discusses the general analytical techniques used for chemical and phase composition analysis, proximate analysis, particle size distribution, surface chemistry, and morphological analysis. The section is also extended to water quality analysis. All analysis was conducted at the School of Chemical and Metallurgical Engineering (CHMT), University of the Witwatersrand unless specified.

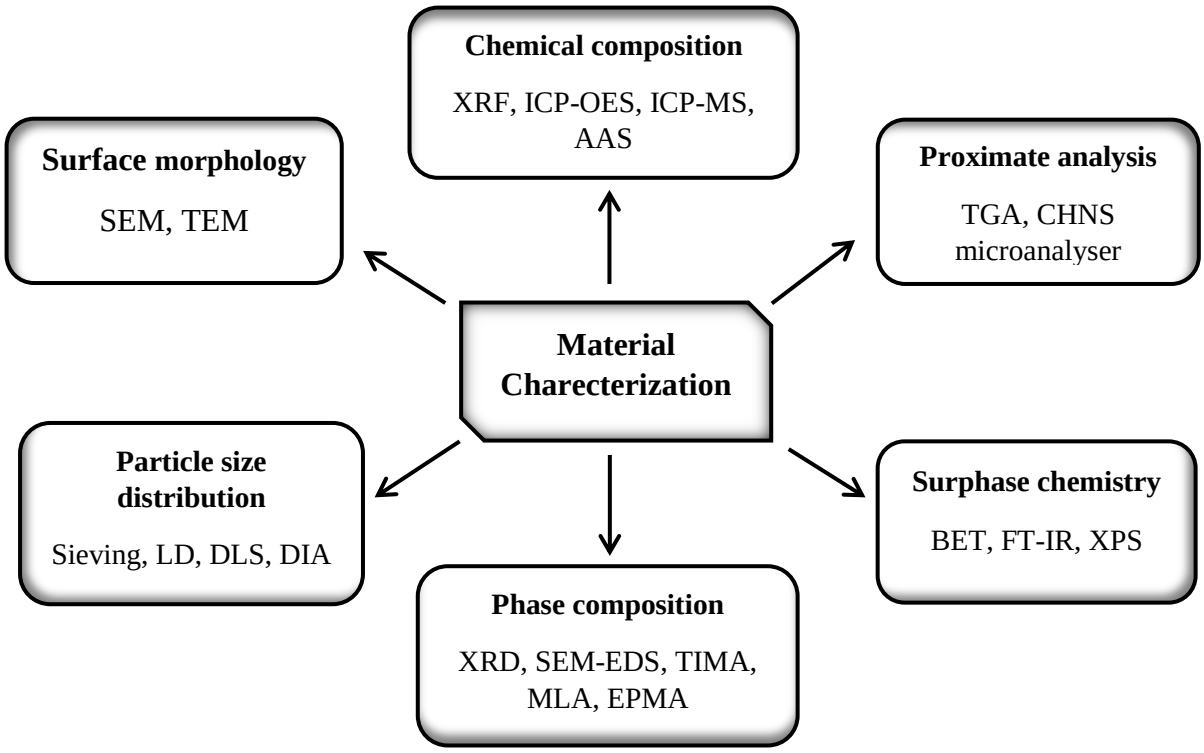

Figure 3.1: Material characterisation techniques through various analytical approaches.

3.2.2.1 Particle size distribution (PSD)

Particle size distribution (PSD) can be determined using various analytical methods such as laser diffraction (LD), dynamic image analysis (DIA), and dynamic light scattering (DLS). In this study, PSD analysis was conducted using a Malvern Mastersizer instrument (200 and 300+, laser diffraction, LD) to understand the distribution of particles and aggregates. The

samples were sonicated for ~5 minutes at 300 rpm to eliminate any agglomerates. Additionally, physical screening was also performed using tests (Fritsch, Germany) of various screen sizes (–38 μm to +212 μm). The test sieves are also presented in **Figure A.1**, **Appendix A**. Malvern 300 Mastersizer instrument and sieve analysis were conducted in the Extractive Metallurgy Laboratory, University of Johannesburg.

3.2.2.2 Proximate analysis

Thermogravimetric analysis (TGA) is an analytical method utilised for grading the quality of coal and CFA. It involves measuring the change in weight of a sample as it is exposed to varying temperatures over time (Zhu, 2014). The analysis can be used to establish the moisture content, volatile matter content, ash content, and fixed carbon content according to the ASTM D-5142A standard. In this study, proximate analysis was performed to establish the quality of coal and CFA samples. A LECO Corp. TGA701 thermogravimetric analyser was used following the procedure described by Zhu (2014).

3.2.2.3 Chemical composition analysis

All the solutions and solid samples were analysed for their elemental compositions. The major chemical elements in the solutions were quantified using Inductively Coupled Plasma-Optical Emission Spectrometry (ICP-OES, Model: PerkinElmer Nexion 1000), while X-ray diffraction (XRF, Model: ARL PERFORM'X) was used for solid samples. The trace chemical compositions of both solid and liquid samples were analysed by Inductively Coupled Plasma-Mass Spectrometry (ICP-MS, Model: PerkinElmer Avio 500). Solid sample preparation for ICP-OES/MS analysis was conducted using the flux fusion method. The analysis was performed at UIS Analytical Services (Pty) Ltd, which is an ISO/IEC 17025 accredited laboratory.

3.2.2.4 Phase composition analysis

Bulk composition analysis of CFA samples in various experimental stages was conducted using Scanning Electron Microscopy-Energy Dispersive Spectroscopy (SEM-EDS), X-ray diffraction (XRD), and a TESCAN Integrated Mineral Analyser (TIMA). A resin-embedded sample was used to determine the phase composition using TIMA and SEM-EDS analyses. Approximately 2 g of the sample was mixed with epoxy resin and hardener, placed into a 25

mm diameter mould, and allowed to cure. The surface of the sample blocks were further polished and carbon-coated before analysis. Sample block preparation and TIMA analysis were conducted at the School of Geoscience, while SEM-EDS was performed at CHMT, University of the Witwatersrand. XRD analysis was conducted at XRD Analytical and Consulting and the Analytical Chemistry Department, University of Johannesburg.

X-ray Diffractometer (XRD)

During XRD analysis, a sample is irradiated with monochromatic X-rays to produce a diffraction spectrum of the crystal structure of the sample (Dutrow and Clark, 2012). In this study, XRD was used to qualitatively and quantitatively identify the crystalline phases and determine the degree of the amorphous composition. The powdered sample was prepared using a back-loading method and analysed using a Malvern Panalytical Aeris diffractometer. The phase composition was identified using the X'Pert Highscore Plus software, and the weight percentage was established using Rietveld method. An external standard method (k-factor) was used to determine the amorphous content.

Scanning Electron Microscope-Energy dispersive spectroscopy (SEM-EDS)

The polished block samples were analysed using SEM with a Philips XL-30 detector to obtain high-resolution backscattered electron (BSE) images and high-count energy dispersive x-ray (EDX) spectra. While the major elements were detected automatically, traces of REEs were selected for detection, and those with a weight percentage greater than the atomic mass were considered present. The analysis was performed using MA 15 EVO SEM ZEISS instrument at a 20kV accelerating voltage.

TESCAN Integrated Mineral Analyser (TIMA)

TIMA is an automated mineralogical system that uses backscattered electrons (BSE) and an energy-dispersive X-ray spectrometer (EDS) signal to quantify minerals/phases and determine their mode of occurrence (Hrstka et al., 2018). In this study, a VEGA3 SEM instrument and the VEGA3 X64 TESCAN TIMA 2.4.1 software were used for analysis. The primary aim of TIMA analysis was to determine the trace elemental distributions and their association with major phase compositions in CFA. Elemental mapping was used as a tool for locating the trace elemental distribution. Neodymium (Nd) and cerium (Ce) were used as proxies for the LREEs while yttrium (Y) was used as a proxy for the HREEs. The choice of elements was based on their higher concentrations in CFA and lower peak overlap during

analysis (Palozzi et al., 2023). Data analysis was performed through modal analysis at high resolution and liberation by dot mapping. A pixel size of 1-4 μm with a working distance of 15 mm was selected for various sample analyses.

3.2.2.5 Morphological analysis

SEM-EDS analysis was also used to investigate the surface transformation of the CFA materials and the synthesised products in different experimental stages. To prepare the samples, a double-sided adhesive carbon tape was mounted onto aluminium stubs, and a small portion of the pulverised powder sample was sprinkled on and dusted with a spray to remove any contamination. The samples were further coated twice with Ag/Pd to avoid surface charging during analysis. Sample preparation was conducted at the Center of Microscopy and Microanalysis Unit (MMU WITS), while SEM-EDS analysis was performed at the CHMT, University of the Witwatersrand (described in **Section 3.2.2.4**) and the Analytical Chemistry Department, University of Johannesburg (Vega3 Tescan model XMU).

3.2.2.6 Determination of functional groups

Fourier Transform-Infrared Spectroscopy (FT-IR) was used to identify and ascertain the functional groups in different experimental stages. The analytical instrument monitors the vibrations of the functional groups that characterise the molecular structure and determines the course of the chemical reactions. The IR region in the electromagnetic spectrum lies between the Ultra violet-visible spectroscopy (UV-Vis) and microwave regions, and the mid-infrared region is the most widely used for chemical characterisation due to its fine structure (stronger line strength) for qualitative information (Dulski, 1996). The FT-IR spectra were directly measured on the solid samples using a PerkinElmer Spectrum 2 device, and the spectra were acquired in the range of 400-4000 cm^{-1}.

3.2.2.7 Brunauer-Emmett-Teller (BET) and Barrett-Joyner-Halenda (BJH)

The Brunauer-Emmett-Teller (BET) method was used to determine the specific surface areas of the CFA samples. The N_2 adsorption and desorption isotherms were obtained using a Micromeritics Tristar 3000 instrument. By analysing the desorption branches of the N_2 isotherms, the pore size distribution was determined and calculated using the Barett-Joyner-Halenda (BHJ) method. All samples were degassed at 200-250℃ under vacuum to remove

moisture before analysis. BET analysis was conducted at the School of Chemistry, University of the Witwatersrand.

3.2.3 Water quality analysis

Water quality parameters were measured as part of the adsorption and coagulation wastewater treatment. The measured parameters were pH, electrical conductivity (EC), turbidity (NTU), and chemical oxygen demand (COD) (mg/L). The pH, EC, and TDS were determined using a portable Hanna HI 9812-5 pH/EC/TDS/temperature metre. Turbidity was measured using the CyberScan TB 100 Portable Turbidity Metre, and COD was measured using a Merck Pharo 300 spectrometer. The sulphate ion concentration was determined using ion chromatography (Merck Spectroquant Pharo 300 spectrophotometer). All instruments were calibrated before analysis.

3.3 Experimental Methodology

3.3.1 Material characterisation

The CFA material used in this study was characterised by investigating its particle size, chemical composition, surface morphology, and phase chemical composition (see **Figure 3.1**).

3.3.2 Dry magnetic separation

The induced roller magnetic separator presented in **Figure 3.2** was used to recover iron from the raw CFA. As reviewed in **Chapter 2** magnetite and haematite are magnetic components in CFA compared to mullite and quartz, which are reported as diamagnetic (Valeev et al., 2019; Cornelius et al., 2021; Rosita et al., 2020). Approximately 500 g (accurately weighed to 0.1 mg) of each CFA material was fed into a vibrating feed hopper using predetermined parameter levels, passed through the induced roller, and collected as fractions of non-magnetic (non-MF), magnetic (CFA-MF), and middling (collected as non-MF). Due to the high magnetic alignment of magnetite (Fe_3O_4), which retains its magnetism after magnetic

separation, in this study, the CFA-MF was collected at the adjustable pole piece, as shown in **Figure 3.2**, whereas the non-MF was collected at the bottom with pans (Dwari et al., 2013; Fears, 2018). Instrument pole pieces are often adjusted according to the particle size of the material. Since CFA is a fine material, the pole piece was maintained at approximately 2 mm to prevent any loss in the magnetic field strength and gradient, which could otherwise affect the separation efficiency. (Fears, 2018). Adjustment of the magnetic current (A) resulted in equivalent magnetic field control and field intensity values (measured by a magnetic field meter). The various parameter levels used in this study are presented in **Table 3.2**. The chemical and phase compositions of the extracted CFA-MF and non-MF samples were characterised. The morphology of the extracted CFA-MF was also analysed and compared to that of raw CFA. MS was conducted at the Extractive Metallurgy Laboratory, University of Johannesburg.

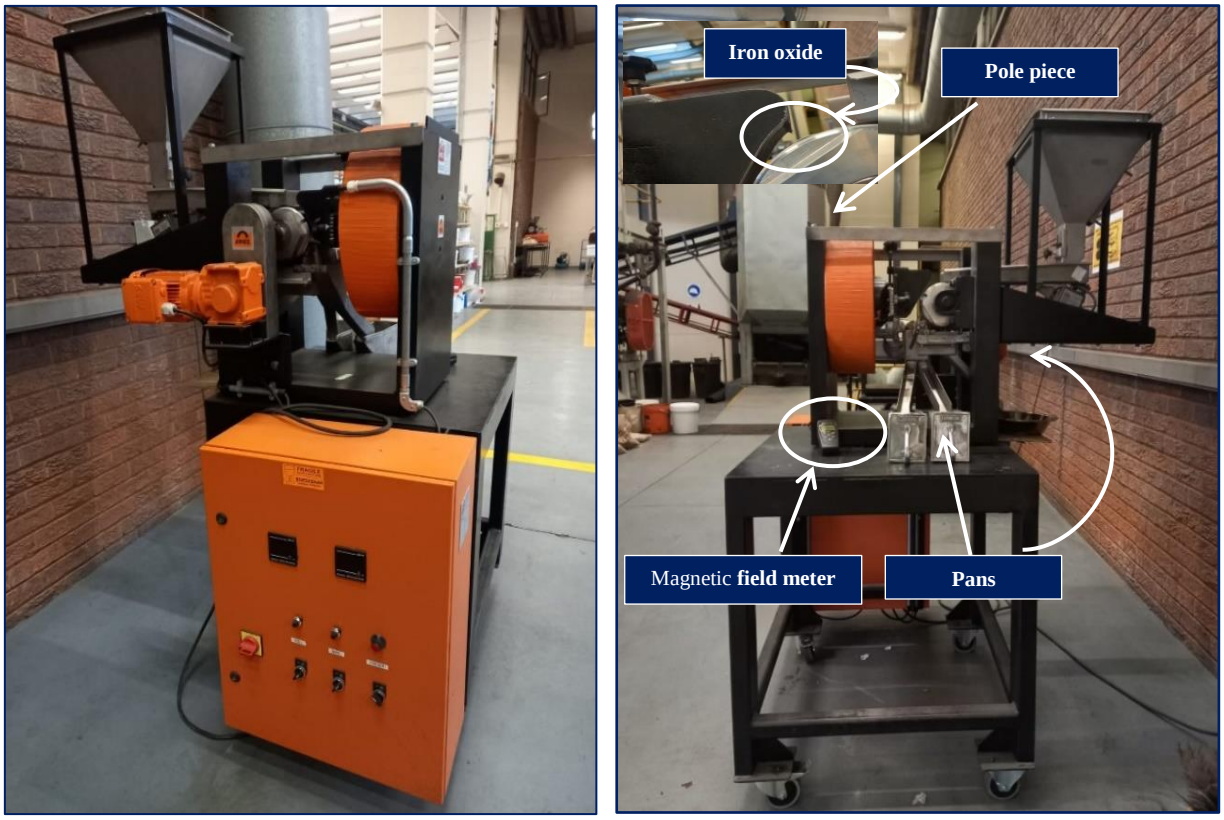

Figure 3.2: The induced roller magnetic separator (Model: IMR roll, supplied by Eziez, South Africa).

Table 3.2: Various parameters of the induced roller magnetic separator

Variables	Units	Levels
Pole piece	mm	2, 4, 6
Splitter plate A, B	Degree theta ($°\theta$)	30, 60
Feed rate	tph	7, 9, 11
Roll speed	rpm	20, 80, 133.2
Magnet field control	V	0.5, 1.5, 3.0, 5.0
Current	Ampere (A)	14, 29, 44, 60
Magnetic field strength	Tesla, T	0.45, 0.57, 0.88, 1.05

Magnetic separation has also been reviewed as a pre-concentration technique for REEs in **Section 2.5.1** (see **Chapter 2**), therefore the enrichment factor (EF) was also calculated according to **Equation 3.1** (Lin et al., 2017; Cornelius et al., 2021).

$$\text{Enrichment factor (EF)} = \frac{C_1}{C_0} \qquad \textbf{3.1}$$

where C_0 is the concentration of REEs before magnetic separation and C_1 is the concentration of REEs after magnetic separation.

3.3.3 Leaching experiments

The metal leaching efficiency was calculated as the ratio of the amount leached in the solution to the initial amount in the sample. The experimental calculations were based on **Equation 3.2**. The non-MF (CFA after magnetic separation) was used in the leaching experiments, and all experiments were conducted in shaking incubators depicted in **Figure 3.3**.

$$\%\ \text{extraction efficiency} = \frac{VC_2}{MC_1} \times 100 \qquad \textbf{3.2}$$

where V is the volume of a leachate in mL and C_2 is the metal concentration in the leachate in μg/mL. M is the mass of the weight sample in g, and C_1 illustrates the metal concentration of the feed sample in μg/g.

Figure 3.3: Leaching test equipment: A scientific shaking incubator (Lenton furnace model 353).

3.3.3.1 Direct acid leaching

Direct acid leaching was investigated using HCl and H_2SO_4 solutions. Approximately 50 g of CFA samples were accurately weighed and transferred to 500 mL Erlenmeyer flasks. Different acidic solutions were added to each flask, and the flasks were sealed for leaching. Leaching experiments were conducted at varying acid concentrations, leaching times, and leaching temperatures. The solid/liquid ratio (1:5) and stirring rate (150 rpm) were based on a literature review and were kept constant (Matjie et al., 2005; Shemi, 2013). The reaction mixtures were filtered, and the filtrates were quantitatively transferred to 500 mL volumetric flasks. In all cases, the acidities of these solutions were adjusted to match those of the standard solution matrix and filled to the mark with water. All solutions were analysed for

their chemical composition. The residues were dried overnight in an oven and further analysed for phase composition and morphology. **Table 3.3** present the leaching parameters utilised in the preliminary test work.

Table 3.3: Leaching parameters and conditions for the preliminary tests using HCl and H_2SO_4

Experimental Run	Leaching conditions				
	Agitation rate (rpm)	**Solid:liquid ratio**	**Acid Concentration (M)**	**Temperature (°C)**	**Time (hrs)**
H_2SO_4 leaching					
Concentrations	160	1:4	0.5, 2, 4, 6	70	10
Temperatures	160	1:4	6	45, 60, 70, 80	10
Leaching times	160	1:4	6	70	6, 10, 15
HCl leaching					
Concentrations	160	1:10	2, 4, 6	70	6
Temperatures	160	1:10	4	45, 60, 70	6

*Analysis in duplicates

3.3.3.2 Indirect acid leaching

The lime-sinter process has been reviewed as an effective pre-treatment technique for CFA processing (Yao et al., 2014; Sibanda et al., 2016). Therefore, CFA samples were also treated by sintering prior acid leaching, as shown in **Figure 3.4**. This section describes the experimental work on pre-treatment and subsequent leaching processes.

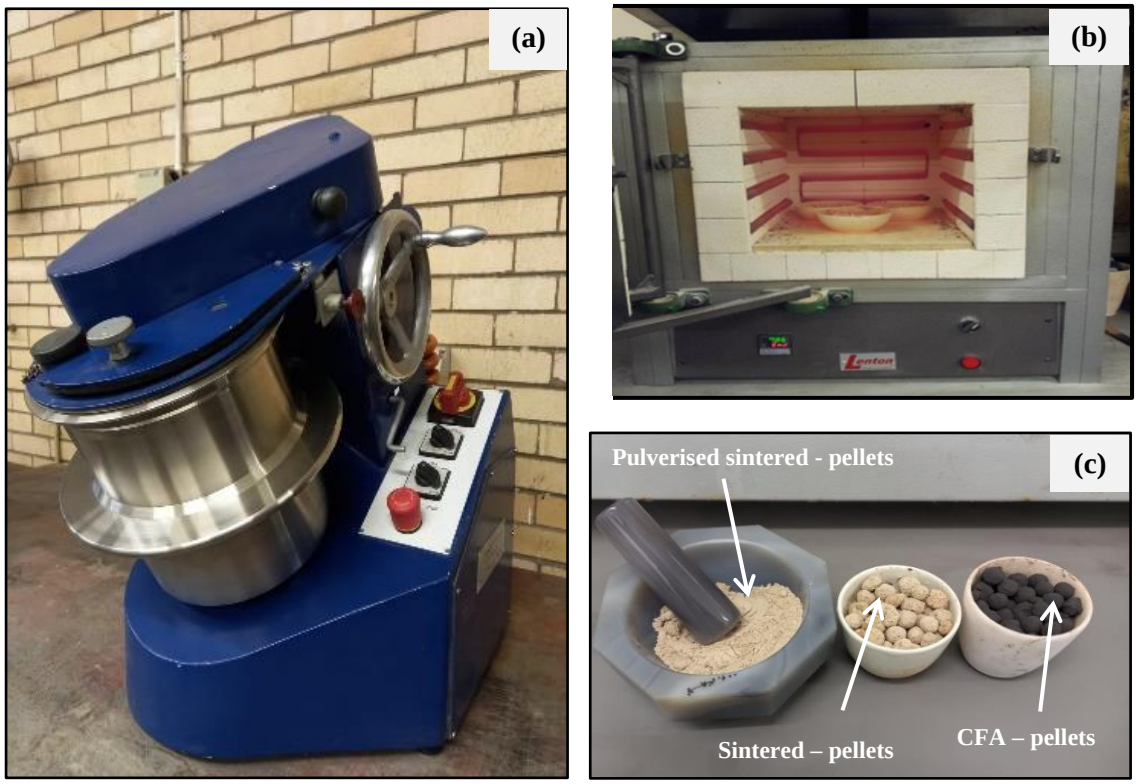

Figure 3.4: (a) Pelletiser equipment (Model: R02, H. Birkenmayer (Pty) Ltd), (b) A Lenton muffle furnace (Model: LLC 13/42-PA), and (c) CFA pellets before and after sintering.

Pelletising

The CFA samples were homogenously mixed with $CaCO_3$ and coal in different mass ratios (5:4:1, 4:4:2 and 5:3:2). Water (10-30%) was added to the mixtures to produce pellets that were sufficiently strong for sintering. Calcium carbonate was used as a source of lime (CaO) to transform the mullite into a soluble form, whereas finely ground coal (similar ground as CFA) was used as a source of carbon to allow uniform heat transformation during sintering (Matjie et al., 2005; Shemi, 2013).

Sintering

The pellets formed were air-dried and sintered in a muffle furnace at 1100°C for 5 hours to produce sintered pellets (Matjie et al., 2005; Shemi, 2013). **Figure 3.4** shows the muffle furnace and the CFA pellets before and after sintering. The key aim of sintering is to convert the mullite ($Al_6Si_2O_{13}$) phase by facilitating a localised melting reaction between particles. This process breaks bonds and forms new compounds without fully melting (Shemi, 2013). The sintered pellets were pulverised into powder, similar to CFA, and further analysed for the chemical and phase composition, including the morphology and particle size distribution.

Post – Sinter Leaching

The sintered CFA was further used in the leaching experiments as previously described in the direct CFA leaching (see **Section 3.3.3.1**). HCl and H_2SO_4 were used as lixiviants, and the effects of leaching parameters were investigated using the experimental conditions listed in **Table 3.3**. The resulting leach liquors and sintered CFA residues were analysed for chemical and phase composition.

3.3.3.3 Dry digestion – water leach

The dry digestion technique was investigated as the second leaching step in this experimental work to extract metals in the sintered CFA solid residue (CFA-SR) after the sinter-H_2SO_4 leach step. Approximately 20 g of the sample was mixed with concentrated H_2SO_4 (or HCl) at a 1:1 S/L ratio, which was sufficient to form a paste. The mixture was further baked in a furnace at various temperatures and baking times to allow for decomposition and crystal deformation (Yahorava et al., 2018). After drying, the samples were cooled to room temperature, pulverised to remove lumps, and transferred to an Erlenmeyer flask for water leaching. The experimental parameters used for dry digestion are listed in **Table 3.4**.

To conduct a water-leaching experiment, the dried samples were quantitatively mixed with water at a S/L ratio of 1:10, agitated at 150 rpm, and leached at 25°C for 24 hours to allow the transfer of the metal sulphates (or chlorides) into the solution. The water-leaching experimental parameters were based on a literature survey (Rivera et al., 2018; Ma et al., 2019). After leaching, the reaction mixture was filtered and quantitatively transferred to a 500 mL volumetric flask. The elemental composition of the filtrate was analysed, and the residue was dried overnight before analysis.

Table 3.4: The experimental test parameters for dry digestion-water leaching

Parameter	Values	Values
Acid type	H_2SO_4	HCl
Baking temperature (℃)	100, 300, 500	70
Baking time (hrs)	6, 12, 24	6, 12, 24
Leaching temperature (℃)	24	24
Leaching time (hrs)	6, 12, 18, 24	6, 12, 18, 24

*Analysis in duplicates

3.3.3.4 Design of Experiments

In this study, the Design Expert® (version 13) software was employed to optimise the sinter-H_2SO_4 process for alumina production. The Design of Experiments (DOE) offers a precise statistical analysis of the variables/factors that affect the experimental process and their interaction (Czitrom, 1999; Barrentine, 1999). Therefore, a 2^4 full factor design was utilised to establish significant variables affecting the extraction of Al from sintered CFA. The process variables and their levels were selected based on the data obtained from preliminary experiments and a literature survey. The variables that were determined as significant were further optimised using the Central Composite Rotatable Design (CCRD) and Response Surface Methodology (RSM).

Identification of Significant Variables

Normal Probability Plot: When evaluating the effect of unreplicated factorials, it is important to consider higher-order interactions that can provide meaningful insights. Therefore, it is imperative to take these interactions into account during the analysis. To simplify this process, the normal probability plot method can be a useful approach (Daniel, 1959). To observe the main effects, **Equation 3.3** is generally used to scale the plot of a straight line. As a result, variables with significant effects will resemble a non-zero mean value and therefore deviate from the straight line.

$$\text{Probability points(P)} = (i_{\text{order number}} - 0.5) \times \frac{100}{m_{\text{number of effects}}} \qquad \textbf{3.3}$$

Pareto Analysis: The use of Pareto charts can illustrate the impact of variables. These charts provide a useful tool for identifying the most significant variables. The Pareto chart is created using an algorithm that determines a significant threshold that is statistically derived. This makes it an effective method for selecting the most important variables. A bar graph that is horizontally shaped represents the significance level. The critical value line that cuts across the bar graphs separates the vital effects from the non-vital effects (Tague, 2005; Wilkinson, 2006).

The optimisation of significant variables was achieved after screening to predict the response value for the significant variables.

Optimisation of Significant Variables

Central Composite Rotatable Design (CCRD): The CCRD can be used for collecting second-order response data. Therefore, the response surface model was proposed by fitting the experimental data in the software, using the quadratic formula in **Equation 3.4**. To check the sufficiency of the model, ANOVA was employed as a statistical tool. Data evaluation was conducted using the t-test (standard errors of model coefficients), F-test (Fisher's test), and R^2 (coefficient of determination) (Shemi, 2013; Tripathy and Murthy, 2012).

$$y = \beta_o + \sum_{i=1}^{k} \beta_i x_i + \sum_{i=1}^{k} \beta_{ii} x_i^2 + \sum_{i=1}^{k} \sum_{j=i+1}^{k} \beta_{ij} x_i x_j + \varepsilon \qquad \textbf{3.4}$$

where, y is the predicted response, k is the number of variables, and ε is a term for variables excluded by the response function. β_o, β_i, β_{ii}, and β_{ij} represent the coefficients for intercepts, linear effects, quadratic effects, and interaction effects, respectively. x_i and x_j are coded predictor variables for the independent factors (Shemi, 2013).

Response Surface Methodology (RSM): The primary goal of RSM is to build the model, and as a result, optimise the variables that greatly influence the process (Tripathy and Murthy, 2012). Based on quadratic programming, RSM and CCRD were used to fit the experimental data and develop the model.

3.3.3.5 Experimental Design

The leaching experimental design is presented in **Table 3.5** showing the experimental test conditions and the starting material used in each stage.

Table 3.5: Leaching experimental design

Test Type	Test parameter	Solvent	Material
Preliminary runs	• Leaching time • Acid concentration • Leaching temperature	HCl H_2SO_4	Raw CFA Sintered CFA
Identification of influential variables	• Leaching time • H_2SO_4 concentration • Solid to liquid ratio • Leaching temperature	H_2SO_4	Sintered CFA
Optimisation of influential variables	• Leaching time • H_2SO_4 concentration • Solid to liquid ratio • Leaching temperature	H_2SO_4	Sintered CFA
Dry digestion technique	• Baking temperature • Baking time • Leaching time	H_2O	Sintered CFA Residue

* All test work was conducted at 160 rpm agitation rate

3.3.4 Purification of CFA leach liquor

A quantitative analysis was performed on the leach liquor to observe the distribution of REEs, Al, Fe, and Ti. The iron speciation and pH adjustment were measured as follows:

- The total Fe (Fe(II)/Fe(III)) concentration was measured by ICP-OES, whereas Fe(II) was determined by the potassium dichromate titration method (Skoog et al., 2004).
- The pH of all the solutions was measured prior to purification, and pH adjustments were conducted using H_2SO_4 and NaOH.

3.3.4.1 Fe reduction and Ti extraction

The first purification step was solvent extraction (SX) of titanium by Primene JM-T/Shellson D70 from the associated elements. Iron filings were added stoichiometrically to the CFA leach liquor to reduce Fe^{3+} to Fe^{2+} and thus prevent co-extraction of Ti^{4+} and Fe^{3+} into the organic phase. The organic solution (Primene JM-T/Shellson D70) and aqueous solution (leached liquor) were mixed in a beaker, reacted until equilibrium, and transferred to the separation funnel for further separation, as shown in **Figure 3.5**. A 1 M NH_4OH solution was used to extract Ti from the organic phase, which was then agitated to facilitate phase separation and $Ti(OH)_4$ precipitation. The precipitate obtained was dried and calcined at 500℃. The experimental parameters were based on a literature survey (Matjie et al., 2005; Rampou et al., 2017). The synthesised TiO_2 was characterised for its chemical composition, phase composition, and physicochemical properties. The purity of the synthesised TiO_2 was measured following ASTM specifications (ASTM, 1988), while the physicochemical properties were graded using a commercial TiO_2 (Degussa P25) (Nachit et al., 2022).

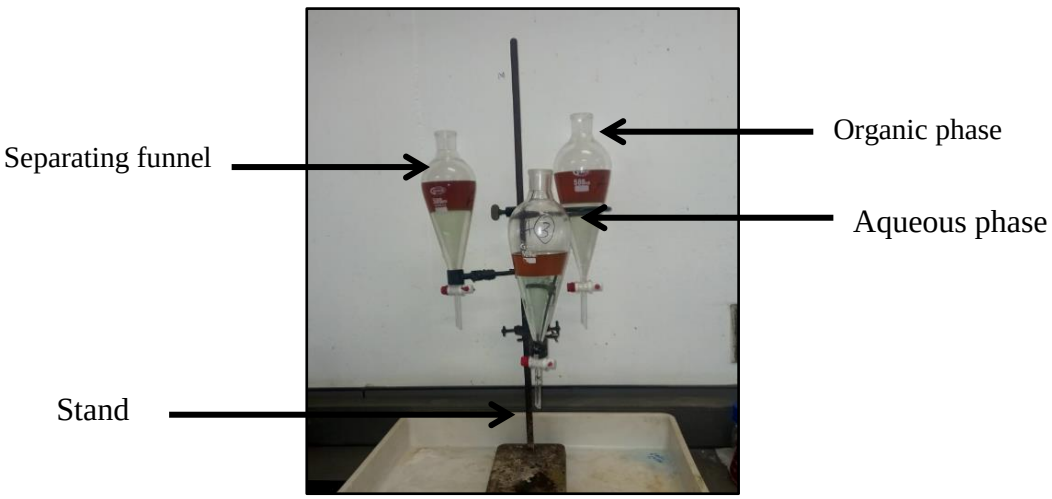

Figure 3.5: Solvent extraction set-up for Ti(IV) using Primene JM-T/Shellson D70.

3.3.4.2 Aluminium crystallisation

Aluminium was crystallised directly from the solution using ammonium sulphate salt. The solution was first heated at 80℃ for 30 minutes to ensure complete solubility and then cooled in an ice bath at 0℃ to facilitate the crystallisation process, as shown in **Figure 3.6** (Ma et al., 2021). The resulting crystals were calcined at 800℃ for 5 hours and analysed for their chemical composition and phase composition. The feed composition used in the Hall-Heroult alumina production served as a benchmark to grade the synthesised alumina (Authier-Martin et al., 2001).

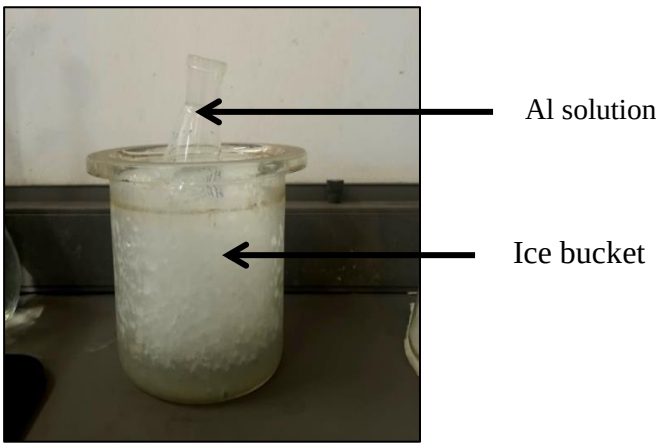

Figure 3.6: The direct aluminium crystallisation set-up in the raffinate.

3.3.4.3 Seeded – Fe(III) precipitation

Fe(II) oxidation-precipitation was conducted in a 1 L reactor set-up by Mwewa et al. (2019), as shown in **Figure 3.7**. The Fe(II) in the solution was oxidised to Fe(III) by aeration, and an oxygen feed pipe was used to transport oxygen at 15 min/L. The reaction was agitated at 300 rev/min, and the temperature was maintained at 25℃. The pH was controlled using an automated pH controller fitted with 2.0 M NaOH and 0.1 M H_2SO_4 to adjust the reaction pH. The reactor was bubbled with nitrogen prior to oxidation to prevent iron pre-oxidation and after the reaction to stop the oxidation. In the seeded precipitation, the magnetic fractions obtained in **Section 3.3.2** were added at different dosages (Cs = 0.0, 0.5, 1.0, and 2.0) prior to oxidation followed by precipitation. The experiment was allowed to proceed for approximately 24 hours to allow for efficient oxidation and precipitation. The precipitates generated were washed, filtered and dried in an oven, and further characterised for their

chemical and phase composition, morphology, and physicochemical properties. An outline of the experimental conditions is given in **Table 3.6**.

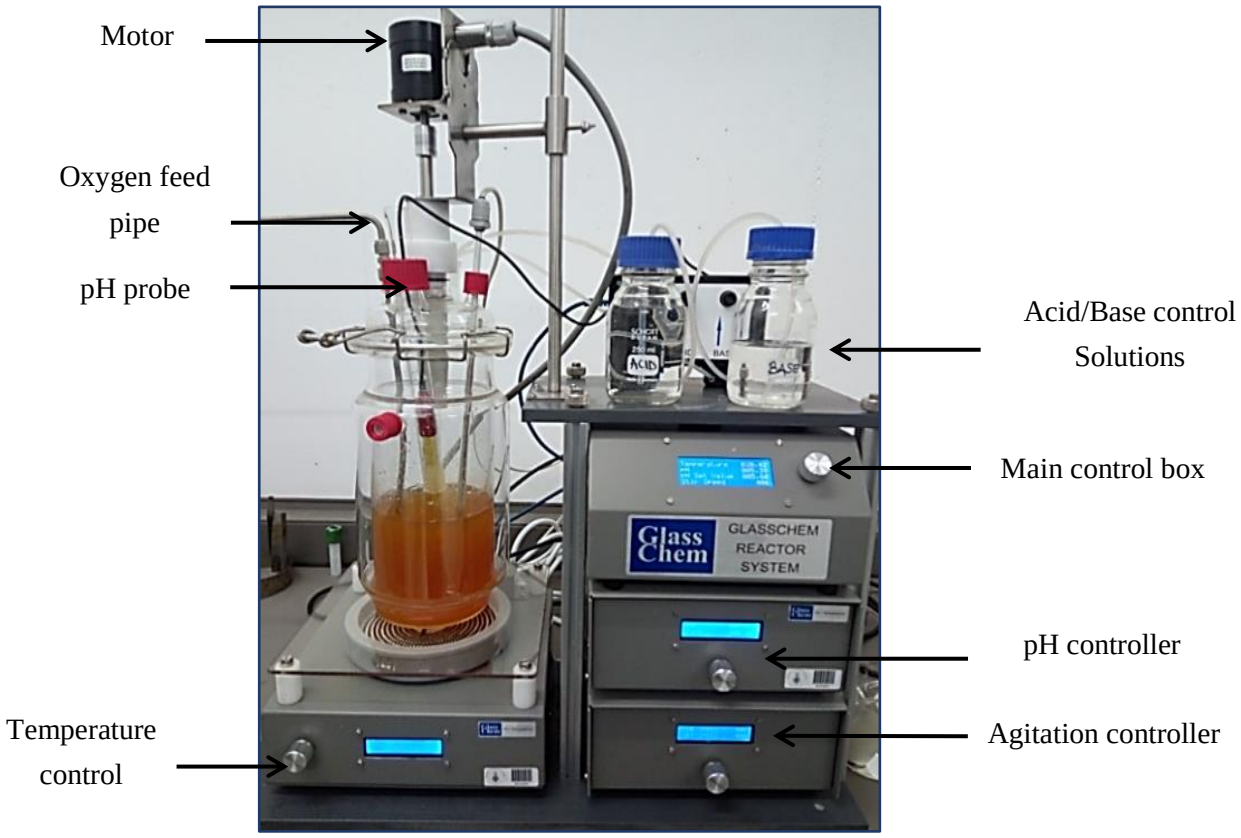

Figure 3.7: Experimental set-up for seeded Fe(II) oxidation and precipitation (adopted from Mwewa et al. (2019)).

Table 3.6: The experimental conditions for Fe(II) oxidation and precipitation.

Parameter	Values
pH	5.0
Reaction temperature, °C	25
Air flowrate, L/min	15
NaOH concentration, M	0.1
H_2SO_4 concentration, M	0.1
Time, hrs	24
Agitation, rev/min	300
Seed concentration, Cs	0.0, 0.5, 1.0, 2.0

*Analysis in duplicates

3.3.4.4 Precipitation of rare earth oxalates

The leach liquor obtained from the second leach stage was also directly precipitated with oxalic acid to produce a rare earth concentrate, which can further be used to separate and process individual REE compounds. A 1 M solution of oxalic acid was prepared and added in excess to the leach liquor to ensure complete precipitation (Chi and Xu, 1999; Ariuntuya, 2018). The experiment was conducted 25℃ and 150 rpm. The solution was filtered, and the filtrate was air-dried, then analysed to establish its purity by determining the chemical composition.

3.3.5 Coagulation and adsorption in wastewater treatment

The generated CFA by-products were further used in adsorption and coagulation. The CFA secondary solid residue (CFA-SSR) was used as the adsorbent, while the seed-Fe(III) precipitate was used to generate coagulants. In the adsorption test work, the adsorption capacity, q_e (mg/g), and adsorption efficiencies (%) were calculated according to **Equations 3.5** and **3.6**. Similarly, the metal recovery R_{metal} (%) in coagulation was also determined using **Equations 3.6**.

$$q_e = \frac{(C_0 - C_1)V}{M} \qquad \textbf{3.5}$$

$$R_{metal} = \frac{C_0 - C_1}{C_0} \times 100\% \qquad \textbf{3.6}$$

Where C_0 is the initial concentration (mg/L) of a particular metal species in solution (mg/L), C_1 is the concentration of a metal species in the effluent (mg/L) after precipitation/adsorption, *M* is the mass of the adsorbent used in grammes (g) and, V (L) is the solution volume.

3.3.5.1 Coagulation experimental procedure

The seeded-Fe(III) precipitate generated in **Section 3.3.4.3** was further used to generate coagulants for wastewater treatment. The optimum dissolution of the precipitate was first determined in dilute H_2SO_4 solutions (0.5-6 M) to allow complete sample dissolution. The dissolved sample was the generated coagulant and used to treat brewery wastewater. A jar

tester in **Figure 3.8** was used to establish the best coagulant dose for treating brewery wastewater by measuring changes in water quality parameters (i.e. pH, conductivity, turbidity, and chemical oxygen demand). In each beaker containing 500 mL of brewery wastewater, coagulant was added at varying dosages and mixed (induced rapidly) for 3 minutes at 25°C and 200 rpm, followed by slow mixing at 20 rpm for 10 minutes. The mixers were then switched off for 30 minutes to allow particles to settle. The settling of flocs was observed in each jar, and supernatant samples were collected using a pipette and placed into sample vials for analysis. The performance evaluation was based on the water quality parameters described in **Section 3.2.3**. The experimental parameters used in the coagulation process are listed in **Table 3.7**.

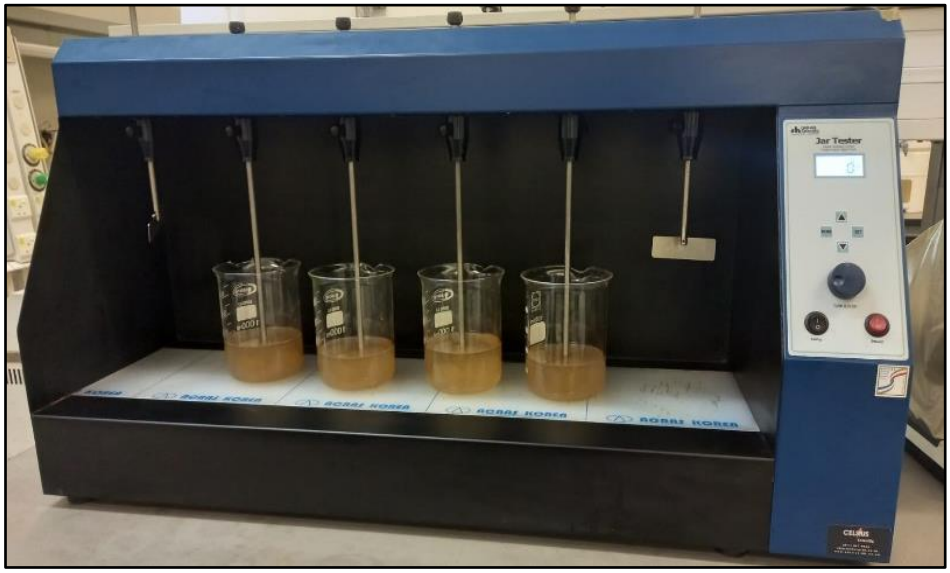

Figure 3.8: Jar tester for coagulation.

Table 3.7: Coagulation experimental parameters

Parameter	Value
Coagulant dose, mg/L	10, 50, 100
Temperature, °C	25
Agitation, rev/min	Fast = 200, slow = 20
Mixing time, min	Rapid = 3, slow = 10
Sedimentation time, min	30

*Analysis in triplicate

3.3.5.2 Adsorption experimental procedure

Coal fly ash-secondary solid residue (CFA-SSR) was characterised as a potential adsorbent in acid mine drainage (AMD) treatment. The material was first characterised for its physicochemical properties, surface charge and morphology, functional group identity, phase composition, and chemical composition (see **Figure 3.1**). The surface charge was determined by measuring the point of zero charge (pHpzc) with a 0.1 M KNO_3 solution using the mass titration method (Mohan and Gandhimathi, 2009). An aliquot of 50 mL of KNO_3 was added to different Erlenmeyer flasks, and a set of different pH values (1-12, pH_i) was adjusted. Approximately 0.5 g of CFA-SSR was added to each flask and agitated at 150 rpm at 25℃ for 24 hours. The solutions were then filtered in a beaker, and the final pH (pH_f) was measured. The pHpzc was established from a plot of the change in pH ($\Delta pH = pH_f - pH_i$) versus pH_i values.

Batch tests were further performed to establish the adsorption capacity of CFA-SSR for heavy metals in AMD solutions. A known amount of adsorbent (0.5-10 g) was placed in contact with 500 mL of AMD solution at known concentrations, and the flasks were sealed and shaken in an incubator (see **Figure 3.3**) at 150 rpm at 25℃ for 300 minutes (maximum). A pH metre was used to measure pH change at predefined intervals, while collecting aliquots of about 10 mL of samples for chemical analysis. Changes in the equilibrium metal ion concentrations were measured in the filtrate to determine the adsorption capacities. The effects of solution pH, adsorbent dosage, and contact time were established, and the chosen experimental parameters were based on a literature survey (Nleya, 2016; Manchisi, 2016; Mosai, 2020).

3.4 Data analysis

The raw data collected from the experimental work was utilised to achieve the objectives outlined in **Chapter 1**, **Section 1.3**. The subsequent chapters of this thesis (**Chapter 4** to **6**) detail the experimental results and discussion.

References

Ariuntuya, B., 2018. Recovery of Rare Earth Elements from Apatite Ores by Hydrometallurgical Process. PhD thesis, Graduate School of Engineering and Resource Science, Akita University, Japan.

Authier-Martin, M., Forte, G., Ostap, S. and See, J., 2001. The mineralogy of bauxite for producing smelter-grade alumina. *JOM* 53, 36-40.

Barrentine, L.B., 1999. An introduction to design of experiments: a simplified approach. ASQ Quality Press. Milwaukee, USA. ISBN: 0-87389-444-8.

Chi, R. and Xu, Z., 1999. A solution chemistry approach to the study of rare earth element precipitation by oxalic acid. *Metallurgical and Materials Transactions B* 30, 189-195.

Cornelius, M.-L.U., Ameh, A.E., Eze, C.P., Fatoba, O., Sartbaeva, A. and Petrik, L.F., 2021. The Behaviour of Rare Earth Elements from South African Coal Fly Ash during Enrichment Processes: Wet, Magnetic Separation and Zeolitisation. *Minerals* 11(9), 950.

Czitrom, V., 1999. One-factor-at-a-time versus designed experiments. The American Statistician 53(2), 126-131.

Daniel, C., 1959. Use of half-normal plots in interpreting factorial two-level experiments. *Technometrics* 1(4), 311-341.

Dulski, T.R., 1996. A manual for the chemical analysis of metals. Americal Society for Testing and Materials (ASTM) International, West Conshohocken. ISBN: 0-8031-2066-4.

Dutrow, B.L., Clark, C.M., 2012. X-ray powder diffraction (XRD). Geochemical Instrumentation and Analysis 1-2.

Dwari, R.K., Rao, D.S., Reddy, P.S.R., 2013. Magnetic separation studies for a low grade siliceous iron ore sample. *International Journal of Mining Science and Technology* 23, 1-5.

Fears, P., 2018. Magnetic Separators for Mineral Processing. Available online: https://www.bunting-redditch.com/magnetic-separators-for-mineral-processing (Accessed on 14-05-2021).

Hrstka, T., Gottlieb, P., Skala, R., Breiter, K. and Motl, D., 2018. Automated mineralogy and petrology-applications of TESCAN Integrated Mineral Analyzer (TIMA). *Journal of Geosciences* 63(1), 47-63.

Lin, R., Howard, B.H., Roth, E.A., Bank, T.L., Granite, E.J. and Soong, Y., 2017. Enrichment of rare earth elements from coal and coal by-products by physical separations. *Fuel* 200, 506-520.

Ma, Y., Stopic, S., Xakalashe, B., Ndlovu, S., Forsberg, K., Friedrich, B., 2021. A cleaner approach for recovering Al and Ti from coal fly ash via microwave-assisted baking, leaching, and precipitation. *Hydrometallurgy* 206, 105754.

Ma, Y., Stopic, S. and Friedrich, B., 2019. Hydrometallurgical Treatment of an Eudialyte Concentrate for Preparation of Rare Earth Carbonate. Johnson Matthey Technology Review 63(1), 2-13.

Manchisi, J., 2016. Development of sustainable adsorbents for wastewater treatment, PhD thesis, School of Chemical Engineering, University of Birmingham, UK.

Matjie, R., Bunt, J. and Van Heerden, J., 2005. Extraction of alumina from coal fly ash generated from a selected low rank bituminous South African coal. *Minerals Engineering* 18, 299-310.

Mohan, S., Gandhimathi, R., 2009. Removal of heavy metal ions from municipal solid waste leachate using coal fly ash as an adsorbent. *Journal of Hazardous Materials* 169, 351-359.

Mosai, A.K., 2020. Development of functionalised zeolite and bentonite for the recovery of platinum group elements (PGEs) and rare earth elements (REEs) from aqueous systems impacted by mining activities. PhD thesis, School of Chmistry, University of the Witwatersrand, South Africa.

Mwewa, B., Stopić, S., Ndlovu, S., Simate, G.S., Xakalashe, B. and Friedrich, B., 2019. Synthesis of poly-alumino-ferric sulphate coagulant from acid mine drainage by precipitation. *Metals* 9(11), 1166.

Nachit, W., Ahsaine, H.A., Ramzi, Z., Touhtouh, S., Goncharova, I. and Benkhouja, K., 2022. Photocatalytic activity of anatase-brookite TiO_2 nanoparticles synthesised by sol gel method at low temperature. Optical Materials 129, 112256.

Nleya, Y., 2016. Removal of toxic metals and recovery of acid from acid mine drainage using acid retardation and adsorption processes. MSc dissertation, School of Chemical and Metallurgical Engineering, University of the Witwatersrand, South Africa.

Palozzi, J., Bailey, J.G., Tran, Q.A. and Stanger, R., 2023. A characterization of rare earth elements in coal ash generated during the utilization of Australian coals. *International Journal of Coal Preparation and Utilization* 43(2), 2106-2135.

Rampou, M., 2018. Purification of coal fly ash leach liquor for alumina recovery. MSc dissertation, University of the Witwatersrand, South Africa.

Rivera, R.M., Ulenaers, B., Ounoughene, G., Binnemans, K. and Van Gerven, T., 2018. Extraction of rare earths from bauxite residue (red mud) by dry digestion followed by water leaching. *Minerals Engineering* 119, 82-92.

Rosita, W., Bendiyasa, I.M., Perdana, I., Anggara, F., 2020. Sequential particle-size and magnetic separation for enrichment of rare-earth elements and yttrium in Indonesia coal fly ash. *Journal of Environmental Chemical Engineering* 8, 103575.

Shemi, A., 2013. Extraction of aluminium from coal fly ash using a two-step acid leach process. MSc dissertation, University of the Witwatersrand, Johannesburg, South Africa.

Sibanda, V., Ndlovu, S., Dombo, G., Shemi, A., Rampou, M., 2016. Towards the utilization of fly ash as a feedstock for smelter grade alumina production: a review of the developments. *Journal of Sustainable Metallurgy* 2, 167-184.

Skoog, D.A., West, D.M., Holler, F.J. and Crouch, S.R., 2004. Fundamentals of analytical chemistry (8th edition). Thomson Brooks/Cole, Australia. ISBN: 10:0-03-035523-0.

Tague, N.R., 2005. The quality toolbox (2nd edition). ASQ Quality Press Milwaukee. ISBN 0-87389-639-4.

Tripathy, S.K. and Murthy, Y.R., 2012. Modeling and optimization of spiral concentrator for separation of ultrafine chromite. *Powder Technology* 221, 387-394.

Valeev, D., Kunilova, I., Alpatov, A., Varnavskaya, A., Ju, D., 2019. Magnetite and Carbon Extraction from Coal Fly Ash Using Magnetic Separation and Flotation Methods. *Minerals* 9, 320.

Wilkinson, L., 2006. Revising the Pareto chart. The American Statistician 60(4), 332-334.

Yahorava, V., Lakay, E. and Clark, W., 2018. Hydrothermal Pre-Treatment Process of phosphogypsum for enhanced rare earths recovery. Beneficiation of phosphates VIII, 4-29 May-April 2018, Century City Conference Center Cape Town, South Africa. Engineering Conferences International (ECI) Digital Archives. Available online https://dc.engconfintl.org/phosphates_viii (Accessed on 07-08-2022).

Yao, Z., Xia, M., Sarker, P., Chen, T., 2014. A review of the alumina recovery from coal fly ash, with a focus in China. *Fuel* 120, 74-85.

Zhu, Q., 2014. Coal sampling and analysis standards. IEA Clean Coal Centre, London, United Kingdom, 143. ISBN: 978-92-9029-555-6.

4 MATERIAL CHARACTERISATION AND PRELIMINARY STUDIES

4.1 Hypothesis and Objectives

Coal fly ash (CFA) has been extensively studied for the extraction of alumina for smelter-grade production (Matjie et al., 2005; Shemi et al., 2015). In this study, the objectives were expanded to include the extraction of REEs, Ti, and Fe as saleable products. Therefore, the main objectives of this part of the experimental work were set as follows:

- It has been established in the literature survey that the extraction of REEs and Al depends on their phase distribution in CFA. Therefore, to develop an efficient extraction process, it is imperative to understand the phase compositions. Based on the literature surveyed, the distribution of Al, Fe, Ti, and selected REEs was determined using XRD, SEM-EDS, and TIMA.
- While knowledge of the phase composition is essential for developing an efficient extraction process, the distribution of REEs in CFA is also reviewed as complex due to their dispersed distribution and trace concentrations. As such, both direct and indirect acid leaching processes were used to determine the leaching behaviour of the selected REEs in the H_2SO_4 system.
- It has also been established from the literature surveyed that Fe-oxide (magnetite/haematite) can occur as a discrete component in CFA; therefore, it can be recovered by physical separation techniques to reduce the costs of downstream processing. In this study, the recovery of Fe through magnetic separation (MS) was reported.

This chapter presents the results and discussions on CFA characterisation (raw CFA and sintered CFA), iron recovery from raw CFA by MS, and the preliminary leaching test work. The experimental procedures followed are presented in **Section 3.3.1** to **3.3.3** (see **Chapter 3**).

4.2 Results and Discussion

4.2.1 Raw CFA characterisation

This section presents the characterisation of raw CFA for its particle size, chemical and phase composition.

4.2.1.1 Particle size distribution analysis

Particle size distribution (PSD) analysis of raw CFA is presented in **Figure 4.1**. Sieve analysis was conducted in the range of –38 µm to +212 µm, and the graph presented in **Figure 4.1 (a)** demonstrates that more than 90% of CFA passes through the 212 µm sieves. Additionally, **Figure 4.1 (b)** presents the PSD curve (histogram), with a d_{50} established at 20.05 µm. Overall, the findings suggest that CFA is a fine material. Therefore, based on the Unified Soil Classification System (USCS), CFA can be classified as primarily silt-sized. Fine-grained materials usually have exposed surfaces for efficient leaching; thus, CFA was used in this study without further grinding (Ghorbani et al., 2011; Shemi et al., 2015; Apua and Nkazi, 2022).

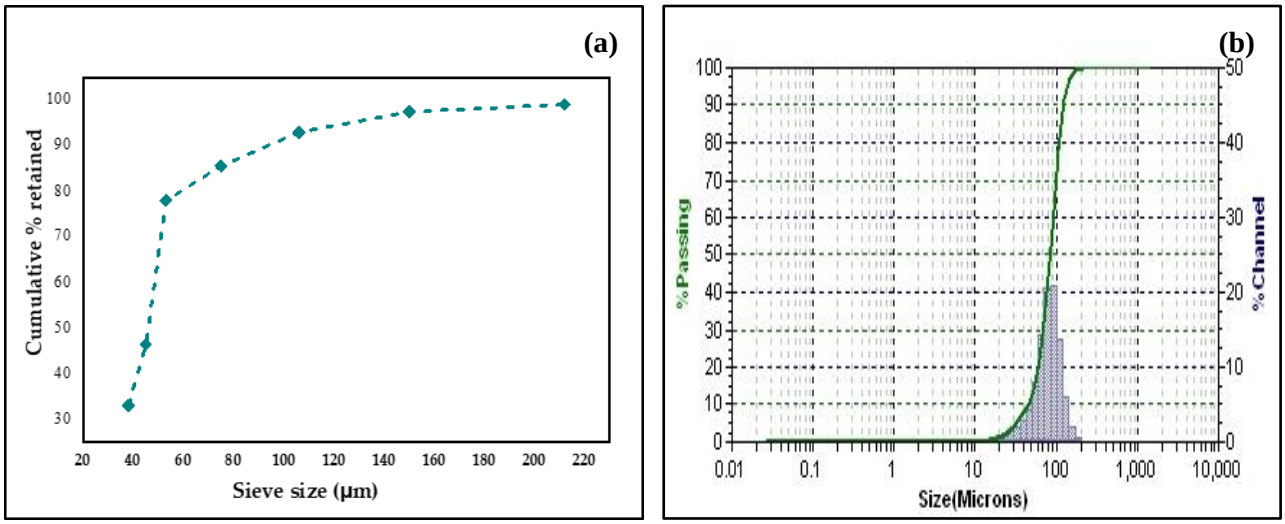

Figure 4.1: Particle size distribution of CFA: (a) sieve analysis and (b) histogram distribution curve by laser particle sizer (LD).

4.2.1.2 Chemical composition analysis

The concentrations of the major oxides in raw CFA were determined using XRF, and the results are shown in **Table 4.1**. According to the South African Coal Ash Association (SACAA), Eskom Power Utility produces Class F CFA, which is siliceous and has a low lime content (<10%) (SACAA, 2021). It can be seen in the table that CFA in this study also had high silica (51.9% SiO_2) with 5.85% CaO; thus, it is a typical representation of South African CFA. XRF analysis also showed that CFA contained 29.2% Al_2O_3, 4.34% Fe-oxide, and 1.70% TiO_2, which are attractive oxides for the objectives set in this study.

Table 4.1: XRF analysis of the major chemical compositions in raw CFA

Analyte	**SiO_2**	**Al_2O_3**	**CaO**	**FeO**	**Fe_2O_3**	**TiO_2**	**MgO**	**MnO**	**Na_2O**	**K_2O**	**P_2O_5**	**L.O.I**
wt. %	54.9	29.2	5.85	0.23	4.11	1.70	1.53	0.06	0.27	0.900	0.610	3.10

Further analysis was conducted using ICP-MS to ascertain the concentrations of REEs. It can be seen in **Figure 4.2** that all REEs were quantified, with a total concentration of 404.54 mg/kg (0.0404%). The LREEs had higher concentrations, with 297.1 mg/kg (0.002971%), than HREEs, with 81.74 mg/kg (0.008174%). Compared to other international markets such as China, the USA, Poland, and India (see **Table 1.2**, **Chapter 1**); REEs in **Figure 4.2** were significantly within range for commercial consideration. For this study, yttrium, lanthanum, cerium, neodymium, and scandium were selected for leaching purposes due to their higher concentrations. Uranium (U) and thorium (Th) were also detected in CFA, and similar to REEs, their concentrations were low at 8.69 mg/kg and 28.6 mg/kg, respectively. Both elements occur exclusively with REEs in the same mineral phases and are regarded as naturally occurring radioactive materials (NORMs) (Krishnamurthy and Gupta, 2005). Since the extraction of U and Th is beyond the scope of the study, a recommendation for future studies is suggested at the end of the thesis (**Chapter 8**).

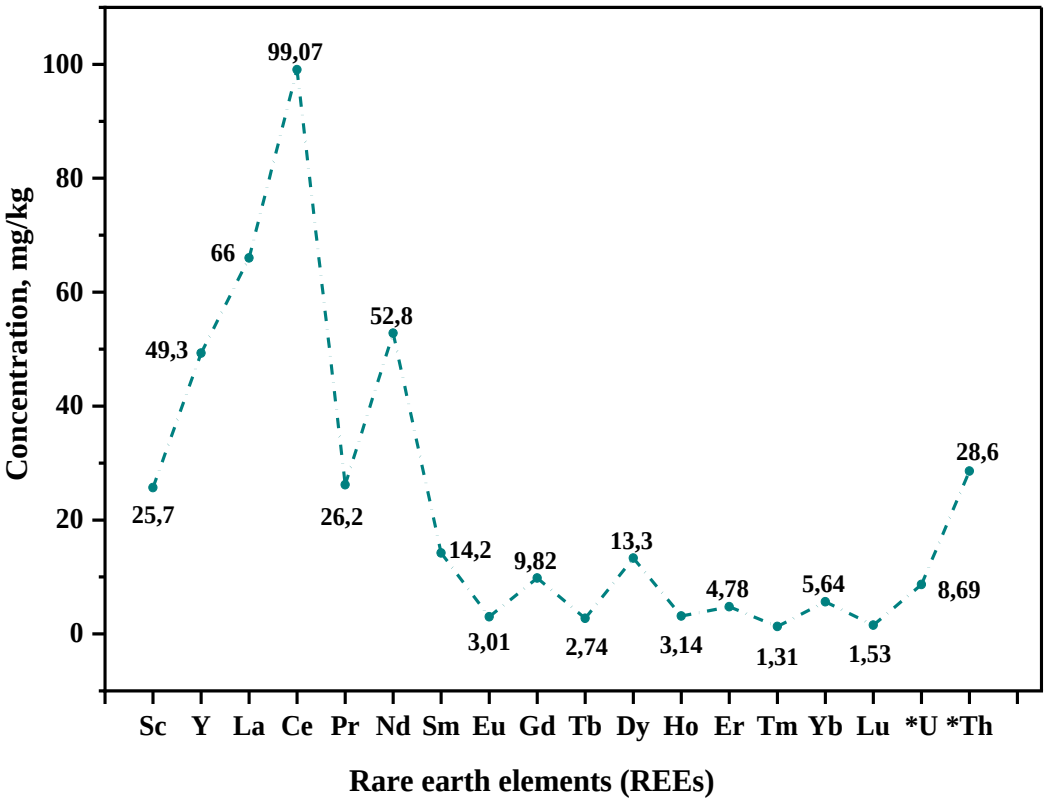

Figure 4.2: ICP-MS analysis of REEs in raw CFA.

4.2.1.3 Phase composition analysis

X-ray diffraction (XRD) was used to identify the phase composition of CFA, and the quantitative results are presented in **Table 4.2** (see **Figure B.1**, **Appendix B** for XRD patterns). The results revealed that CFA was predominantly 60% amorphous. The remaining components were crystalline mullite ($Al_6Si_2O_{13}$), quartz (SiO_2), magnetite (Fe_3O_4), and haematite (Fe_2O_3) at 24.4%, 7.4%, 0.8%, and 0.5%, respectively. The mullite is known to be the non-stoichiometric component of SiO_2 and Al_2O_3; therefore, further calculations based on **Equation B.1** (see **Appendix B**) showed that approximately 60% of Al_2O_3 occurred in the mullite while 40 wt.% is distributed in the amorphous phase. Overall, XRD analysis in this study was consistent with those reported for South African CFA, showing both amorphous and crystalline components (i.e. mullite, quartz, calcite, and magnetite/haematite) (Shemi, 2013; Cornelius et al., 2021; Ndlovu et al., 2023).

Table 4.2: XRD analysis of the phase compositions in raw CFA

Phase composition	Chemical formulae	Concentration, wt.%	
		Phase	Al_2O_3
Mullite	$Al_6Si_2O_{13}$	28.9	60.04
Quartz	SiO_2	12.0	--
Magnetite	Fe_3O_4	1.5	--
Haematite	Fe_2O_3	0.3	--
Amorphous	--	57.3	39.96

-- Not available

SEM-EDS analysis was utilised to understand the distribution of trace elements (i.e. selected REEs) and their association with major phase compositions. The polished block samples were used for analysis, and the SEM micrographs with EDS analysis at specific points are shown in **Figure 4.3**. The polished block samples showed a composition of both spherical and non-spherical (irregular) grains, which are predominantly Al-Si-rich in varying proportions. The bright white grains were concentrated with Fe, suggesting the presence of Fe-oxide component (see **Figure 4.3 (c)**, **grain C**). Previous studies by Valeev et al. (2019) and Strzałkowska (2021) also observed that the bright white grains were haematite/magnetite. Further petrographic analyses can be used to distinguish between haematite and magnetite (Valeev et al., 2019; Strzałkowska, 2021). Nevertheless, some spherical Al-Si-rich grains (see **Figure 4.3 (c)**, **grain A**) also appeared slightly bright, but the two phases were easily distinguishable from each other at the same brightness level owing to their textural differences.

In the literature survey, the mullite phase is defined as an aluminosilicate (Al-Si-rich) component with elongated needles (Kutchko and Kim, 2006; Vu et al., 2019; Dai et al., 2014; Li et al., 2020). This study did not detect such observations for the polished blocks and mounted samples using SEM analysis. However, a similar grain identified as the mullite host by Dai et al. (2014) and Li et al., (2020), was observed in **Figure 4.3 (c)**, **grain A**. In the study by Dai et al. (2014), the grain was slightly cracked, showing the enclosed mullite needles, whereas in the study by Li et al. (2020) the mullite needles could be observed through the transparent host particle (see **Figure 2.3**, **Chapter 2**). Nonetheless, traces of Fe, Mg, and Ti were also quantified in this phase. The REEs were mostly associated with

irregularly shaped Al-Si-rich grains and Al-rich grains. Similar to the study by Bielowicz (2020), Sc was notably associated with the Al-rich phase.

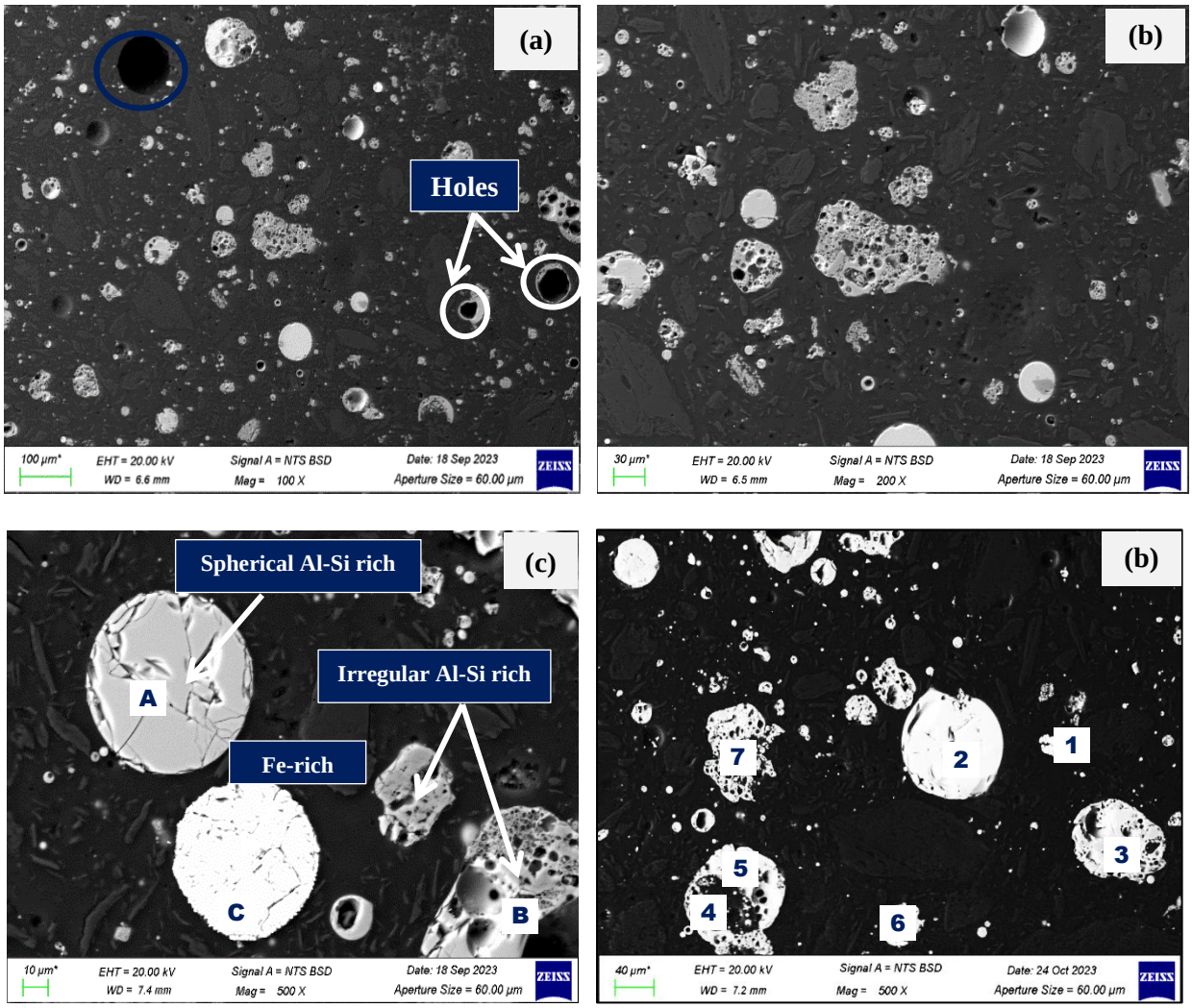

wt%	C	O	Si	Ca	Al	Ti	Fe	Y	Sc	La	Nd	Ce	Others	Phase
2	--	46.5	20.5	8.6	12.6	1.1	9.7	--	--	0.1	0.2	0. 2	1.21	**Al-Si-rich**
3	42.5	37.3	10.6	1.1	5.93	0.5	1.5	--	--	0.06	--	0.07	0.6	**Al-Si-rich**
A	--	46.7	21.6	7.7	10.2	1.7	8.33	--	--	--	--	--	--	**Al-Si-rich**
B	42.78	36.96	11.99	1.02	5.77	0.77	0.29	0.02	--	--	--	--	--	**Al-Si-rich**
5	--	47.1	22.9	1.2	13.7	1.3	7.2	--	--	--	--	--	7.4	**Al-Si-rich**
1	8.9	26.2	1.5	--	1.5	--	61.1	--	--	--	--	--	2.1	**Fe-rich**
C	3.25	27.72	--	--	0.23	--	69.21	--	--	--	--	--	--	**Fe-rich**
6	--	46.4	4.6	7.6	31.1	2.3	0.8	0.28	0.08	--	0. 5	--	2.8	**Al-rich**
4	84.3	10.6	0.9	--	0.37	0.01	--	0.30	0.04	--	--	0.20	1.5	--

Figure 4.3: SEM micrographs of raw CFA at high resolution and a semi-quantitative EDS analysis of the specific marked points.

Automated mineralogical techniques, such as TIMA and MLA (Mineral Liberation Analyser), are well known for their robustness and capacity to determine the mineralogy and distribution of trace elements (Hrstka et al., 2018; Tuhý et al., 2020). Therefore, TIMA analysis was conducted to further understand the distribution of trace elements (i.e. REEs) and their association with the major phase composition. To provide a more comprehensive representation of the sample, a total of 345 grains with different compositions were selected and analysed for the phase composition. The chosen grain count was according to a study by Moila et al. (2017) and the results are presented in **Figure 4.4**. Similar to SEM-EDS analysis, the major phase composition identified was the aluminosilicate (Al-Si-rich phase). The various grains of the Al-Si also contained Fe and Ca in various proportions as Fe-Al-Si and Ca-Al-Si, respectively. A similar trend was also observed in SEM-EDS analysis (see **Figure 2.3**). These grains were also observed to have spherical and irregular shapes (see **Figure 4.5 (a)** and **(b)**). Other phases identified included the Fe-rich, Si-rich, and Ca-rich. Traces of elements such as Si, Fe, Ti, Al, and Ca were also quantified in the major phase compositions. Van Alphen et al. (2007) and Rerani et al. (2024) used QEMSCAN and MLA, respectively, and confirmed that the South African CFA primarily comprises of aluminosilicates as the primary phase, with additional phases such as Fe-oxides and silica (quartz) also identified. Overall, the TIMA results in the figure below were consistent with SEM-EDS and XRD analyses.

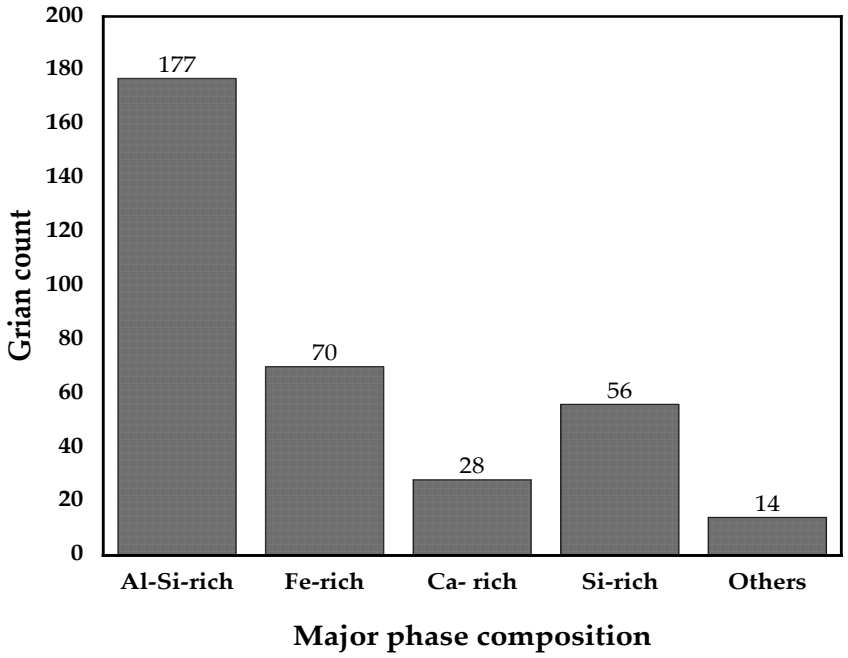

Figure 4.4: Major phase composition and particle count in raw CFA.

Elemental maps were used to locate the trace distribution of selected REEs, Fe, and Ti. **Figure 4.5** shows the BSE images for the distribution of Ti and Fe, along with their normalised weight concentrations. Iron was found as discrete grains and also occurred within the Al-Si-rich grains. The Fe-rich grains resembled Fe-oxide and contained traces of Si, Al, Ca, and Mg. These Fe-oxide grains are shown in **Figure 4.5 (c)**, grain 9 and 10. The Al-Si-rich grains (3, 8, and 14) in **Figure 4.5 (c)**, **(d)**, and **(e)** also showed traces of Fe and Ti in their chemical composition, and the results are also tabulated in **Figure 4.5**. While Ti was detected in the Al-Si-rich phase, it was also quantified in the Fe-oxide phase in grain 17 (see **Figure 4.5 (d)**). In a study conducted by Yang et al. (2021), Ti and Fe from high alumina CFA (HAFA) were distributed in magnetic particles (haematite/magnetite), the amorphous phase, and crystalline phases (mullite, corundum and quartz). Dai et al. (2010) observed the distribution of Ti and Fe in the magnetic fraction and amorphous phase. Overall, the results of this study were consistent with the literature (Dai et al., 2010; Yang et al., 2021).

The distribution of the selected REEs (Ce, Nd, and Y) is also reported in **Figure 4.6**. In **Figure 4.6 (a)**, the REE-phosphates were detected in the Al-Si-rich grain, while in **Figure 4.6 (b)**, they appeared as discrete grains. In a study by Palozzi et al. (2023) using TIMA, monazite (Ce, Th, La, Nd)PO_4 was identified as a REE-bearing mineral that was somewhat bound to either silica or Al-Si-rich phases. Their study also revealed that monazite was decomposed, showing surface fragmentation (Palozzi et al., 2023). Rerani et al. (2024) used MLA and quantified xenotime and monazite as the REE-phosphate minerals. A similar pattern was observed in this study with Y-phosphate and Ce/Nd-phosphate identified. Zircon has also been quantified as an REE-bearing mineral in CFA (Thompson et al., 2018; Liu et al., 2019; Rerani et al., 2024). Some Al-Si-rich grains resembling zircon as a solid solution were also quantified in this study, as presented in **Figure 4.6 (c)** and **(d)**. In **Figure 4.6 (d)**, the elemental map shows the distribution of Y, Nd and Ce in the zircon grain. However, due to the trace concentrations of REEs in this grain, their colour mapping was moderate. Nonetheless, chemical analysis of the zircon grain in **Figure 4.6 (c)**, grain 3, showed traces of elements such as Fe and Ca.

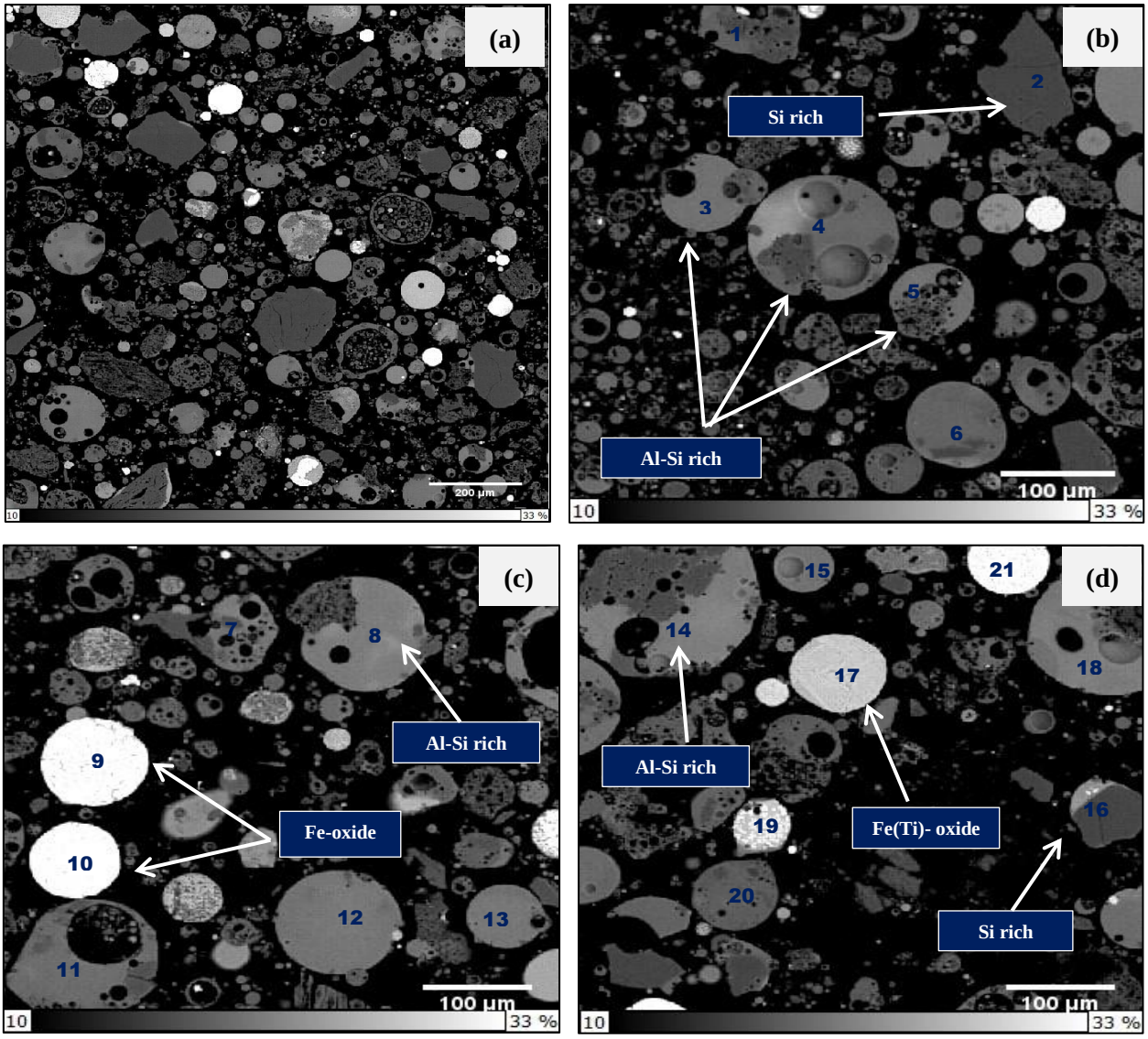

wt%		O	Si	Al	Fe	Ti	Ca	Mg	Mn	Others	Phase
Figure (b)	3	48.51	24.90	15.57	1.61	1.02	6.42	1.96	--	--	Al-Si-rich
	4	43.90	22.47	11.23	1.26	--	16.36	--	--	--	Al-Si-rich
	2	51.81	40.21	1.44	--	--	0.66	--	--	5.88	Si-rich
Figure (c)	9	32.33	3.26	2.34	61.43	--	0.64	--	--	--	Fe-rich
	10	32.65	2.42	1.93	62.08	--	0.92	--	--	--	Fe-rich
	8	41.81	22.97	10.39	7.25	0.57	14.47	2.51	0.01	--	Al-Si-rich
	12	47.10	25.55	12.96	1.09	--	--	3.98	--	1.76	Al-Si-rich
Figure (d)	16	54.56	45.44	--	--	--	--	--	--	--	Si-rich
	17	34.13	5.63	4.79	28.84	24.62	0.70	0.67	0.66	--	Fe-rich
	14	43.45	21.97	15.60	4.42	0.57	12.18	1.81	--	--	Al-Si-rich

Figure 4.5: BSE images of raw CFA and a semi-quantitative phase chemistry of selected grains showing Ti and Fe distribution.

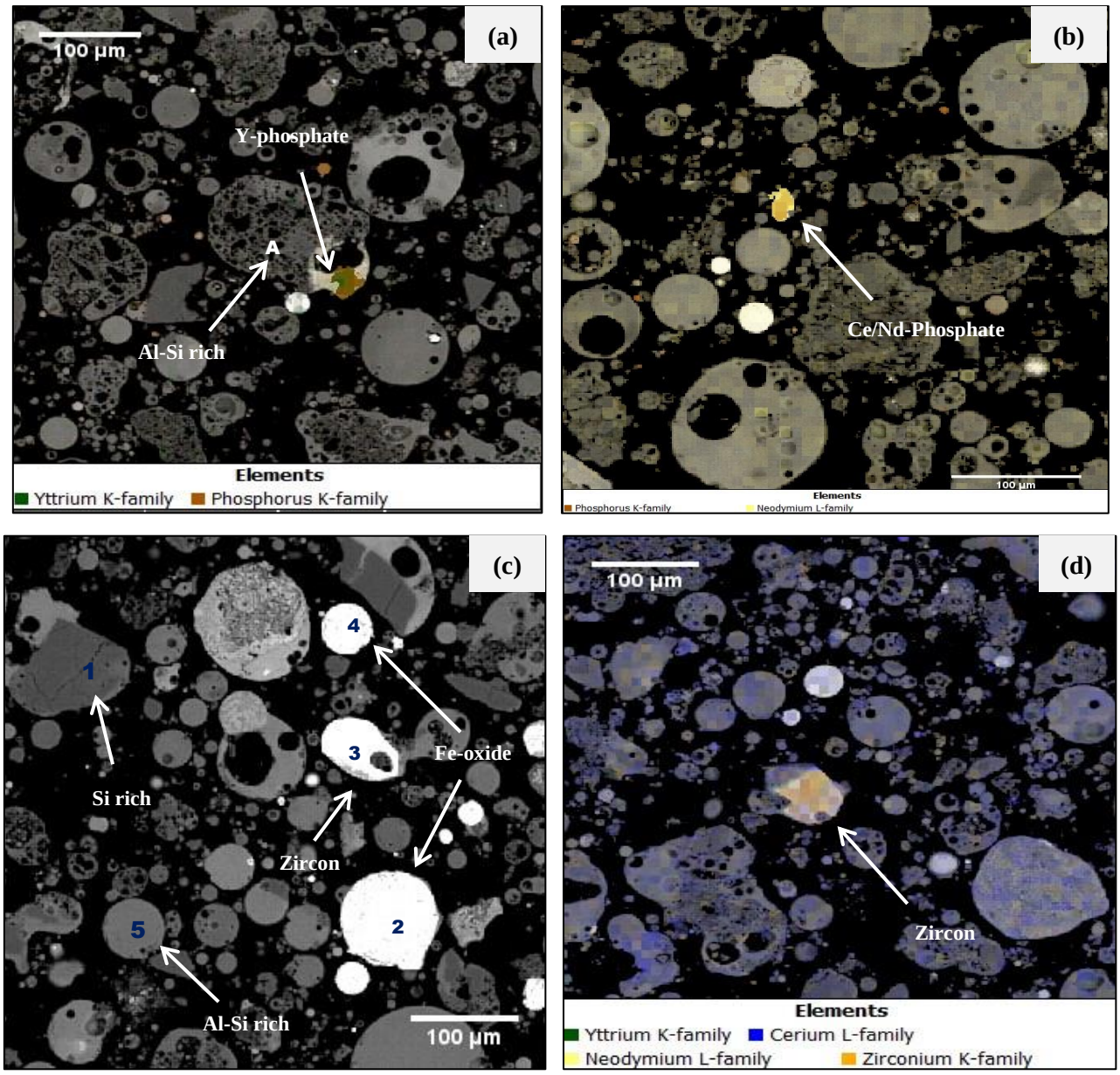

wt%	O	Zr	Si	Al	Fe	Ca	Mg	Ti	Others	Phase
1	54.71	--	43.37	1.93	--	--	--	--	--	**Si-rich**
2	33.10	--	3.21	2.38	60.65	0.29	--	--	--	**Fe-rich**
3	35.19	40.27	18.17	3.22	1.06	2.10	--	--	--	**Zr-rich**
4	31.57	--	2.85	2.26	62.83	0.52	--	--	--	**Fe-rich**
5	47.01	--	23.84	13.67	0.13	10.74	4.41	0.21	--	**Al-Si-rich**

Figure 4.6: Elemental maps showing the distribution of REE-bearing grains from raw CFA and a semi-quantitative phase chemistry of selected grians in micrograph C.

The overall findings of this study are consistent with the existing literature on the occurrence of REEs in CFA (Hower et al., 2013; Kolker et al., 2017; Hower et al., 2019; Wu et al., 2022). Liu et al. (2019) used SEM-EDS and μXANES techniques and observed that in CFA, the LREEs are mostly found in monazite, while the HREEs are present in xenotime and zircon. This study also observed a similar trend for the REE-phosphates (monazite/xenotime). However, in this study, zircon (REE-silicate) was found to contain both LREEs and HREEs.

4.2.2 Iron recovery from raw CFA by dry magnetic separation

In the above section, iron was quantified in the Al-Si-rich grains and as discrete grains. Therefore, MS was considered to recover discrete Fe-oxide grains. Dry MS was carried out using the induced roll magnetic separator (IRS) shown in **Figure 3.3** of **Chapter 3**. In the IRS process, the feed material is fed into the vibrating feed hopper, passed through the induced roller, and collected as fractions of magnetic (MF) and non-magnetic (non-MF) components as shown in **Figure 4.7.** In this study, the magnetic fraction (MF) was collected on the adjustable pole piece, whereas the non-magnetic fraction (non-MF) was collected at the bottom using pans. A detailed experimental procedure and the operating instrumental parameters are discussed in **Section 3.3.2** of **Chapter 3**. This section discusses the effect of the magnetic field intensity and the characterisation of the magnetic fraction.

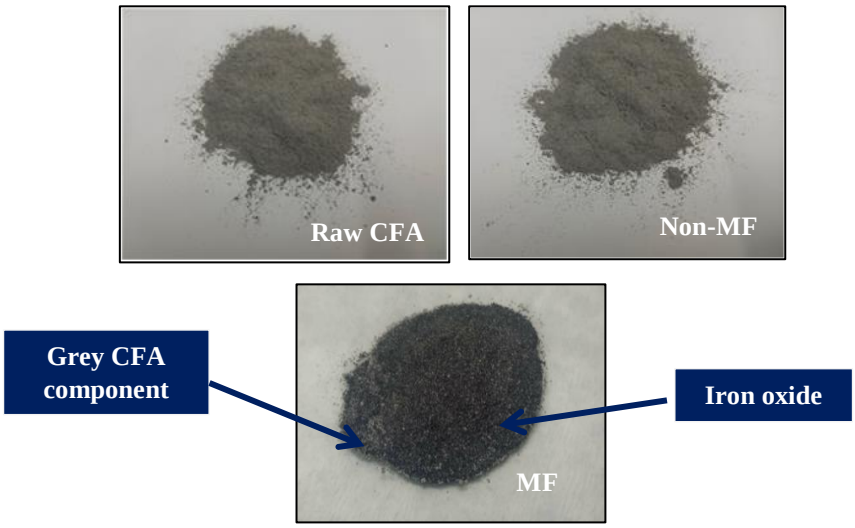

Figure 4.7: Raw CFA and the recovered fractions (MF and non-MF, 1: 100) after magnetic separation.

4.2.2.1 Effect of magnetic field intensity

The effect of magnetic field intensity on Fe-oxide recovery is presented in **Figure 4.8**. The results show that Fe-oxide recovery increases with an increase in the induced current. Therefore, a maximum recovery of 65.9% can be achieved at 1.05 T. Valeev and colleagues investigated wet and dry MS to recover magnetite from Omsk CFA (Valeev et al., 2019). In wet MS, a maximum of 73.16% Fe-oxide was recovered at 0.11 T with 26.58% Al_2O_3 and 23.17% SiO_2 impurities. The maximum Fe-oxide recovery in the dry MS was approximately the same (~73%). However, the alumina and silica impurities were 5% higher; thus, in their study, wet MS was chosen as the best technique (Valeev et al., 2019). In this study, the impurities of alumina and silica were also quantified and will be discussed further in the following sections. It is also noteworthy that, as established in **Section 2.5.1**, **Chapter 2**, the recovery of Fe in CFA can be achieved using various MS techniques for high Fe recovery or low impurities. Therefore, for the purpose of this study, the maximum recovery obtained at 1.05 T was sufficient.

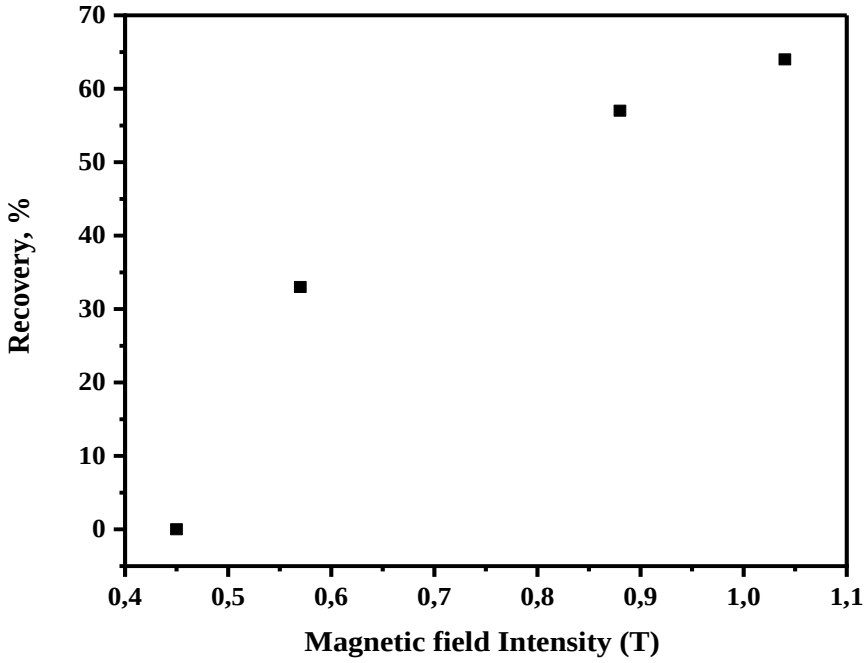

Figure 4.8: The effect of magnetic field intensity on Fe recovery from raw CFA.

4.2.2.2 Magnetic fraction characterisation

In this section, the extracted CFA magnetic fraction (CFA-MF) at 1.05 T, was further characterised and compared with the raw CFA composition.

Phase Composition Analysis

The XRD patterns for raw CFA and CFA-MF are reported in **Figure 4.9**. In **Section 2.5.1** of **Chapter 2**, it was reviewed that mullite and quartz (including the amorphous component) are the diamagnetic components in CFA, while magnetite/haematite are the magnetic components. However, as shown in the figure, quartz and mullite phases were co-extracted with magnetite/haematite in the magnetic fraction. Shoumkova (2011) reported that a level of mullite and quartz impurities is anticipated during magnetic separation due to the agglomerated particles of CFA. The agglomeration of CFA particles was also observed in this study (see **Figure 4.10 (a)** and **(b)**). This observation has also been reported in both wet and dry magnetic separations by other researchers (Valeev et al., 2019; Strzałkowska, 2021; Cornelius et al., 2021).

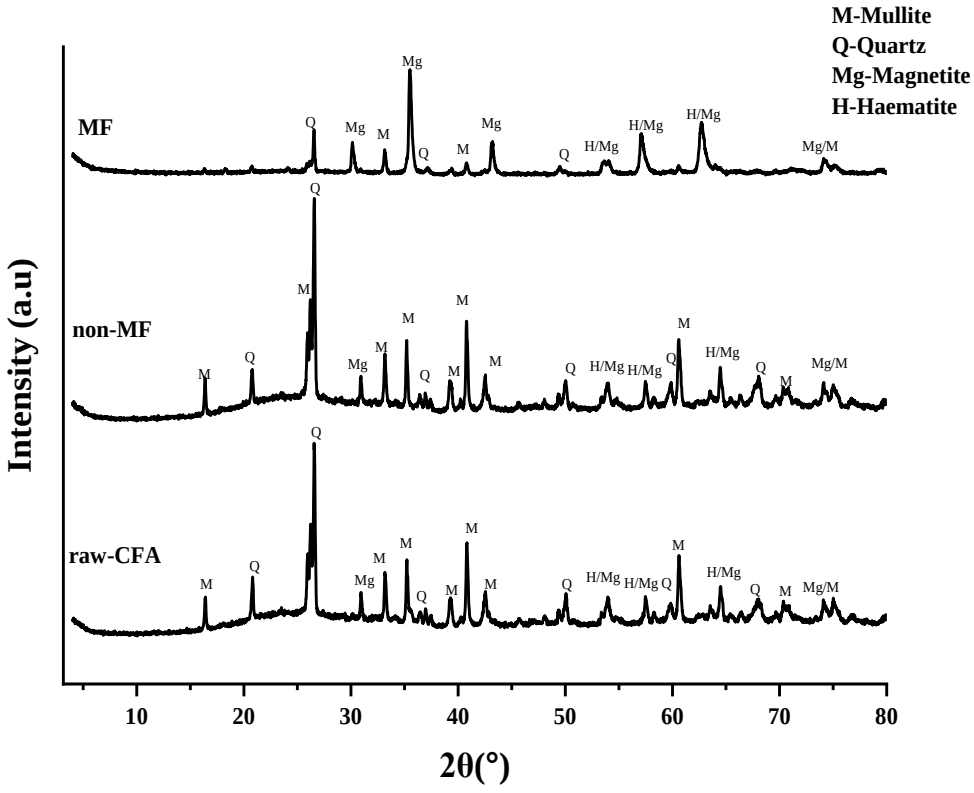

Figure 4.9: XRD patterns of raw CFA and CFA magnetic fractions (MF and non-MF).

Chemical Composition Analysis

Further analysis was conducted by XRF, and the results are presented in **Table 4.3**. The high concentration of Fe-oxide in CFA-MF concurred with magnetite/haematite as the major component of the magnetic fraction. The results also showed high silica and alumina co-extraction due to the presence of mullite, quartz, and amorphous components. Valeev et al. (2019) reported that magnetite is a solid solution between FeO and Fe_2O_3, with a spinel structure that can accommodate atoms such as calcium, magnesium, and manganese. Therefore, these elements are often quantified in the magnetic component with Fe-oxide. Similar impurities of Ca, Mg, and Mn were also quantified in this study (see **Table 4.3**), suggesting that they could be a result of the spinel effect and the co-extracted phases (i.e. mullite and amorphous) that contain these elements as a solid solution. Lastly, in this study, Ti was found to be associated with the Al-Si-rich phase and the Fe-oxide phase (see **Figure 4.5**). Consequently, high concentrations of Ti were also observed in the CFA-MF.

Table 4.3: XRF analysis of the major chemical compositions in raw CFA, non-MF and MF

wt. %	SiO_2	Al_2O_3	CaO	FeO	Fe_2O_3	TiO_2	MgO	MnO	Na_2O	K_2O	P_2O_5	LOI
CFA	56.32	28.82	5.85	0.23	4.11	1.70	1.53	0.06	0.26	0.84	0.60	2.6
Non-MF	54.9	29.2	5.44	0.022	1.73	1.59	1.64	0.035	0.18	0.76	0.76	2.7
MF	33.0	19.1	2.9	0.20	36.4	1.4	0.9	0.038	0.26	0.60	0.60	0.8

The distribution of REEs during magnetic separation is also reported in **Table 4.4**. The REEs were also quantified in the CFA-MF component, with a total concentration of 158.5 mg/kg. Magnetic separation is reported as an alternative pre-concentration method for upgrading REEs from CFA (Lin et al., 2018; Rosita et al., 2020; Cornelius et al., 2021; Pan et al., 2020; Li et al., 2023). As a result, the enrichment factor (EF value) was also calculated in this study using **Equation 3.1** (see **Section 3.3.2**, **Chapter 3**) and the EF values in the non-MF ranged between 0.69 and 1.59. Cornelius et al. (2021) also quantified low EF values of REEs, which were between 0.6 and 1.0, using a wet magnetic separation technique. The results observed in this study also support the observation by Rybak and Rybak (2021), which suggests that while MS can be used as a pre-concentration method, the EF value of MS alone is relatively low. Therefore, a combination of more than one pre-concentration technique could be an effective alternative option.

Table 4.4: The REE concentrations and enrichment factors after magnetic separation

Analyte	Concentration, mg/kg				
	CFA	**Non - MF**	**EF**	**CFA-MF**	**EF**
Sc	25.7	31.4	1.22	14.2	0.55
Y	49.3	65.9	1.34	28.6	0.58
La	92	82.1	0.89	35.3	0.38
Ce	99.07	155.1	1.57	66.7	0.67
Pr	26.2	22.2	0.85	9.6	0.37
Nd	52.8	76.7	1.45	33.4	0.63
Sm	14.2	15.8	1.11	7.0	0.49
Eu	3.01	2.8	0.93	1.2	0.40
Gd	9.82	12.0	1.22	5.2	0.53
Tb	2.74	1.9	0.69	<1	-
Dy	13.3	13.8	1.04	6.1	0.46
Ho	3.14	2.3	0.73	1.0	0.32
Er	4.78	**7.6**	1.59	**3.4**	0.71
Tm	1.31	**1.2**	0.92	**<1**	--
Yb	5.64	**6.7**	1.19	**3.0**	0.53
Lu	1.53	**<1**	--	**<1**	--
Total (LREEs)	**297.1**	**366.8**		**158.5**	
Total (HREEs)	**81.74**	**90.9**		**39.2**	
Total (REEs)	**404.54**	**560.8**		**241.7**	

--Not available

In this study, no REEs were associated with the Fe-oxide (magnetite/haematite) component during phase composition analysis in **Section 4.2.1.3**. However, REEs appeared to be associated with the Al-Si-rich grains, which were co-extracted as impurities during MS and also occurred as discrete grains (phosphates and silicates). It was also reviewed in **Section 2.4.1.2** of this study that REE-phosphate minerals such as monazite are magnetic and therefore are often separated from gangue minerals by MS. As such, in this study, it could not be concluded whether the extracted REEs resulted from the Al-Si-rich grains or discrete REE-bearing grains such as monazite, which are magnetic. However, a thorough mineralogical analysis can be conducted to gain a better understanding of this phenomenon, which was beyond the scope of this study.

Surface Morphology and Particle Size Distribution Analysis

The surface morphologies of raw CFA and extracted CFA-MF were determined by SEM, and the analysis is reported in **Figure 4.10**. In **Figure 4.10 (a)** and **(b)**, raw CFA predominantly consisted of spherical and irregular non-spherical particles. The Al-Si-rich particles were dominant, and this observation was consistent with SEM-EDS and TIMA analysis on the polished blocks in **Figure 4.3** and **Figure 4.5**, respectively. It was also observed in the figures below that the raw CFA particles were of various sizes and mostly occurred agglomerated. These morphologies of raw CFA align with other studies conducted on South African CFA (Cornelius et al., 2021; Ndlovu et al., 2023). The morphology of CFA-MF is presented in **Figure 4.10 (d)** and **(e)**. Similar to raw CFA, the particles in CFA-MF were spherical and had various sizes. The Fe-oxide particles in CFA-MF were distinguished by their rough surface texture, which appeared to have smaller particles agglomerated on the surface (see **Figure 4.10 (c)**, **(e)**, and **(f)**). Czech (2022) also studied the morphology of magnetic Fe-oxides from CFA and observed a similar rough surface with small flakes on the "mother" particles. Valeev et al. (2019) reported that the surface of these particles can also have star-like surfaces with 4-6 rays and hexagonal bulk agglomerates. Overall, the rough surface texture of the Fe-oxide particles can be easily distinguished from the smooth Al-Si particles. More analysis of raw CFA and CFA-MF particles is reported in **Figure B.2 (Appendix B)**.

The particle sizes of various CFA-MF spheres were also measured using ImageJ software on the SEM micrograph, and the analysis is reported in **Figure 4.11**. The CFA-MF spheres had sizes ranging from 2 µm to 75 µm, but they were predominantly smaller than 5 µm. The raw CFA showed more variation in particle sizes, ranging between 2 µm and 350 µm, with an average size of 55 µm. According to Chen et al. (2016), fine particles of CFA-MF have higher surface energy and disperse well in water. Therefore, they can be beneficial as seeding material. CFA-MF is characterised as a spherical component with diverse particle size distribution. Consequently, the material was further pursued as potential seeding material and further studies are discussed in **Chapter 6**. The non-MF fraction was further processed for the leaching studies, as detailed in **Section 4.2.3** and **4.2.4**.

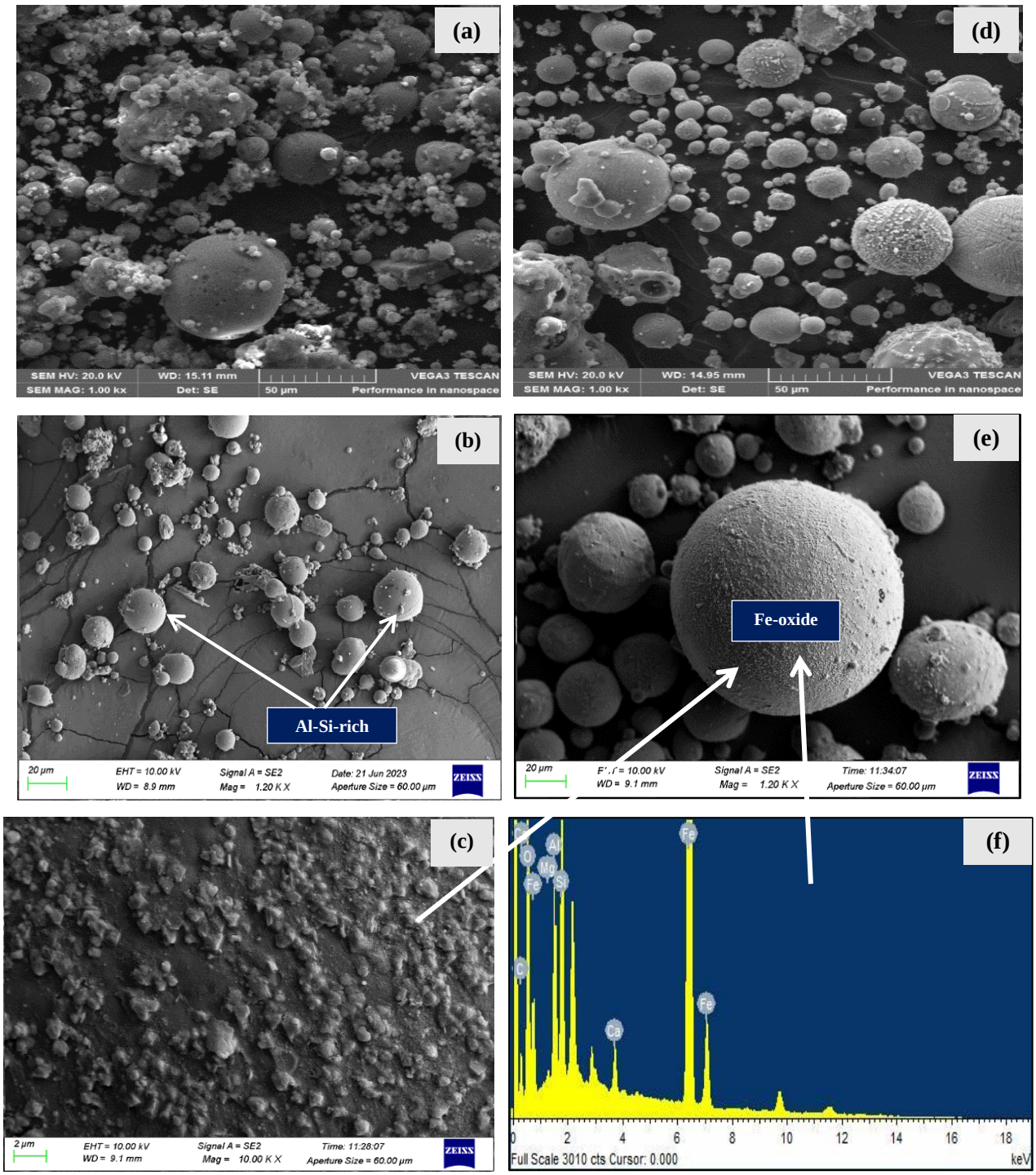

Figure 4.10: Morphological analysis of (a-b) raw CFA and (c-e) CFA-MF showing spherical particles with (f) EDS analysis of CFA-MF.

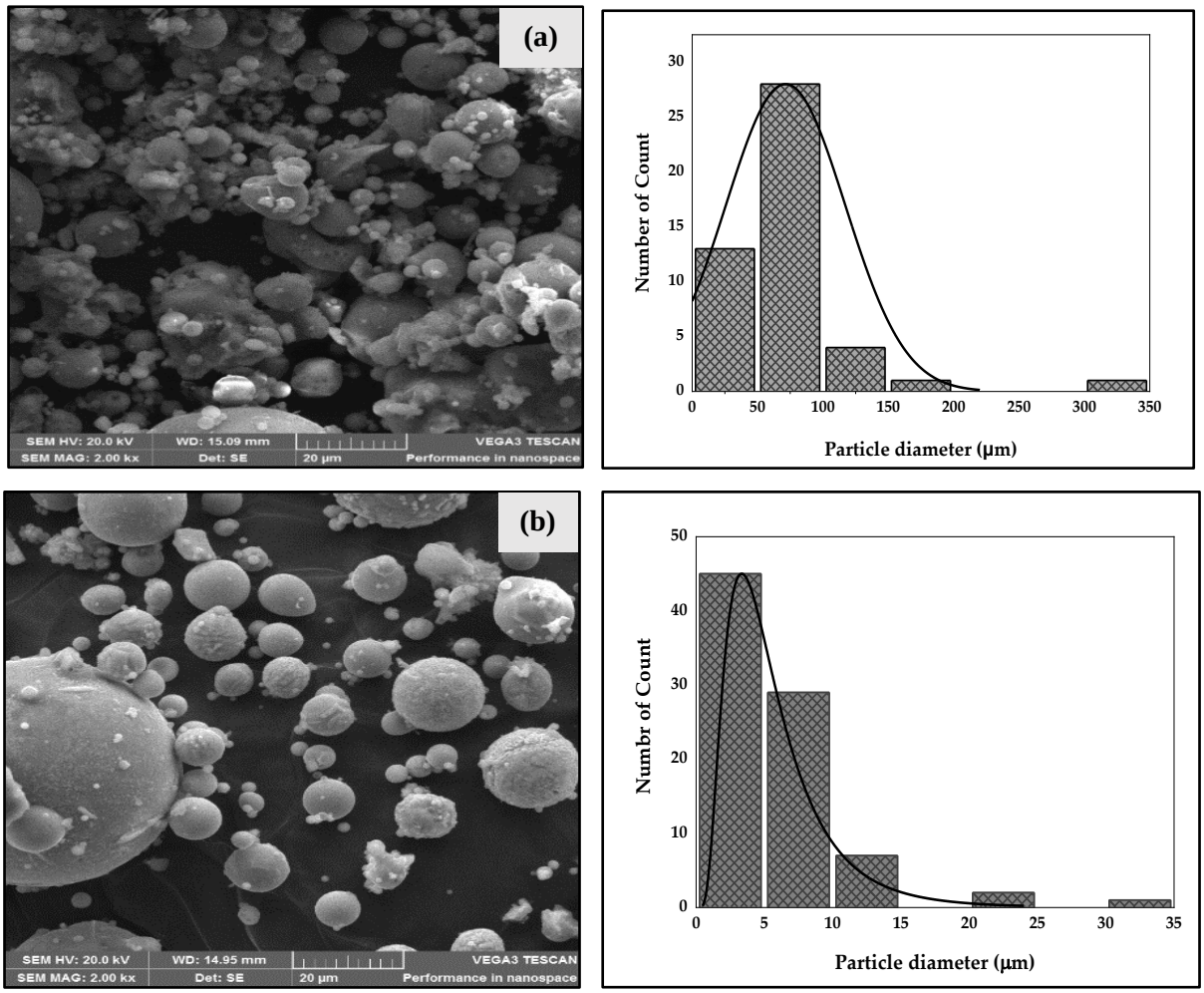

Figure 4.11: SEM images with corresponding PSD analysis for (a) raw CFA and (b) CFA-MF.

4.2.3 Pelletisation and sintering

In **Section 4.2.1.3**, it was established that alumina is mostly distributed in the refractory mullite. Therefore, sintering was considered as a pre-treatment method. The non-MF was used as a CFA resource while calcium carbonate was used as a source of lime to decompose mullite according to **Equation 4.1**. Coal with a fixed carbon content of 54.3% (see **Figure B.3**) was used for uniform heat transformation of the mullite to plagioclase/anorthite, as shown in **Equation 4.2**. The effect of sintering at different ratios (Coal: CFA: $CaCO_3$) is also presented in **Table 4.5** (see **Figure B.4** for XRD patterns). It can be seen in the table that the mullite was significantly transformed into a calcium aluminosilicate in all ratios investigated. The maximum transformation of 77.74% was observed at a ratio of 4:4:2 (56.9% anorthite), and this ratio was further used in the leaching experiments. These results were also consistent

with those obtained by Shemi et al. (2015). In their study, a CFA residue obtained after direct acid leaching of raw CFA was sintered at a ratio of 5:4:1, and 75.0% of mullite was transformed into plagioclase.

$$CaCO_3 \rightarrow CaO + CO_2 \quad \textbf{4.1}$$

$$3Al_2O_3 \cdot 2SiO_2 + 3CaO + 4SiO_2 \xrightarrow{1100℃} 3(CaO \cdot Al_2O_3 \cdot 2SiO_2) \quad \textbf{4.2}$$

Table 4.5: Phase composition analysis of CFA and sintered CFA at different ratios

CFA Phase	Chemical Formulae	Composition, wt.%			
		CFA	Sintered CFA		
		--	4:4:2	5:4:1	5:3:2
Amorphous	--	54.7	33.5	35.5	37.2
Quartz	Quartz	14.7	3.1	5.5	2.4
Calcite	$CaCO_3$	--	0.6	0.0	0.1
Mullite	$Al_6Si_2O_{13}$	29.2	0.2	6.5	0
Anorthite	$CaAl_6Si_2O_{14}$	--	56.9	48.7	53.0

--Not available

4.2.3.1 Surface morphology and particle size distribution analysis

The results presented in **Figure 4.12** show the PSD analysis and morphologies of the non-MF and sintered CFA. SEM-EDS analysis was carried out to observe the surface transformation of CFA before and after sintering, and the micrographs are reported in **Figure 4.12 (b)** and **(c)**. Based on the morphologies, most of the spherical CFA particles were transformed into non-spherical components during the sintering process (see EDS spectra in **Figure B.5**). Therefore, these results confirmed that a reaction took place during sintering. The PSD of the sintered CFA was also analysed and compared to the non-MF, as shown in **Figure 4.12 (a)** and **(b)**. Before sintering, the non-MF had a diameter size of less than 8.87 µm with 50% below 18.90 µm and 90% below 48.29 µm. After sintering, the d_{90}, d_{50}, and d_{10} shifted from the initial values to 5.48 µm, 16.2 µm, and 36.46 µm, respectively. Overall, the results

demonstrated that the sintered CFA was pulverised similar to non-MF. Consequently, both samples were further used in the leaching stage (see **Section 4.2.4**).

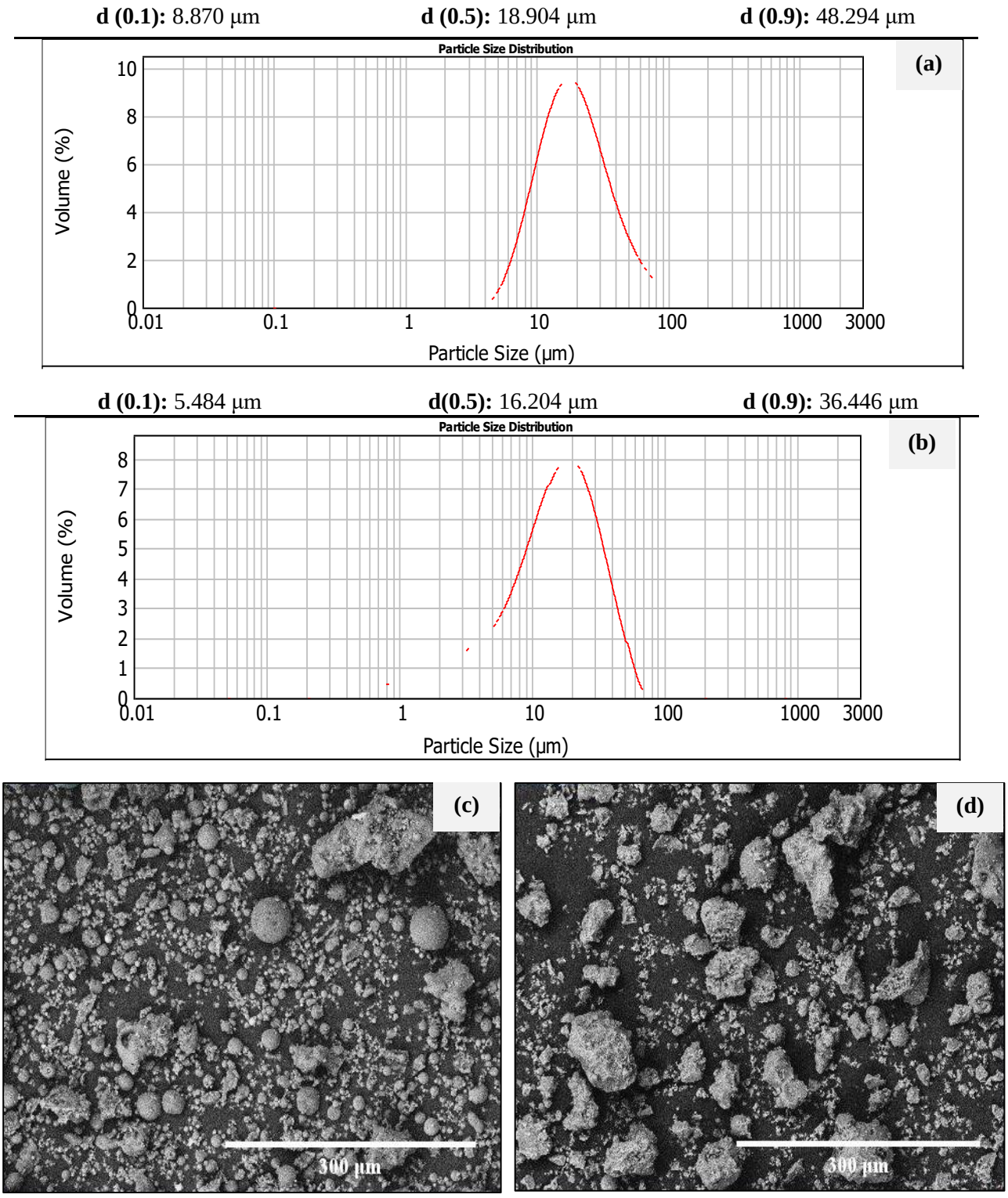

Figure 4.12: Particle size distribution of (a) CFA non-MF and (b) sintered CFA with SEM images of (c) CFA non-MF and (d) sintered CFA.

4.2.3.2 Chemical composition analysis

The thermal pre-treatment of CFA, which involves calcination and roasting, has also been reviewed in **Section 2.5.3** of **Chapter 2** as an alternative to improving the leaching efficiency of REEs. Therefore, given that sintering was used in this study, it was imperative to analyse the composition of coal and sintered CFA. It is worth noting that coal, which is primarily used as a source of heat transformation in the sintering process, is also reviewed as an REE resource (Dai et al., 2014; Lin et al., 2018). Therefore, both coal and sintered CFA were analysed for REEs, and the results are presented in **Table 4.6**. The analysis in the table revealed that coal also contains a substantial concentration of REEs (78.14 mg/kg). However, compared to the raw CFA in **Figure 4.2** of **Section 4.2.1**, the concentrations in coal were low. The combination of coal and CFA (non-MF) in the sintering process gave a total concentration of 455.13 mg/kg REEs, which suggested that both coal and non-MF could be used as resources for the extraction of REEs from sintered CFA.

Table 4.6: ICP-MS analysis of REEs in coal and sintered CFA

Analyte	**Concentration, mg/kg**	
	Coal	**Sintered - CFA**
Sc	6.46	36.5
Y	21.2	88.8
La	20.1	149
Ce	32.7	103
Pr	4.13	24.2
Nd	15.6	51.3
Sm	2.91	14.8
Eu	0.6	2.86
Gd	2.1	9.97
Tb	0.59	2.71
Dy	3.8	12.8
Ho	0.79	2.99
Er	1.26	4.54
Tm	0.37	1.21
Yb	1.57	5.37
Lu	0.45	1.29
(U)	2.56	10.9
(Th)	6.8	37.2
Total (REEs)	**78.14**	**455.13**
Total (LREEs)	**30.03**	**119.71**
Total (HREEs)	**114.63**	**611.34**

The major oxides quantified in non-MF were also analysed in coal and sintered CFA, and the findings are presented in **Table 4.7**. The analysis revealed the presence of Al, Fe, and Ti in coal. However, their concentrations were significantly lower compared to sintered CFA. Therefore, for the purpose of this study, these elements were regarded as insignificant in coal. In the sintered CFA, they were relatively high, suggesting that the non-MF was a significant source of Al, Fe, and Ti.

Table 4.7: The major chemical compositions in coal and sintered CFA at 4:4:2

wt. %	SiO_2	Al_2O_3	CaO	FeO	Fe_2O_3	TiO_2	MgO	MnO	Na_2O	K_2O	P_2O_5
Coal	14.3	1.4	1.1	--	0.4	--	0.3	0.0	3.4	0.1	--
Sintered CFA	42.33	22.06	19.46	4.8	1.20	1.16	0.33	0.25	0.33	0.81	0.63

--Not available

4.2.3.3 Phase composition analysis

While the primary aim of sintering was to transform mullite, as shown in **Equation 4.1** and **4.2**, it was also imperative to monitor the transformation of REEs during this process. In **Section 4.2.1.3**, a possible occurrence of REE-bearing phases such as phosphates and silicates (i.e. zircon) was discussed. Therefore, according to Wu et al. (2007) and Manhique et al. (2003), both phases can transform into oxides and carbonates during the sintering process, as shown in **Equation 4.3** to **4.5**. This process allows for the transformation and liberation of REEs for adequate leaching.

$$2\mathrm{REEPO_{4(s)}} + 3\mathrm{CaO_{(s)}} \xrightarrow{\mathrm{C,\ 1000℃}} \mathrm{RE_2O_{3(s)}} + \mathrm{Ca_3(PO_4)_{2(s)}} \qquad \textbf{4.3}$$

$$\mathrm{ZrSiO_{4(s)}} + \mathrm{CaO_{(s)}} \xrightarrow{\mathrm{C,\ 1000℃}} \mathrm{CaZrO_{3(s)}} + \mathrm{O_{2(g)}} \qquad \textbf{4.4}$$

$$\mathrm{ZrSiO_{4(s)}} + \mathrm{CaO_{(s)}} \xrightarrow{\mathrm{C,\ 1000℃}} \mathrm{ZrO_{2(s)}} + \mathrm{CaSiO_{3(s)}} \qquad \textbf{4.5}$$

As previously observed, coal also contains REEs (see **Table 4.7**). Therefore, a possible mineralogical contribution of REEs from coal is expected in the sintered CFA. In coal deposits, REEs have been reported to be associated with both organic and mineral components and occur as xenotime, monazite, and zircon. Therefore, in the coal combustion process (CCP), organic components are combusted, resulting in CFA enriched with REEs (see **Section 2.2.2.1**, **Chapter 2**). REE-bearing minerals such as xenotime, monazite, and zircon are also reported to be stable during CCP (~1000℃); thus, they are concentrated in CFA and are distributed within the Al-Si-rich grains or occur as discrete minerals (Harrar et al., 2022; Fu et al., 2022). Nonetheless, while a detailed knowledge of the distribution of REEs in coal and during CCP is fundamental, the mineralogical analysis of coal was beyond the scope of this study. As a result, only the sintered CFA was analysed for the REEs.

Similar to raw CFA, the phase composition of the sintered CFA was analysed using SEM-EDS and TIMA. SEM micrographs and EDS analysis of specific points are presented in **Figure 4.13**. The analysis showed that most of the spherical Al-Si-rich grains were transformed into irregular shapes. These findings are similar to the morphological analysis on the mounted stubs in **Figure 4.12**, which showed irregular spherical particles after sintering. In **Figure 4.13 (c)** to **(d)**, the Fe-oxide grains were also quantified, suggesting that the particles remained spherical with no phase transformation during the sintering process. Nonetheless, traces of REEs, Fe, Ti, and Mg were also identified in the transformed non-spherical Al-Si-rich particles.

The elemental maps showing the distribution of REEs are also presented in **Figure 4.14**. In **Figure 4.14 (c)** and **(e)**, the REE-phosphate grains were identified, suggesting that during sintering, they might have been liberated from the host grains (i.e. Al-Si-rich). However, since the phosphates were still mapped with REEs, it could not be concluded whether the REE-phosphates transformed into oxide during sintering. Literature also suggests that during the phase transformation, the REE-bearing particles will crack, as an indication of the phase transformation (Manhique et al.,2003; Wu et al., 2007; Moila et al., 2017). In this study, an indication of cracks on the REE grains was also not observed. Nonetheless, some REE grains associated with phosphates in **Figure 4.14 (c)** and **(f)** showed no mapping of the phosphate element in the grain, suggesting a possible phase transformation or liberation (i.e. REE-silicate) of the REEs during sintering.

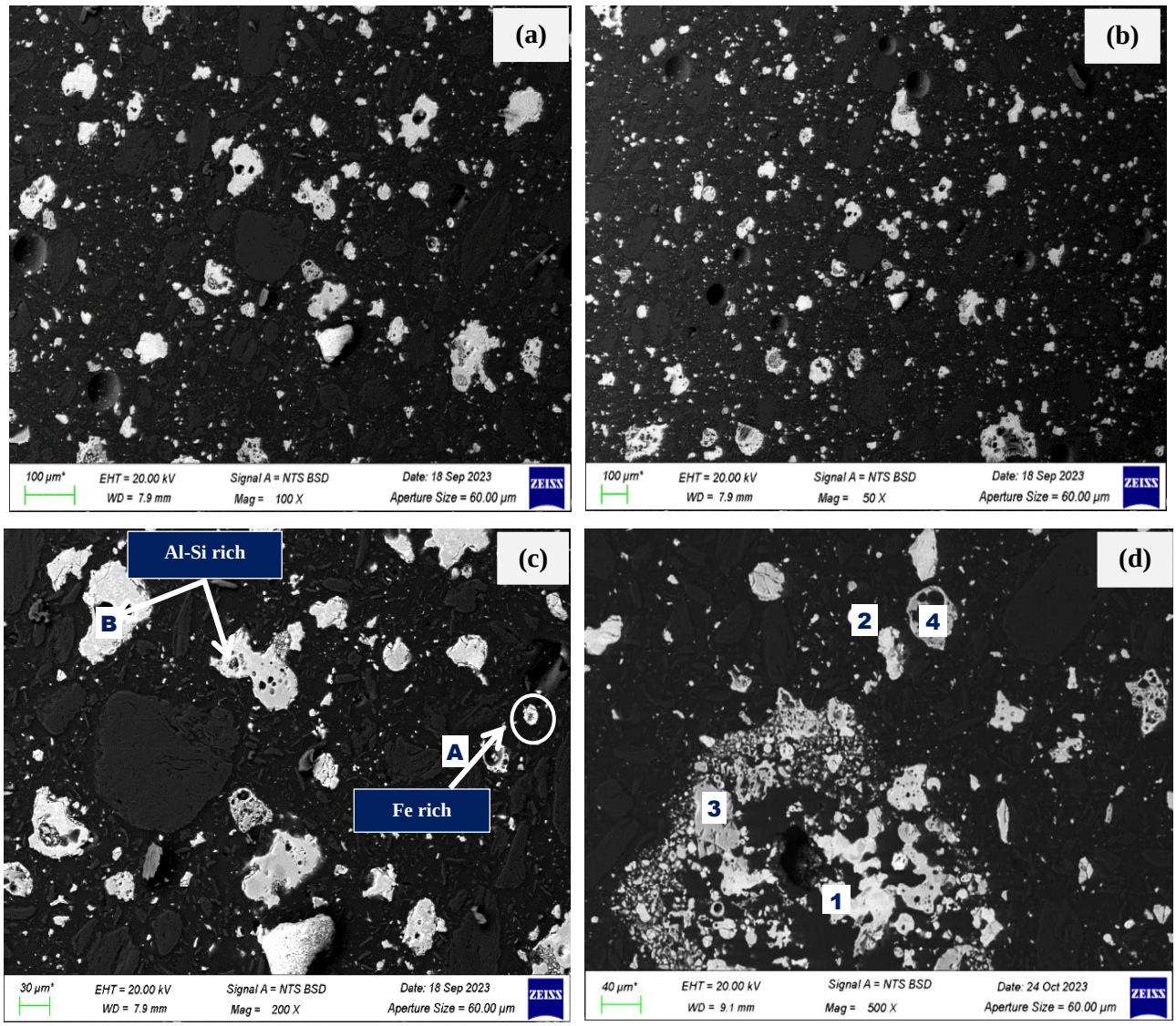

wt%	C	O	Si	Ca	Al	Ti	Fe	Sc	La	Nd	Ce	Others	Phase
(b)	73.3	18. 9	3.2	2.3	1.6	--	0.50	--	--	--	--	0.29	**Al-Si-rich**
1	--	53.0	23.6	11.3	6.5	0.57	2.50	0.02	0.07	0.05	0.06	--	**Al-Si-rich**
B	--	52.3	16.3	5.20	22.04	--	--	--	--	--	--	4.16	**Al-Si-rich**
2	8.8	38.3	--	0.6	0.44	0.09	51.83	--	--	--	--	0.47	**Fe-rich**
A	5.25	51.3	--	0.8	0.55	--	42.1	--	--	--	--	--	**Fe-rich**
3	--	56.4	44.3	--	0.02	0.04	--	0.02	0.13	--	0.17	1.45	**Si-rich**
4	77.3	21.7	0.13	--	0.08	--	--	0.02	--	0.06	--	1.01	--

Figure 4.13: SEM micrographs of sintered CFA and a semi-quantitative EDS analysis of the specific marked points.

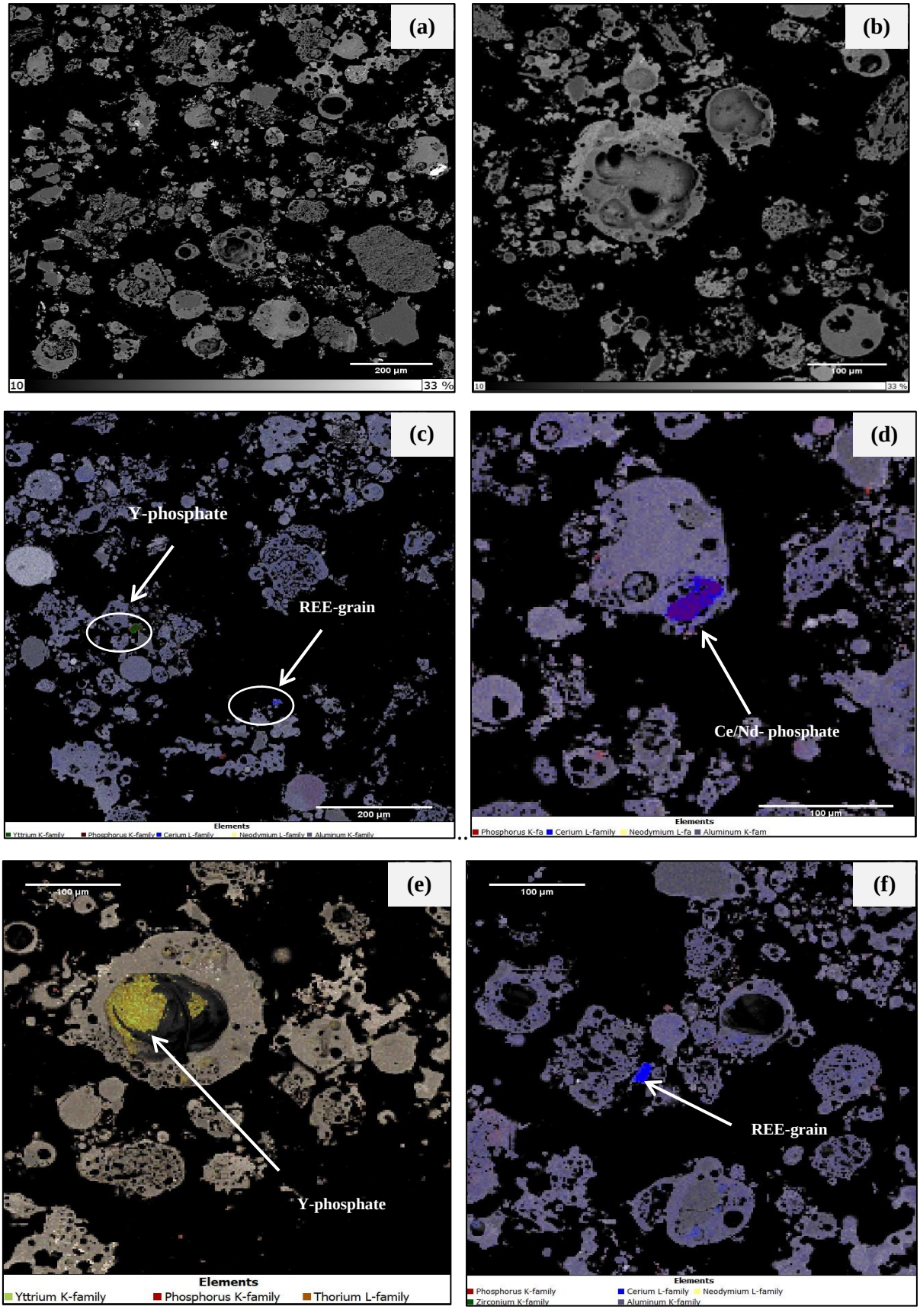

Figure 4.14: BSE images and elemental maps showing the distribution of REEs in sintered CFA.

4.2.4 Preliminary acid leaching

A preliminary investigation was carried out to understand the leaching behaviour of Al, Fe, Ti, and selected REEs (Sc, Y, Nd, Ce, and La). Therefore, the effects of H_2SO_4 and HCl are reported in this section. The experimental parameters were based on a literature survey, and thus, the effects of acid concentration, leaching temperature, and leaching time are reported. Prelimiary studies were conducted using non-MF (CFA) and sintered non-MF (sintered CFA). A detailed experimental methodology is also provided in **Section 3.3.3** of **Chapter 3**.

4.2.4.1 Effect of H_2SO_4 leaching

Sulphuric acid was reviewed in **Section 2.5.2**, **Chapter 2** as an effective leaching reagent for the dissolution of Al from CFA. However, there have been limited studies reported on the leaching behaviour of REEs in this system. Therefore, this section reports on the leaching behaviour of Al, Fe, Ti, and REEs using both direct and indirect leaching processes. The latter involves sintering as a pre-treatment method prior to leaching.

Direct Leaching

The effect of leaching temperature was first investigated using CFA, and the results are presented in **Figure 4.15**. In **Figure 4.15 (a)**, the extraction of metal sulphates, such as $Al_2(SO_4)_3$ and $Fe_2(SO_4)_3$, increases with a leaching temperature from 45 to 80°C. This could be because molecules require thermal energy at higher temperatures for an effective reaction. A similar leaching behaviour was observed by Apua (2023) in the extraction of Al and Fe from raw CFA. The extraction of the selected $REE_2(SO_4)_3$ was also observed in the solution (see **Figure 4.15 (b)**). However, similar to the major elements (i.e. Al, Fe, and Ti), the leaching efficiency remains relatively low. The possible low recoveries might result from the complex phase composition, as discussed in **Section 4.2.1.3**. The amorphous phase has been reviewed as a more soluble phase than the mullite (Al-Si) (Shemi et al., 2015; Apua 2023). Shemi et al. (2015) observed that due to the dissimilar alumina distribution, only the amorphous phase can be directly leached in acid. However, Apua (2023) observed that due to the complex amorphous composition, some Al-Si-rich phases not associated with mullite remain undissolved at low temperature and pressure conditions. Therefore, the same observation can be extended to this study, since CFA was identified by SEM-EDS and TIMA as an Al-Si-rich component. The low solubility of this phase consequently results in low Ti

and Fe dissolutions, which occur as a solid solution in the Al-Si-rich phase. The REEs also occurred as solid solutions in the Al-Si-rich phase. However, phosphates and silicates were also identified as the REE-bearing phases. These phases require pre-treatment for easy solubility (Krishnamurthy and Gupta, 2005; Moila et al., 2017).

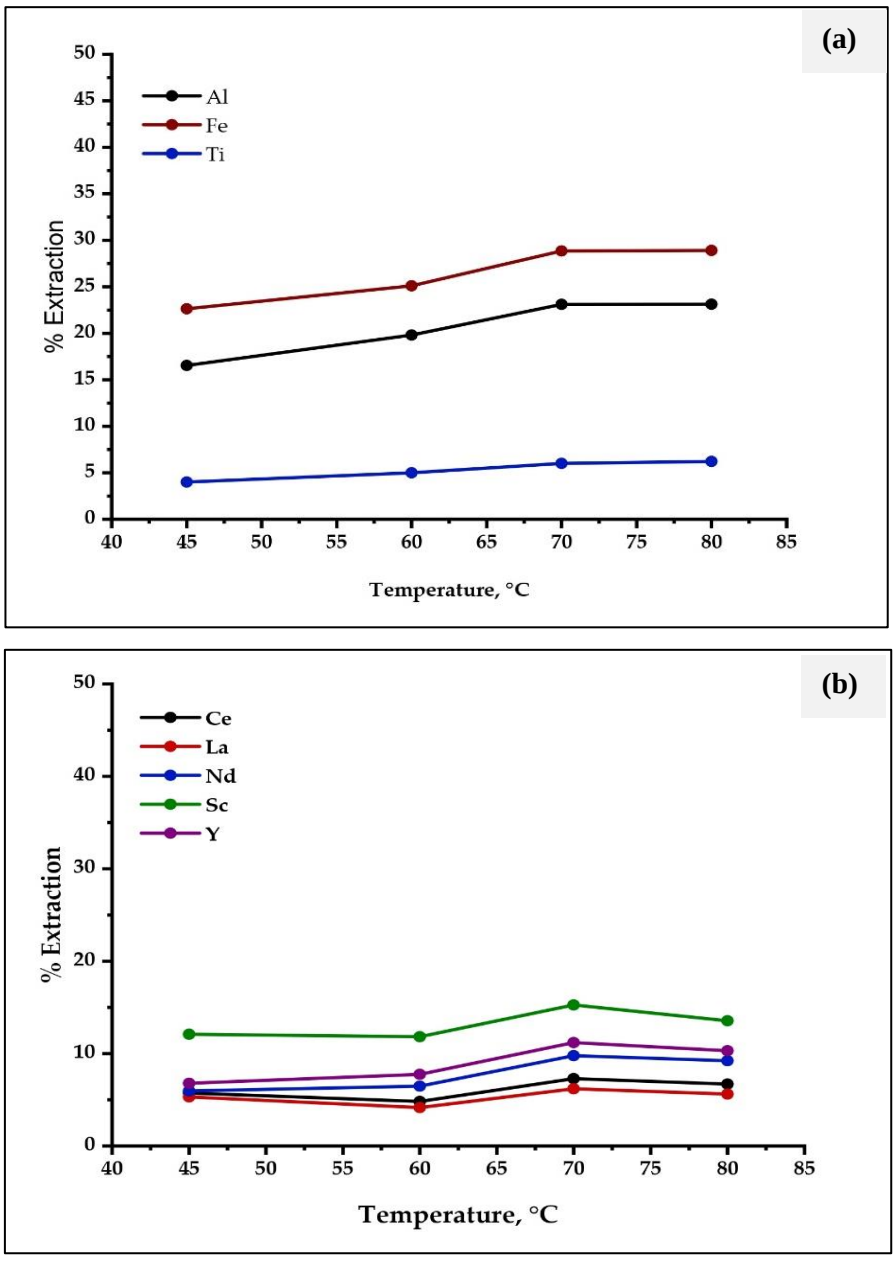

Figure 4.15: Effect of leaching temperature on the extraction of (a) major elements and (b) selected REEs from CFA at 6 M H_2SO_4, 1:4 S/L ratio leaching for 10 hours.

The effect of acid concentration was investigated from 0.5 to 6 M H_2SO_4, and the results are presented in **Figure 4.16**. The highest extraction efficiency for the major elements (Al, Fe, and Ti) was observed at 6 M H_2SO_4, with 25% Al, 19% Fe, and 7% Ti extraction. Sedres

(2016) also reported low recoveries of Ti and Fe through direct H_2SO_4 leaching at 0.5-8 M H_2SO_4. However, increasing the acid concentration to 15 M H_2SO_4 improved Al and Ti extraction to 54% and 58%, respectively. Working at such high acid concentrations allowed for the disintegration of the Al-Si-rich phase (Sedres, 2016). However, Nayak and Panda (2010) reported that concentrated H_2SO_4 is too viscous, hindering further leaching process. Consequently, these extreme conditions were not considered in this study. Nevertheless, the extraction of the selected REEs was also relatively low and did not improve by leaching at different acid concentrations (see **Figure 4.16 (b)**).

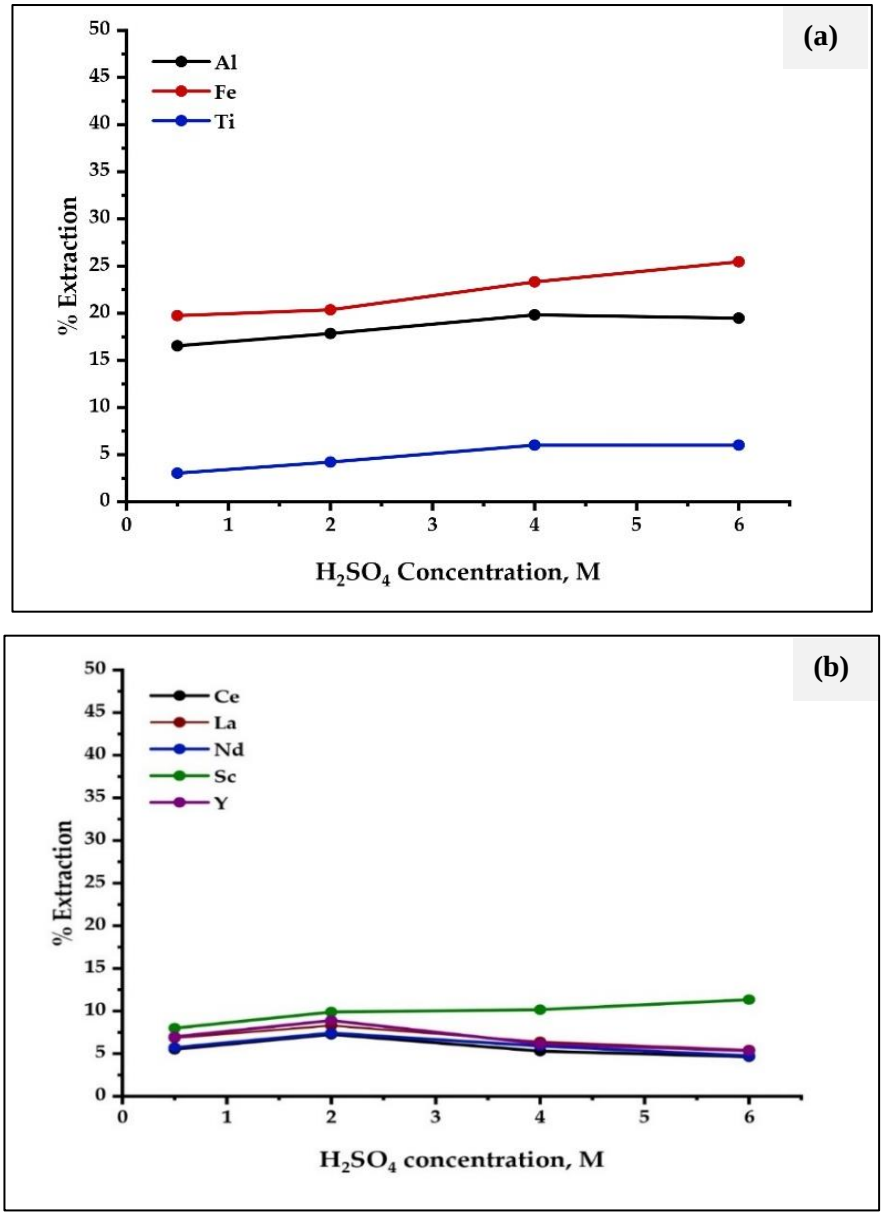

Figure 4.16: Effect of sulphuric acid concentration on the extraction of (a) major elements and (b) selected REEs from CFA at 70°C, 1:4 S/L ratio leaching for 10 hours.

The effect of leaching time on the metal sulphates is also presented in **Figure 4.17 (a)** and **(b)**. Evidently, time had no discernible effect on the extraction of the major elements and selected REEs. Seidel and Zimmels (1998) postulated that the formation of a product layer covers CFA over time and thus prevents further leaching. Therefore, no significant improvement is observed.

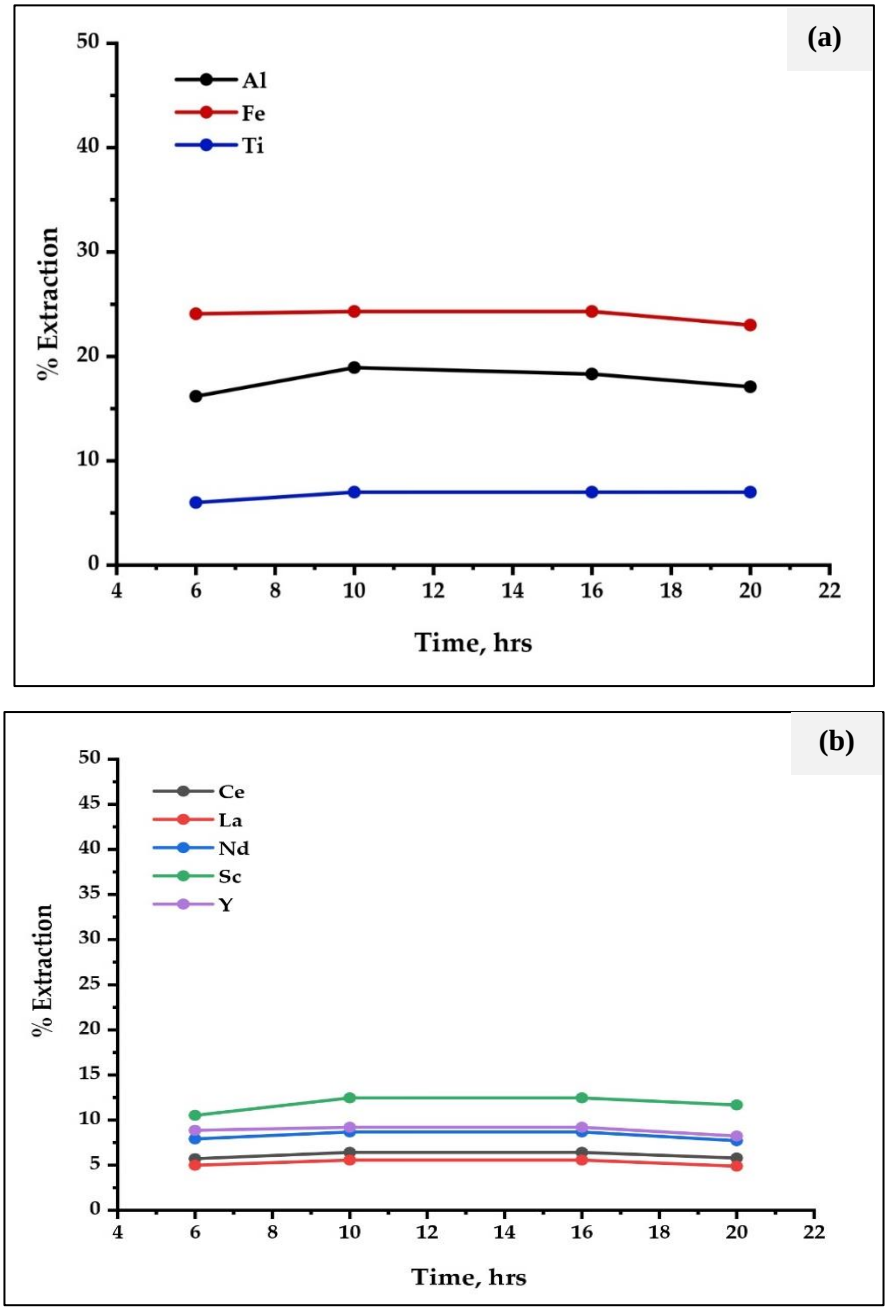

Figure 4.17: Effect of leaching time on the extraction of (a) major elements and (b) selected REEs from CFA at 6 M H_2SO_4, 1:4 S/L ratio leaching at 70°C.

In **Section 4.2.1.3**, the phase composition analysis of raw CFA showed that the material was predominantly composed of the Al-Si-rich phase, with traces of elements such as Fe, Ti, Mg, and REEs. The overall low solubility of this phase explains the low recoveries of both major and trace elements. Additionally, some REE grains (i.e. phosphates), which require pre-treatment for efficient dissolution, were also quantified, as discussed in **Section 4.2.3.3**. As a result, further leaching studies were conducted by sintering the CFA before leaching.

Indirect Leaching

The sintered CFA was further used to understand the leaching behaviour of the major elements and selected REEs. The effect of sulphuric acid concentration on sintered CFA was first investigated, and the results are reported in **Figure 4.18**. The extraction of major elements significantly improved compared to the results obtained in the direct acid leaching processes (see **Figure 4.18 (a)**). The maximum recoveries were observed at 6 M H_2SO_4 with 72.3% Al, 63.4% Fe, and 40.1% Ti extraction. These results were consistent with the findings reported by Matjie et al. (2005). The extraction of the selected REEs also increased from 0.5-2 M H_2SO_4 but declined above 2 M H_2SO_4 (see **Figure 4.18 (b)**). Kashiwakura et al. (2013) conducted research on the extraction of REEs from CFA and observed similar trends where the extraction efficiency decreased with an increase in H_2SO_4 concentration. Other researchers have also recommended that, for high REE extraction efficiency, one must operate at a lower acid concentration (<2 M H_2SO_4) (Perämäki, 2014; Peiravi et al., 2017; Ariuntuya, 2018). However, operation at low acid concentrations proved to be difficult in this study due to the formation of silica gel, which made the filtration process difficult. Additionally, although Sc is associated with REEs due to its occurrence in the same mineral ores, in this study, it was observed that the extraction of Sc increased with an increase in H_2SO_4 concentration, similar to the major elements (Al, Fe, and Ti). Phase composition analysis by SEM-EDS also detected Sc in the Al-rich phase. Therefore, altering the Al-rich phase during sintering may have also liberated Sc. Nonetheless, at 6 M H_2SO_4, a maximum Sc content of 35% was extracted.

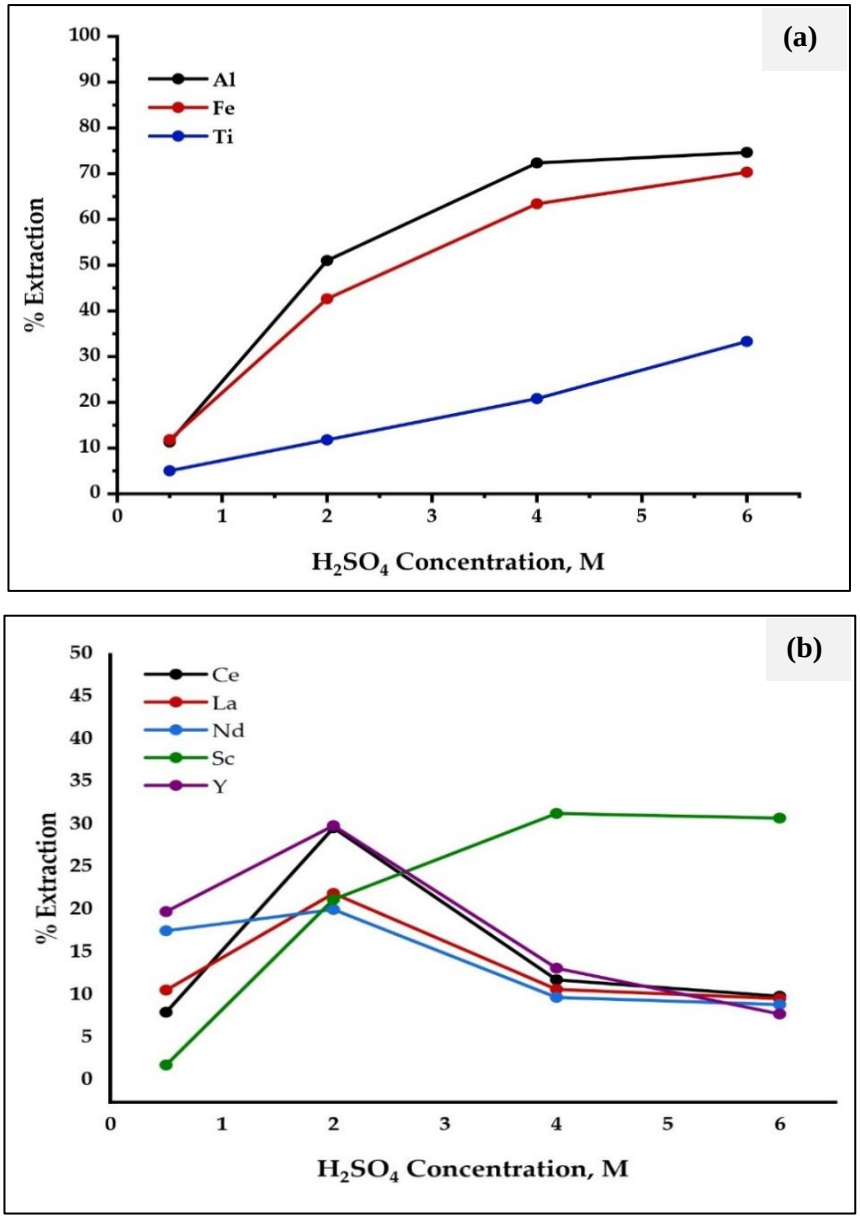

Figure 4.18: Effect of sulphuric acid concentration on the extraction of (a) major elements and (b) selected REEs from sintered CFA at 70°C, 1:4 S/L ratio leaching for 10 hours.

The effect of leaching temperature was also investigated, and the results are reported in **Figure 4.19**. Similar to the impact of acid concentration, raising the leaching temperature resulted in a higher extraction of Al, Fe, Ti, and Sc. In contrast, the extraction of REEs (Ce, La, and Nd) showed no significant increase, with less than 20% extraction. A slight drop in REE extraction was also observed at 60°C. Diwa et al. (2023) conducted research on the extraction of REEs from phosphogypsum and observed that temperature has a catalytic effect on REEs. However, a drop in REE extraction was also observed at 70°C. In their study, the drop was a result of fluoride dissolution, which subsequently reacted with REEs to form an

insoluble precipitate. A further increase in temperature to 80℃ was attributed to side reactions. In this research study, a possible explanation can be the dissolution of calcium in sulphuric acid, which results in the formation of the insoluble REE-sulphates at 60℃ (Kul et al., 2008). Stopic Srecko (2018) also reported that higher temperatures hinder the dissolution of REEs in sulphuric acid leaching since the solubility of rare earth sulphates increases as temperature decreases.

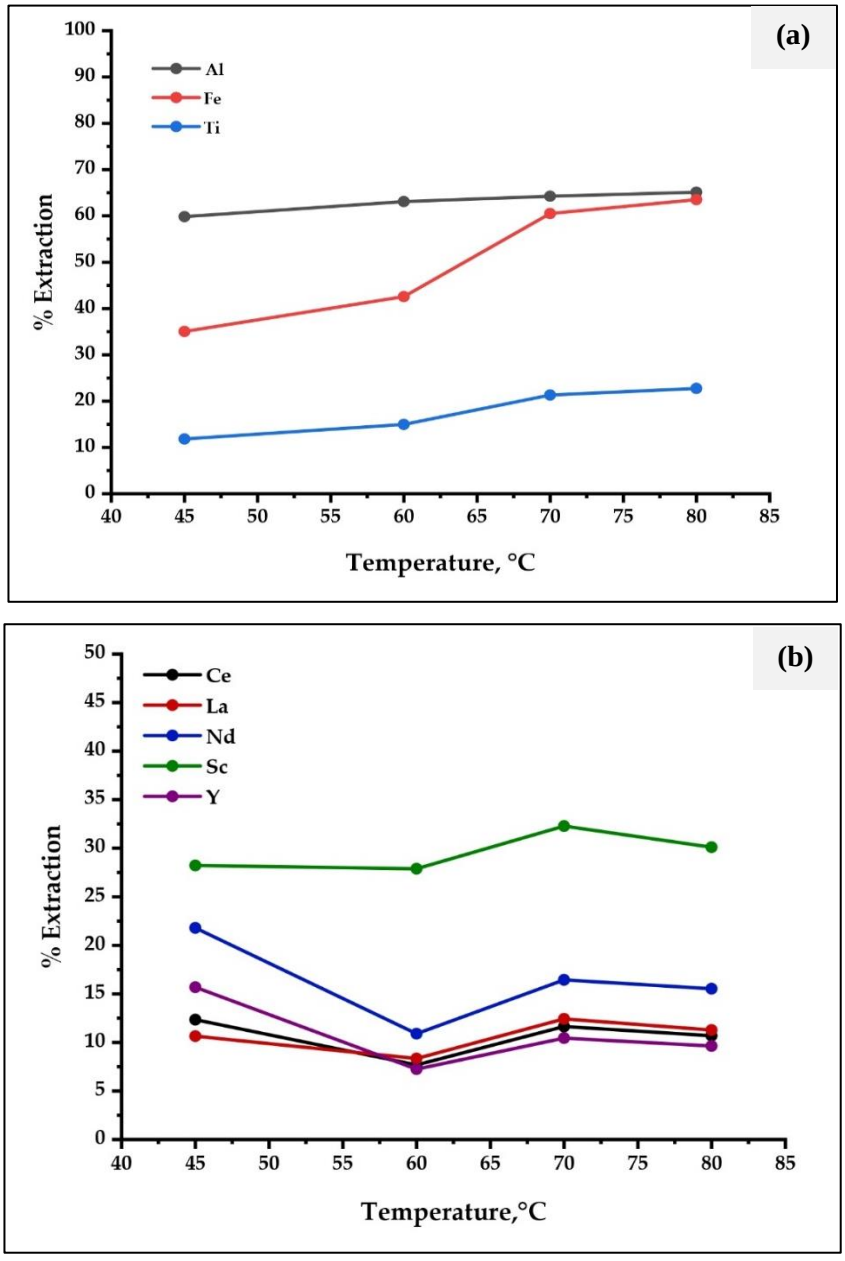

Figure 4.19: Effect of leaching temperature on the extraction of (a) major elements and (b) selected REEs from sintered CFA at 6 M H_2SO_4, 1:4 S/L ratio leaching for 10 hours.

Leaching from 6 to 15 hours showed that the extraction of Al, Fe, Ti, and Sc increases, as illustrated in **Figure 4.20 (a)** and **(b)**. However, beyond 15 hours, no improvement in the extraction efficiency was observed due to the formation of a product layer (Seidel and Zimmels, 1998; Shemi et al., 2015). The extraction of REEs (La, Nd, and Ce) remained slightly steady with no significant improvement.

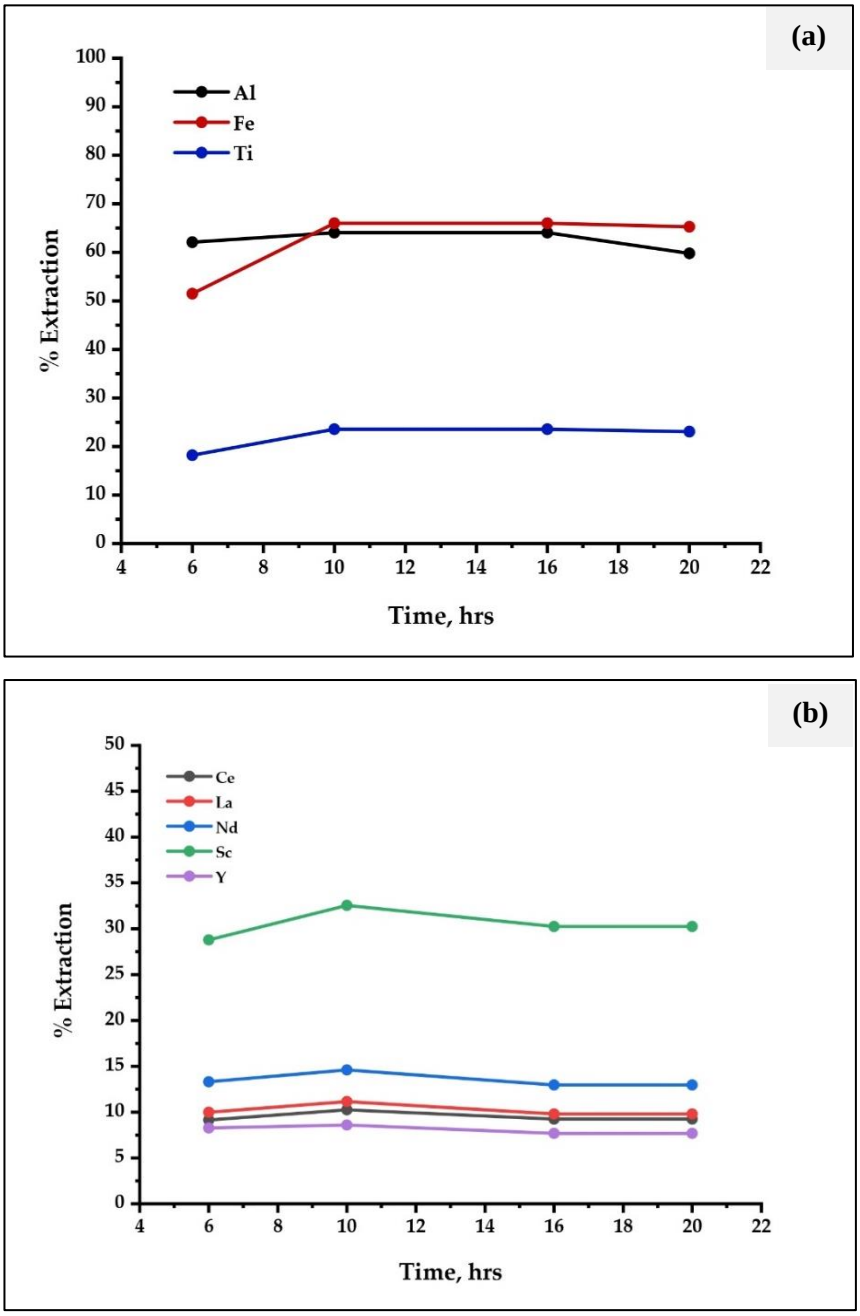

Figure 4.20: Effect of leaching time on the extraction of (a) major elements and (b) selected REEs from sintered CFA at 6 M H_2SO_4, 1:4 S/L ratio leaching at 70°C.

4.2.4.2 Effect of HCl leaching

The results obtained in the above section indicate that although CFA has a complex phase composition, sulphuric acid may not be adequate as a leaching reagent for the extraction of REEs (except for Sc), as no significant improvement was observed after sintering. According to the literature (King et al., 2018; Cao et al., 2018; Tang et al., 2019; Kumari et al., 2019; Wang et al., 2019), hydrochloric acid is considered the most effective leaching reagent for the extraction of REEs. Therefore, the effect of hydrochloric acid leaching was further investigated using sintered CFA to determine whether there would be any significant improvement in the extraction of REEs. The experimental parameters were based on a literature survey.

The effect of acid concentration was investigated using 2 to 6 M HCl in a 1:10 S/L ratio for 6 hours at 70°C. The results presented in **Figure 4.21 (a)** show that the extraction of the selected REEs was significantly improved, and increasing the HCl concentration from 2 to 4 M HCl further enhanced the extraction. However, as shown in the graph, increasing the HCl concentration to 6 M did not lead to a notable improvement in REE extraction. Therefore, the optimum extraction concentration was determined to be 4 M HCl, resulting in 51.3% Ce, 49.7% La, 57.8% Nd, and 34.2% Sc extraction. Cao et al. (2018) conducted a study using 3 M HCl leaching for 3 hours at 60°C and obtained a similar extraction efficiency. It is worth noting that in their study, CFA was used without pre-treatment. Nevertheless, the improvement in REE extraction aligns with previous research, suggesting that pre-treatment of CFA can enhance their extraction efficiency and that HCl is an effective leaching reagent (King et al., 2018; Tang et al., 2019; Wang et al., 2019).

The effect of leaching temperature was also investigated at 45°C, 60°C, and 70°C, with leaching conducted for 6 hours in a 4 M HCl solution. The results are graphically reported in **Figure 4.21 (b)**. Leaching at 70°C yielded the highest extraction with 57.8% Ce, 53.79% La, 51.29% Nd, and 57.01% Y. Chi et al. (2006) stated that in the extraction of REEs with HCl, increasing the leaching temperature enhances the leaching reaction, resulting in an exothermic reaction. Furthermore, at higher temperatures (60-90°C), HCl may have a higher diffusion rate due to the increased thermal or activation energies.

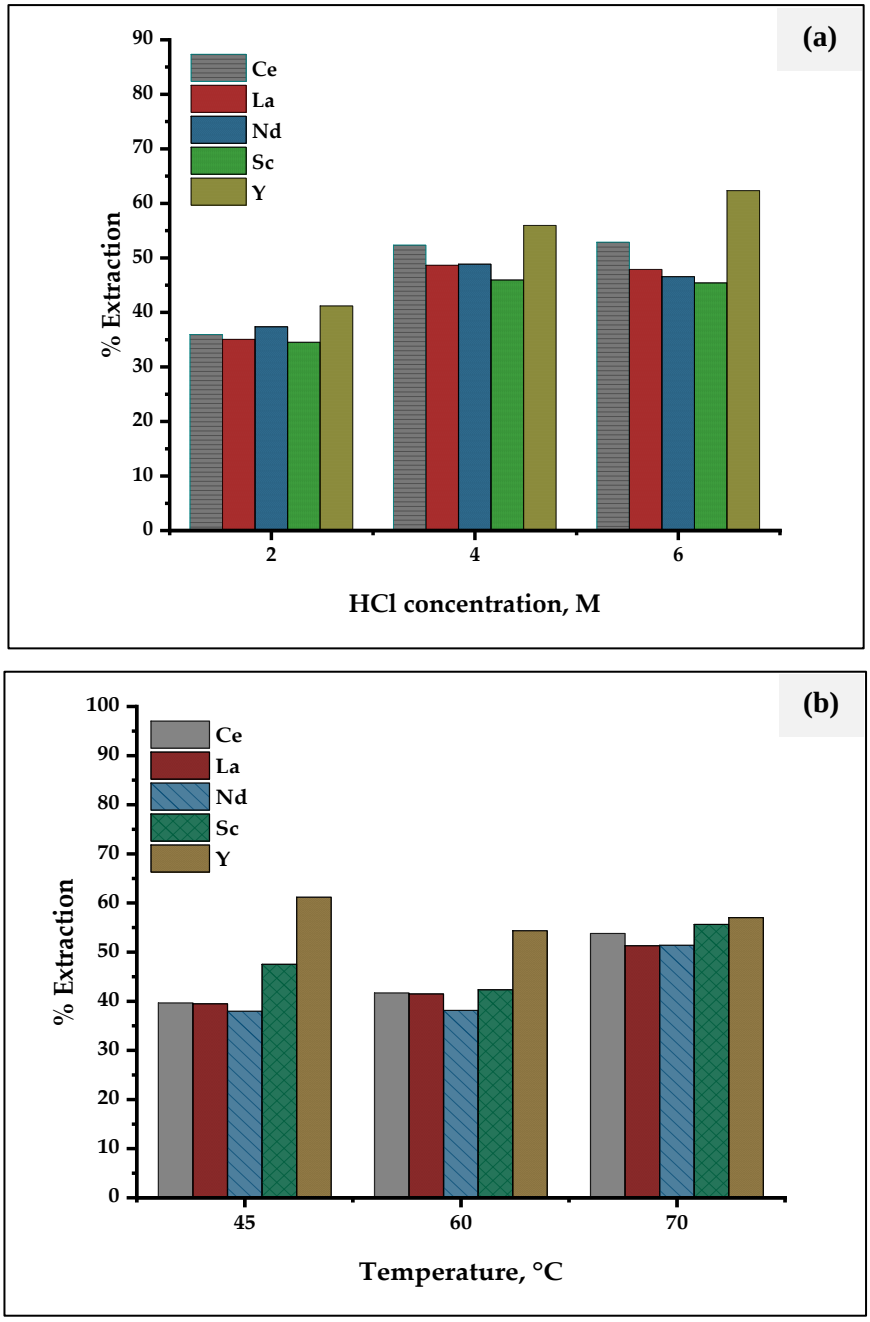

Figure 4.21: Effect of (a) acid concentration and (b) leaching temperature on the extraction of REEs from sintered CFA using HCl.

4.2.4.3 Comparison of the sinter – HCl and sinter – H_2SO_4 leaching

Considering the leaching efficiency and selectivity, H_2SO_4 is a suitable lixiviant for the extraction of Al (70%, ~8.27 g/L), Fe (63%, ~1.5 g/L), and Ti (40%, ~0.8 g/L) under optimum conditions. However, the selected REEs (except Sc) showed poor extraction in the sulphate system (15.3% Y, 12.11% La, 13.29% Ce, and 12.05% Nd). Nonetheless, a change

in the lixiviant to HCl increased the extraction of the selected REEs. **Figure 4.22** presents a graphical comparison of the selected REEs under optimum conditions in a sulphate and chloride system. In the HCl system, the extraction efficiency at maximum conditions improved to 42.9% for Ce (10.5 mg/L), 52.2% for La (4.62 mg/L), 56.01% for Nd (4.5 mg/L), and 65.1% for Y (2.45 mg/L).

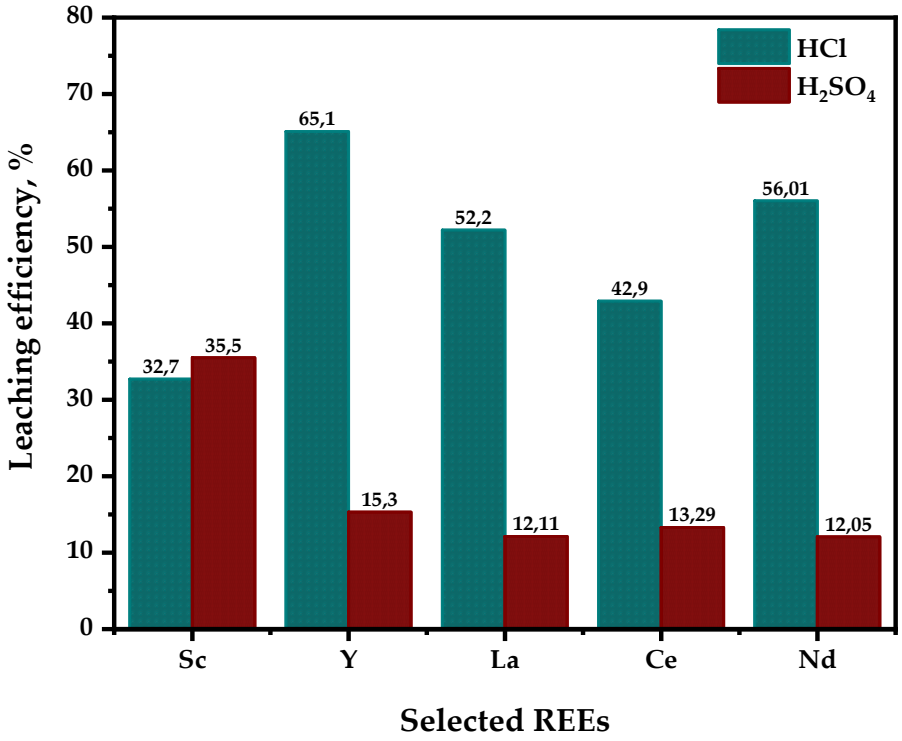

Figure 4.22: Leaching efficiency of sintered CFA using 6 M H_2SO_4 at 70°C for 10 hours and 4 M HCl at 70°C for 6 hours.

It has been established that at high acid concentrations and leaching temperatures, calcium can react with sulphates to form insoluble calcium sulphate (see **Figure 4.6** and **4.7**). This formation of calcium sulphate will consequently cause precipitation of metals such as Al, Fe, and Ti, reducing their extraction efficiency (Binnemans et al., 2015; Shemi et al., 2015; Yahorava et al., 2016). XRD analysis was further performed on the residual sintered CFA to observe any formation of calcium sulphates and the spectra are shown in **Figure 4.23**. After sulphuric acid leaching, calcium sulphate was formed as a secondary phase in both the 2 M and 6 M leached residues, and it was quantified as anhydrite. Kashiwakura et al. (2013) considered the controlling mechanism to be diffusion through the product layer. Leaching in HCl did not result in the formation of calcium sulphate due to the solubility of calcium

chloride ($CaCl_2$). In this case, Cao et al. (2018) reported a chemical reaction as the controlling mechanism, as the diffusion of hydrogen ions was kinetically fast. This is a result of the soluble calcium chloride, which does not result in the formation of the unwanted product layer.

$$Ca(OH)_2 + 2H^+ + SO_4^{2-} \rightarrow CaSO_4 + 2H^+ + 2OH^- \quad \textbf{4.6}$$

$$CaSO_4 + M_2(SO_4)_3 \rightarrow CaSO_4M_2(SO_4)_{3(s)} \quad \textbf{4.7}$$

where M=Al, Fe, Ti and REEs

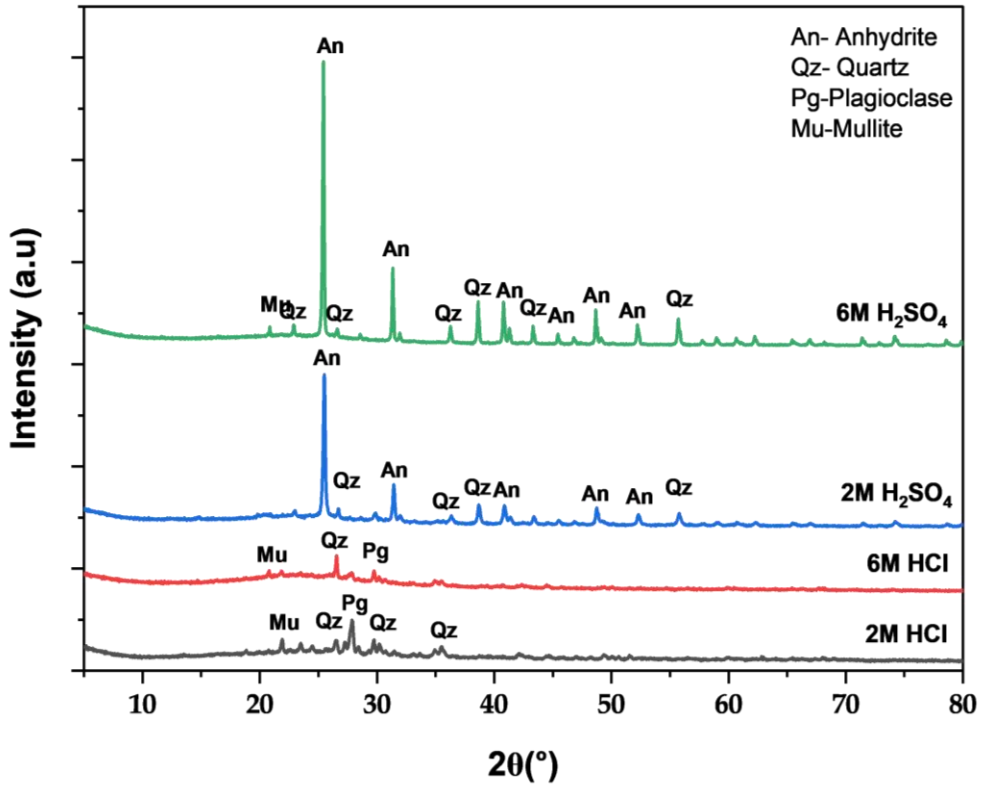

Figure 4.23: XRD patterns of sintered CFA solid residues after HCl and H_2SO_4 leaching.

The morphologies of the sintered CFA solid residues in HCl and H_2SO_4 are presented in **Figure 4.24**. The SEM micrographs of the HCl-leached residue showed that the particles were predominantly amorphous. In the H_2SO_4 residue, a mixture of amorphous and needle-like particles was observed. The EDS analysis of the needle-like particles showed particles

with calcium, silica, and sulphur as the major components, thus confirming the possible formation of calcium sulphates. In contrast, the amorphous particles contained Al, Fe, Ti, Ca, and Si as the main elements. The regions containing REEs could not be quantified on the mounted stubs. Nonetheless, the overall results obtained indicate that the sinter-H_2SO_4 process is not suitable for REE in CFA, whereas the sinter-HCl process is much more suitable.

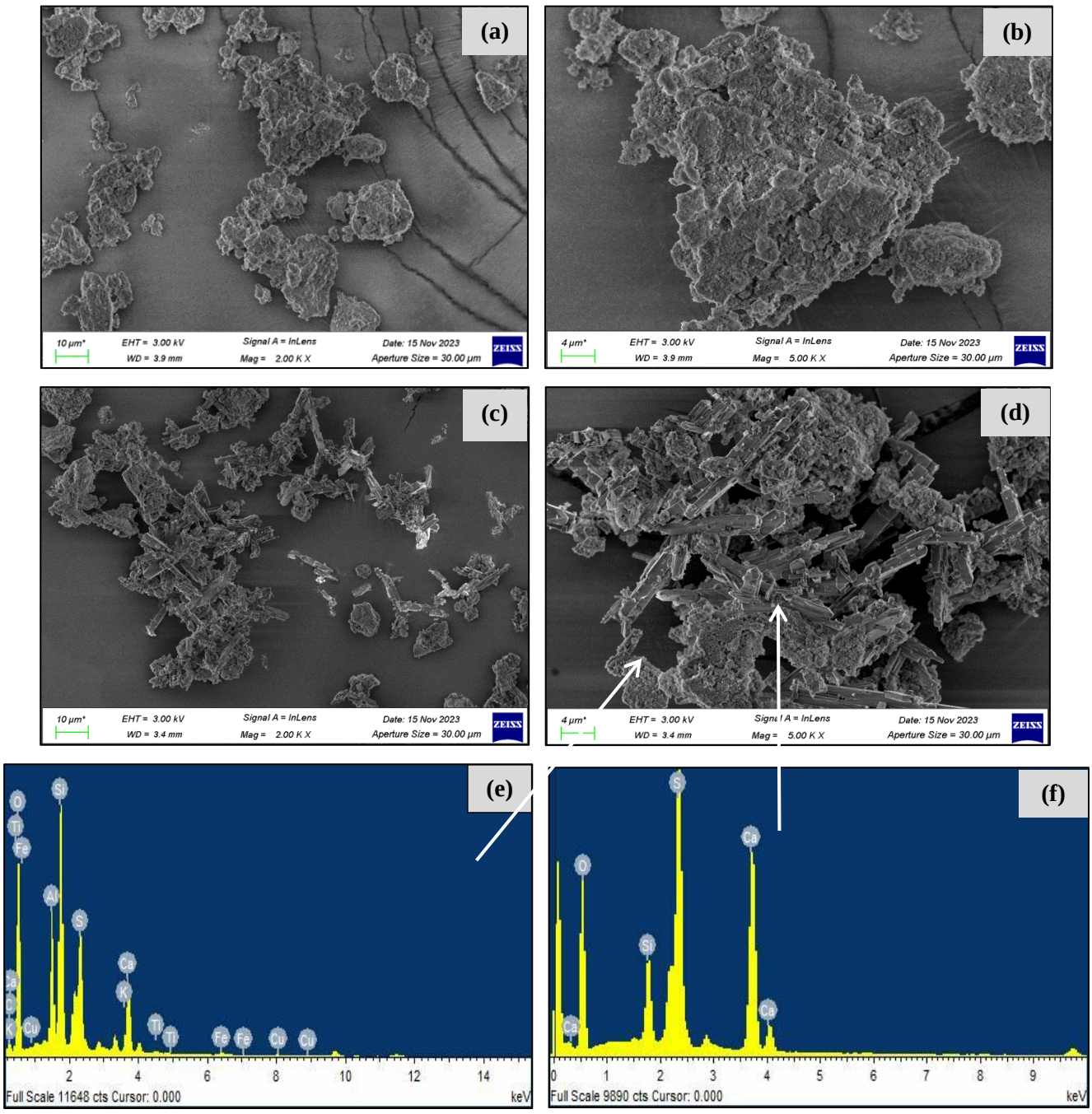

Figure 4.24: Surface morphology of sintered CFA solid residue leached in (a)-(b) 4 M HCl and (c)-(d) 6 M H_2SO_4.

Although the sinter-HCl process yields higher extraction efficiency, there are still some REEs that remain undissolved. This implies that, in addition to the impact of sulphuric acid, the mineralogical distribution of REEs in the sintered CFA still significantly affects their extraction. In **Section 4.2.1.3**, it was mentioned that in raw CFA, REEs can occur as discrete minerals or be partially and fully integrated with the Al-Si-rich phase. Consequently, during the sintering process (see **Section 4.2.3.3**), those REEs that are fully integrated into the Al-Si-rich phase may be released from the host (i.e. Al-Si), but they do not undergo decomposition into their soluble form (i.e. oxides).

4.3 Conclusion

The primary objective of this chapter was to characterise CFA and evaluate the distribution of alumina, iron, titanium, and selected REEs. This was achieved through several analytical techniques and preliminary studies. The main conclusions are as follows:

- CFA used in this study contained Al, Fe, Ti, and REEs, which were significant for the set objectives. XRD analysis showed that CFA was predominantly amorphous and contained mullite, quartz, and iron oxide (i.e. magnetite/haematite) as the main crystalline phases. Microanalysis revealed that CFA contains Al-Si-rich, Si-rich, Ca-rich, and Fe-rich grains as the major phase compositions. Traces of Fe, Ti, Ca, and REEs were relatively dispersed through different phases (crystalline and amorphous) and were either partially associated, included within grains, or occurred as discrete grains.

- Magnetic separation was successfully conducted to recover discrete Fe-oxide (magnetite/haematite) phases. A maximum recovery of 65.9% Fe was achievable at 1.05 T. However, due to the agglomerated CFA particles, the extracted magnetic fraction also contained mullite and quartz as impurities. The characterisation of this material as a spherical component of various sizes was proposed as a seeding material for further processing in **Chapter 6**.

- Preliminary leaching tests were carried out to understand the leaching behaviour of Al, Fe, Ti, and REEs in a sulphate system. Direct acid leaching showed poor extraction due to the distribution of these elements in the refractory phases (i.e. Al-Si and phosphates). Sintering, which transformed the spherical Al-Si-rich phases into

irregular phases, resulted in a much higher extraction of Al, Fe, and Ti. However, the extraction efficiency of REEs remained relatively low. A change in the lixiviant to HCl resulted in an improved extraction of REEs; thus, the poor extraction of REEs in the sinter-H_2SO_4 leaching was attributed to the phase composition (untransformed REE-phosphates) and the effect of calcium sulphate. Nonetheless, while HCl is a better lixiviant for REEs, it requires expensive equipment due to its corrosive properties. In addition, REEs occur in trace concentrations compared to the major elements Al, Fe, and Ti, therefore, sulphuric acid can be used as an alternative to concentrate REEs and subsequently selectively extract them.

This chapter has covered material characterisation and preliminary studies to determine the leaching behaviour of the elements of interest. The next chapter focuses on the optimisation of the sinter-H_2SO_4 leach process and producing saleable materials after metal extraction.

References

Apua, M.C. and Nkazi, B.D., 2022. Leaching of coal fly ash with sulphuric acid for synthesis of wastewater treatment composite coagulant. *Canadian Metallurgical Quarterly* 61(3), 309-331.

Apua, M.C., 2023. Development of leaching predictive models for elements extraction from coal fly ash in sulphuric acid solution: application of Eureqa Newtonian software. *Journal of Chemical Technology & Metallurgy* 58(1), 187-199.

Ariuntuya, B., 2018. Recovery of Rare Earth Elements from Apatite Ores by Hydrometallurgical Process. PhD thesis, Graduate School of Engineering and Resource Science, Akita University, Japan.

Bielowicz, B., 2020. Ash characteristics and selected critical elements (Ga, Sc, V) in coal and ash in polish deposits. *Resources* 9(9), 115.

Binnemans, K., Jones, P.T., Blanpain, B., Van Gerven, T., Pontikes, Y., 2015. Towards zero-waste valorisation of rare-earth-containing industrial process residues: a critical review. *Journal of Cleaner Production* 99, 17-38.

Cao, S., Zhou, C., Pan, J., Liu, C., Tang, M., Ji, W., Hu, T. and Zhang, N., 2018. Study on influence factors of leaching of rare earth elements from coal fly ash. *Energy and Fuels* 32(7), 8000-8005.

Chen, Y., Luo, M. and Cai, W., 2016. Influence of operating parameters on the performance of magnetic seeding flocculation. *Environmental Science and Pollution Research* 23, 2873-2881.

Chi, R.A., Tian, J., Zhu, G.C., Wu, Y.X., Li, S.R., Wang, C.W. and Zhou, Z.A., 2006. Kinetics of rare earth leaching from a mangnese-removed weathered rare-earth mud in hydrochloric acid solutions. *Separation Science and Technology* 41(06), 1099-1113.

Cornelius, M.L.U., Ameh, A.E., Eze, C.P., Fatoba, O., Sartbaeva, A. and Petrik, L.F., 2021. The Behaviour of Rare Earth Elements from South African Coal Fly Ash during Enrichment Processes: Wet, Magnetic Separation and Zeolitisation. *Minerals* 11(9), 950.

Czech, T., 2022. Morphology and chemical composition of magnetic particles separated from coal fly ash. *Materials* 15(2), 528.

Dai, S., Zhao, L., Hower, J.C., Johnston, M.N., Song, W., Wang, P. and Zhang, S., 2014. Petrology, mineralogy, and chemistry of size-fractioned fly ash from the Jungar power plant, Inner Mongolia, China, with emphasis on the distribution of rare earth elements. *Energy and Fuels* 28(2), 1502-1514.

Dai, S., Zhao, L., Peng, S., Chou, C.-L., Wang, X., Zhang, Y., Li, D., Sun, Y., 2010. Abundances and distribution of minerals and elements in high-alumina coal fly ash from the Jungar Power Plant, Inner Mongolia, China. *International Journal of Coal Geology* 81, 320-332.

Diwa, R.R., Tabora, E.U., Haneklaus, N.H. and Ramirez, J.D., 2023. Rare earths leaching from Philippine phosphogypsum using Taguchi method, regression, and artificial neural network analysis. *Journal of Material Cycles and Waste Management* 25(6), 3316-3330.

Fu, B., Hower, J.C., Zhang, W., Luo, G., Hu, H. and Yao, H., 2022. A review of rare earth elements and yttrium in coal ash: Content, modes of occurrences, combustion behavior, and extraction methods. *Progress in Energy and Combustion Science* 88, 100954.

Ghorbani, Y., Becker, M., Mainza, A., Franzidis, J.P. and Petersen, J., 2011. Large particle effects in chemical/biochemical heap leach processes-A review. *Minerals Engineering* 24(11), 1172-1184.

Harrar, H., Eterigho-Ikelegbe, O., Modiga, A. and Bada, S., 2022. Mineralogy and distribution of rare earth elements in the Waterberg coalfield high ash coals. *Minerals Engineering* 183, 107611.

Hower, J.C., Groppo, J.G., Joshi, P., Dai, S., Moecher, D.P., Johnston, M., 2013. Location of cerium in coal-combustion fly ashes: implications for recovery of lanthanides. *Coal Combustion and Gasification Products* 5, 73-78.

Hower, J.C., Qian, D., Briot, N.J., Santillan-Jimenez, E., Hood, M.M., Taggart, R.K. and Hsu-Kim, H., 2019. Nano-scale rare earth distribution in fly ash derived from the combustion of the fire clay coal, Kentucky. *Minerals* 9(4), 206.

Hrstka, T., Gottlieb, P., Skala, R., Breiter, K. and Motl, D., 2018. Automated mineralogy and petrology-applications of TESCAN Integrated Mineral Analyzer (TIMA). *Journal of Geosciences* 63(1), 47-63.

Kashiwakura, S., Kumagai, Y., Kubo, H. and Wagatsuma, K., 2013. Dissolution of rare earth elements from coal fly ash particles in a dilute H_2SO_4 solvent. *Open Journal of Physical Chemistry* 3(2), 69-75.

King, J.F., Taggart, R.K., Smith, R.C., Hower, J.C. and Hsu-Kim, H., 2018. Aqueous acid and alkaline extraction of rare earth elements from coal combustion ash. *International Journal of Coal Geology* 195, 75-83.

Kolker, A., Scott, C., Hower, J.C., Vazquez, J.A., Lopano, C.L. and Dai, S., 2017. Distribution of rare earth elements in coal combustion fly ash, determined by SHRIMP-RG ion microprobe. *International Journal of Coal Geology*, 184, 1-10.

Kul, M., Topkaya, Y.A.V.U.Z. and Karakaya, İ., 2008. Rare earth double sulfates from pre-concentrated bastnasite. *Hydrometallurgy* 93(3-4), 129-135.

Kumari, A., Parween, R., Chakravarty, S., Parmar, K., Pathak, D.D., Lee, J. and Jha, M.K. 2019. Novel approach to recover rare earth metals (REMs) from Indian coal bottom ash. *Hydrometallurgy* 187, 1-7.

Kutchko, B.G. and Kim, A.G., 2006. Fly ash characterisation by SEM-EDS. *Fuel* 85(17-18), 2537-2544.

Krishnamurthy, N. and Gupta, C.K., 2005. Extractive metallurgy of rare earths. CRC press, New York. ISBN: 0-415-33340-7.

Li, C., Zhou, C., Li, W., Zhu, W., Shi, J. and Liu, G., 2023. Enrichment of critical elements from coal fly ash by the combination of physical separations. *Fuel* 336, 127156.

Li, J., Zhuang, X., Querol, X., Font, O. and Moreno, N., 2020. A review on the applications of coal combustion products in China. Coal Geology of China, 141-186. ISBN:9780429449369.

Lin, R., Stuckman, M., Howard, B.H., Bank, T.L., Roth, E.A., Macala, M.K., Lopano, C., Soong, Y. and Granite, E.J., 2018. Application of sequential extraction and hydrothermal treatment for characterization and enrichment of rare earth elements from coal fly ash. *Fuel* 232, 124-133.

Liu, P., Huang, R. and Tang, Y., 2019. Comprehensive understandings of rare earth element (REE) speciation in coal fly ashes and implication for REE extractability. *Environmental Science and Technology* 53(9), 5369-5377.

Manhique, A., Kwela, Z. and Focke, W.W., 2003. De wet process for the beneficiation of zircon: Optimization of the alkali fusion step. *Industrial and Engineering Chemistry Research* 42(4), 777-783.

Matjie, R., Bunt, J., Van Heerden, J., 2005. Extraction of alumina from coal fly ash generated from a selected low rank bituminous South African coal. *Minerals Engineering* 18, 299-310.

Moila, A., Chetty, D. and Ndlovu, S., 2017. The application of process mineralogy on a tailings sample from a beach placer deposit containing rare earth elements. *Journal of the Southern African Institute of Mining and Metallurgy* 117(7), 615-621.

Nayak, N. and Panda, C.R., 2010. Aluminium extraction and leaching characteristics of talcher thermal power station fly ash with sulphuric acid. *Fuel* 89(1), 53-58.

Ndlovu, N.Z., Ameh, A.E., Petrik, L.F. and Ojumu, T.V., 2023. Synthesis and characterisation of pure phase ZSM-5 and sodalite zeolites from coal fly ash. *Materials Today Communications* 34(117371), 105436.

Palozzi, J., Bailey, J.G., Tran, Q.A. and Stanger, R., 2023. A characterization of rare earth elements in coal ash generated during the utilization of Australian coals. *International Journal of Coal Preparation and Utilization* 43(2), 2106-2135.

Pan, J., Nie, T., Hassas, B.V., Rezaee, M., Wen, Z. and Zhou, C., 2020. Recovery of rare earth elements from coal fly ash by integrated physical separation and acid leaching. *Chemosphere* 248, 126112.

Peiravi, M., Ackah, L., Guru, R., Mohanty, M., Liu, J., Xu, B., Zhu, X. and Chen, L., 2017. Chemical extraction of rare earth elements from coal ash. *Minerals & Metallurgical Processing* 34, 170-177.

Perämäki, S., 2014. Method development for determination and recovery of rare earth elements from industrial fly ash. PhD thesis, Department of Chemistry, University of Jyväskylä.

Rosita, W., Bendiyasa, I.M., Perdana, I. and Anggara, F., 2020. Sequential particle-size and magnetic separation for enrichment of rare-earth elements and yttrium in Indonesia coal fly ash. *Journal of Environmental Chemical Engineering* 8(1), 103575.

Rerani, V.; Mabowa, H. Wagner, N.; 2024, Characterisation of Rare Earth Element-Bearing Mineral Phases Present in South African Coal Ash Using Mineral Liberation Analysis. Fuel 368, 131661.

Rybak, A. and Rybak, A., 2021. Characteristics of some selected methods of rare earth elements recovery from coal fly ashes. *Metals* 11(1), 142.

Sibanda, V., Ndlovu, S., Dombo, G., Shemi, A. and Rampou, M., 2016. Towards the utilization of fly ash as a feedstock for smelter grade alumina production: a review of the developments. *Journal of Sustainable Metallurgy* 2, 167-184.

South African Coal Fly Ash Association (SACAA) 2021. Available online: https://www.sacaa.co.za (Accessed on 21-10-2021).

Sedres, G., 2016. Recovery of SiO_2 and Al_2O_3 from coal fly ash. MSc dissertation, Department of Chemistry, University of the Western Cape, South Africa.

Seidel, A., Zimmels, Y., 1998. Mechanism and kinetics of aluminum and iron leaching from coal fly ash by sulfuric acid. *Chemical Engineering Science* 53, 3835-3852.

Shemi, A., Ndlovu, S., Sibanda, V. and Van Dyk, L., 2015. Extraction of alumina from coal fly ash using an acid leach-sinter-acid leach technique. *Hydrometallurgy* 157, 348-355.

Shoumkova, A.S., 2011. Magnetic separation of coal fly ash from Bulgarian power plants. *Waste Management and Research* 29(10), 1078-1089.

Stopić, S.R. and Friedrich, B.G., 2018. Leaching of rare earth elements with sulfuric acid from bastnasite ores. *Vojnotehnički Glasnik* 66(4), 757-770.

Strzałkowska, E., 2021. Morphology, chemical and mineralogical composition of magnetic fraction of coal fly ash. *International Journal of Coal Geology* 240, 103746.

Tang, M., Zhou, C., Pan, J., Zhang, N., Liu, C., Cao, S., Hu, T., Ji, W., 2019. Study on extraction of rare earth elements from coal fly ash through alkali fusion-Acid leaching. *Minerals Engineering* 136, 36-42.

Thompson, R.L., Bank, T., Montross, S., Roth, E., Howard, B., Verba, C. and Granite, E., 2018. Analysis of rare earth elements in coal fly ash using laser ablation inductively coupled plasma mass spectrometry and scanning electron microscopy. *Spectrochimica Acta Part B: Atomic Spectroscopy* 143, 1-11.

Tuhý, M., Hrstka, T. and Ettler, V., 2020. Automated mineralogy for quantification and partitioning of metal (loid) s in particulates from mining/smelting-polluted soils. *Environmental pollution* 266, 115118.

Valeev, D., Kunilova, I., Alpatov, A., Varnavskaya, A. and Ju, D., 2019. Magnetite and Carbon Extraction from Coal Fly Ash Using Magnetic Separation and Flotation Methods. *Minerals* 9(5), 320.

Van Alphen, C., Matjie, R.H. and Rajoo, P., 2007. QEMSCAN Analysis of Coal and Fly Ash Formation Model-New Developments. Automated Mineralogy, Minerals Engineering (MEI) Conferences. 1-2 September 2007, Brisbane, Australia.

Vu, D.H., Bui, H.B., Kalantar, B., Bui, X.N., Nguyen, D.A., Le, Q.T., Do, N.H. and Nguyen, H., 2019. Composition and morphology characteristics of magnetic fractions of coal fly ash wastes processed in high-temperature exposure in thermal power plants. *Applied Sciences* 9(9), 1964.

Wang, Z., Dai, S., Zou, J., French, D. and Graham, I.T., 2019. Rare earth elements and yttrium in coal ash from the luzhou power plant in Sichuan, southwest China: Concentration, characterization and optimized extraction. *International Journal of Coal Geology* 203, 1-14.

Wu, L., Ma, L., Huang, G., Li, J. and Xu, H., 2022. Distribution and Speciation of Rare Earth Elements in Coal Fly Ash from the Qianxi Power Plant, Guizhou Province, Southwest China. *Minerals* 12(9), 1089.

Wu, W.Y., Xue, B., Wu, Z.Y., Sun, S.C. and Tu, G.F., 2007. Reaction process of monazite and bastnaesite mixed rare earth minerals calcined by CaO-NaCl-$CaCl_2$. *Transactions of Nonferrous Metals Society of China* 17(4), 864-868.

Yahorava, V., Bazhko, V. and Freeman, M., 2016. Viability of phosphogypsum as a secondary resource of rare earth elements. XXVIII International Mineral Processing Congress Proceeding, 11-15 September 2016, Quebec City, Canada. Canadian Institute of Mining Metallurgy & Petroleum (CIM), 1-16.

Yang, C., Zhang, J., Hou, X., Li, S., Li, H., Zhu, G. and Qi, F., 2021. Study on the correlation between Fe/Ti forms and reaction activity in high-alumina coal fly ash. *Science of the Total Environment* 792, 148419.

5 OPTIMISATION OF THE SINTER – H_2SO_4 LEACH FOR ALUMINA PRODUCTION AND THE EXTRACTION OF REEs BY DRY DIGESTION – WATER LEACH FROM THE RESIDUE

5.1 Hypothesis and Objectives

The results presented in the previous chapter (see **Chapter 4**, **Section 4.2.4**) demonstrated that sulphuric acid is a suitable lixiviant for the extraction of Al, Fe, and Ti, while REEs (except Sc) will mostly report to the residue. Consequently, the objectives of this part of the experimental work were set to achieve the following:

- Optimise the alumina sinter-H_2SO_4 leach process using a statistical Design of Experiments (DOE). DOE is a method used to analyse the interaction between variables that affect the leaching process and thus, allow optimisation of the process parameters (Box et al., 1978). Consequently, a CFA leach liquor and a residue (silica-rich) are generated for further processing.
- It has been reviewed and observed in the preliminary tests that the acid-based leaching processes are often non-selective. Therefore, the extraction of Al will also result in Ti and Fe as major impurities. To minimise downstream purification costs, this chapter will focus on the recovery of Al_2O_3 and TiO_2 as saleable products. Therefore, an integrated solvent extraction (SX) and crystallisation process is considered.
- According to the literature surveyed, the dry digestion-water leach process is a suitable technique used to process silicate minerals such as zinc ores and eudialyte for metal extraction (Terry, 1983). In lieu of this, the generated residue (silica-rich) was characterised and processed for metal extraction (REEs, Ti, Al, and Fe) using the dry digestion-water leach process to generate a rare earth concentrate.

5.2 Results and Discussion

5.2.1 Optimisation of sinter – H_2SO_4 process

The sinter-H_2SO_4 leach process is established in **Section 2.5.2.2** of **Chapter 2** as an efficient alumina process for commercial processing. Therefore, this section focuses primarily on determining and optimising the variables that affect Al extraction from sintered CFA. DOE was used to establish significant variables that affect the process. Once these variables were identified, response surface methodology (RSM), which is a standard tool in the software, was used to study the variables and their interactions for process optimisation. A detailed methodology for data analysis is provided in **Section 3.3.3.4** of **Chapter 3**.

5.2.1.1 Significant variables

The experimental variables that were employed in this research are listed in **Table 5.1**. The variables are also presented in coded form (i.e. –1 or +1) for a consistent comparison. The selection of these variables and their levels was based on preliminary tests in **Section 4.2.4** of **Chapter 4** and a literature survey (McDowell and Seeley, 1981; Shemi et al., 2014).

Table 5.1: Experimental variables and their coded levels

Experimental variables	Low (–1)	Centre (0)	High (+ 1)
Leaching time (hrs)	6	8	10
Leaching temperature (°C)	45	60	75
Solid:Liquid (S/L) ratio	1:3	1:4	1:6
H_2SO_4 concentration (M)	4	6	8
*Agitation rate (rpm)	160	160	160

A 2^4 full factorial design was used to set up the experimental runs for Al extraction, as presented in **Table 5.2**. The results in the table were further utilised to identify the key variables and their interactions.

Table 5.2: The percentage extraction of Al using 2^4 full factorial designs

Standard run order	Random run Order	Control variables				% Al Extraction
		A	B	C	D	
1	1	–1	–1	–1	–1	57.0
2	4	+1	–1	–1	–1	51.0
3	14	–1	+1	–1	–1	59.3
4	18	+1	+1	–1	–1	52.4
5	6	–1	–1	+1	–1	54.5
6	19	+1	–1	+1	–1	68.5
7	25	–1	+1	+1	–1	52.2
8	15	+1	+1	+1	–1	65.6
9	24	–1	–1	–1	+1	53.9
10	5	+1	–1	–1	+1	49.4
11	7	–1	+1	–1	+1	51.7
12	27	+1	+1	–1	+1	58.5
13	10	–1	–1	+1	+1	58.8
14	26	+1	–1	+1	+1	72.1
15	17	–1	+1	+1	+1	60.8
16	9	+1	+1	+1	+1	70.5

The actual factor: A = Acid concentration, M; B = Leaching time, hrs; C = Leaching temperature, ℃; D = Solid: Liquid ratio

Pareto Chart and Variance Analysis

The Pareto chart and analysis of variance are reported in **Figure 5.1** and **Table 5.3**, respectively. The Pareto chart indicates that the leaching temperature and H_2SO_4 concentration are the significant variables among the four variables investigated. Furthermore, there was a statistical interaction between temperature and H_2SO_4 concentration (AC). In **Table 5.3**, the F-value of 17.00 indicates the significance of the model, as there is only a 0.01% chance that it could be due to noise. A P-value greater than 0.100 is considered insignificant, whereas a P-value less than 0.0500 indicates the significance of the model terms. In this case, the model terms A, C, and AC were significant, with P-values of 0.0158, 0.0003, and 0.0010, respectively.

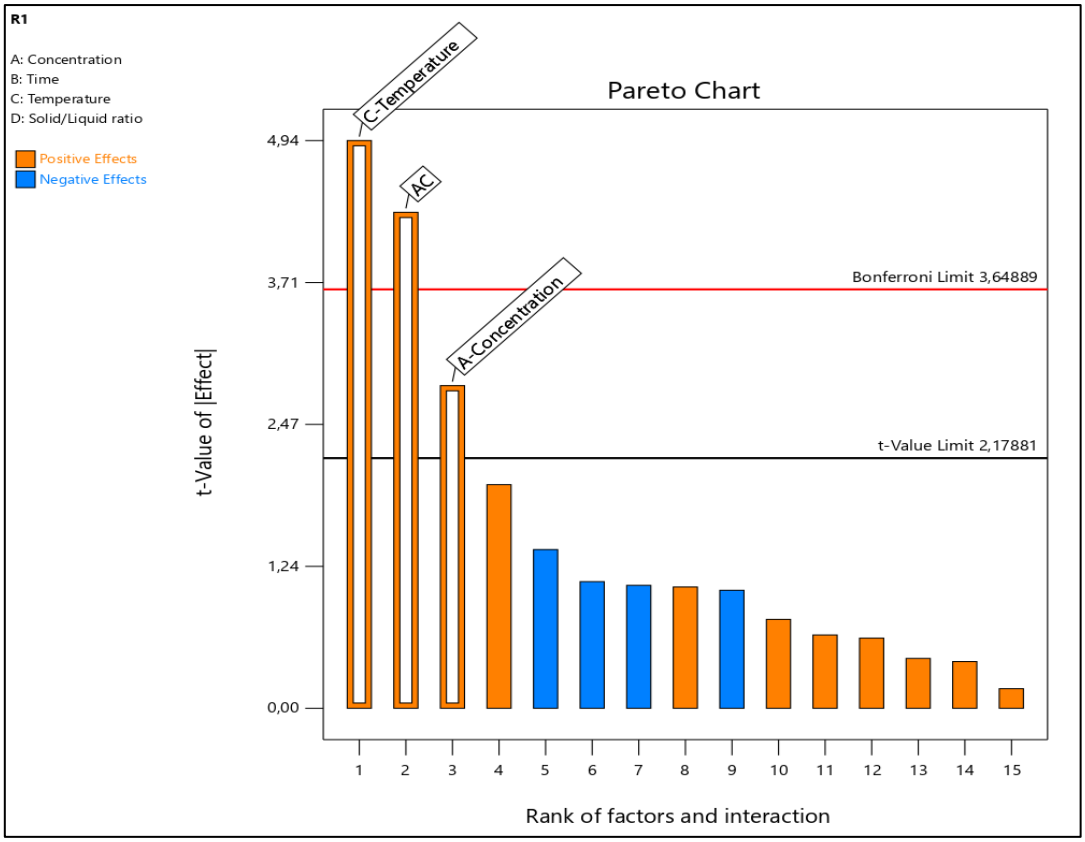

Figure 5.1: A bar graph showing significant variables in the Al extraction process.

Table 5.3: Analysis of variance for selected factorial model

Source	Sum of Squares	DF	Mean Square	F-Value	Prob > F	
Model	634.47	3	211.49	17.00	0.0001	Significant
A- H_2SO_4 concentration	98.21	1	98.21	7.89	0.0158	
C -Temperature	304.15	1	304.15	24.45	0.0003	
AC	232.11	1	232.11	18.66	0.0010	
Residual	149.28	12	12.44	17.00	0.0001	
Cor Total	783.75	15	211.49	7.89	0.0158	

The correlation between the response and the significant variables is further illustrated by the fitted model, as shown in **Equation 5.1**. Additional validation of the model can be observed through the graphical residual analysis presented in **Figure C.1** (see **Appendix C**).

$$\mathbf{R} = 58.53 + 2.48X_A + 4.48X_C + 3.81X_{AC} \qquad \mathbf{5.1}$$

where **R** is the aluminum extraction

Influence of Factors and Factor Interaction

The influence of different variables/factors on Al extraction is shown in **Figure 5.2**. Sulphuric acid concentration and leaching temperature had a positive effect on the extraction of Al. A positive significant effect implies that an increase in the variable will result in a notable increase in the response. In contrast, a decrease in the variable will result in a significant decrease in the response value.

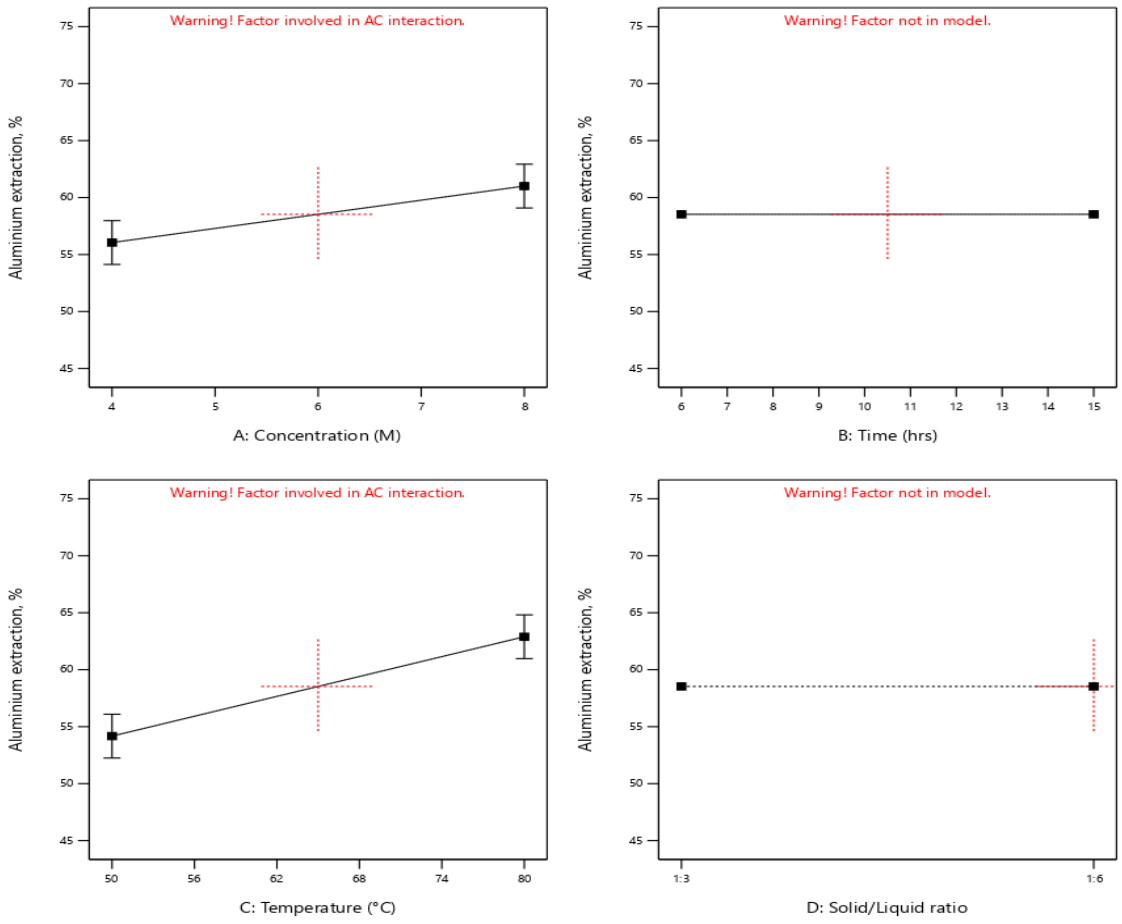

Figure 5.2: Effect of experimental variables (A: H_2SO_4 concentration, B: time, C: temperature, and D: S/L ratio) on the extraction of Al from sintered CFA.

The interaction between H_2SO_4 concentration and leaching temperature is also shown in **Figure 5.3**. An interaction of variables refers to a situation in which the impact of one variable on a process is modified by the presence of other variables. In this study, the leaching temperature had a positive effect on Al extraction, whereas the H_2SO_4 concentration had a negative effect. This effect may be due to the precipitation of metal sulphates, as shown in **Equation 4.6** and **4.7** (see **Section 4.2.4.3**, **Chapter 4**), which creates boundary layers that generate passivation species, restricting the diffusion of reactants and products on the surface (Seidel and Zimmels, 1998; Shemi, 2013). Consequently, to optimise Al extraction, it is necessary to maintain high leaching temperatures and low H_2SO_4 concentrations.

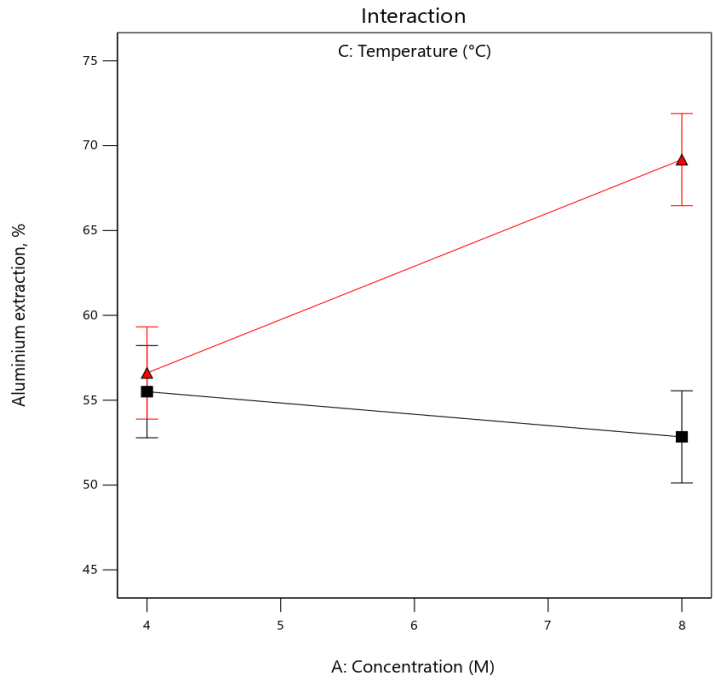

Figure 5.3: The interaction between H_2SO_4 concentration and leaching temperature in the Al extraction from sintered CFA.

5.2.1.1 Optimisation of significant factors variables

Significant variables of a process can be optimised to achieve the highest possible performance. Sulphuric acid concentration and leaching temperature were identified as significant variables in the screening test work above. Therefore, in this section, RSM and central composite rotatable design (CCRD) were used to optimise the process.

Derivation of the Model

A CCRD was used to collect experimental data and the findings are reported in **Table 5.4**. The results were used to fit the second-order response and estimate the regression model coefficients.

Table 5.4: Observed percentage extraction of Al using CCRD

Standard run	Coded		Actual		% Al Extraction [Observed]
	A	B	A	B	
1	–1	–1	6	65	68.3
2	–1	+1	6	80	71.8
3	+1	–1	8	70	74.3
4	+1	+1	8	80	65.7
5	0	–1.414	7	62	69.2
6	0	+1.414	7	83	66.0
7	–1.414	0	5.6	73	73.3
8	+1.414	0	8.4	73	71.9
9	0	0	7	73	71.9
10	0	0	7	73	73.5
11	0	0	7	73	73.0
12	0	0	7	73	71.9
13	0	0	7	73	71.5

The actual factor: A = Acid concentration, M; B = Leaching temperature, °C.

The re-fitted quadratic model in terms of actual variables is shown in **Equation 5.2.**

$$-229{,}47 + 61{,}62x_1 + 2{,}53\,x_2 + -0{,}403x_1x_2 + -2{,}399x_1^2 + 0{,}0018x_2^2 \qquad \textbf{5.2}$$

Where, x_1 is the leaching temperature, and x_2 is H_2SO_4 concentration, within predictor variable limits:

Statistical analysis also revealed that the results could be well expressed by the model, with an R^2 value of 0.9639. The lack of fit was found to be insignificant ($p \leq 0.05$) compared to pure error for the variable, indicating that the model is statistically accurate. The analysis of variance for the re-fitted model is shown in **Table 5.5**, whereas the Fit Statistics are presented in **Table C.1 (Appendix C)**.

Table 5.5: Analysis of variance for the re-fitted quadratic model

Source	Sum of squares	df	Mean square	F-value	P-value	
Model	89.97	5	17.99	37.42	< 0.0001	Significant
A- Concentration	11.58	1	11.58	24.08	00017	
B-Temperature	0.5407	1	0.5407	1.12	0.3242	
AB	36.60	1	36.60	76.11	< 0.0001	
A^2	40.03	1	40.03	83.24	< 0.0001	
B^2	0.0713	1	0.0713	0.1483	0.7116	
Residual	3.37	7	0.4809			
Lack of Fit	0.4943	3	0.1648	0.2295	0.8717	Not significant
Pure Error	2.87	4	0.7180			
Cor Total	93.33	12				

Optimisation of Variables

A 3D surface plot in **Figure 5.4** illustrates the variation of Al extraction with temperature and H_2SO_4 concentration. The plot reveals that to maximise Al extraction, the leaching temperature should be increased while acid concentration is minimised. Optimisation was performed using the desirability function (discussed in **Section 3.3.3.4**, **Chapter 3**) in the software. The solution with the highest Al extraction was $\hat{Y} = 74.81\%$, which was selected as the optimised condition. The numerical optimum level graphs and the contour plots showing the relationship between the factor desirability levels and predicted Al extraction are also presented in **Figure C.2**, **Appendix C**.

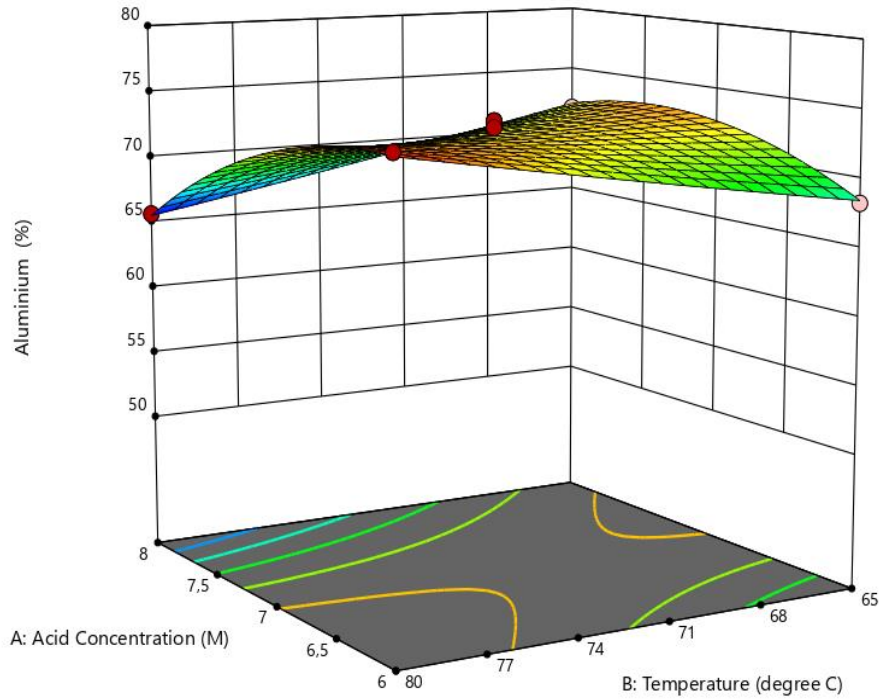

Figure 5.4: A 3D response surface for the percentage extraction of Al as a function of temperature and H_2SO_4 concentration from sintered CFA.

The validity of the model was also tested through confirmatory experiments, and the analysis is reported in **Table 5.6**. The extraction of Al was performed at 80°C, 1:5, and 6 M H_2SO_4 by leaching for 10 hours. At these experimental parameters, 77.1% of Al was extracted with a 3.1% error margin compared to the predicted model. Overall, these results were satisfactory.

Table 5.6: Aluminium extraction at optimum leaching conditions from sintered CFA

Parameter	Temperature (°C)	Concentration (M)	% Al Extraction
Model	80	6	74.8
Confirmation	80	6	77.1

Based on the confirmation analysis, a CFA leach liquor and residue were generated as by-products and as a result, further processing was necessary.

5.2.2 Purification of CFA leach liquor

The extraction of 77.1% Al also resulted in a 52.7% Ti extraction and 80.2% Fe extraction after optimisation. Therefore, in this study, it was pertinent to purify the CFA leach liquor to produce smelter-grade Al_2O_3. A stock solution was prepared in a 1 L volumetric flask and analysed for its major chemical composition using ICP-OES. The elemental analysis of the CFA leach liquor is reported in **Table 5.7**. As anticipated, the major Al impurities were Fe, Ti, and Mg. The concentration of REEs was also analysed using ICP-MS and data analysis is reported in **Figure 5.5.** The REEs were quite low in the leach liquor due to their lower solubility in a sulphate system (discussed in **Section 4.2.4, Chapter 4**) and lower concentrations in CFA compared to major elements.

Table 5.7: Elemental analysis of the major components in a CFA leach liquor

Analyte	pH	Al^{3+}	Fe^{3+}	Fe^{2+}	Ti^{4+}	Mg^{2+}	Ca^{2+}	Si^{4+}
mg/L	-0.1	9580.0	791.44	139.63	489	791.89	10.5	5.99

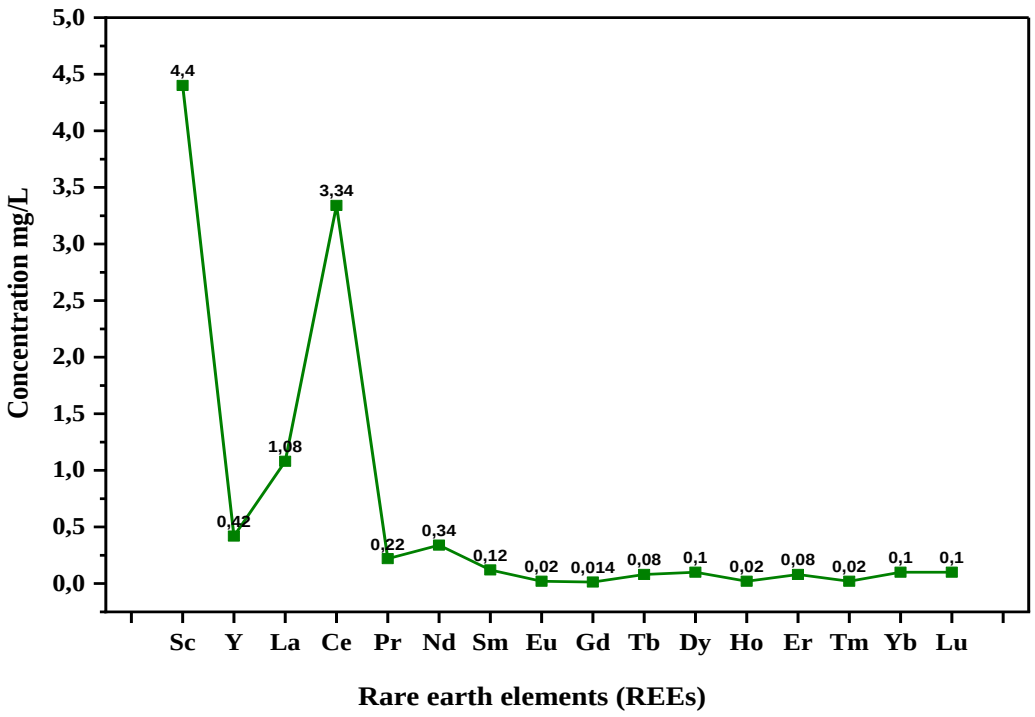

Figure 5.5: Elemental analysis of REEs in a CFA leach liquor.

This section focuses on the purification of major elements (Al, Fe, and Ti), while only tracking the distribution of the selected REEs (Sc, Y, La, Nd, and Ce). An integrated SX and crystallisation process is reported for Ti and Al recovery. Furthermore, the generated compounds are used to synthesise smelter-grade alumina and high-purity titania. A detailed experimental procedure for the purification steps is described in **Section 3.3.4** of **Chapter 3**.

5.2.2.1 Titanium extraction

The pH of the generated CFA leach liquor in **Table 5.7** was recorded as -0.1, indicating high concentrations of H^+ in the solution. Under these pH conditions, $FeHSO_4^{2+}$ and $Ti(OH)_3HSO_4$ are the dominant species (see **Figure 2.21** and **Figure 2.22**). They can also be selectively extracted from Al(III) by SX with primary amines (Gil et al., 1995; Sole, 1999). However, Rushwaya (2016) reported that Fe(III) has poor loading capacity during SX in this pH range (pH <1). Therefore, in this study, it was decided to reduce all Fe(III) in the solution to Fe(II) by adding iron filings in a 1:2 ratio as shown in **Equation 5.3**. As a result, only Ti(IV) was selectively extracted, as shown in **Equation 5.4**.

$$2Fe^{3+} + Fe \rightarrow 2Fe^{2+} \qquad \textbf{5.3}$$

$$Ti(OH)_3HSO_{4(aq)} + (RHN_3)_2(SO)_{4(org)} \rightarrow (RNH_3)_2SO_4 \cdot Ti(OH)_3HSO_{4(org)} \qquad \textbf{5.4}$$

Titanium (Ti(IV)) was extracted using Primene JM-T/Shellsol D70, and the experimental setup is presented in **Figure 3.5**. Data analysis is reported in **Table 5.8**, and the results show that Ti(IV) is selectively extracted, while Al(III), Mg(II), and Fe(II) remain in the aqueous phase. The loading capacity of Primene JM-T was also tested at different concentrations, and at all ratios, more than 90% of the Ti was loaded into Primene JM-T/Shellsol D70. Therefore, the optimum conditions for Ti extraction were 30 minutes with 10% Primene JM-T/Shellsol D70 at a 1:1 aqueous/ organic ratio. These findings are similar to the study by Rampou et al. (2017) and Rushwaya and Ndlovu (2017).

Table 5.8: Extraction of Ti with Primene/Shellsol D70 in a sulphate system

Primene JMT	Aqueous phase % Recovery				Organic phase % Recovery			
	Ti^{4+}	Al^{3+}	Fe^{2+}	Mg^{2+}	Ti^{4+}	Al^{3+}	Fe^{2+}	Mg^{2+}
10	2.76	100.3	99.8	99.8	97.1	0.1	0.0	0.0
20	2.67	100.01	99.9	99.9	97.3	0.3	0.0	0.0
30	2.65	99.7	99.6	99.6	97.2	0.03	0.0	0.0

N = 2 replicates

The final step involved stripping the loaded Ti(IV) and calcining it to produce titania (TiO_2). Various acidic/alkaline stripping reagents have been reported in the literature. However, acid-based reagents often require high acid concentrations (i.e. >3 M for H_2SO_4), which can lead to degradation of the organic phase and limit its recycling potential (Sole, 1999). Therefore, the extracted Ti(IV) was stripped using 1 M NH_4OH (Matjie et al., 2005), as shown in **Equation 5.5**, followed by calcination at 500℃ to produce TiO_2 in **Equation 5.6.**

$$(RNH_3)_2SO_4 \cdot Ti(OH)_3HSO_{4(org)} + 2NH_4OH_{(aq)} \rightarrow Ti(OH)_{4(s)} + (RNH_3)_2SO_{4(org)} + (NH_4)_2SO_{4(aq)} + H_2O \quad \textbf{5.5}$$

$$Ti(OH)_{4(s)} \xrightarrow{500℃} TiO_{2(s)} + 2H_2O_{(g)} \quad \textbf{5.6}$$

FT-IR analysis was used to confirm the synthesis of TiO_2, and the spectrum is shown in **Figure 5.6**. In titanium hydroxide, the Ti-O bending mode and Ti-OH stretching mode were assigned at 470 cm^{-1} and 1739 cm^{-1}, respectively (Chougala et al., 2017; Villabona-Leal et al., 2020). The titanium hydroxide also showed minor peaks at 1739 cm^{-1}, 1444 cm^{-1}, 1364 cm^{-1} and 1216 cm^{-1}. The presence of these peaks may have occurred due to the organic phase functional groups (Primine JM-T/ShellsolD70) during solid-liquid separation. Nonetheless, the FT-IR spectrum of the calcined TiO_2 did not show any functional groups indicating a possible evaporation of the organic phase. The calcined TiO_2 also showed a broad peak at 470 cm^{-1}, indicating a possible Ti-O vibration. Overall, these results confirmed the possible synthesis of TiO_2.

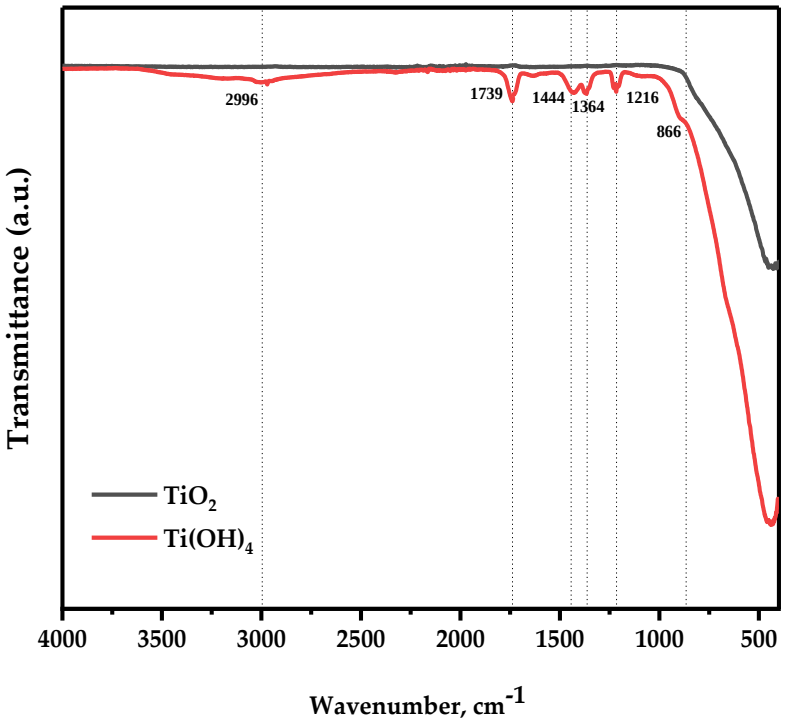

Figure 5.6: FT-IR spectrum of TiO_2 calcined at 500℃.

5.2.2.2 Aluminium crystallisation

The extraction of Ti(IV) using SX was followed by the direct crystallisation of Al in the raffinate. Crystallisation was achieved by adding $(NH_4)_2SO_4$ to the raffinate and allowing the solution to crystallise at 0℃ (Ma et al., 2021). The pH of the raffinate after crystallisation was recorded as pH 1.2. The white alumina crystals were subsequently filtered and calcined at 800℃ to simulate smelter-grade Al_2O_3 (**Equation 5.7** and **5.8**).

$$Al_2(SO_4)_{3(aq)} + (NH_4)_2SO_{4(aq)} + 40H_2O \rightarrow 2(NH_4)Al(SO_4)_2 \cdot 20H_2O_{(s)} \qquad \textbf{5.7}$$

$$2(NH_4)Al(SO_4)_2 \cdot 20H_2O_{(s)} \xrightarrow{800℃} Al_2O_{3(s)} + 4SO_{3(g)} + 2NH_{3(g)} + 21H_2O \qquad \textbf{5.8}$$

FT-IR analysis (see **Figure 5.7**) was also used to observe the structural changes from aluminium crystallisation to calcined Al_2O_3. In the spectra of pure $(NH_4)_2SO_4$, strong peaks were observed between 3500 and 2500 cm^{-1}. These peaks can be assigned to the symmetric

O-H stretch at 3012.37 cm^{-1} and the overlapping N-H asymmetric stretch at 3012.37 and 3012.37 cm^{-1}. Additionally, the N-H symmetric bend is observed at 1394.73 cm^{-1}, while SO overlaps at 1046.56 cm^{-1} (υ_{ss} SO_4) and 1002.95 cm^{-1} (υ_{ss} SO_4) (Bourahla et al., 2014; Sanna et al., 2016; Rajan et al., 2020). In alumina ammonium crystals, characteristic adsorption peaks were observed at 3500, 1630, 1120, 1070, and 980 cm^{-1}. The O-H stretch shifted to 3195.68 cm^{-1}, while the N-H stretch shifted to 3056.85 cm^{-1}. The shift in the spectra indicates a possible reaction between the Al in solution and ammonium salt. The spectrum of the Al crystals was similar to that obtained by Rajan et al. (2020). The calcined Al_2O_3 had no distinct functional groups, suggesting that the ammonium salt evaporated during calcination, resulting in a metal oxide product.

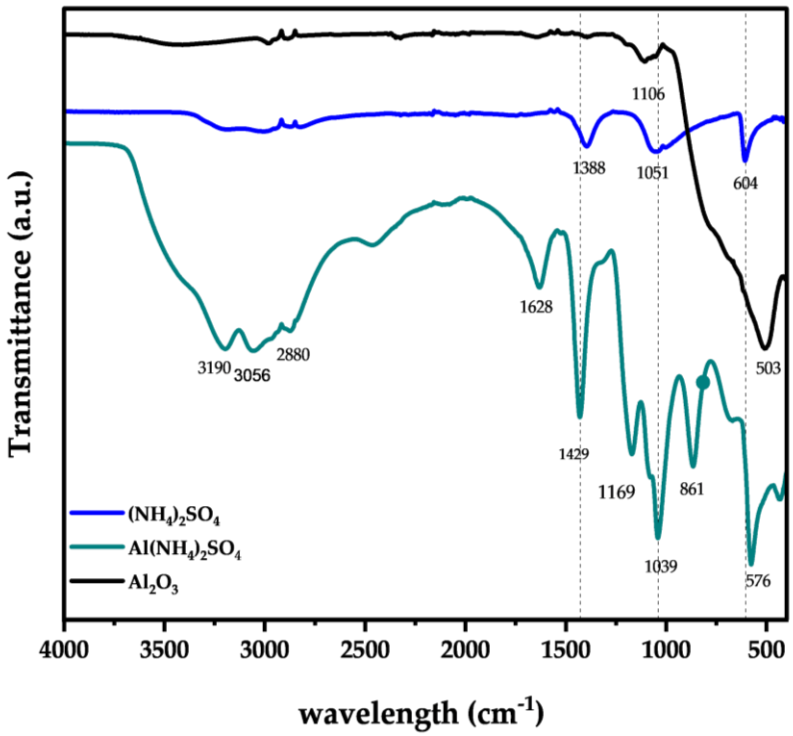

Figure 5.7: FT-IR spectroscopic results for $(NH_4)_2SO_4$, $Al(NH_4)_2SO_4$, and Al_2O_3.

5.2.2.3 Composition of CFA leach liquor before and after Al and Ti recovery

An integrated SX and crystallisation process was used to recover saleable Ti and Al products. **Table 5.9** shows the composition of the CFA leach liquor before and after Al and Ti recovery. A solution concentrated in Fe(II) was generated as a by-product, and further processing is discussed in **Chapter 6**.

Table 5.9: CFA leach liquor before and after Al and Ti extraction

Analyte, mg/L	pH	Al^{3+}	Ti^{4+}	Fe^{3+}	Fe^{2+}	Mg^{2+}
CFA leach liquor	-0.1	9580.0	489.77	791.44	139.63	791.89
After Fe reduction	-0.1	9580.0	490.21	1.39	1126.40	791.80
After Ti SX	--	9580.0	10.36	1.32	1125.91	791.66
Al crystallisation	1.2	2.67	0.45	0.14	1130.15	791.56

--Not available

The selected REEs were also tracked during an integrated SX and crystallisation process, and the results are presented in **Table 5.10**. In **Section 2.6.2**, **Chapter 2**, it was reviewed that REEs are also extracted with Primene JM-T in a sulphate system. In this study, Y, La, Nd, and Ce were retained in the raffinate. According to the literature (Desouky, 2006; Hiskey and Copp 2018), HREEs are extracted into the organic phase using Primene JM-T at pH >0. At pH ~2, both HREEs and LREEs are extracted into the organic phase. The poor extraction of both LREEs and HREEs in this study may be a result of a very low pH (<0) of the leach liquor and the low concentrations of these elements in the solution. Notably, in this study, Sc was extracted with Ti into the organic phase. In a study by Schack (1965), a wolframite mineral dissolved in 6 M H_2SO_4 was purified by SX using Primene JM-T/kerosene. In the process, Sc was co-extracted with Ti and Th. The extracted solution was stripped twice with a 2 M HNO_3 solution, and the selective separation of Sc from these impurities was further studied by ion exchange (IX) with a thiocyanide solution. Wang et al. (2011) and Salman et al. (2022) also showed that selective stripping of Sc can be achieved in an alkaline solution (i.e. Na_2CO_3 and NH_4OH). Thus, similar to Ti(IV), selective stripping of Sc can be achieved using NH_4OH to form $Sc(OH)_3$, as shown in **Equation 5.9** and **5.10**. Lastly, according to the metal hydroxide precipitation table (see **Figure 2.17**), the LREEs and HREEs mostly precipitate at pH >5 (except Ce^{4+}). Thus, after Al crystallisation at pH 1.5, REEs remained in the solution with Fe(II).

$$Sc_3HSO_{4(aq)} + (RHN_3)_2(SO)_{4(org)} \rightarrow (RNH_3)_2SO_4 \cdot Sc_3HSO_{4(org)} \quad \textbf{5.9}$$

$$(RNH_3)_2SO_4 \cdot Sc_3HSO_{4(org)} + NH_4OH_{(aq)} \rightarrow Sc(OH)_{3(s)} + (RNH_3)_2SO_{4(org)} + (NH_4)_2SO_{4(aq)} + H_2O \quad \textbf{5.10}$$

Table 5.10: Concentration of selected REEs in CFA leach liquor during purification

Analyte, mg/L	pH	Sc	Ce	La	Nd	Y
CFA Leah liquor	-0.1	4.40	3.34	1.08	0.34	0.42
After SX	--	0.21	3.36	1.05	0.35	0.41
After Al extraction	1.2	0.26	3.32	1.05	0.35	0.41

--Not available

5.2.2.4 Characterisation of potential saleable products

The primary objective of the purification step was to generate TiO_2 and Al_2O_3, which have market value. Therefore, the synthesised products shown in **Figure 5.8** were characterised for their compatibility as saleable products.

Figure 5.8: Synthesised aluminium oxide and titanium dioxide.

Alumina Smelter Resource

To validate the synthesised alumina, the chemical composition of the calcined Al_2O_3 was analysed using XRF as shown in **Table 5.11**. The results show that more than 99 wt.% Al_2O_3 was generated with less than 1% impurities. This suggests that the generated product could be recommended as a smelter-grade resource for the Hall-Heroult process. These findings are also similar to those obtained by Matjie et al. (2005), Rampou et al. (2017), and Ma et al. (2021). Further analysis was conducted using XRD, and the results are reported in **Figure 5.9**. The analysis clearly reveals an amorphous component in the products, suggesting that the calcination temperature or time could be increased to obtain a more crystalline product. Nonetheless, the reflection peaks at ~20.48°, 32.3°, 37.5°, 39.5°, 45.8°, 60.65°, and 66.8° clearly resemble those of Al_2O_3. All these peaks were accounted for; thus, it was concluded that the generated Al_2O_3 was a pure metal oxide.

Table 5.11: XRF analysis of synthesised Al_2O_3 and the required smelter-grade

Analyte, wt.%	Al_2O_3	Fe_2O_3	TiO_2	CaO	Na_2O	SiO_2	SO_3
Synthesised Al_2O_3	99.02	0.020	0.010	0.020	0.110	0.025	0.150
Smelter-grade	98.3	0.014	0.002	0.016	0.310	0.013	0.200

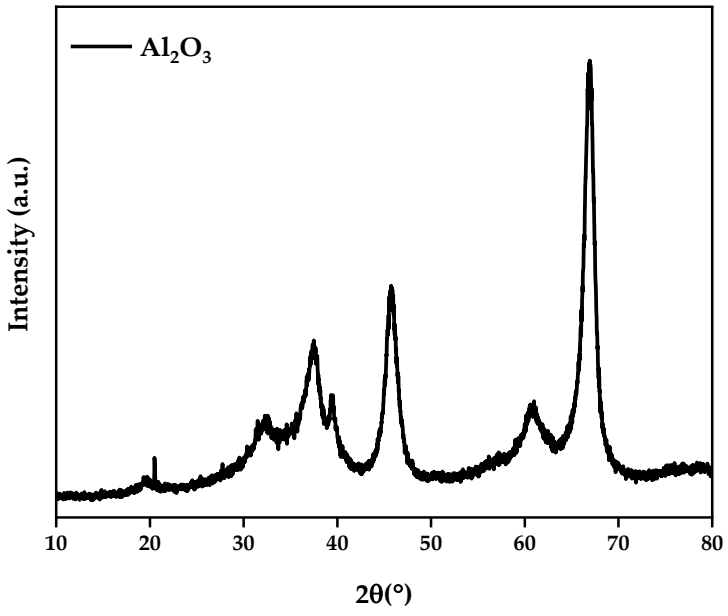

Figure 5.9: XRD pattern of Al_2O_3 calcined at 800°C.

Titania Wastewater Resource

In **Section 2.7.2.2** of **Chapter 2**, it was reviewed that TiO_2 is commonly used as an adsorbent and photocatalyst in wastewater treatment. Therefore, in this section, the synthesised TiO_2 was characterised for potential application in wastewater treatment. The purity of the synthesised TiO_2 was first compared with that of commercial TiO_2, and the results are presented in **Table 5.12**. According to the American Standard for Testing and Materials (ASTM, 1988), the synthesised TiO_2 falls under Type II pigment grade (see **Table 5.12**), which is mostly used in coatings and paints (Gázquez et al., 2014). Degussa P25 is a common commercial TiO_2 used in wastewater treatment (Nachit et al., 2022). The purity of this product ranges from 99.5-99.99% as shown in **Table 5.12** for applications as a photocatalyst (sigmaaldrich.com). Therefore, further purification would be necessary to consider the synthesised TiO_2 as a photocatalyst.

Table 5.12: XRF analysis of the synthesised TiO_2 compared with pigment grade and Degussa P25 quality

Analyte, wt.%	TiO_2	Fe_2O_3	Al_2O_3	CaO	Na_2O	SiO_2	SO_3	ZnO
Synthesised TiO_2	95.03	1.211	0.461	0.614	0.268	0.399	0.237	0.011
Pigment grade (Type II)	≥ 94	--	--	--	--	--	--	--
Degussa P25	99.5-99.99	--	--	--	--	--	--	--

--Not available

The synthesised TiO_2 was further analysed by XRD and SEM to understand the crystal structure. The XRD pattern in **Figure 5.10 (a)** showed distinct peaks at 25.3°, 37.79°, 45.0°, 48.04°, 53.87°, 55.11°, 62.66°, 68.71°, 70.19°, 75.09°, and 82.60°, confirming the presence of anatase as a TiO_2 polymorph. Both anatase and rutile are TiO_2 polymorphs used in water treatment. Electron microscopy was utilised to study the morphology of TiO_2, and the micrographs are reported in **Figure 5.10 (b)** and **(c)**. The analysis revealed the presence of spherical grain-like nanoparticles. In a study by Keiteb et al. (2016), TEM analysis was performed to observe the morphology of TiO_2 calcined at 500-800℃. Notably, at lower calcination temperatures, the morphology appeared spherical with no defined shape (as observed in this study). Conversely, at higher temperatures (800℃), the particles became more irregular with different particle sizes but also resembled a clear octahedral structure.

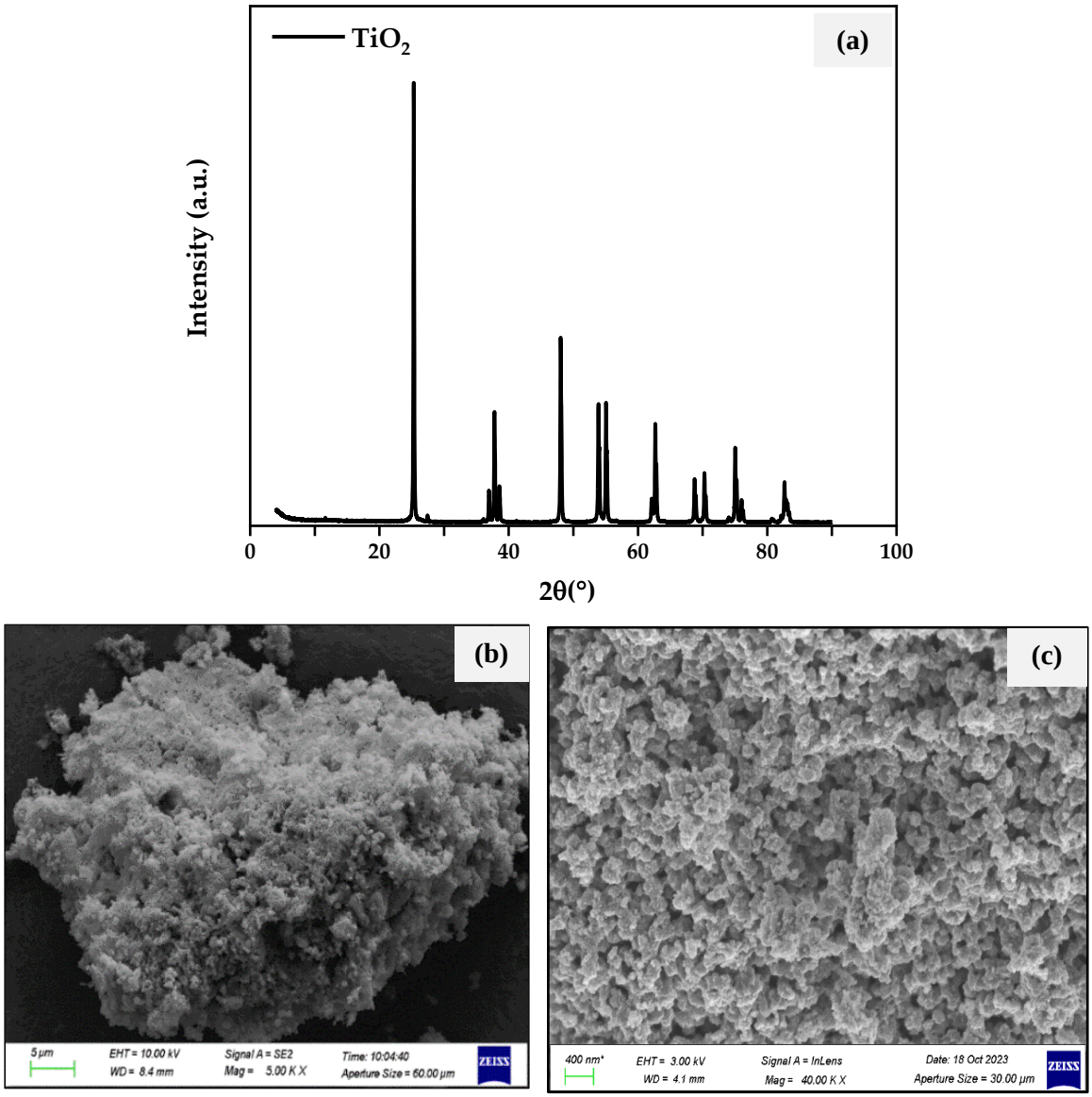

Figure 5.10: (a) XRD pattern of TiO_2 calcined at 500℃ and (b)-(c) SEM images showing spherical grain-like nanoparticles.

The textural properties of the synthesised TiO_2 are presented in **Table 5.13**. The BET surface area (S_{BET}), pore volume (V_p) and pore diameter (D_p) were 10.052 m^2/g, 0.0154 cm^3/g, and 6.14 nm, respectively. Degussa P25 has a S_{BET} of 35-65 m^2/g (Nachit et al., 2022), which is higher than the value obtained in this study. The surface properties of TiO_2 can be influenced by various parameters, such as the synthesis method and calcination temperature (Irshad et al., 2021). Nonetheless, similar to Degussa P25, the synthesised TiO_2 in this study was mesoporous. The isotherm for the synthesised TiO_2 is also shown in **Figure 5.11**. The graph

shows a type-IV pattern with an H3 hysteresis loop, confirming the mesoporous nature of the compound.

Table 5.13: Textural properties of TiO_2 calcined at 500°C

TiO_2	S_{BET} (m^2/g)	V_p (cm^3/g)	D_p (nm)
This study	10.0521	0.015436	6.1425
Degussa P25	35-65	--	--

--Not available

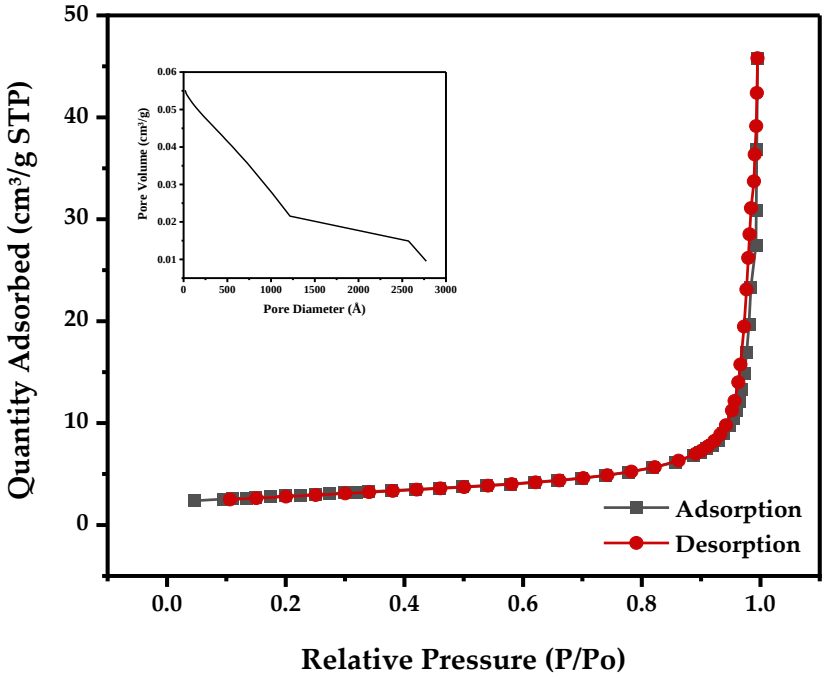

Figure 5.11: N_2 adsorption-desorption isotherm and the respective pore diameter distribution curves for TiO_2 calcined at 500°C.

The overall results obtained in this section indicate that the synthesised TiO_2 can be used for pigment production. For wastewater treatment utilisation, higher purity and better surface properties are required. Therefore, further investigations can be conducted using alternative stripping agents (to prevent stripping of impurities) or by improving the surface properties through compositing or doping (discussed in **Section 2.7.2.2** of **Chapter 2**). The latter is the current trend in TiO_2 synthesis, which enhances its photoactivity (Hlekelele, 2017).

5.2.3 Characterisation and processing of the generated sintered CFA – SR

A white-grey solid residue (CFA-SR), shown in **Figure 5.12**, was also generated after the optimisation of the sinter-H_2SO_4 leach process. Therefore, in this section, the sintered CFA-SR was characterised for further processing.

Figure 5.12: The images of sintered CFA and sintered CFA residue (CFA-SR).

5.2.3.1 Particle size distribution analysis

Particle size distribution (PSD) of the sintered CFA-SR is given in **Figure 5.13**. The PSD analysis after the leaching process shows a d_{90} of 63.104 µm, a d_{50} of 32.098 µm, and a d_{10} of 14.359 µm. The small average particle size eliminates the need for further pulverisation for the subsequent leaching process. Therefore, the material was further used as-is.

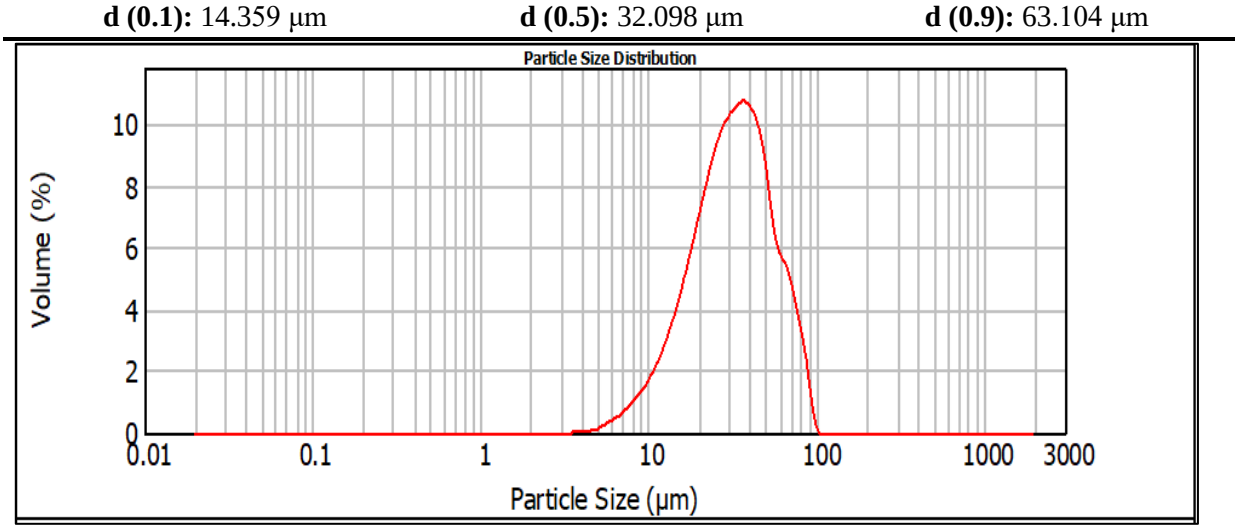

Figure 5.13: Particle size distribution of the sintered CFA-SR.

5.2.3.2 Chemical composition analysis

The major chemical composition of the sintered CFA-SR is reported in **Table 5.14**. As anticipated, alumina was significantly reduced during the leaching stage, with Al_2O_3 dropping from 29 wt.% to 9.02 wt.%. A similar reduction was also observed with 2.82 wt.% Fe_2O_3 and 0.03 wt.% TiO_2. The sintered CFA-SR was mainly composed of calcium, silica, and sulphates, with 22.53 wt.%, 33.31 wt.%, and 34.12 wt.% respectively. The REEs were also analysed using ICP-MS, and the findings are presented in **Figure 5.14**. The figure shows that all REEs are quantifiable in the residue with a total concentration of 404.54 mg/kg (0.0404%). A comparison with REEs in the sintered CFA (see **Table 4.6**, **Section 4.2.3**) also shows that REEs are enriched by a factor of ~2 in the sintered CFA-SR.

Table 5.14: Chemical composition of major elements in sintered CFA-SR

Analyte	SiO_2	Al_2O_3	CaO	Fe_2O_3	TiO_2	MgO	MnO	SO_3	Si/Al
wt. %	33.31	9.08	22.53	2.82	0.03	--	--	34.12	3.67

--Not available

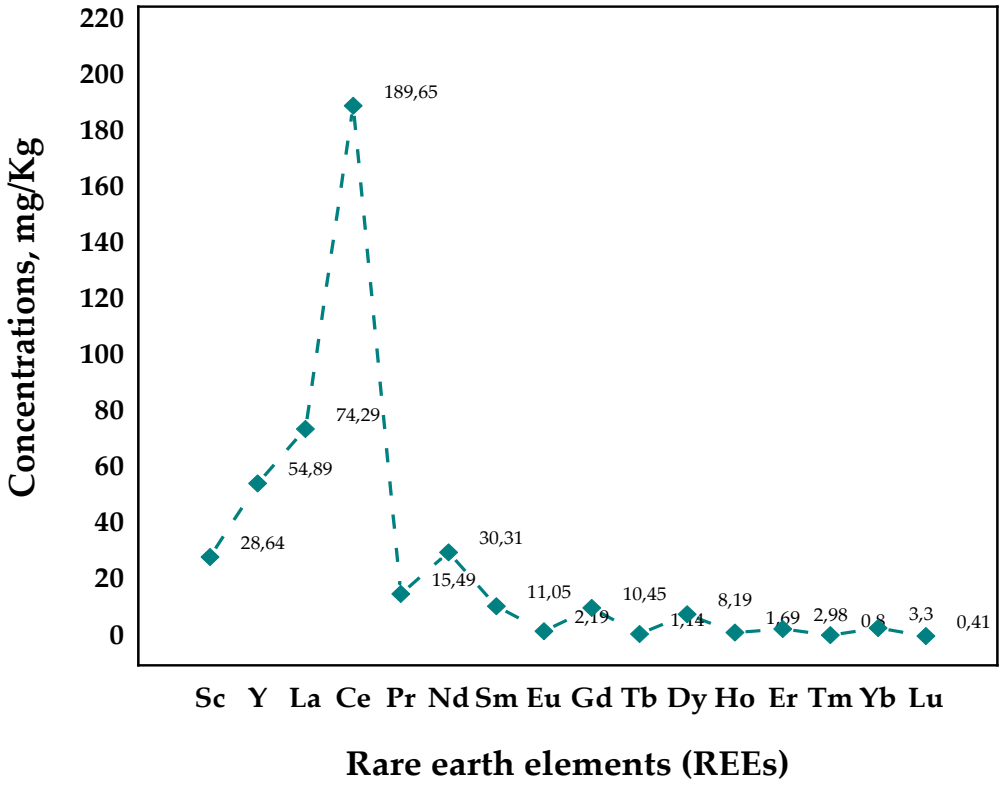

Figure 5.14: The concentration of REEs in sintered CFA-SR.

5.2.3.3 Phase composition analysis

X-ray diffraction analysis confirmed the presence of silica, calcium, and sulphates in sintered CFA-SR, and the results are presented in **Figure 5.15**. Anhydrite ($CaSO_4$, 36 wt.%) was quantified as the main crystalline component, with 1 wt.% basanite and 1.4 wt% quartz. The minor presence of alunogen ($Al_2(SO_4)_3$) may have occurred due to the low leaching efficiency, as it is soluble or may have resulted from the precipitation of calcium sulphates as discussed in **Section 4.2.4.3**, **Chapter 4**. In **Section 2.6.1** of **Chapter 2**, it was described that Jarosite can precipitate in acid sulphate solutions and high temperatures (80-90°C) with sodium sulphate (in this case calcium sulphate), which may explain the presence of Fe in the sintered CFA-SR. However, the presence of haematite (Fe_2O_3, 0.6%) as the crystalline Fe-oxide component could not be concluded. Nonetheless, the remaining composition of the sintered CFA-SR was predominantly 54% amorphous.

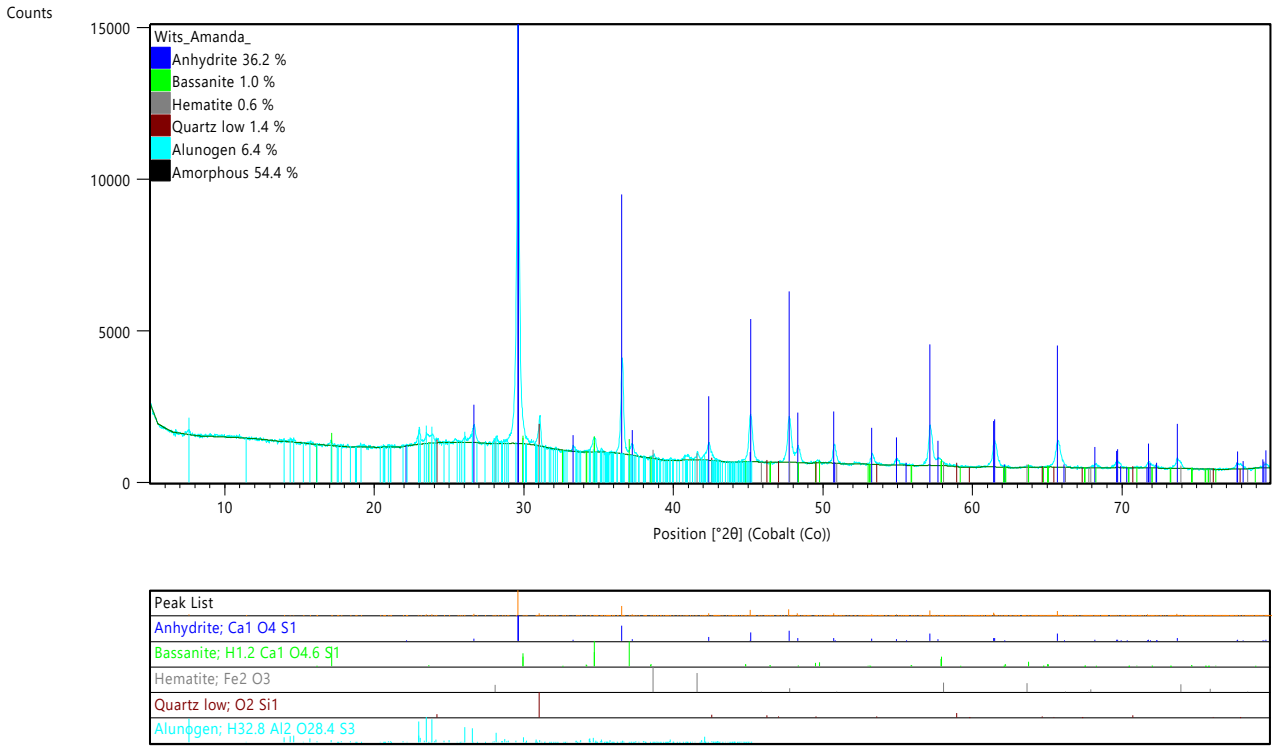

Figure 5.15: XRD analysis of sintered CFA-SR.

SEM-EDS analysis was conducted to establish the distribution of selected REEs, Al, Fe, and Ti in the sintered CFA-SR. **Figure 5.16** presents SEM micrographs of the residue, along with the EDS analysis of specific grains. Surface analysis of the polished block revealed that the residue contained elongated needles and irregular non-spherical particles. EDS analysis of specific points confirmed that the elongated needles were composed of calcium sulphate, while the latter was predominantly a Si-rich phase with traces of elements such as S, Ca, Al, Fe, and REEs. Additionally, as seen in **Figure 5.16 (b)**, calcium sulphates were found both as an independent phase on the surface and entangled within the amorphous component. Further EDS analysis of specific points indicated that REEs were associated with both the Si-rich phase and calcium sulphates.

TIMA analysis was further carried out to establish the distribution of REEs, and the elemental maps are presented in **Figure 5.17**. The morphology of the sintered CFA-SR was similar to that of SEM-EDS analysis, showing calcium sulphate needles and Si-rich amorphous components, as presented in **Figure 5.17 (b)**. The REEs (Ce, Nd, and Y) were detected in amorphous Si-rich components as shown in **Figure 5.17 (c)** to **(f)**. However, due to the nature of the sample, it could not be concluded whether REEs were adsorbed or included within the phases. Nonetheless, the overall results obtained support the observation of the sinter-HCl leaching process, where some REEs remained undissolved even after the pre-treatment process and the changing of lixiviant from H_2SO_4 to HCl (see **Section 4.2.4**, **Chapter 4**). It is therefore recommended that for a thorough comprehension of REEs during the leaching process, mineralogy be conducted on the sintered CFA-SR leached in both HCl and H_2SO_4.

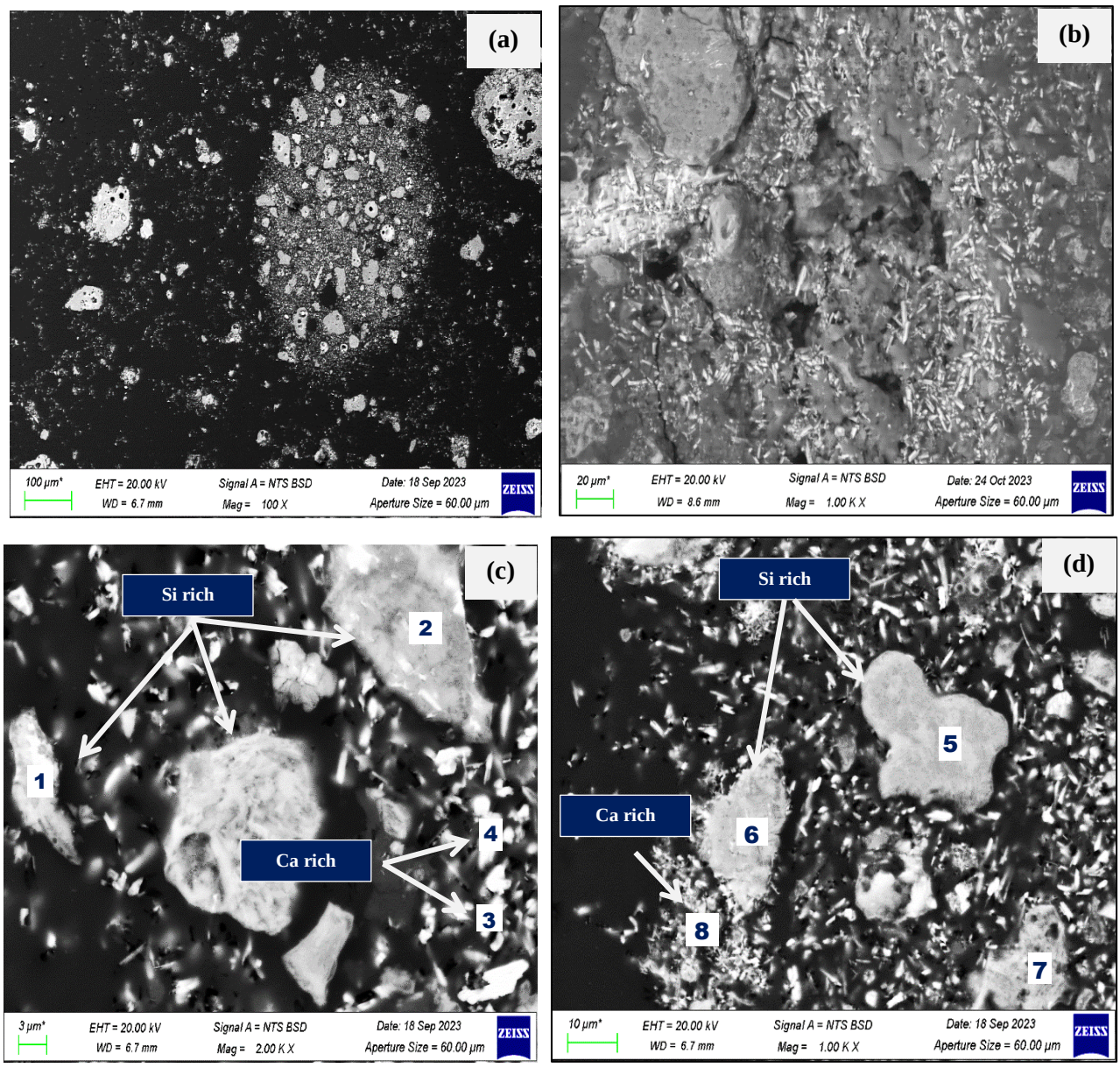

wt.%	C	O	Si	S	Ca	Al	Ti	Fe	Y	Sc	La	Nd	Ce	Others	Phase
1	40.2	38.7	10.6	0.42	0.31	0.45	3.29	5.64	--	--	--	--	--	--	**Si-rich**
2	40.5	39.9	18.09	0.52	0.24	0.37	0.08	0.14	--	--	--	--	--	--	**Si-rich**
3	46.8	25.2	1.13	12.02	13.57	0.17	--	--	0.63	0.21	--	0.03	0.04	--	**Ca-rich**
4	39.6	30.9	1.57	12.67	14.50	0.17	--	--	0.22	0.14	0.04	--	0.04	--	**Ca-rich**
5	49.8	42.9	--	3.45	1.87	0.93	0.31	0.26	--	0.08	--	0.35	--	1.61	**Si-rich**
6	56.5	41.01	--	1.88	0.36	--	--	--	--	--	0.15	0.01	0.15	--	**Si-rich**
7	43.5	37.7	16.78	0.90	0.53	0.26	0.07	0.11	--	0.02	0.03	--	0.12	--	**Si-rich**
8	36.8	38.6	2.99	10.21	11.26	0.09	--	0.02	--	0.09	--	--	--	--	**Ca-rich**

Figure 5.16: SEM analysis of the sintered CFA-SR and EDS analysis of selected marked points.

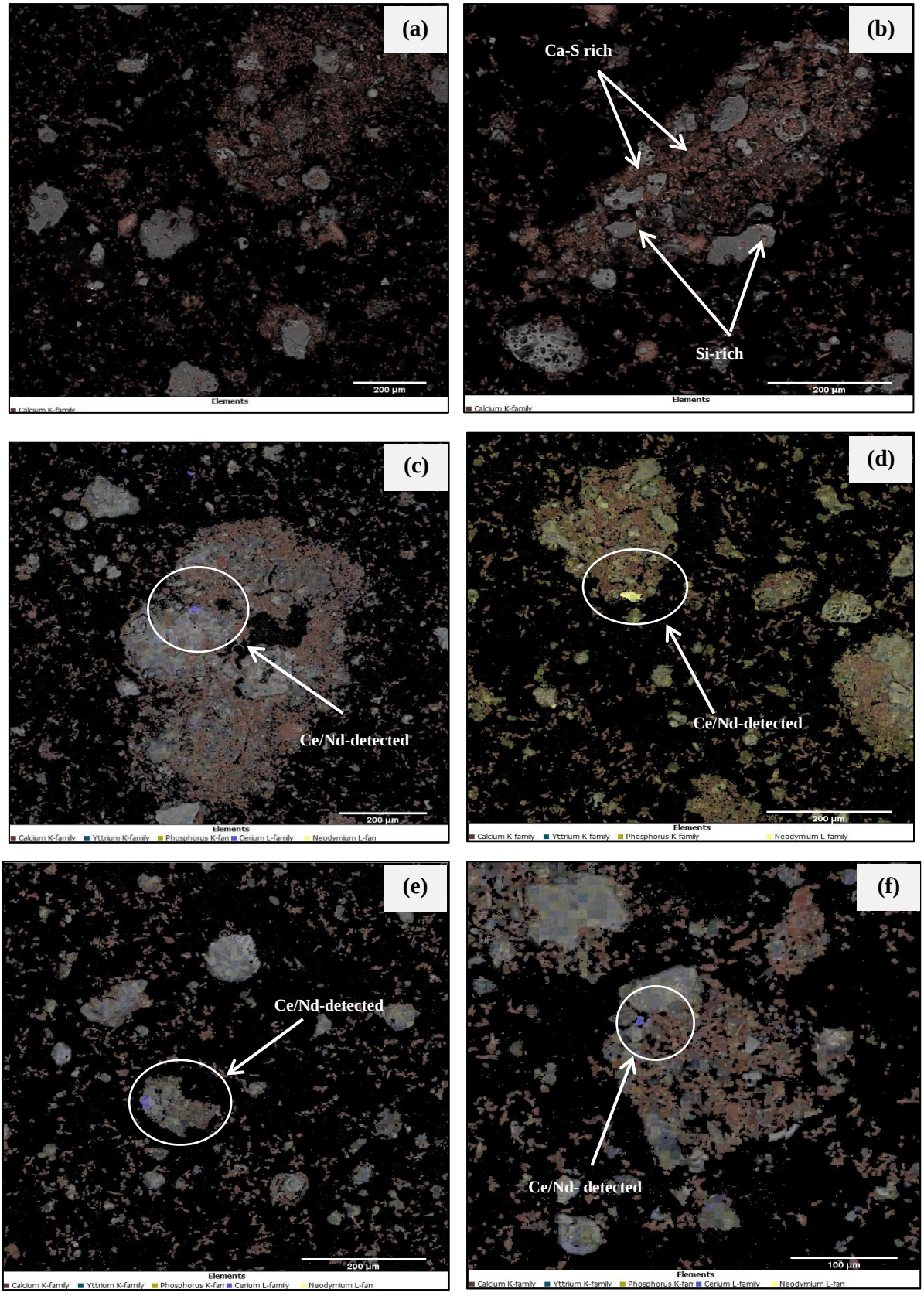

Figure 5.17: Elemental maps showing the distribution of REEs in sintered CFA-SR and their association with the Si-rich and Ca-rich components.

5.2.3.4 Dry digestion – water leach process

The dry digestion-water leach process was considered in this section to further extract metals from the sintered CFA-SR. This technique has been studied for extracting REEs from monazite, eudialyte, and bauxite residue (Liu et al., 2014; Zhang et al., 2015; Maluleke et al., 2023). It is primarily applied to reject impurities such as Si during the leaching process while simultaneously decomposing the REE-bearing minerals (i.e. phosphates identified in **Section 5.2.3.3**). Therefore, the method was also considered in this section. The effect of baking temperature and baking time was investigated in a sulphate system, and the chosen parameters were based on a literature survey (Liu et al., 2014; Zhang et al., 2015; Rivera et al., 2018). In the dry digestion process, the sintered CFA residue was mixed with H_2SO_4 (1:1) to form a paste, followed by fuming at 100-500℃. The dried samples were leached in water at a ratio of 1:10 S/L for 24 hours at 25°C. The pH of the water-leached solution was monitored and controlled at 3-4 (Zhang et al., 2015; Rivera et al., 2018). A detailed experimental procedure is explained in **Section 3.3.3.3**, **Chapter 3**.

Metal Extraction in a Sulphate System

The effect of baking temperature was first evaluated, and the results given in **Figure 5.18** show that an increase in baking temperature leads to an increase in the extraction of metals. These results were anticipated since it is known that an increase in roasting temperature increases the decomposition kinetics of metal sulphates (Borra et al., 2016). However, beyond 300°C, a slight decrease in the extraction was observed. A similar observation was made by Mwamba et al. (2022) for the dry digestion of Co and Cu from an oxide mineral. It was reported that due to the boiling point of sulphuric acid at 337°C, the rate of evaporation results in incomplete sulphation (Mwamba et al., 2022). In this sudy, the metal extraction efficiency was also low, and at 300°C, a maximum of 49.7% Al, 41.8% Fe, and 11% Ti were observed with <30% extraction for the selected REEs. Nonetheless, the primary aim of the dry digestion technique was to control silica gel formation, and indeed silica remained relatively low in solution. Adib et al. (2021) observed a similar behaviour in the apatite ore process.

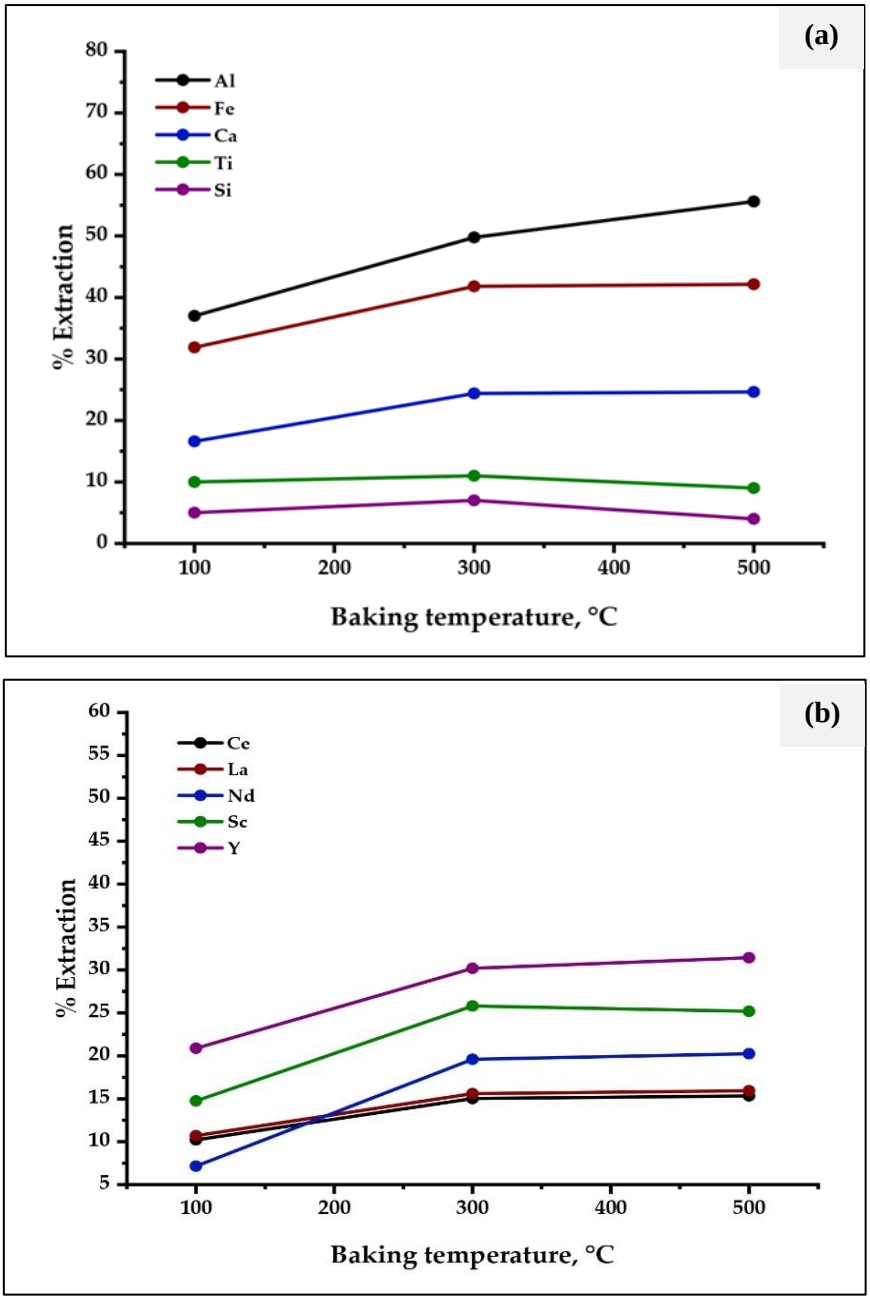

Figure 5.18: Effect of sulphate baking temperature on the extraction of (a) major elements and (b) selected REEs from sintered CFA-SR by baking for 12 hours followed by water leaching at 25℃ for 24 hours.

The effect of baking time was further established over a period of 6 to 24 hours in a sulphate system, with 300℃ used as the optimum baking temperature. It can be observed in **Figure 5.19** that 12 hours is sufficient to bake the metal sulphates, and there is no significant improvement beyond this time. At 12 hours of baking time, the extraction efficiency for REEs was 32.2% Nd, 16.7% La, 15.5% Ce, 31.3% Sc, and 34.5% Y.

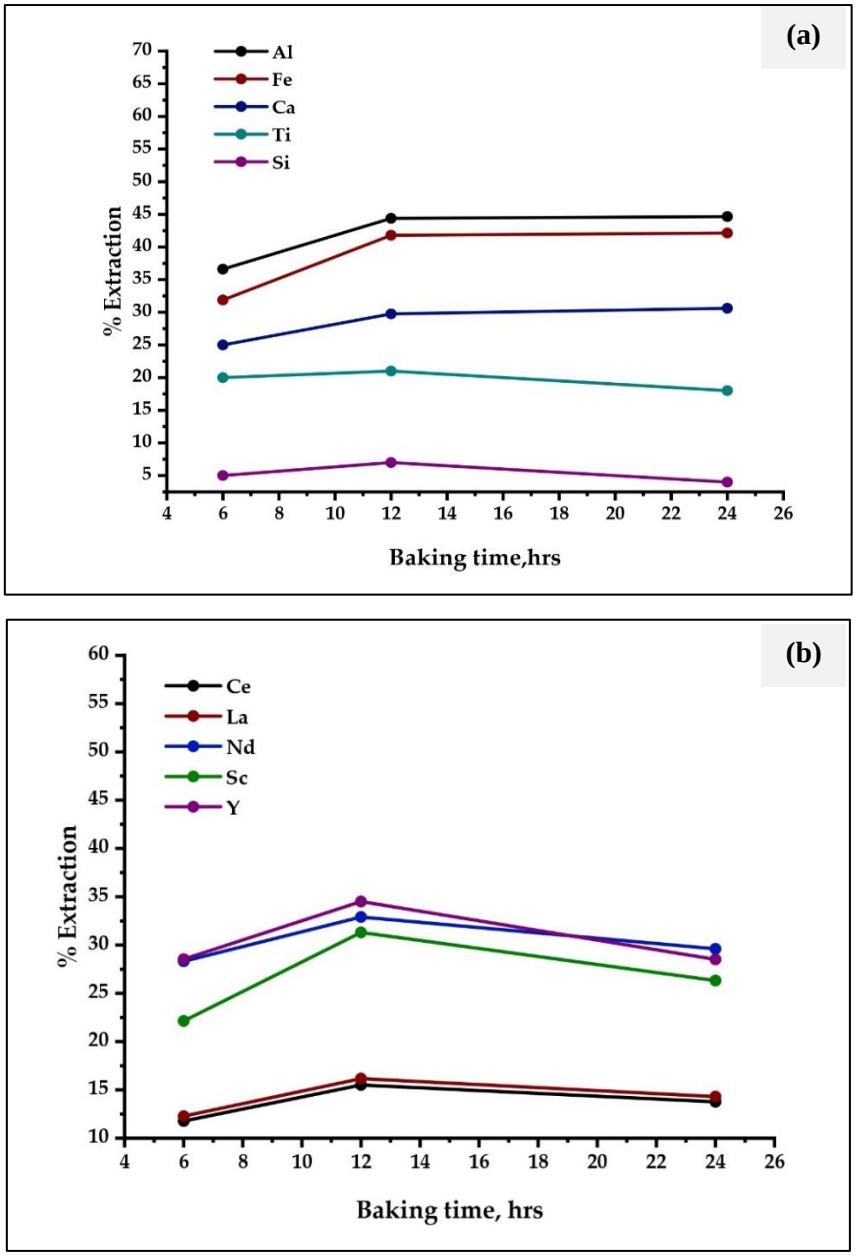

Figure 5.19: Effect of sulphate baking time on the extraction of (a) major elements and (b) selected REEs from sintered CFA-SR by baking at 300℃ followed by water leaching for at 25℃ for 24 hours.

Effect of Dry Digestion on Sintered CFA-SR

The above results also indicate that the maximum extraction of REEs is below 40%. Therefore, similar to the previous chapter, it appears that sulphuric acid may not be a suitable lixiviant for extracting REEs even in the dry digestion technique. One possible explanation for this is that sulphuric acid baking results in a thick, high-strength pasty mass that dries out during the baking process (Alkan et al., 2019). Consequently, further analysis was conducted

in a chloride system to observe any improvement in the percentage extraction. The CFA residue was also mixed homogeneously with HCl (1:1) to form a paste, followed by fuming at 70℃. The fuming temperature was maintained at 70℃ since hydrochloric acid has a low boiling point (Ma et al., 2019). The dried paste was then leached with water at 25℃ for 24 hours, and the results are shown in **Figure 5.20**. A slight improvement in metal extraction was noticed; however, the recovery of REEs remained relatively low. Nonetheless, a maximum extraction was obtained by baking for 6 hours with 44.29% Nd, 45.7% La, 35% Ce, 12% Sc, and 48.1% Y.

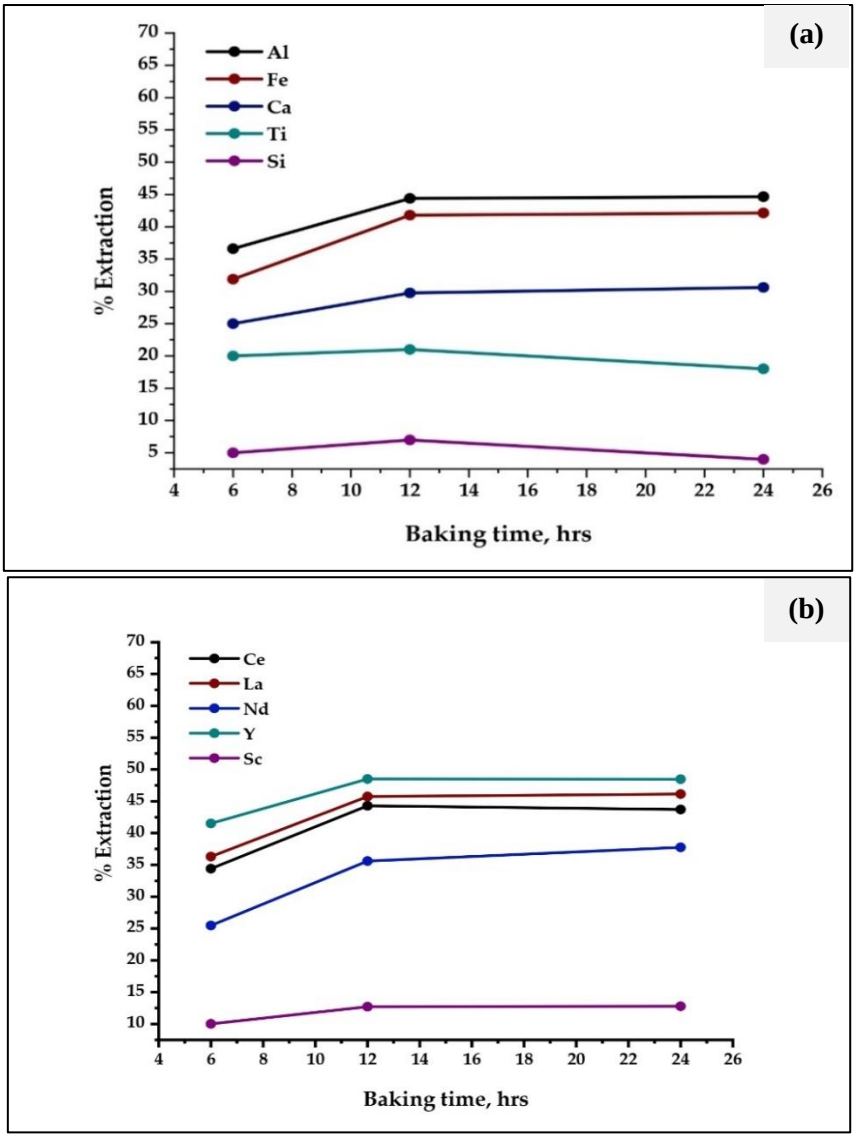

Figure 5.20: Effect of baking time on the extraction of (a) major elements and (b) selected REEs from sintered CFA-SR by baking at 70℃ followed by water leaching for at 25℃ for 24 hours.

SEM analysis in **Figure 5.21** was conducted further to observe the surface transformation of the dried samples in HCl and H_2SO_4. Initially, the sintered CFA-SR displayed smooth, elongated needle-shaped calcium sulphate with an amorphous component containing mixtures of elements such as Si, Al, Fe, Ti, Ca, and S (see **Figure 5.21 (a)**). The dried sample in HCl at 70℃ showed minor chipping on the surface of the calcium sulphate, with no significant transformation observed in the amorphous component. In the sulphate-dried sample at 300℃, the amorphous component also remained relatively unchanged; however, the smooth needle-shaped calcium sulphates, showed some chipping and cracks on the surface due to the higher baking temperature (see **Figure 5.21 (b)**). In a study by Brückner et al. (2020), a monazite REE-bearing grain showed some cracks in phosphogypsum processing with the dry digestion technique in the sulphate system. Such observations were not detected in this study, both on the mounted stubs and polished blocks due to the trace concentrations of REEs. Therefore, it is recommended that the transformation of REEs in the dried samples be further studied for a comprehensive understanding of their behaviour.

The phase composition analysis in **Section 5.2.3.3** showed that REEs could be associated with crystalline calcium sulphates and amorphous Si-rich phases. **Section 2.5.3.3** of **Chapter 2** discussed the precipitation of REEs with calcium sulphate in three ways: (i) adsorption on the surface, (ii) integrated, or (iii) independent sulphate (Guan et al., 2022; Yahorava et al., 2018; Walawalkar et al., 2016). The three precipitation mechanisms of the REEs with calcium sulphate could assist in understanding their leaching behaviour in the residue. However, this study could not quantify how REEs were precipitated in the sintered CFA residue due to the nature of the sample. Nonetheless, based on the phase composition analysis, it can be hypothesised that the low recovery results from the association with the Si-rich phase, calcium sulphates, and discrete minerals that did not transform in the sintering process as discussed in **Section 4.2.3.3** of **Chapter 4**.

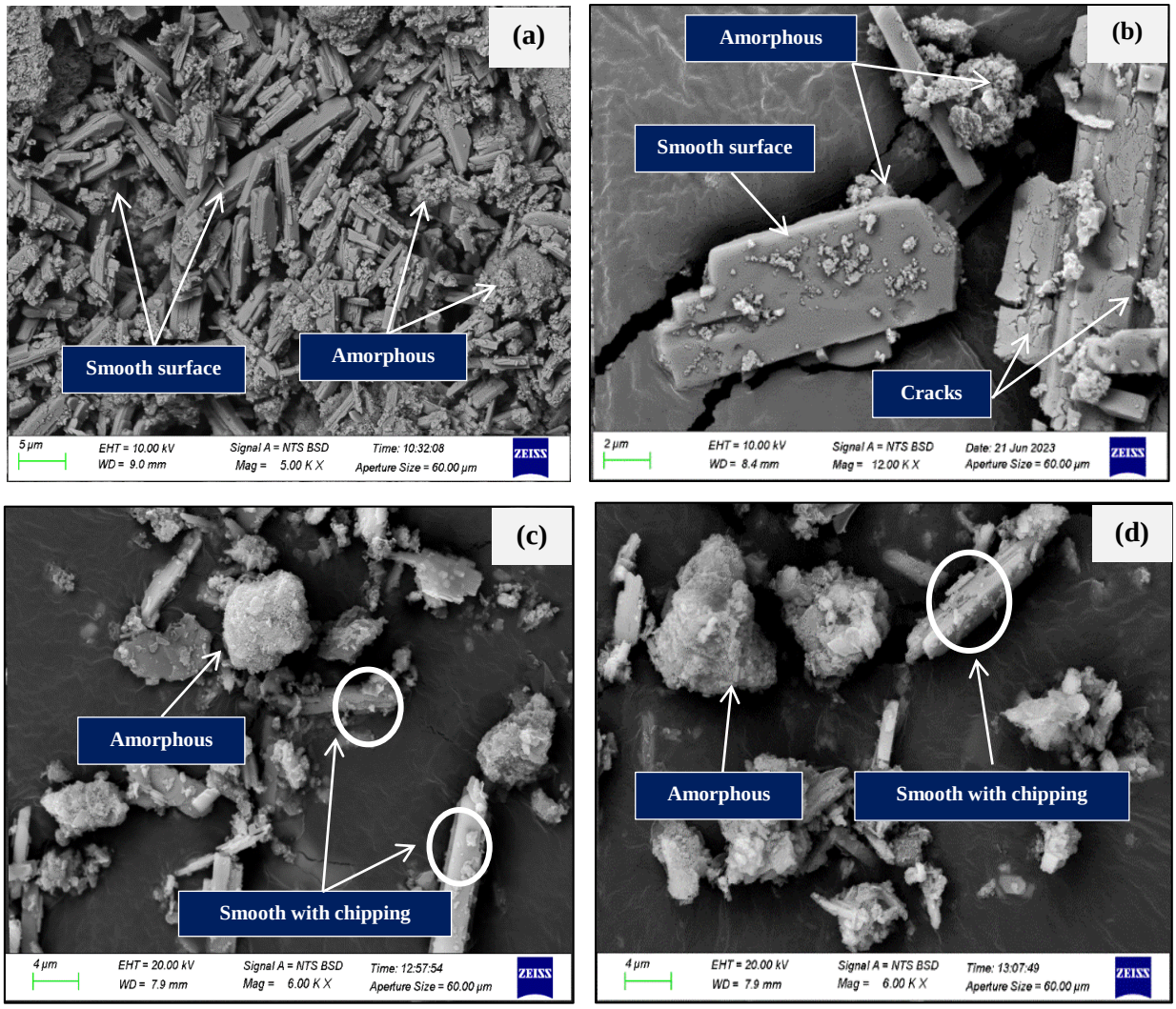

Figure 5.21: SEM micrograph analysis of sintered CFA-SR (a) before treatment and (b-c) after dry digestion in H_2SO_4 and HCl.

5.2.3.5 Production of REE concentrate

The REE-chloride solution from the above section was further processed to produce REE concentrate due to the higher concentrations in the solution. An orange precipitate in **Figure 5.22** was generated after the dry digestion-water leach process in an attempt to generate an REE concentrate. Previous research suggests that rare earth oxalates can be selectively precipitated at pH ~2 from impurities such as Al, Fe, and Ti (Chi and Xu, 1999; Yang et al., 2016). However, precipitation was not detected by visual inspection in this research, possibly due to the trace concentration of REEs in the solution. Consequently, adjusting the pH to >2 led to the formation of the orange precipitate. SEM analysis showed irregularly shaped blocks that are agglomerated, and the micrograph of the precipitate is presented in **Figure 5.22** (see

Figure B.6 for EDS analysis). XRF and ICP-MS were further conducted to determine the chemical composition of the oxalate precipitate and the analysis is presented in **Table 5.15**.

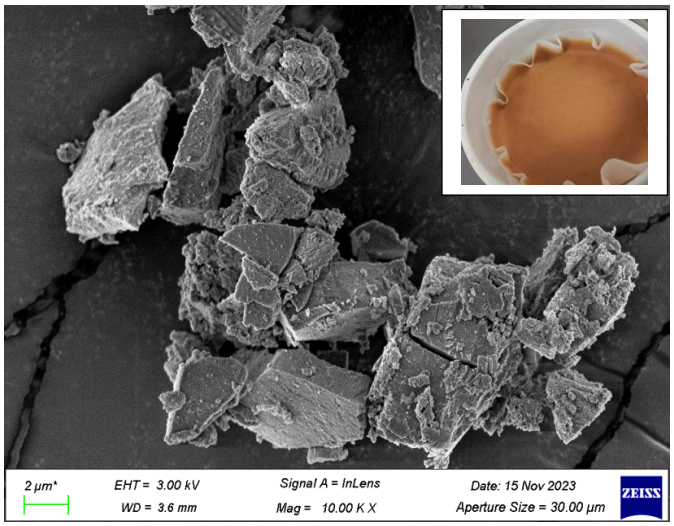

Figure 5.22: The generated concentrate after oxalate precipitation.

Table 5.15: Bulk chemical composition of the oxalate precipitate.

Analyte	Fe_2O_3	Al_2O_3	SiO_2	TiO_2	CaO	ZrO	MnO	SO_3	ΣREEs (ppm)
wt.%	7.656	10.395	1.534	0.355	0.262	0.019	0.021	0.014	66.21

The concentrate contained elevated concentrations of impurities such as Al and Fe. These impurities may have resulted from the complexation of these elements with oxalate in the solution, leading to their co-precipitation with REEs. Normally, REE-oxalates are reported as a white precipitate, but in this study, an orange oxalate, often caused by iron complexation, was observed (Kumari et al., 2021; Liu et al., 2023). FT-IR analysis was also used to confirm the precipitation of metal oxalates, and the spectrum is presented in **Figure 5.23**. Metal ions can coordinate with organic ligands, resulting in a shift of the peaks after coordination (Kim et al., 2020). Similarly, in this study, there was a shift in the major peaks from oxalate to metal oxalate.

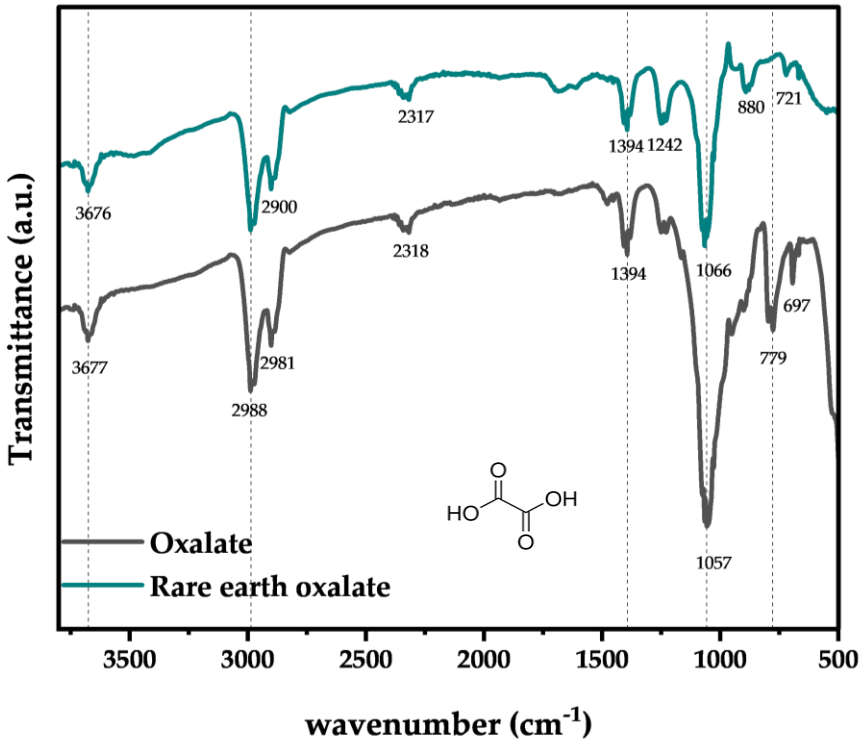

Figure 5.23: FT-IR spectrum of the generated concentrate after oxalate precipitation.

The overall findings suggest that the REE-concentrated solution from the dry digestion sample could be further purified to produce a cleaner concentrate for the SACREF feed. Alternatively, the generated REE-oxalate precipitate could be compared to the standard for the SACREF feed, which is currently unavailable.

5.3 Conclusion

This chapter explored the optimisation of the sinter-H_2SO_4 leach process for alumina production and further processing of the generated CFA leach liquor and sintered CFA residue. The key findings are summarised as follows:

- In the optimisation process, leaching temperature and H_2SO_4 concentration were identified as the significant variables. The interaction between these variables was also observed, and it was found that leaching temperature has a positive effect on Al extraction, while H_2SO_4 concentration has a negative effect. Consequently, to optimise the process, the latter was maximised at 80℃, while the former was decreased to 6 M H_2SO_4 to attain 77.1% Al extraction.

- The generated CFA leach liquor was processed to simulate smelter-grade alumina. Due to the high Ti and Fe concentrations in the solution, an integrated SX and crystallisation process followed by calcination was used to produce TiO_2 and Al_2O_3. The synthesised Al_2O_3 was graded according to smelter quality and was found to be suitable for commercial applications. The synthesised TiO_2 was graded as a Type II pigment product. However, for consideration in wastewater treatment, it was found to have low purity and surface properties. Consequently, further research was recommended to improve these properties for the application of TiO_2 as a photocatalyst. In the overall process, an Fe(II)-rich solution was generated and will be further processed in **Chapter 6**.

- The sintered CFA-SR was used as the feed concentrate for the second leaching stage. The residue was characterised by XRD as amorphous with anhydrite and quartz as the main crystalline compoments. REEs were associated with the Si-rich and Si-Ca-rich phases and also occurred as discrete REE-bearing phases. Therefore, a dry digestion-water leaching technique was employed for metal extraction, minimising the formation of silica gel. The dry digestion process resulted in low recoveries of REEs in both the sulphates and the chloride system due to the complex phase composition and nature of the residue. However, the dried sample with HCl gave better REE extraction and thus, the REE-concentrated solution was subsequently used for selective oxalate precipitation. However, the precipitate generated contained high levels of impurities.

- Overall, the experimental results indicate that a two-step leaching process can be employed to extract Al, Fe, Ti, and REEs. This would involve using the sinter-H_2SO_4 leach process, which is efficient for extracting Al, Fe, and Ti, followed by an alternative process (dry digestion-water leach) for the extraction of REEs from the sintered CFA-SR.

In this chapter, smelter-grade alumina and pigment-grade titania were produced as potential saleable products. A rare earth concentrate was also generated to be considered as a SACREF feed. However, due to the low purity of the concentrate, the REE-concentrated solution obtained after the dry digestion-water leach process was regarded as the final product for further economic evaluation in **Chapter 7**. In addition, an Fe(II)-rich solution and a

secondary solid residue were generated as by-products. Therefore, the next chapter (**Chapter 6**) will focus on the potential applications of these by-products for wastewater treatment.

References

Adib, A., Ahmadi, R. and Rahimi, E., 2021. The Recovery of Rare-Earth Elements from Apatite Concentrate by Acid and Digestion-Water Leaching Processes in Morvarid Iron Mine, Iran. *Journal of Mining Science* 57, 131-143.

Alkan, G., Yagmurlu, B., Gronen, L., Dittrich, C., Ma, Y., Stopic, S. and Friedrich, B., 2019. Selective silica gel free scandium extraction from Iron-depleted red mud slags by dry digestion. *Hydrometallurgy* 185, 266-272.

Borra, C.R., Mermans, J., Blanpain, B., Pontikes, Y., Binnemans, K. and Van Gerven, T., 2016. Selective recovery of rare earths from bauxite residue by combination of sulfation, roasting and leaching. *Minerals Engineering* 92, 151-159.

Bourahla, S., Ali Benamara, A. and Kouadri Moustefai, S., 2014. Infrared spectra of inorganic aerosols: ab initio study of $(NH_4)_2SO_4$, NH_4NO_3, and $NaNO_3$. *Canadian Journal of Physics* 92(3), 216-221.

Box, G.E., Hunter, W.H. and Hunter, S., 1978. Statistics for experimenters. John Wiley and sons New York.

Brückner, L., Elwert, T. and Schirmer, T., 2020. Extraction of rare earth elements from phospho-gypsum: concentrate digestion, leaching, and purification. *Metals* 10(1), 131.

Chi, R. and Xu, Z., 1999. A solution chemistry approach to the study of rare earth element precipitation by oxalic acid. *Metallurgical and Materials Transactions B* 30, 189-195.

Chougala, L.S. and Yatnatti, M.S., Linganagoudar, R.K., Kamble, R.R. and Kadadevarmath, J.S., 2017. A simple approach on synthesis of TiO_2 nanoparticles and its application in dye sensitized solar cells. *Journal of Nano and Electronic Physics* 9(4), 04005.

Desouky, O.A.E.N., 2006. Liquid-liquid extraction of rare earth elements from sulphuric acid. PhD thesis, Department of Chemistry, University of Leeds, England.

Gázquez, M.J., Bolívar, J.P., García-Tenorio García-Balmaseda, R. and Vaca, F., 2014. A review of the production cycle of titanium dioxide pigment. *Materials Sciences and Applications* 5(7), 441-458.

Gil, A.F., Salgado, L., Galicia, L. and González, I., 1995. Predominance-zone diagrams of Fe (III) and Fe (II) sulphate complexes in acidic media. Voltammetric and spectrophotometric studies. *Talanta* 42(3), 407-414.

Guan, Q., Sui, Y., Liu, C., Wang, Y., Zeng, C., Yu, W., Gao, Z., Zang, Z. and Chi, R.A., 2022. Characterization and leaching kinetics of rare earth elements from phosphogypsum in hydrochloric acid. *Minerals* 12(6), 703.

Hiskey, J.B. and Copp, R.G., 2018. Recovery of yttrium and neodymium from copper pregnant leach solutions by solvent extraction. *Hydrometallurgy* 177, 21-26.

Hlekelele, L., 2017. Synthesis, Characterization and Photocatalytic Activity of TiO_2 and TiO_2 Based Quaternary Mixed Metal Oxides Supported on Carbon and Fly Ash Based Materials. PhD thesis, Department of Chemistry, University of the Witwatersrand, South Africa.

Irshad, M.A., Nawaz, R., UR Rehman, M.Z., Adrees, M., Rizwan, M., Ali, S., Ahmad, S. and Tasleem, S., 2021. Synthesis, characterization and advanced sustainable applications of titanium dioxide nanoparticles: A review. *Ecotoxicology and Environmental Safety* 212, 111978.

Keiteb, A.S., Saion, E., Zakaria, A., Soltani, N. and Abdullahi, N., 2016. A modified thermal treatment method for the up-scalable synthesis of size-controlled nanocrystalline titania. *Applied Sciences* 6(10), 295.

Kim, S.M., Yoon, I.H., Kim, I.G., Park, C.W., Sihn, Y., Kim, J.H. and Park, S.J., 2020. Cs desorption behavior during hydrothermal treatment of illite with oxalic acid. *Environmental Science and Pollution Research* 27, 35580-35590.

Kumari, A., Raj, R., Randhawa, N.S. and Sahu, S.K., 2021. Energy efficient process for recovery of rare earths from spent NdFeB magnet by chlorination roasting and water leaching. *Hydrometallurgy* 201, 105581.

Liu, P., Zhao, S., Xie, N., Yang, L., Wang, Q., Wen, Y., Chen, H. and Tang, Y., 2023. Green Approach for Rare Earth Element (REE) Recovery from Coal Fly Ash. *Environmental Science and Technology* 57(13), 5414-5423.

Liu, Y., Liu, Z. and Liu, M., 2014. Decomposition process of rare earth rough concentrate by low temperature sulfation. *Journal of Non-Ferrous Metals* 24, 3147-3154.

Ma, Y., Stopic, S. and Friedrich, B., 2019. Hydrometallurgical Treatment of an Eudialyte Concentrate for Preparation of Rare Earth Carbonate. *Johnson Matthey Technology Review* 63(1), 2-13.

Ma, Y., Stopic, S., Xakalashe, B., Ndlovu, S., Forsberg, K. and Friedrich, B., 2021. A cleaner approach for recovering Al and Ti from coal fly ash via microwave-assisted baking, leaching, and precipitation. *Hydrometallurgy* 206, 105754.

Maluleke, K.C., Goso, X.C. and Ndlovu, S., 2023. Investigations into the extraction of rare earth elements from Zandkopsdrift ore using the sulfation roasting process. *Minerals Engineering* 191, 107902.

Matjie, R., Bunt, J. and Van Heerden, J., 2005. Extraction of alumina from coal fly ash generated from a selected low rank bituminous South African coal. *Minerals Engineering* 18(3), 299-310.

McDowell, W.J., Seeley, F.G., 1981. Recovery of Aluminum and other Metal Values from Fly Ash. U.S. Patent 4252777.

Mwamba, P., Masinja, J.H., Manchisi, J. and Kabondo, L., 2022. Sulphuric acid bake-leach process for the treatment of mixed copper-cobalt oxide ores. *Journal of Minerals and Materials Characterization and Engineering* 10(2), 174-184.

Nachit, W., Ahsaine, H.A., Ramzi, Z., Touhtouh, S., Goncharova, I. and Benkhouja, K., 2022. Photocatalytic activity of anatase-brookite TiO_2 nanoparticles synthesised by sol gel method at low temperature. *Optical Material*s 129, 112256.

Rajan, N.D., Jayakumar, S., Krishnan, S., Rajesh, G.M., Sambasivam, R., Sylaja, R., Gayathri, G.S. and Alwar, S., 2020. Growth and Studies on Aluminium Ammonium Sulphate Single Crystal, *International Journal for Research in Applied Science and Engineering Technology* 8(1), 421-427.

Rampou, M., Ndlovu, S. and Shemi, A., 2017. Purification of coal fly ash leach liquor for alumina recovery using an integrated precipitation and solvent extraction process. *Journal of Sustainable Metallurgy* 3, 782-792.

Rivera, R.M., Ulenaers, B., Ounoughene, G., Binnemans, K. and Van Gerven, T., 2018. Extraction of rare earths from bauxite residue (red mud) by dry digestion followed by water leaching. *Minerals Engineering* 119, 82-92.

Rushwaya, M. and Ndlovu, S., 2017. Purification of coal fly ash leach liquor by solvent extraction: identification of influential factors using design of experiments. *International Journal of Mineral Processing* 164, 11-20.

Salman, A.D., Juzsakova, T., Mohsen, S., Abdullah, T.A., Le, P.C., Sebestyen, V., Sluser, B. and Cretescu, I., 2022. Scandium recovery methods from mining, metallurgical extractive industries, and industrial wastes. *Materials* 15(7), 2376.

Sanna, A., Gaubert, J. and Maroto-Valer, M.M., 2016. Alternative regeneration of chemicals employed in mineral carbonation towards technology cost reduction. *Chemical Engineering Journal* 306, 1049-1057.

Schack, C.H., 1965. Recovery of scandium from uranium plant iron sludge and from wolframite concentrates. US Department of the Interior, Bureau of Mines.

Seidel, A. and Zimmels, Y., 1998. Mechanism and kinetics of aluminum and iron leaching from coal fly ash by sulphuric acid. *Chemical Engineering Science* 53(22), 3835-3852.

Shemi, A., Ndlovu, S., Sibanda, V. and Van Dyk, L., 2014. Extraction of aluminium from coal fly ash: identification and optimization of influential factors using statistical design of experiments. *International Journal of Mineral Processing* 127, 10-15.

Sole, K.C., 1999. Recovery of titanium from the leach liquors of titaniferous magnetites by solvent extraction: Part 1. Review of the literature and aqueous thermodynamics. *Hydrometallurgy* 51(2), 239-253.

Sing, K. S., 1985. Reporting physisorption data for gas/solid systems with special reference to the determination of surface area and porosity (Recommendations 1984). *Pure and Applied Chemistry* 57(4), 603-619.

Terry, B., 1983. The acid decomposition of silicate minerals part II. Hydrometallurgical applications. *Hydrometallurgy* 10(2), 151-171.

Villabona-Leal, E.G., Escobar-Villanueva, A.G., Ovando-Medina, V.M., Pérez-Pérez, E.B., Díaz-Flores, P.E., Romero-Galarza, A. and Marquez-Herrera, A., 2020. Semiconducting polypyrrole@ TiO_2 pure anatase nanoparticles for photodegradation of reactive red 120 azo dye. *Journal of Materials Science: Materials in Electronics* 31, 12178-12190.

Walawalkar, M., Nichol, C.K. and Azimi, G., 2016. Process investigation of the acid leaching of rare earth elements from phosphogypsum using HCl, HNO_3, and H_2SO_4. *Hydrometallurgy* 166, 195-204.

Wang, W., Pranolo, Y. and Cheng, C.Y., 2011. Metallurgical processes for scandium recovery from various resources: A review. *Hydrometallurgy* 108(1-2), 100-108.

Yahorava, V., Bazhko, V. and Freeman, M., 2016. Viability of phosphogypsum as a secondary resource of rare earth elements. XXVIII International Mineral Processing Congress Proceeding, 11-15 September 2016, Quebec City, Canada. Canadian Institute of Mining Metallurgy & Petroleum (CIM), 1-16. ISBN: 978-1-926872-29-2.

Yahorava, V., Lakay, E. and Clark, W., 2018. Hydrothermal Pre-Treatment Process of phosphogypsum for enhanced rare earths recovery. Beneficiation of phosphates VIII, 4-29 May-April 2018, Century City Conference Center Cape Town, South Africa. Engineering Conferences International (ECI) Digital Archives. Available online https://dc.engconfintl.org/phosphates_viii (Accessed 07-08-2022).

Yang, Y., Wang, X., Wang, M., Wang, H. and Xian, P., 2016. Iron recovery from the leached solution of red mud through the application of oxalic acid. *International Journal of Mineral Processing* 157, 145-151.

Zhang, Z., Jia, Q. and Liao, W., 2015. Progress in the separation processes for rare earth resources. *Handbook on the Physics and Chemistry of Rare Earths* 48, 287-376.

6 POTENTIAL COAGULANT AND ADSORBENT FROM CFA PROCESSING

6.1 Hypothesis and Objectives

In **Chapter 5**, an iron-rich solution and a CFA secondary solid residue (CFA-SSR) were generated as by-products. Therefore, in this chapter, the potential applications as a coagulant and an adsorbent were respectively evaluated. The objectives of this part of the experimental work were set to achieve the following:

- A literature survey in **Section 2.7.1** of **Chapter 2** established that Al and Fe-based coagulants can be generated from CFA for commercial applications. In this study, Al was recovered as a smelter-grade resource; therefore, only the Fe-based coagulant was considered. Chemical precipitation is commonly used to generate coagulants from mine solutions (Han et al., 2015; Hove et al., 2009; Mwewa et al., 2019). Therefore, the precipitation process was utilised to recover iron(III) hydroxide/oxyhydroxide from the Fe(II)-rich solution generated in **Section 5.2.2**, **Chapter 5** for the potential synthesis of Fe-based coagulants.
- It has also been reviewed that while chemical precipitation is cost-effective and easy to operate, the hydroxide sludge generated is often difficult to dewater. The addition of seeding materials (i.e. magnetite/haematite) has been reported to provide a large surface area, which consequently promotes settling and solid-liquid separation (Karapinar, 2003; Hove et al., 2009). In this study, the extracted CFA-MF in **Section 4.2.2**, **Chapter 4**, was recycled as a potential seed for ferrihydrite precipitation.
- The literature surveyed in **Section 2.7.2** of **Chapter 2** also suggests that the development of adsorbent materials from waste resources, such as CFA, provides an inexpensive alternative for wastewater treatment. In this study, the generated CFA-SSR in **Section 5.2.3**, **Chapter 5**, was characterised and analysed as a potential adsorbent for wastewater treatment.

6.2 Results and Discussion

6.2.1 Recovery of Fe – based coagulants

The following sections present the synthesis of Fe-based coagulant and its potential application in wastewater treatment. A detailed experimental procedure is reported **Section 3.3.4.3** and **3.3.5.1 (**see **Chapter 3**).

6.2.1.1 Fe(II) oxidation and precipitation

According to the metal hydroxide solubility table in **Figure 2.17** (see **Chapter 2**), ferrous sulphates can be directly precipitated by $Ca(OH)_2$ or NaOH at pH >6 to produce ferrous hydroxide/oxyhydroxide ($Fe(OH)_2$). In this study, ferric hydroxide/oxyhydroxide ($Fe(OH)_3$), which precipitates at pH ~3, was considered to minimise alkaline consumption and co-precipitation with elements such as Mg, Mn, and REEs. Additionally, a literature survey also indicated that the rate of Fe(II) oxidation is strongly dependent on pH >4 (Hove et al., 2009; Mwewa et al., 2019). Therefore, in this study, Fe(II) oxidation and precipitation were considered at pH 5 (see **Equation 6.1** to **6.4**) (Daoud and Karamanev, 2006). The standard acid-base titration method shown in **Figure 6.1** was used to adjust the solution pH, and approximately 110 mL of NaOH was required to increase the pH from 1.2 to 5.1.

$$4Fe^{2+} + 4H^{+} + O_{2(aq)} \xrightarrow{Air/O_2} 4Fe^{3+} + 2H_2O \quad \textbf{6.1}$$

$$Fe^{3+} + H_2O \leftrightarrow FeOH^{2+} + H^{+} \quad \textbf{6.2}$$

$$Fe^{3+} + 2H_2O \leftrightarrow Fe(OH)_2^{+} + 2H^{+} \quad \textbf{6.3}$$

$$Fe^{3+} + 3H_2O \leftrightarrow Fe(OH)_3 + 3H^{+} \quad \textbf{6.4}$$

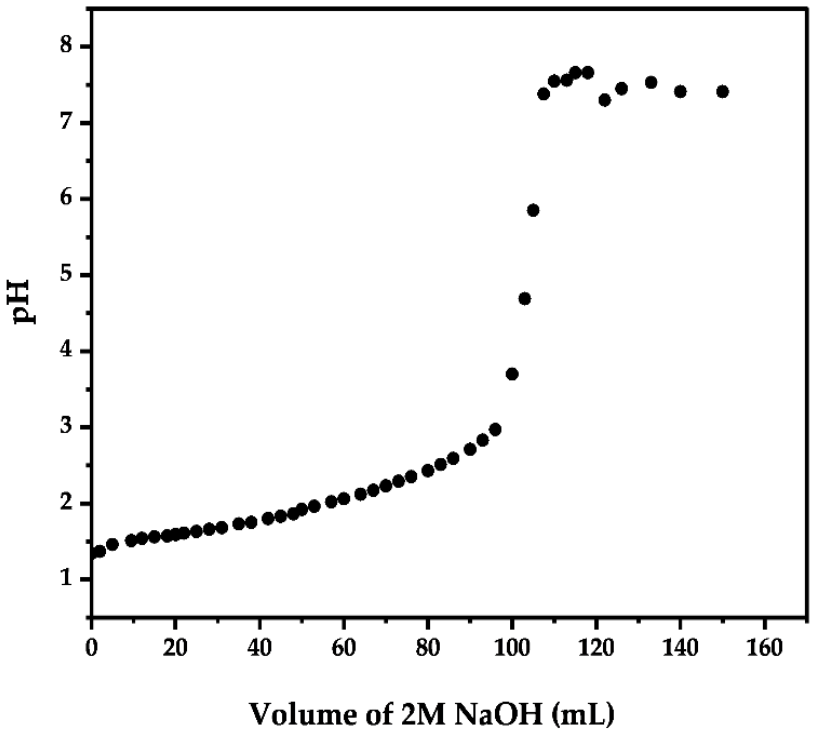

Figure 6.1: Standard acid base titration curve with 2 M NaOH.

A major challenge often encountered in the precipitation of iron(III) hydroxide/oxyhydroxide from mine effluents/solutions is the formation of a gelatinous precipitate that is difficult to dewater. Seeding has been reported as an effective alternative for iron recovery by promoting settling and solid-liquid separation. The addition of seeding materials results in supersaturation and suppresses homogeneous nucleation (Karapinar, 2003; Hove et al., 2009; Han et al., 2015; Kefeni et al., 2017). Karapinar (2003) investigated the magnetic water separation (MWS) of ferrihydrite using magnetite as the seeding material. During MWS, magnetite was dispersed in the solution and provided a surface for the nucleation of the ferrihydrite precipitate. In the process, more than 90% of Fe(III) was easily recovered at pH >6. A similar effect was noted by Hove et al. (2007) and Han et al. (2015) during the precipitation process, where magnetite (Fe_3O_4), haematite (Fe_2O_3), and goethite (FeOOH) were used as solid seeds for Fe(III) recovery. Notably, in these studies, the seeding material was either purchased commercially or obtained from mineral ore processing. Consequently, in this study, the extracted CFA-MF in **Section 4.2.2** of **Chapter 4** was characterised as a magnetite/haematite component with crystalline mullite and quartz. Therefore, CFA-MF was considered a cost-effective solid seed for Fe(III) recovery.

The iron (Fe(II))-rich solution generated in **Section 5.2.2**, **Chapter 5**, was processed in this study using oxidation and precipitation processes in a 1 L reactor, as shown in **Figure 3.7** (see **Chapter 3**). The change in ferrous (Fe(II)) concentration at pH 5 was monitored, and the analysis is presented in **Figure 6.2**. As demonstrated in the graph, Fe(II) oxidation was achieved over time in seeded and unseeded solutions. Hove et al. (2009) used haematite and goethite as solid seeds and reported that they have a catalytic effect on ferrous oxidation. As shown in the graph, the rate of oxidation after seeding (Cs = 0.5 and 1.0) was also slightly faster than that of the baseline (Cs = 0). The reactions were allowed to proceed for 24 hours to ensure efficient oxidation and precipitation.

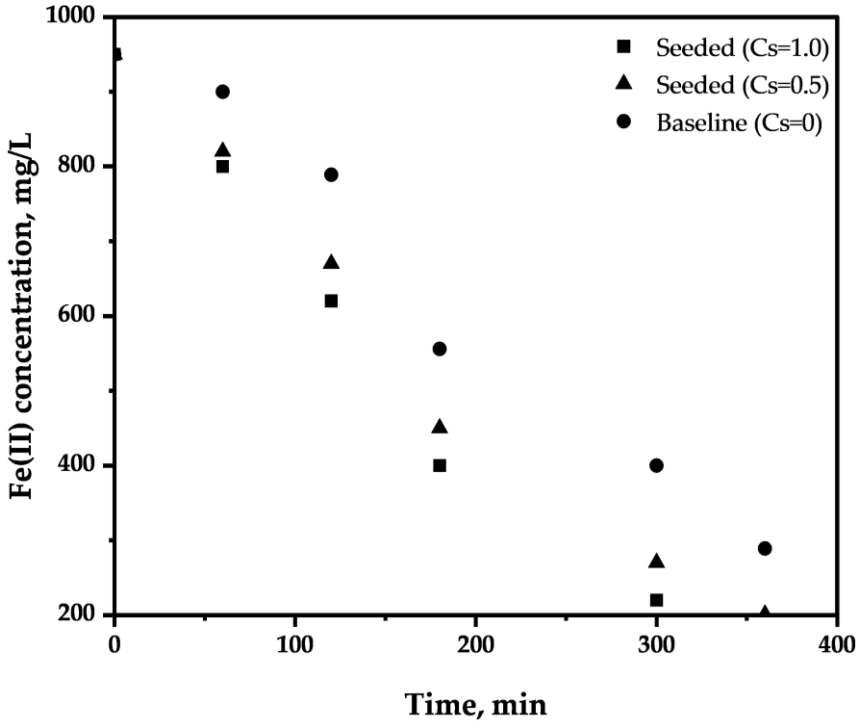

Figure 6.2: Plot of Fe(II) oxidation over time at pH 5 and 25℃.

The effect of seeding on Fe(III) recovery is also presented in **Figure 6.3**. The recoveries are the average of n = 3 (triplicate analysis) with error bars related to the standard deviation (SD). Although no significant difference was observed in the Fe(III) recoveries before and after seeding, the seeded iron precipitates were easily filtered using vacuum filtration. Additionally, the analysis given in **Table 6.1** showed that elements such as Ca, Mn, Mg, Zn, and REEs remain in the solution after precipitation (see **Table B.2**, **Appendix B** for REEs). Similar findings by Wei and Viadero (2007) and Mwewa et al. (2019) also showed that at pH

5-7, the precipitation of these elements is almost negligible. It is also noteworthy that in this pH range, saleable products such as magnesium sulphate (Epsom) and zinc sulphate can be recovered; however, this was beyond the scope of this section.

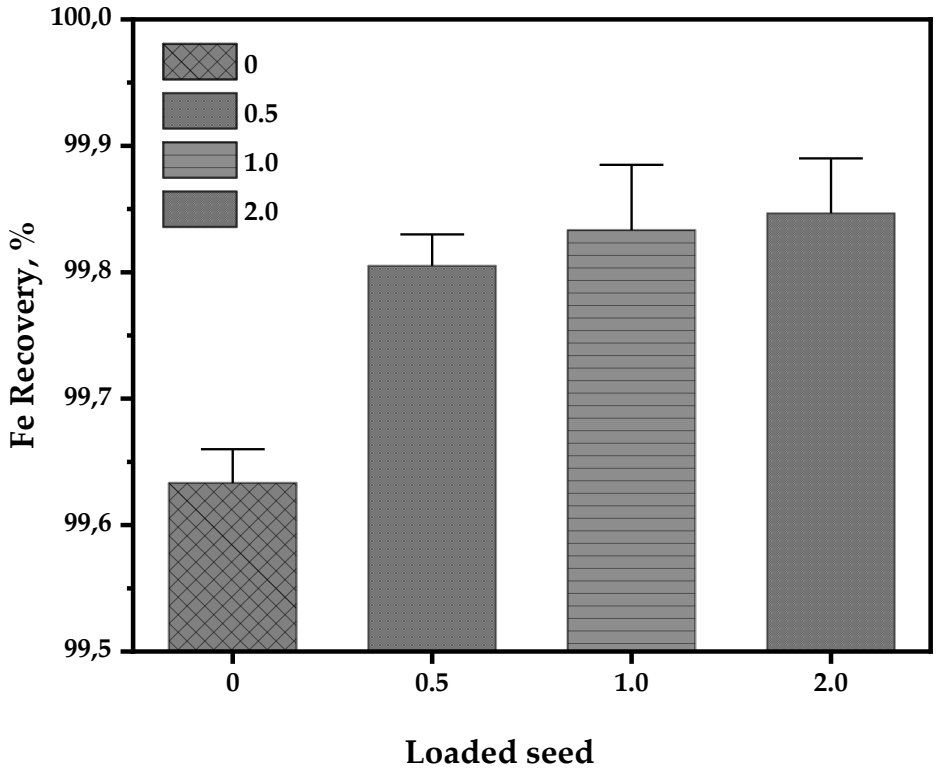

Figure 6.3: The effect of seeding on the Fe(III) recovery at pH 5 and 25°C.

Table 6.1: Composition of CFA leach liquor before and after Fe(III) precipitation

Analyte	Metal concentration (mg/L)							
	pH	Al(III)	Fe_{total}	Mn(II)	Mg(II)	Ti(IV)	Ca(II)	Zn(II)
Iron solution	1.2	2.67	1130.1	18.32	792.0	0.23	15.21	6.75
Cs = 0.0	5.1	0.03	3.6	17.01	808.0	--	16.20	6.59
Cs = 0.5	5.1	0.0	1.31	16.9	810.0	--	15.91	7.21
Cs = 1.0	5.1	0.0	1.29	17.21	799.2	--	15.92	6.92
Cs = 2.0	5.1	0.0	0.95	18.01	779.6	--	14.88	6.66

--Not detected

6.2.1.2 Characterisation of Fe(III) precipitates

To further understand the effect of seeding, the iron precipitates in **Figure 6.4** were characterised for their composition, functional group identity, physicochemical properties, and surface morphologies. The following subsections detail the results and provide a comprehensive discussion.

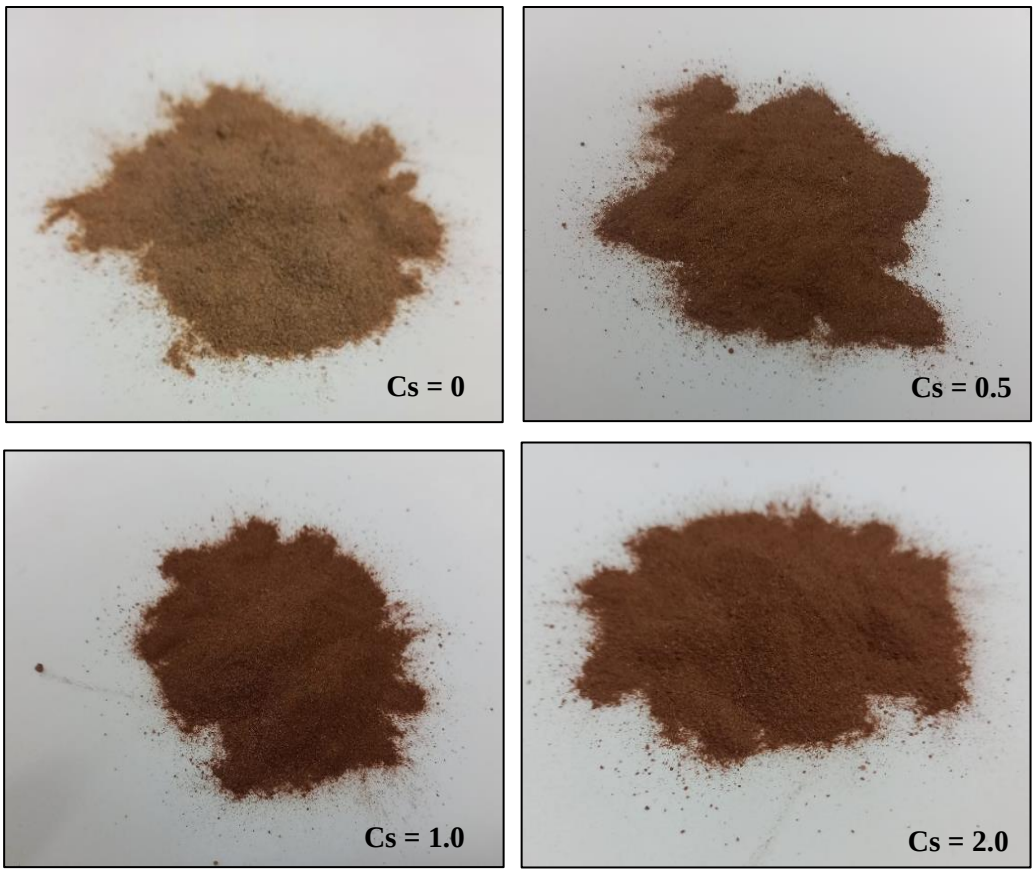

Figure 6.4: Reddish-brown Fe(III) precipitates generated by NaOH precipitation at pH 5, 25℃.

Phase Composition Analysis

The XRD pattern of the Fe(III) precipitates is presented in **Figure 6.5** (also see **Figure B.7**, **Appendix B**). In this study, the Fe(III) hydroxide/oxyhydroxide precipitates at all concentrations (Cs = 0, 0.5, and 1.0) were largely amorphous with no defined peaks. It has been reported that at higher pH values (pH >3), Fe(III) in the solution rapidly forms ferric hydroxide/oxyhydroxides through hydrolysis; thus, the XRD patterns are not always well-defined (Murad and Schwertmann, 1980; Grundl and Delwiche, 1993). However, the

commonly reported phase is ferrihydrite ($Fe_2O_3(OH)_9$), which is a poorly crystalline iron compound that transforms into goethite (α-FeOOH) at pH 2-5 (Hove et al., 2009; Wang et al., 2013; Han et al., 2020). Thenardite, a sodium sulphate compound, was also detected in all the precipitates. The formation of this compound may have occurred due to pH adjustment using sodium hydroxide. As expected, all the seeded precipitates (Cs = 0.5, 1.0) showed well-defined crystalline phases of mullite, quartz, and magnetite/haematite. These results are consistent with the composition of CFA-MF reported in **Figure 4.9**, **Chapter 4**.

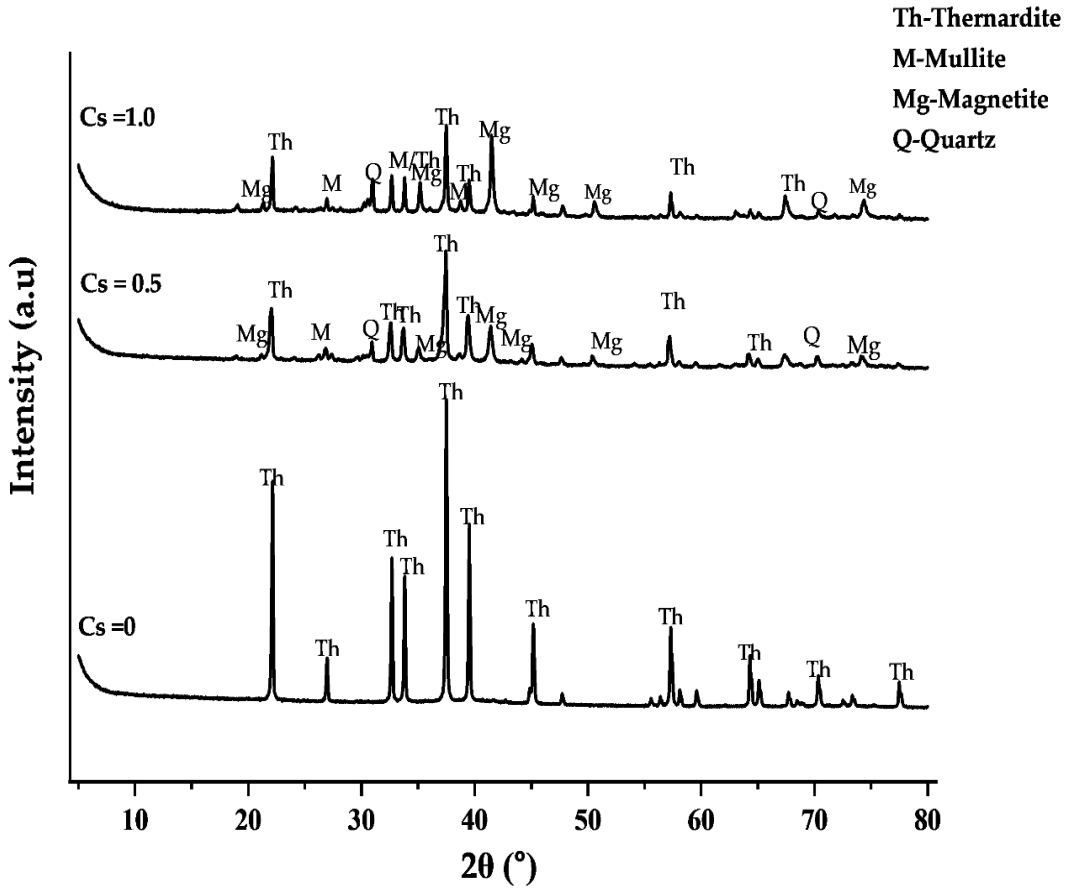

Figure 6.5: XRD analysis of the Fe(III) precipitates before and after seeding at pH 5, 25 ℃.

Functional Group Analysis

Fourier transform-infrared spectroscopy (FT-IR) was used to validate the XRD results, and the spectra of the Fe(III) precipitates and CFA-MF are shown in **Figure 6.7**. In the CFA-MF, the weak absorbent at 1057 cm^{-1} was assigned to Si-O-Si, which is similar to the raw CFA

(see **Figure 6.17**), suggesting the presence of quartz (SiO_2). Li et al. (2023) also studied the CFA-MF and assigned Fe-O at 560 cm^{-1}. In this study, the peak intensities were relatively low for assigning further functional groups in CFA-MF. Nonetheless, the Fe precipitate at Cs = 0 was also analysed and showed distinct peaks that resembled those of sodium sulphate (Periasamy et al., 2009). The peak at 1101 cm^{-1} was allocated to the asymmetric stretching of the SO_4 group (υ_{as} SO_4), while 630 cm^{-1} and 614 cm^{-1} were a result of asymmetric bending (υ_{ab} SO_4). Sodium sulphate was also quantified in all the precipitates after seeding. It was also noted that in the seeded precipitates, the composition peaks of CFA-MF were mostly consumed by the strong sodium sulphate peaks. However, a shift in the peak intensities was noted in the seeded and unseeded precipitates, thereby confirming the occurrence of a reaction. As a result, these FT-IR results were concluded to be consistent with the XRD findings in **Figure 6.5**.

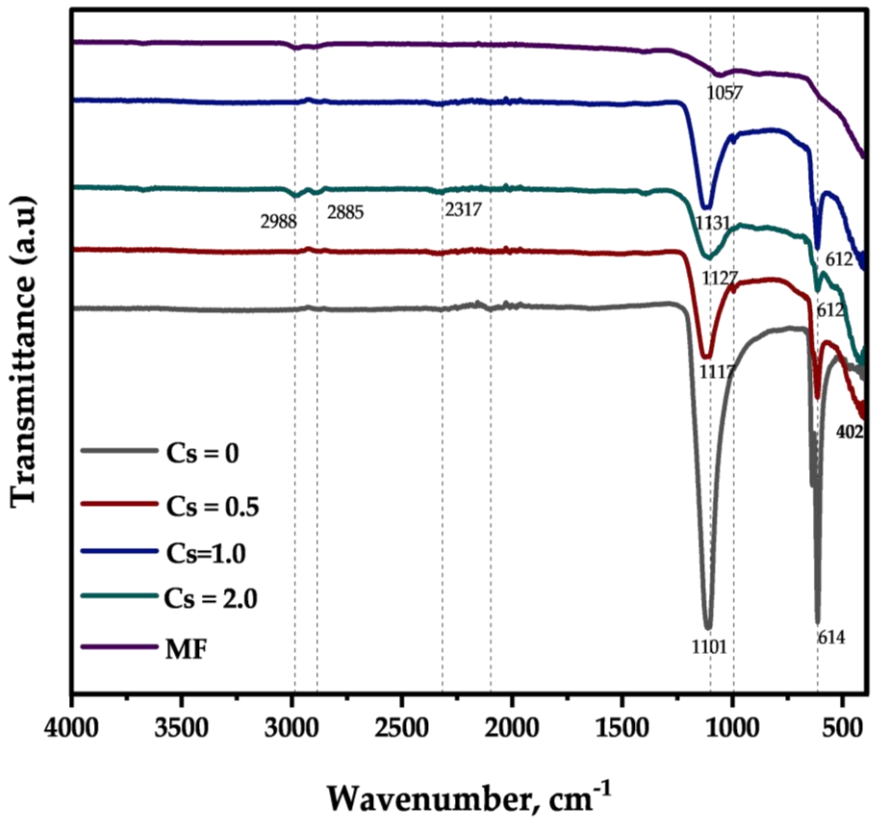

Figure 6.6: The FT-IR spectra of the Fe(III) precipitates before and after seeding and CFA-MF at pH 5, 25 ℃.

Surface Morphology

In **Section 4.2.2** of **Chapter 4** (see **Figure 4.10** and **Figure 4.11**), the morphology of the seed material (CFA-MF) was described as spherical, with particles that vary in size. The surface of the Fe-oxide was rough, with small particles covering the main particle, while the co-extracted phases (i.e. amorphous, mullite, and quartz) had a smooth surface. Therefore, this subsection will discuss the morphology of the Fe(III) precipitates.

The surface morphology of the Fe(III) precipitates was analysed to establish the nature of the compounds formed before and after seeding. The morphologies of the Fe precipitates are presented in **Figure 6.7**. The micrographs of the Fe(III) precipitates before seeding show a smooth surface and compact flocs as reported in **Figure 6.7 (a)** and **(b)**. These micrographs are identical to those obtained by Kefeni et al. (2017) and Linnikov et al. (2022) for the analysis of AMD sludge and Fe(III) precipitates from a nickel solution, respectively. After seeding, the micrographs showed that the Fe(III) precipitates are mostly agglomerated on the spherical CFA-MF particles, which might explain the improved filtration observed by visual inspection. Sha et al. (2022) used microscopic analysis to study the microstructures of flocs formed before and after adding CFA-MF in the treatment of a phosphate solution with polyaluminum chloride (PAC) and polyacrylamide (PAM). The treatment of phosphates using PAC and PAM alone resulted in small flocs that were observed scattered under a microscope. The addition of CFA-MF (PAC + PAM + CFA-MF) resulted in an improved specific gravity of the flocs; under a microscope, the flocs agglomerated to CFA-MF with visible black dots. The same observation can be extended to this study, with Fe(III) precipitates agglomerating on the CFA-MF. It can also be seen that the compact Fe(III) precipitates in **Figure 6.7 (a)** and **(b)** become more compact after seeding due to smaller aggregates clumping together into spherical particles. This observation is reported in **Figure 6.7 (d)** and **(f)**.

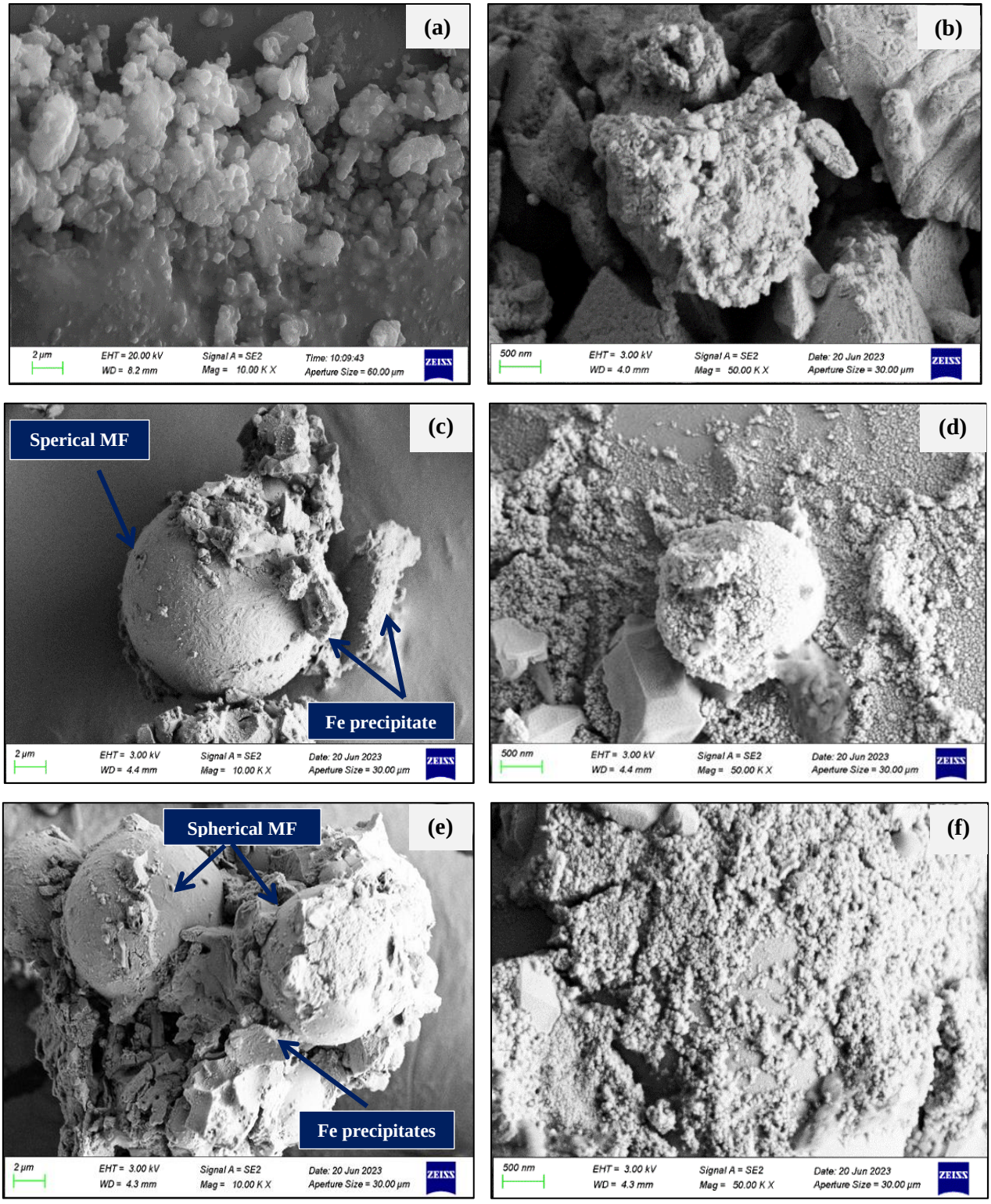

Figure 6.7: SEM micrographs of (a)-(b) CFA-MF and (c)-(f) Fe(III) precipitates formed at pH 5, 25°C (Cs=0, 1.0, 0.5).

Physicochemical Properties

The effect of seeding on textural properties was studied using the BET method in the N_2 adsorption-desorption system, and the results are reported in **Table 6.2**. The CFA-MF had a BET surface area (S_{BET}) of 0.3810 m^2/g, a pore volume (V_p) of 0.000291 cm^3/g, and a pore diameter (D_p) of 3.0530 nm. Gilbert et al. (2019) also observed that the S_{BET} of the extracted magnetic fraction from CFA is low at 1.34 m^2/g with a V_p of 0.00001 m^3/g. This analysis is also extended to the study by Zheng et al. (2022) with a S_{BET} of 1.67 m^2/g and a V_p of 0.004 cm^3/g. Notably, as discussed in the literature survey (see **Section 2.2.2.1**, **Chapter 2**), the composition and properties of CFA may differ depending on the coal combustion process; thus, in this study, the S_{BET} was lower. Nevertheless, the results reported in the table also showed that the S_{BET} at Cs = 0 increased from 0.78 m^2/g to 4.8 and 7.9 m^2/g upon seeding (Cs = 0.5, 1.0) with a V_p of 0.001309 cm^3/g at Cs =0, 0.007696 cm^3/g at Cs = 0.5, and 0.010264 cm^3/g at Cs = 1.0. The observed increase in the S_{BET} after seeding could be attributed to the smaller iron particles at Cs = 0 that reacted with the CFA-MF after seeding. This further illustrates that the agglomerated particles influence the size of the particles and, consequently, the surface area of the Fe(III) precipitates. As a result, it can also be concluded that the textural properties of the Fe(III) precipitates before and after seeding concur with the SEM results reported in **Figure 6.7**. The average D_p of the precipitates in this study also increased from the baseline (Cs = 0) to the seeded precipitates (Cs = 0.5, 1.0), as shown in the table. The D_p values of the Fe precipitates fall between 2 and 50 nm; therefore, according to the BDDT classification, all the materials have mesopores (Sing, 1985).

Table 6.2: Textural properties of CFA-MF and Fe(III) precipitates before and after seeding

Sample	S_{BET} (m^2/g)	V_p (cm^3/g)	D_p (nm)
CFA-MF	0.3810	0.000291	3.0530
Cs = 0	0.7813	0.001309	6.7013
Cs = 0.5	4.8378	0.007696	6.3636
Cs = 1.0	7,8736	0,010264	5.2143

The N_2 adsorption-desorption isotherms of the precipitates are presented in **Figure 6.8**. The CFA-MF plot in **Figure 6.8 (a)** reveals a type-IV isotherm with minimal hysteresis (Sing, 1985). This isotherm is similar to that obtained by Sha et al. (2022) for the characterisation of the magnetic fraction. **Figure 6.8 (b)** to **(d)** also shows Fe(III) precipitate plots with type-IV isotherms. An increase in the area under the hysteresis loop at a relative pressure (P/P_0) ranging from 0.4-1.0 is also observed upon seeding. Consequently, all the precipitates (before and after seeding) exhibit characteristics of a mesoporous structure.

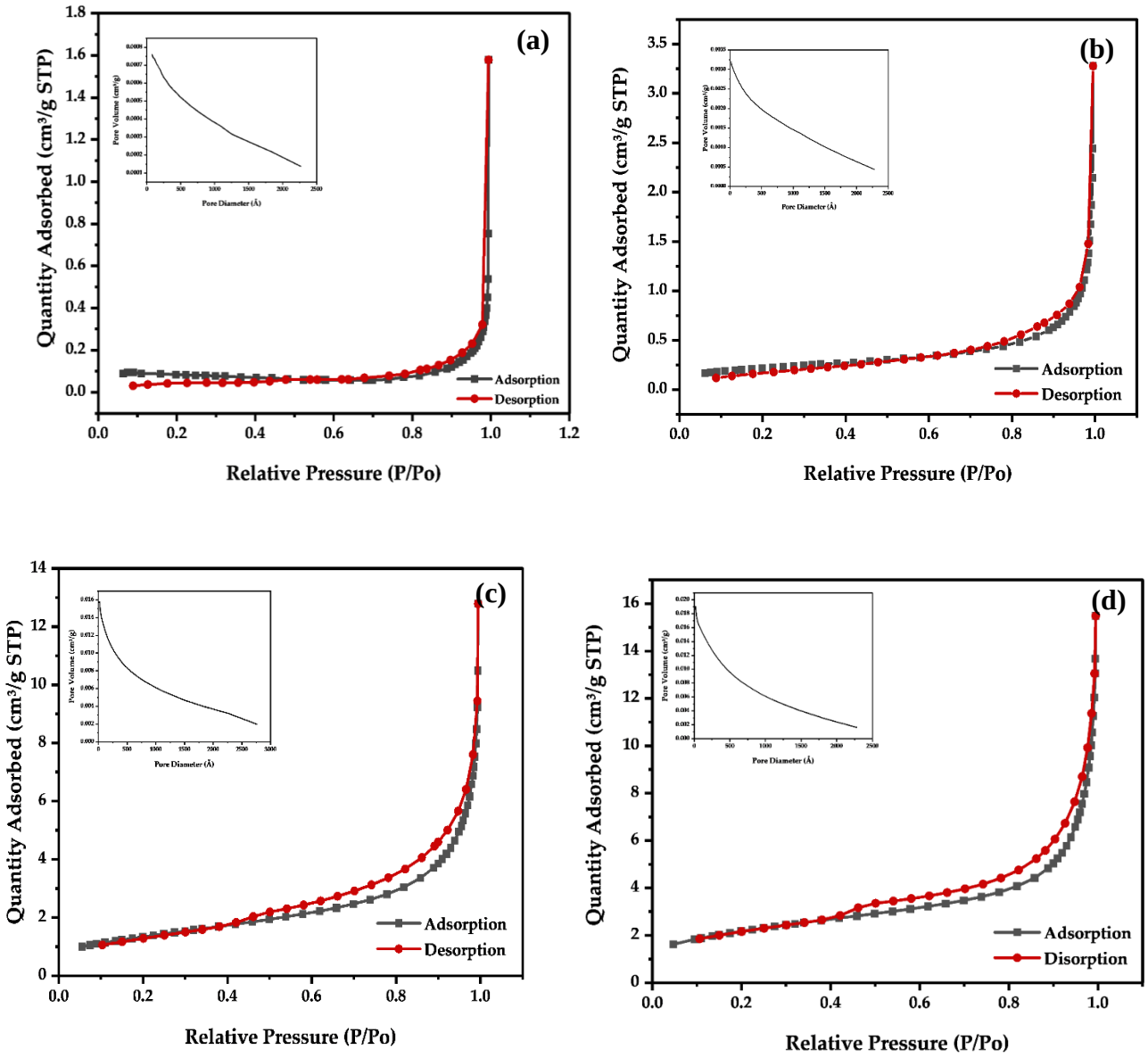

Figure 6.8: N_2 adsorption-desorption isotherm and the respective pore diameter distribution curves for the (a) Seed material (MF) and (b)-(d) Fe(III) precipitates.

6.2.1.3 Solubility of the precipitate and coagulant production

The seeded precipitate at Cs = 1.0 was further used to generate Fe-based coagulants. Since CFA-MF was used as the seed material, the precipitate was dissolved in sulphuric acid (0.5-6 M H_2SO_4) at 80℃ with a 1:6 S/L ratio for 10 hours. As anticipated, the results reported in **Figure 6.9** showed that an increase in acid concentration leads to an increase in the precipitate dissolution. The maximum solubility of the precipitate was observed at 4-8 M H_2SO_4; therefore, 4 M H_2SO_4 was chosen as the optimal solution. The CFA-MF consists of both amorphous and crystalline components. Therefore, the insoluble residue may have occurred due to the low solubility of quartz and mullite in sulphuric acid systems by direct acid leaching, as discussed in **Section 4.2.4**, **Chapter 4**.

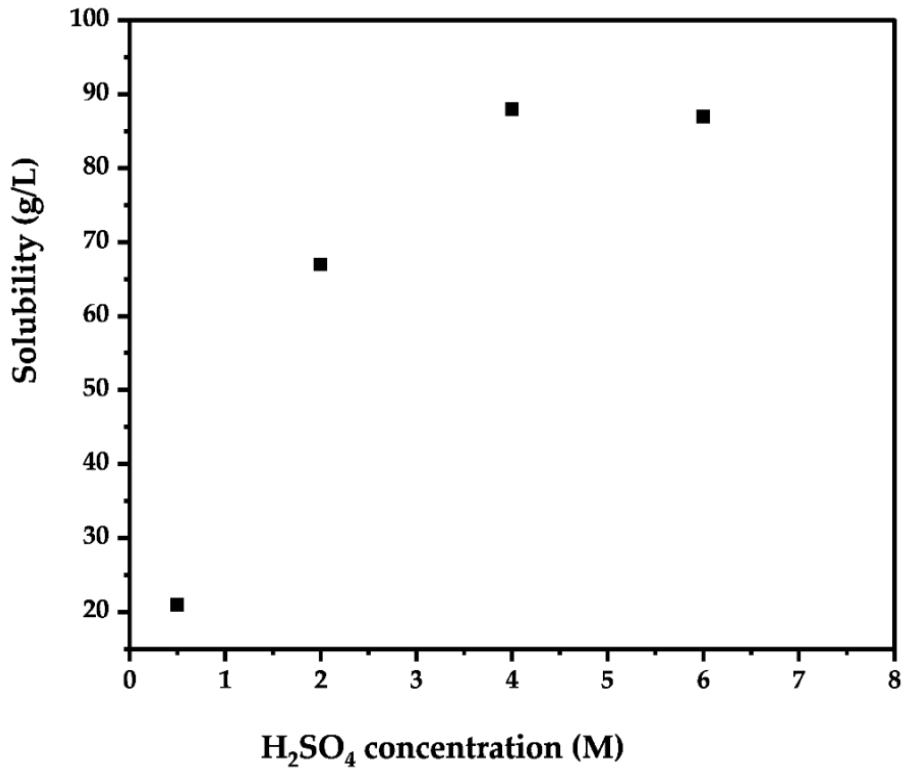

Figure 6.9: Solubility of the seeded Fe(III) precipitate dissolved in sulphuric acid.

The CFA-PFS coagulant generated was a yellow solution depicted in **Figure 6.10**, and its chemical composition is reported in **Table 6.3**. The chemical composition primarily consisted of Fe (8876.67 mg/L) and showed some CFA-MF components, such as Al, Mg, and Mn. The chemical composition of the synthesised CFA-PFS coagulants is similar to that of

commercial PFS as demonstrated in the table. However, the commercial PFS coagulant contains higher concentrations of sulphates and elements such as Fe, Mn, and Al. Thus, based on the composition of the synthesised CFA-PFS in this research, possible implications for feasible commercial utilisation are likely to occur at higher dosages of CFA-PFS compared to commercial PFS.

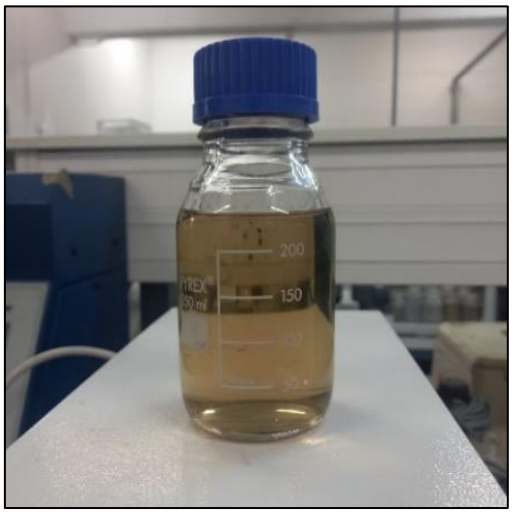

Figure 6.10: Synthesised CFA-PFS coagulant.

Table 6.3: Chemical composition of CFA-PFS

Analyte	Metal concentration (mg/L)						
	SO_4^{2-}	$Fe_{(total)}$	Al	Mn	Mg	Ca	Si
CFA-PFS	116,000	8876.67	256.8	60.6	158.5	5.68	--
Commercial PFS	130,800	115,000	4419	1585	160.6	77.2	22.4

--Not available

6.2.1.4 Performance of CFA – PFS coagulant on wastewater

The synthesised CFA-PFS coagulant was further used to treat brewery wastewater using the Jar tester method (see **Figure 3.8**). The characteristics of the brewery wastewater used are presented in **Table 6.4**, and the wastewater was evaluated for chemical oxygen demand (COD), turbidity, and electrical conductivity (EC).

Table 6.4: Characteristics of brewery wastewater

Parameters	Brewery wastewater
pH	9.61 ±0.1
UV_{254}	3160 ±0.01
(TDS) (mg/L)	1810 ±0.25
Turbidity (NTU)	99± 0.32
Conductivity (mS/cm)	3510 ±0.33

Turbidity refers to the optical clarity of water, while COD is the amount of oxygen needed to break down inorganics in wastewater (Cheng et al., 2005). The effects of coagulant dosage on turbidity and COD were determined, and the findings are presented in **Figure 6.11**. As presented in the figure, an increase in the CFA-PFS dosage increased the turbidity recovery from 18.1% at 10 mg/L to 69.5% at 100 mg/L. These results are similar to those obtained from the synthesis of AMD-PFS and commercial PFS by Mwewa et al. (2019). However, in their study, the performance was slightly higher, which may be due to higher Al concentration, aiding coagulation in both the synthesised AMD-PFS and commercial PFS. Similar increased performance has also been reported in synthesised PFS from CFA by Li et al. (2009) and Yan et al. (2012), where the better performance was due to the elevated levels of Al and Si in the generated coagulant. The removal of COD also increased with CFA-PFS dosage, and a maximum of 52% of COD was removed with a 100 mL CFA-PFS dosage.

Conductivity is another water parameter that indicates the total amount of dissolved salts and inorganics (Oyem et al., 2014; Aniyikaiye et al., 2019). In this study, EC increased from 3510 to 4110 µS/cm. The increase in EC might be explained by the presence of dissolved ions in the brewery wastewater, dissolved ions in the coagulants, and the NaOH used for pH adjustment. Miranda et al. (2015) and Mwewa et al. (2019) reported a comparable effect during wastewater treatment.

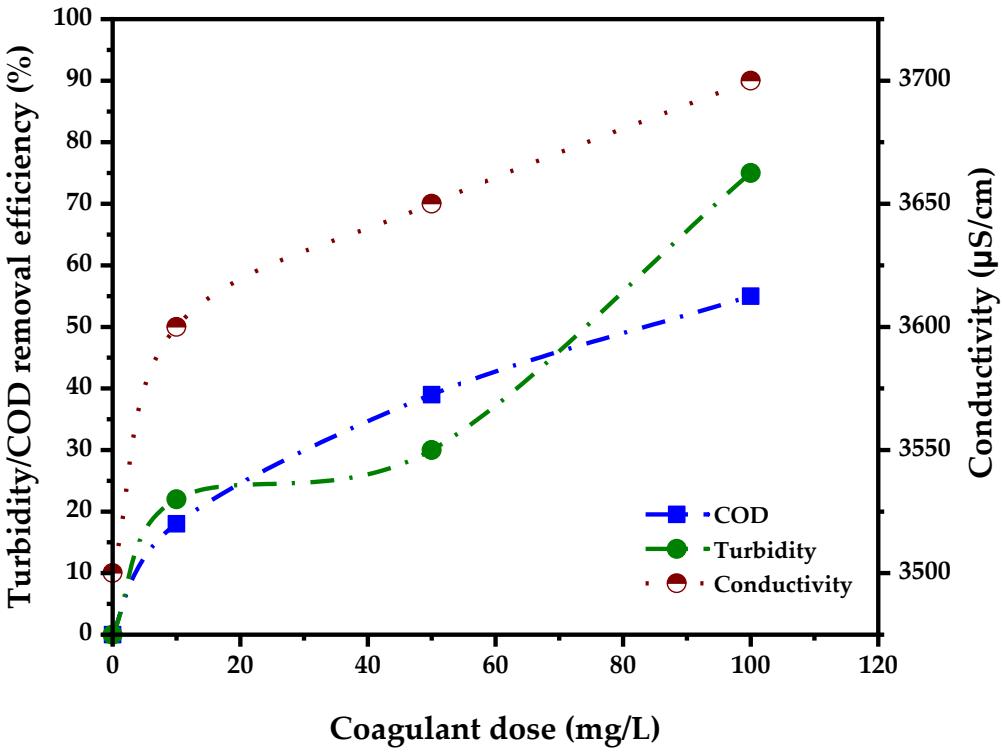

Figure 6.11: Performance of CFA-PFS during the treatment of brewery wastewater.

6.2.2 Characterisation of CFA – SSR as a potential adsorbent

A grey-white CFA-SSR shown in **Figure 6.12** was generated as a solid by-product in **Section 5.2.3** of **Chapter 5**. According to the South Africa Waste Management Act (Act No. 59 of 2008), it is imperative to responsibly manage the disposal of both solid and liquid wastes to prevent pollution and health risks. Therefore, this section will discuss the characterisation of CFA-SSR as a potential adsorbent for wastewater treatment.

Figure 6.12: The generated CFA secondary solid residue (CFA-SSR).

6.2.2.1 Physicochemical properties

Particle size distribution (PSD) is a crucial parameter that influences various adsorption factors, such as adsorption equilibria and the available surface area for adsorption (Manchisi, 2016). Therefore, in this study, the PSD of the generated CFA-SSR was first determined, and the analysis is presented in **Figure 6.13**. As depicted in the graph, CFA-SSR had a d_{10} value of 14.62 µm, a d_{50} value of 44.76 µm, and a d_{90} value of 79.83 µm. These results align with the PSD analysis of raw CFA (see **Figure 4.12**), which is commonly investigated as an adsorbent for wastewater treatment (discussed in **Section 2.7.2.1**, **Chapter 2**). Therefore, for this study, the PSD of CFA-SSR was found to be adequate for further investigation.

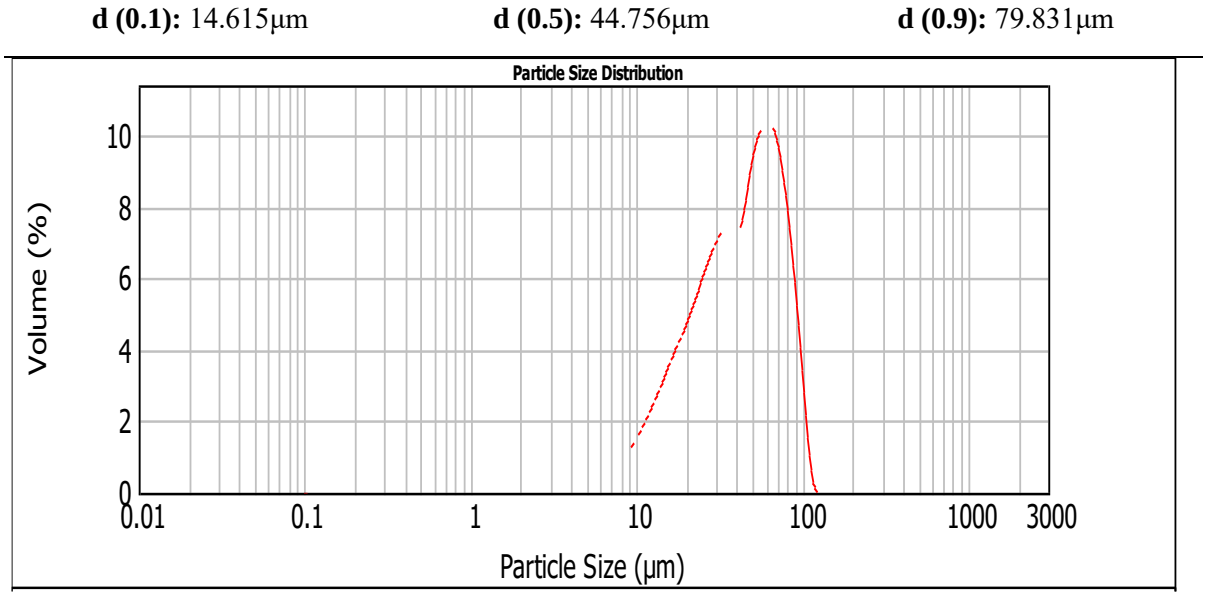

Figure 6.13: Particle size distribution of CFA-SSR.

Since adsorption is a surface phenomenon, the BET adsorption of N_2 gas was also used to determine the textural properties of CFA-SSR, and the results are presented in **Table 6.5**. The results reported in the table show that the S_{BET} of raw CFA increased from 1.444 m^2/g to 29.236 m^2/g in CFA-SSR. A high surface area is a key requirement for any adsorbent. Therefore, compared to commercial adsorbents such as activated carbon and zeolites, the surface area of CFA-SSR is relatively low. However, when compared to low-cost adsorbents such as CFA, slags, and phosphogypsum, the results were quite satisfactory (see **Table 6.5**) (Manchisi, 2016; Sithole et al., 2021; Kurniawati et al., 2021). Similarly, the Vp and Dp increased from raw CFA to CFA-SSR. The CFA-SSR was mesoporous, with a Vp of 0.0697 cm^3/g and a Dp of 11.7079 nm.

Table 6.5: Texture properties of the generated CFA-SSR, commercial adsorbent and industrial by-products

Sample	S_{BET} (m^2/g)	V_P (cm^3/g)	D_p (nm)	Reference
CFA - SSR	29.236	0.069770	11.7079	This study
Raw CFA	1.444	0.001341	4.3969	
Raw CFA	1.52	--	--	(Van der Merwe et al., 2014)
Furnace slag	2.381	0.0123	--	(Manchisi, 2016)
Gypsum	17.5	0.05	10.7	(Canut et al., 2008).
Activated Carbon	1105	0.5008	1.67	(Vunain et al., 2017)
Zeolite, 4A	559.13	0.2462	58.143	(Sowunmi et al., 2018)
Zeolite 13X	310.090	0.135951	7.2752	

--Not available

The N_2 adsorption-desorption isotherms for raw CFA and CFA-SSR are presented in **Figure 6.14**. These isotherms typically exhibit Type-IV behaviour with an H3 hysteresis loop at a relative pressure (P/P_0) of 0.6-1.0, which is characteristic of mesoporous material. Similar adsorption-desorption isotherms were observed by Balkaya and Cesur (2008) for phosphogypsum and by Manchisi (2016) for a furnace slag. In summary, it can be concluded that the pre-treatment and leaching processes described in **Chapter 5** significantly altered the textural properties of CFA-SSR for potential utilisation as an adsorbent material.

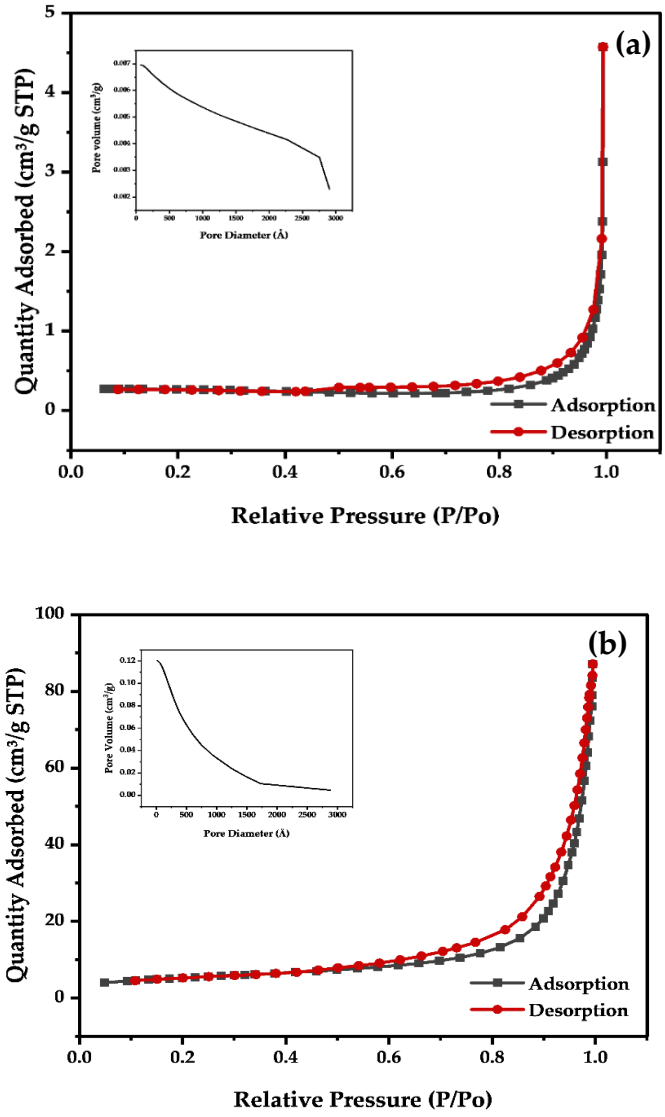

Figure 6.14: N_2 adsorption-desorption isotherms for (a) raw CFA and (b) CFA-SSR.

6.2.2.2 Surface morphology

The morphology of CFA-SSR was also analysed using SEM, and the micrographs are reported in **Figure 6.15**. The micrograph in **Figure 6.15 (a)** clearly shows the transformed spherical morphology of CFA (see **Figure 4.10**) into a CFA-SSR composition with amorphous nanoparticles and a calcium sulphate rhombohedral-like component. The amorphous nanoparticles have been reviewed as potential adsorbents due to their porosity and large surface area (Al-Shehri et al., 2019). In this study, magnification at 30 000x and 70 000x (see **Figure 6.15 (c)** and **(d)**) hardly revealed any surface porosity. However, the magnified images of the nanoparticles showed spherical particles of various sizes.

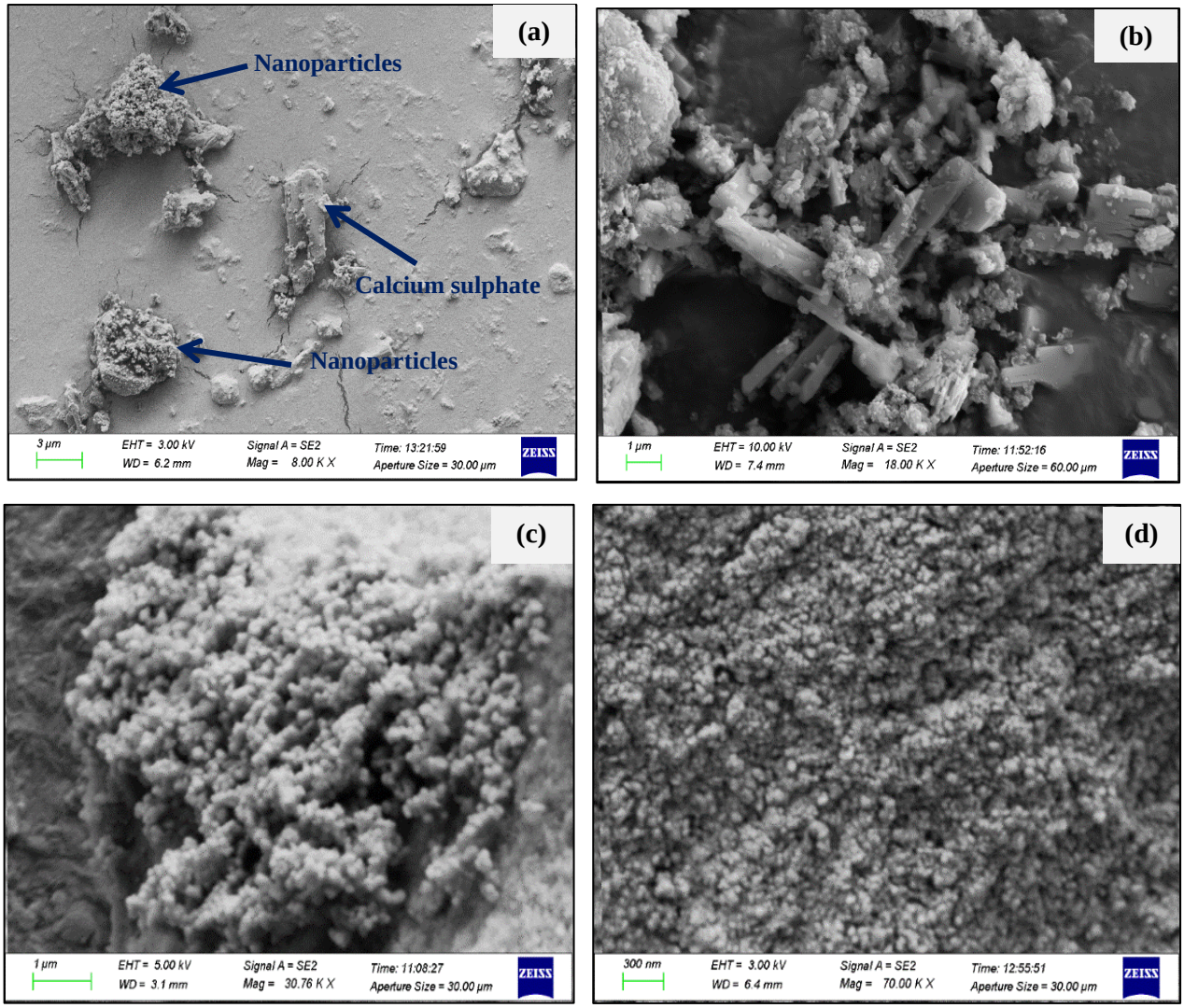

Figure 6.15: Surface morphology of CFA-SSR showing amorphous nanoparticles and the calcium sulphates rhombohedral-like component.

6.2.2.3 Phase composition analysis

The XRD analysis of CFA-SSR is presented in **Figure 6.16**. The results show that the material is largely amorphous, with anhydrite as the major crystalline phase. The other quantified phases are quartz (SiO_2) and cristobalite (SiO_2). In the literature surveyed in **Section 2.7.2**, the amorphous and crystalline components are essential in supporting adsorption. However, crystalline phases have a higher adsorption capacity for metal ions. Calcium sulphate, derived from industrial waste (i.e. phosphogypsum), has been identified as an effective adsorbent for heavy metals such as Cd, Zn, Ni, Pb, and Cu (Raii et al., 2014; Wang et al., 2017; Es-Said et al., 2020). Quartz is reported as a supporting material for other adsorbents with high affinities for heavy metals. One common approach involves modifying

the quartz surface by introducing specific functional groups or coating it with other materials that possess adsorption properties (Wang et al., 2023).

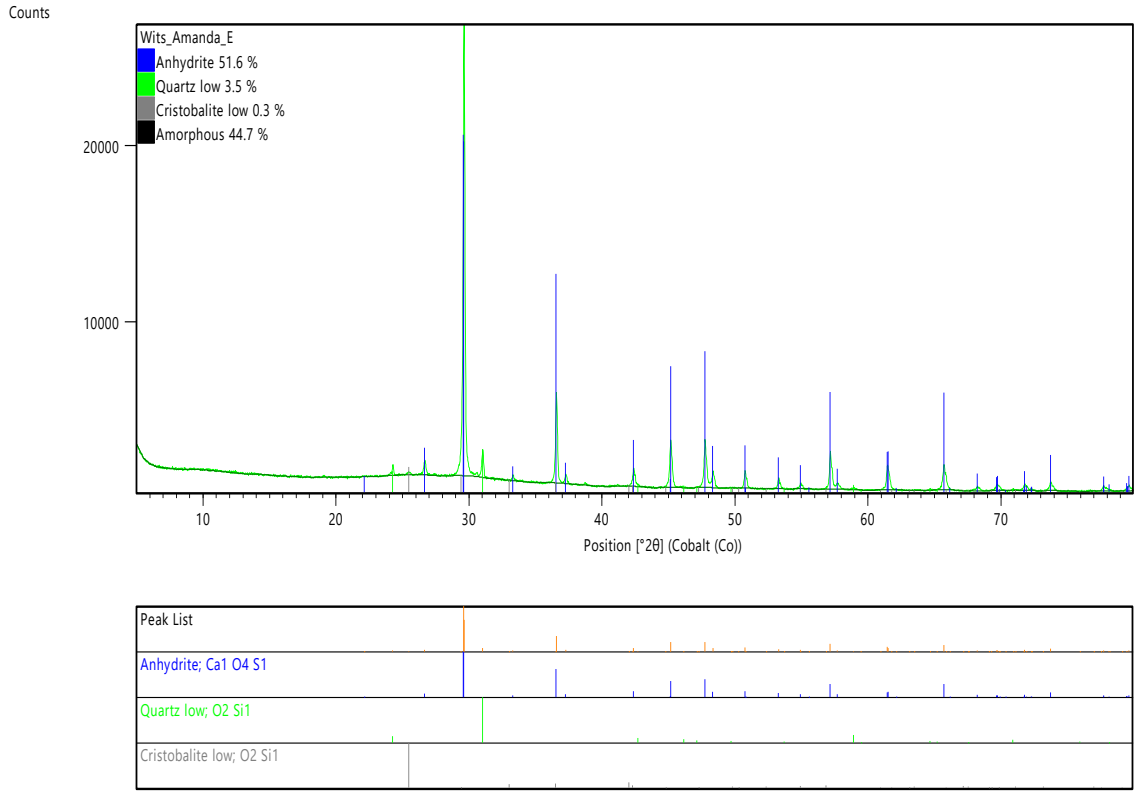

Figure 6.16: XRD analysis of the generated CFA-SSR.

6.2.2.4 Functional group analysis

The functional groups in CFA-SSR were also identified using FT-IR analysis, and the findings are presented in **Figure 6.17**. Although adsorption is a complex phenomenon, various functional groups are known to interact with metal ions as adsorbents. In the figure below, distinct peaks are observed at 500-1500 cm^{-1}, which resembles the presence of calcium sulphate in CFA-SSR. The adsorption bands at 1131 cm^{-1}, 671 cm^{-1}, and 595 cm^{-1} are attributed to the vibration modes of calcium sulphate (Balkaya and Cesur, 2008; Liu et al., 2009; Bishop et al., 2014; Nafai et al., 2017). The silica stretching mode is observed at 952 cm^{-1} and 793 cm^{-1}. Overall, these results align with XRD analysis, which shows anhydride and quartz/cristobalite as the major crystalline phases. A summary of the major peak transformations from raw CFA to CFA-SSR is also presented in **Table 6.6**.

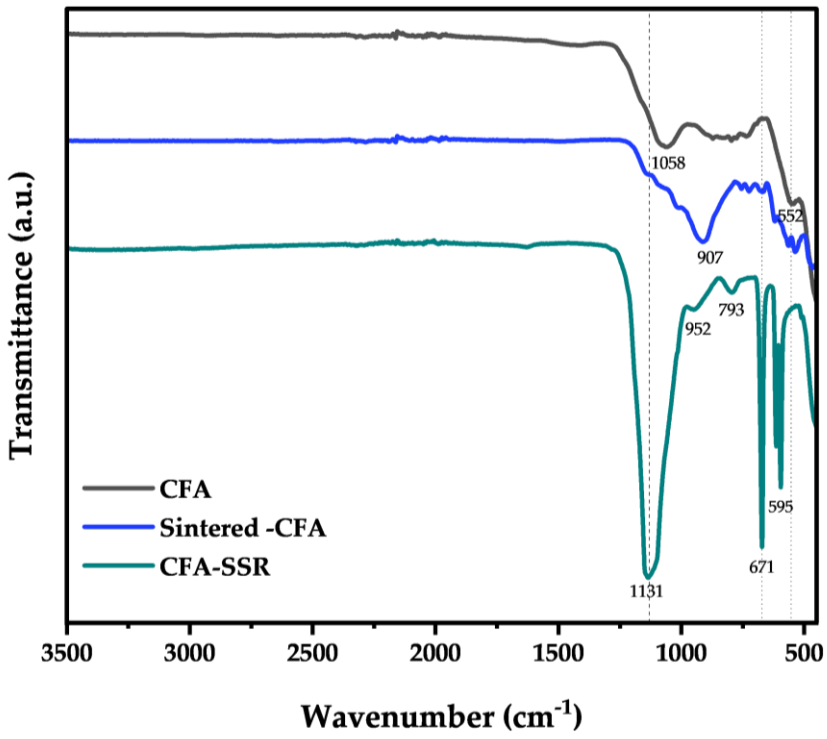

Figure 6.17: FT-IR spectrum for raw CFA, sintered CFA and CFA-SSR.

Table 6.6: Assignments of infrared wavenumbers for raw CFA, sintered CFA and CFA-SSR

Wave numbers (cm^{-1})			Functional group	Vibration mode
Raw CFA	**sintered CFA**	**CFA-SSR**		
1059	907	952,793	Si-O-Si	stretching
552	501	--	Si-O-Al	bending
--	--	595, 671	υ_4 (SO_4^{2-})	bending
--	--	952, 793	υ_1 (SO_4^{2-})	stretching
--	--	1131	υ_3 (SO_4^{2-})	stretching

--Not available

6.2.2.5 Chemical composition analysis

Oxides such as SiO_2, Al_2O_3, and Fe_3O_4 have been reported in the literature to be desirable in adsorption since they provide a large surface area in adsorption (Kalombe et al., 2020; Manchisi et al., 2020). **Table 6.7** shows that CFA-SSR is mainly composed of SiO_2, CaO,

and SO_3, with traces of TiO_2, Al_2O_3, and Fe_2O_3. Moreover, the Si/Al mass ratio is calculated as 16.6. Therefore, according to Querol et al. (2002), CFA-SSR can be classified as a high-silica aluminosilicate adsorbent that contains a lower pore size (2.3A), lower cation exchange capacity of metals, and more Si-O-Si links instead of Si-O-Al.

Table 6.7: Chemical composition of the generated CFA-SSR and industrial by-products

Analyte, wt.%	SiO_2	Al_2O_3	CaO	Fe_2O_3	TiO_2	MgO	MnO	SO_3	Si/Al
CFA-SSR	43.041	0.596	19.486	0.414	0.245	--	--	25.158	16.6
CEM I[a]	21.9	4.75	65.44	3.68	0.49	2.17	0.40	--	--
WFGD gypusm[b]	2.0	1.1	50.8	0.64	0.1	1.06	0.6	42.7	--
Furnace slag[c]	35.51	13.72	35.09	1.75	0.63	--	1.37	*1.05	--

--Not available, ***** Elemental Sulphur, [a](Shabalala and Basitere, 2020),[b](Sithole et al., 2021)**,**[c] (Kambole et al., 2019)

Due to the high SiO_2 and CaO contents, the chemical composition of the generated CFA-SSR was also compared to that of a furnace slag, Portland cement (CEM I), and WFGD gypsum (see **Table 6.7**). These materials are commonly utilised in various industries such as wastewater treatment (Balkaya and Cesur, 2008; Lu et al., 2023), the fertiliser industry (Canut et al., 2008), and the building and construction industry (Sithole et al., 2021). In the fertiliser industry, calcium and sulphur in anhydrite are used as sources of nutrients for plants and soil amendment (Canut et al., 2008). In the construction sector, calcium sulphate (i.e. WFGD gypsum) is utilised in concrete and cement (Shabalala and Basitere, 2020**;** Sithole et al., 2021). However, in this sector, it is noted that the high SO_3 content can affect the quality of bricks and blocks; thus, the WFGD gypsum dosage is regulated **(**Sithole et al., 2021). In this study, the SO_3 in CFA-SSR was also high. Thus, similar to WFGD gypsum, the utilisation of CFA-SSR would need to be regulated in the construction sector. Nonetheless, calcium sulphate (i.e. gypsum and phosphogypsum) has also been utilised in wastewater treatment for the adsorption of heavy metals such as Zn, Pb, and Cd (Xu and McKay, 2017; Wang et al., 2017; Es-Said et al., 2020). Therefore, since the generated CFA-SSR was rich in

silica and calcium sulphate and the primary objective of the study was set to contribute to wastewater treatment; further characterisation was conducted to assess the potential application of CFA-SSR as an adsorbent material.

6.2.2.6 Point of Zero Charge (pH_{PZC})

The pH_{PZC} is the critical adsorbent surface property in adsorption. It can be described as the point at which the surface anions and cations are equal (Mohan and Gandhimathi, 2009). In this study, pH_{PZC} was determined by the mass titration method using 0.1 M KNO_3. It is evident from **Table 6.8** that the pH_{PZC} decreased from raw CFA (10.6) to CFA-SSR (3.2). Noh and Schwarz (1990) reported that a decrease in pH_{PZC} results from the addition of acidic groups to the surface of the adsorbent. This statement concurs with the FT-IR results shown in **Figure 6.17**, which show the sulphate functional groups due to sulphuric acid leaching in the sinter-H_2SO_4 leach process, forming a calcium sulphate compound. During the adsorption process, the solution pH (pH_S) is often linked to the pH_{PZC} of the adsorbent material. Therefore, in this study, the pH_{PZC} for CFA-SSR adsorbent is 3.2. This suggests that the sorption of anions in solution will be favoured at $pH_S < pH_{PZC}$ (3.2) since the CFA-SSR surface has a positive charge. The sorption of cations, on the other hand will be favoured at $pH_S > pH_{PZC}$ (3.2).

Table 6.8: The pH_{PZC} value for raw CFA and CFA-SSR

Adsorbent	pH_{PZC}
Raw CFA	10.6 ± 0.65
CFA-SSR	3.2 ± 0.44

6.2.2.7 Batch adsorption studies

Batch experiments were conducted to further investigate the potential application of CFA-SSR as an adsorbent material. Therefore, this section discusses the characteristics of the treated wastewater, including batch adsorption tests.

Wastewater Characteristics

The characteristics of raw AMD and AMD effluent are presented in **Table 6.9**. Raw AMD is characterised as highly acidic (pH <3) wastewater with high concentrations of heavy metals that exceed the discharge limit set by the Department of Water Affairs and Sanitation (DWAS) in South Africa (Sithole et al., 2020). The results presented in the table below show that the raw AMD used in this study is a typical South African AMD concentrated with Fe and heavy metals, such as Zn, Mn, and Mg (Skousen et al., 1993; Simate and Ndlovu, 2014). In a study by Mwewa et al. (2019), AMD effluent with the characteristics shown in **Table 6.9** was produced after Al and Fe recovery by precipitation. The effluent enriched in heavy metals (i.e. Mg, Mn, Zn, and Ni) was generated. High levels of these metal ions are commonly reported in mine wastewater and are known to accumulate in organisms, causing diseases or disorders in aquatic and terrestrial ecosystems and human health (Bailey et al., 1999). Therefore, in an effort to meet the stipulated DWAS range, the adsorption of heavy metals in raw AMD and AMD effluent using CFA-SSR was evaluated. It is also noteworthy that raw AMD is acidic with high concentrations of heavy metals, whereas the AMD effluent is alkaline, with high concentrations of heavy metals (except for Al and Fe).

Table 6.9: Chemical composition of raw AMD and AMD-effluent

Analyte	Raw AMD	AMD Effluent	*DWAS Guideline
pH	2.1	5.0	6-9
Turbidity (NTU)	547	0.4	<5
EC (mS/cm)	240	47.1	<700
$Fe_{(Total)}$ (mg/L)	4290.0	14.0	<0.1
Al (mg/L)	396.0	2.7	<1.0
Ca (mg/L)	503.02	500.0	<30
Mg (mg/L)	474.0	454.0	<30
Mn (mg/L)	93.9	89.3	<0.05
Zn (mg/L)	14.3	14.1	<0. 5
Ni (mg/L)	1.7	1.6	<0.1
Cu (mg/L)	0.5	0.5	<1.0
SO_4^{2-} (mg/L)	3730	276.2	<500

*Holmes, 1996; Kalombe et al., 2020

Effect of Operation Conditions

The adsorption capacities of Fe, Mg, Mn, Zn, and Ni are described in this section. The performance of the adsorbent was based on its capacity to neutralise and precipitate heavy metal ions. Therefore, the effects of the solution pH, adsorbent dosage, and contact time were based on a literature survey conducted on silica-based materials, such as CFA, bentonite, furnace slag, and agricultural soil (Nleya, 2016; Manchisi, 2016; Mosai and Tutu, 2018).

The effect of solution pH was first determined using raw AMD (pH 2.1) and AMD effluents (pH 5 and pH 7). The effluent with pH 7 was adjusted using 2 M NaOH from pH 5.1 and all results are presented in **Figure 6.18**. As shown in the figure, the adsorption of heavy metals was low in raw AMD, and at pH 5 and 7, the percentage removal increased. The maximum removal efficiencies were 15.67% Mg, 25.66% Mn, 35.01% Zn, 56.9% Fe, and 20.5% Ni, at pH 7. This observation concurs with the pH_{PZC} values in **Table 6.8**, suggesting that metal ion adsorption occurs at a pH greater than that of the pH_{PZC}. The results further support an observation in the literature that the adsorption of multimetal ions by silica-based adsorbents (i.e. furnace slag, bentonite) is mostly effective in alkaline pH due to competitive adsorption of H^+ (see **Equation 6.5** to **6.7**). Dimitrova and Mehanjiev (2000) used furnace slag to study the effect of the initial pH on Pb^{2+} adsorption. The authors obtained 98% efficiency at pH > 6. The increase in pH was a result of hydrolysis and ion exchange of the amorphous phase.

$$\mathrm{SiOH} + \mathrm{Ca^{2+}} + 2\mathrm{OH^-} \leftrightarrow \mathrm{SiOCa} + 2\mathrm{HOH} \qquad \textbf{6.5}$$

$$(\mathrm{SO})_2\mathrm{H^+} + \mathrm{Ca^{2+}}_{(aq)} + \mathrm{M^{2+}}_{(aq)} \leftrightarrow (\mathrm{SO})_2^-\mathrm{Ca^{2+}} + \mathrm{H^+}_{(aq)} + \mathrm{M^{2+}}_{(aq)} \qquad \textbf{6.6}$$

$$\mathrm{M^{2+}} + \mathrm{OH^-} \leftrightarrow \mathrm{M(OH)}_{2(s)} \qquad \textbf{6.7}$$

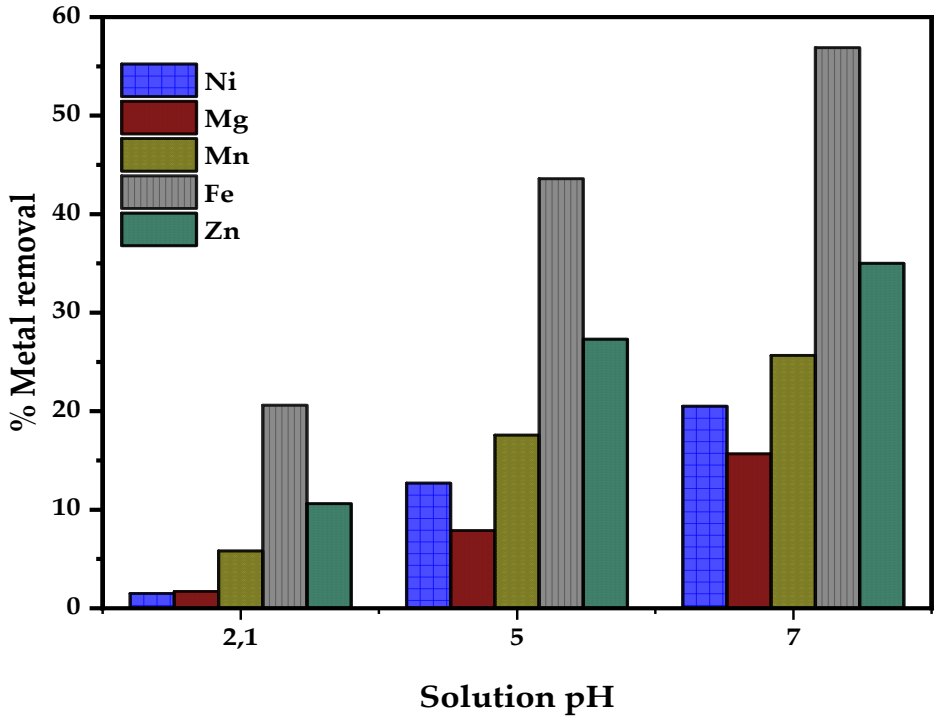

Figure 6.18: Effect of initial solution pH on the adsorption of heavy metals: Adsorbent dosage: 5 g, Agitation speed= 150 rpm, Contact time = 6 hours.

The AMD effluent at pH 7 was chosen as the optimum pH for further investigations, and the effect of the CFA-SSR dosage on the selected metal ions is shown in **Figure 6.19**. Es-said et al. (2021) reported that the adsorbent mass is directly proportional to heavy metal removal, as there is greater accessibility to replaceable active sites for adsorption. In this study, there was a slight increase in the percentage of metal removal from 0.5 to 2.5 g loading; however, beyond 2.5 g loading, no significant improvement in metal adsorption was observed. The increase in adsorption with increasing CFA-SSR dosage may be a result of the higher surface area, which increased the number of adsorption sites. Alternatively, the low adsorption capacity may be due to competing ions in the solution (Mosai and Tutu, 2018; Mnasri-Ghnimi and Frini-Srasra, 2019).

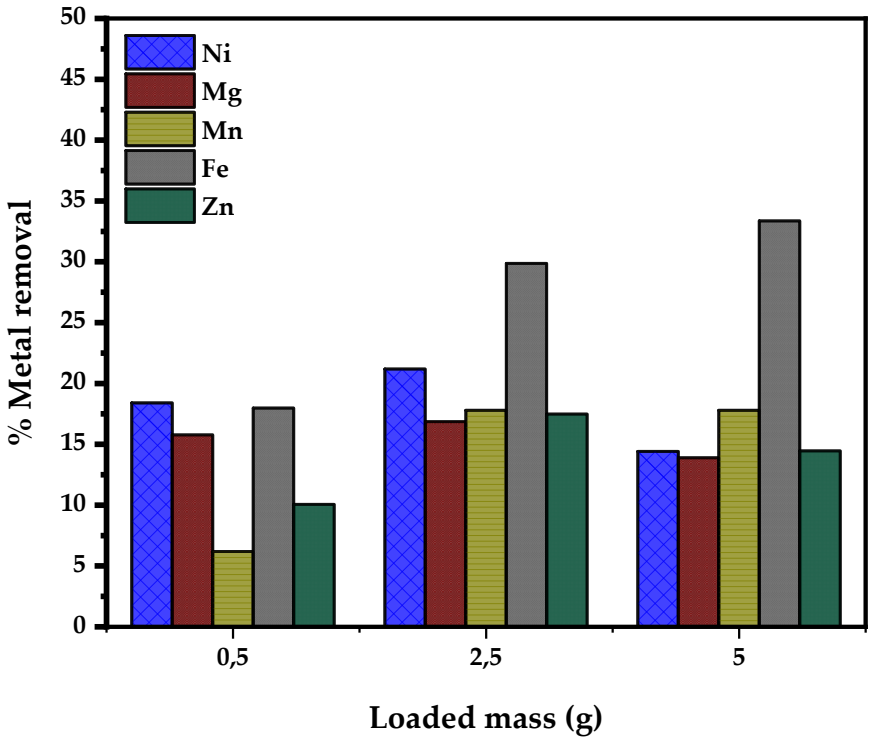

Figure 6.19: Effect of adsorbent dosage on metal ions using AMD effluent at pH 7, 150 rpm, ~25°C, for 6 hours.

The loaded mass of 2.5 g was further used to test the effect of contact time, and the findings are presented in **Figure 6.20**. Sufficient contact time is crucial for the accessibility of metals to active adsorption sites. In this study, the adsorption of metal ions increased over time, particularly for Fe, Zn, and Ni. The removal percentage of Mg and Mn was low, and beyond 6 hours, there was no significant improvement in the removal percentage (see **Figure 6.20 (a)**). Mosai and Tutu (2018) explained that during the adsorption process, different elements have different atomic radii, valences, and hard-soft Lewis acid-base properties. Borderline Lewis acids (i.e. Cu^{2+}, Ni^{2+}, and Zn^{2+}) would preferentially bind to a hard Lewis base on the surface of the adsorbent rather than to hard acids (e.g. Mg^{2+}, K^{+}, and Ca^{2+}). The same explanation can be extended to the adsorption of heavy metals using CFA-SSR. The sulphate concentration in the solution was also monitored without any reduction or neutralisation. A slight increase in sulphate concentration corroborates the slight drop in solution pH, as shown in **Figure 6.20 (b)**. These effects on pH and sulphate concentration may have occurred due to the dissolution of Ca^{2+} and SO_4^{2-} from the calcium sulphate in CFA-SSR. A similar effect

was reported by Raii et al. (2014) in the adsorption of Pd(II) and Cd(II) using gypsum waste as the adsorbent.

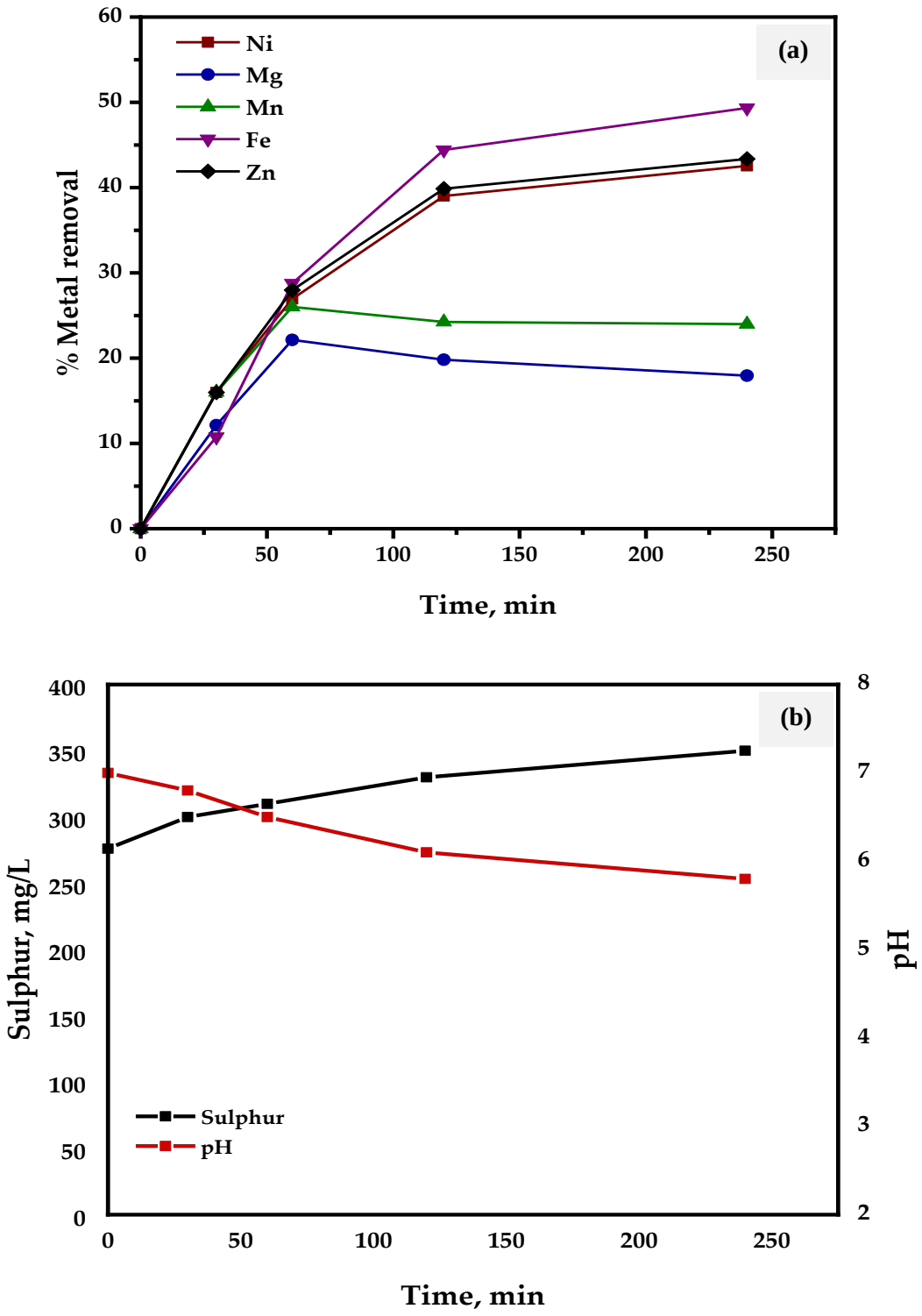

Figure 6.20: Effect of contact time on the adsorption of (a) metal ions including (b) sulphate ions and solution pH in AMD effluent: pH 7, 150 rpm, ~25°C.

Analysis of Adsorbent Capacity

The adsorptive capacity of the generated CFA-SSR was also compared with that of other secondary solid waste materials, and the results are presented in **Table 6.10**. Apart from the differences in experimental conditions and physicochemical properties, CFA-SSR can be used as an adsorbent for the recovery of heavy metals. A review by Al-Shehri et al. (2019) highlighted that silica-containing materials (bentonite, furnace slag, and CFA) can be functionalised with different complexes (Fe_2O_3/EDTA) to recover heavy metals from wastewater solutions. CFA-SSR also contains high silica content; therefore, such an approach can be an attractive alternative for future studies. In a study by Mosai and Tutu (2022), bentonite clay with 51.49% silica was functionalised with APDEMS (3-aminopropyl (diethoxy) methylsilane) to adsorb >90% Pt(IV). The Pt(IV) uptake was due to electrostatic interactions with the amine groups of APDEMS. This approach can be further investigated by using CFA-SSR for the adsorption of REEs which have been reported in AMD solutions by other researchers (Ayora et al., 2016; Royer-Lavallée et al., 2020; Li et al., 2022).

Table 6.10: Comparison of maximum adsorption efficiency in wastewater by CFA-SSR and industrial by-produtcs

Adsorbent	Phase composiion	Experimental conditions	Q_{max} (mg/g)	Reference
CFA-SSR	Amorphous crystalline	AMD effluent, pH 7, 25℃	0.6 mg/g Ni^{2+}, 1.67 mg/g Zn^{2+}, 0.4 mg/g Mg^{2+}, 15.6 mg/g Mn^{2+}, 75.6 mg/g $Fe^{2+/3+}$	This study
Blast furnace slag (BFS)	crystalline	AMD solution, pH 3.50, 22℃, phase ratio 30 g/L	1.44 mg/g Cd^{2+}, 0.39 mg/g Co^{2+}, 10.11 mg/g Cu^{2+}, 0.17 mg/g Mn^{2+}	(Manchisi, 2016)
Phosphogysum	crystalline	Stock solution, pH 7, 25℃, 1hour	0.730 mg/g Cd^{2+}, 0.635 mg/g Cu^{2+}, 0.560 mg/g Zn^{2+}	(Es-Said et al., 2020)
Coal fly ash (Afsin-Elbistan and Seyitomer)	crystalline amorphous	Stock solutipon, pH 3, 25℃, 1hour	96.0% Ni^{2+}, 98.0% Cu^{2+}, 93.3% Zn^{2+} 88.6% Ni^{2+}, 94.5% Cu^{2+}, 85.7% Zn^{2+}	(Bayat, 2002)

6.3 Conclusion

This chapter of the research evaluated the potential synthesis of Fe-based coagulants and the characterisation of CFA-SSR for wastewater treatment. The concluding remarks are as follows:

- The Fe(II)-rich solution was processed using an oxidation-precipitation process to recover ferrous hydroxide/oxyhydroxide at pH 5, with sodium hydroxide. The results showed that more than 99% of Fe(III) was recovered. To enhance settling and solid-liquid separation, the magnetic fraction extracted in **Chapter 4** was recycled as seeding material to reduce supersaturation and improve the filtration process. The impact of seeding (Cs = 0, 0.5, 1.0) was verified through XRD, SEM, and BET analyses. Before seeding, the Fe precipitate was amorphous with a S_{BET} of 0.78 m^2/g. The seeded Fe precipitates showed both amorphous Fe precipitates and spherical CFA-MF particles, which consisted of magnetite, mullite, and quartz as crystalline phases. The S_{BET} also increased to 4.8 and 7.9 m^2/g upon seeding (Cs = 0.5, 1.0). The micrographs of the seeded precipitates revealed that the increase in S_{BET} was due to compact Fe precipitates agglomerating onto the spherical CFA-MF particles.

- Fe-based coagulants were successfully synthesised from seeded Fe precipitate at Cs = 1.0 by dissolution in dilute H_2SO_4. In addition to Fe (III), the synthesised Fe-based coagulants (CFA-PFS) contained soluble elements in CFA-MF, such as Al(III), Mg(II), and Mn(II). The performance of CFA-PFS was also tested on brewery wastewater by evaluating water parameters. A dosage of 100 mg/L of CFA-PFS was sufficient to recover 52% COD and 69.5% turbidity. The findings were compatible with the performance of commercial PFS and the coagulants generated by other researchers (AMD-PFS and CFA-PFS). It was concluded that the coagulants generated in this study can be easily incorporated into the mine water treatment process, generating revenue and subsidising treatment costs. As a result, mine plants can comply with effluent discharge limits by treating the generated wastewater.

- CFA-SSR was also characterised for its potential application in wastewater treatment. XRF analysis showed that approximately 90% of the CFA-SSR was composed of SiO_2, CaO, and sulphur. While a high CaO content can neutralise wastewater through adsorption, XRD analysis showed that CaO occurs as a calcium sulphate compound. Furthermore, the material was found to be amorphous, with quartz being the primary

silica phase. The physicochemical properties demonstrated a potential adsorbent, with mesopores measuring 11.7 nm, a S_{BET} of 29.236 m^2/g, and a d_{50} of 44.76 µm.

- Batch adsorption tests demonstrated that CFA-SSR can adsorb heavy metals such as Zn and Ni in AMD solutions. The adsorption of metal ions was more pronounced at pH >5, indicating that hydrolysis and ion exchange processes could be involved in the adsorption process. Nevertheless, further research is necessary to fully comprehend the mechanisms involved in the adsorption of metal ions in multimetal ion solutions, such as AMD. Additionally, by functionalising the CFA-SSR, the adsorbent capacity could be expanded to include critical elements, such as REEs, which have been reported in AMD.

The next chapter presents the process flowsheet and economic evaluation of the extraction of valuable resources from CFA.

References

Al-Shehri, B.M., Abd El Rahman, S.K., Ashour, S.S. and Hamdy, M.S., 2019. A review: the utilization of mesoporous materials in wastewater treatment. *Materials Research Express* 6(12), 122002.

Aniyikaiye, T.E., Oluseyi, T., Odiyo, J.O. and Edokpayi, J.N., 2019. Physico-Chemical Analysis of Wastewater Discharge from Selected Paint Industries in Lagos, Nigeria. *The International Journal of Environmental Research and Public Health* 16, 1235.

Ayora, C., Macías, F., Torres, E., Lozano, A., Carrero, S., Nieto, J.M., Pérez-López, R., Fernández-Martínez, A. and Castillo-Michel, H., 2016. Recovery of rare earth elements and yttrium from passive-remediation systems of acid mine drainage. *Environmental Science and Technology* 50(15), 8255-8262.

Bailey, S.E., Olin, T.J., Bricka, R.M. and Adrian, D.D., 1999. A review of potentially low-cost sorbents for heavy metals. *Water Research* 33(11), 2469-2479.

Balkaya, N. and Cesur, H., 2008. Adsorption of cadmium from aqueous solution by phosphogypsum. *Chemical Engineering Journal* 140, 247-254.

Bayat, B., 2002. Comparative study of adsorption properties of Turkish fly ashes: I. The case of nickel (II), copper (II) and zinc (II). *Journal of Hazardous Materials* 95(3), 251-273.

Bishop, J.L., Lane, M.D., Dyar, M.D., King, S.J., Brown, A.J. and Swayze, G.A., 2014. Spectral properties of Ca-sulphates: Gypsum, bassanite, and anhydrite. *American Mineralogist* 99, 2105-2115.

Canut, M.M.C., Jacomino, V.M.F., Bråtveit, K., Gomes, A.M. and Yoshida, M.I., 2008. Microstructural analyses of phosphogypsum generated by Brazilian fertilizer industries. *Materials Characterization* 59, 365-373.

Cheng, W.P., Chi, F.H., Yu, R.F. and Lee, Y.C., 2005. Using chitosan as a coagulant in recovery of organic matters from the mash and lauter wastewater of brewery. *Journal of Polymers and the Environment* 13, 383-388.

Daoud, J. and Karamanev, D., 2006. Formation of jarosite during Fe^{2+} oxidation by Acidithiobacillus ferrooxidans. *Minerals Engineering* 19(9), 960-967.

Dimitrova, S.V. and Mehanjiev, D.R., 2000. Interaction of blast-furnace slag with heavy metal ions in water solutions. *Water Research* 34(6), 1957-1961.

Es-Said, A., Nafai, H., Hamdaoui, L.E., Bouhaouss, A. and Bchitou, R., 2020. Adsorptivity and selectivity of heavy metals Cd (II), Cu (II), and Zn (II) toward phosphogypsum. *Desalination and Water Treatment* 197, 291-299.

Es-Said, A., Nafai, H., Lamzougui, G., Bouhaouss, A. and Bchitou, R., 2021. Comparative adsorption studies of cadmium ions on phosphogypsum and natural clay. *Scientific African* 13, 00960.

Gilbert, C., Ayanda, O.S., Fatoba, O.O., Madzivire, G. and Petrik, L.F., 2019. A novel method of using iron nanoparticles from coal fly ash or ferric chloride for acid mine drainage remediation. *Mine Water and the Environment* 38(3), 617-631.

Grundl, T. and Delwiche, J., 1993. Kinetics of ferric oxyhydroxide precipitation. *Journal of Contaminant Hydrology* 14(1), 71-87.

Han, H., Sun, W., Hu, Y., Tang, H. and Yue, T., 2015. Magnetic separation of iron precipitate from nickel sulfate solution by magnetic seeding. *Hydrometallurgy* 156, 182-187.

Han, H., Sun, Wenjuan, Sun, Wei, Hu, Y., 2020. Magnetic Separation of Impurities from Hydrometallurgy Solutions and Waste Water Using Magnetic Iron Ore Seeding, in: Iron Ores. IntechOpen. DOI: 10.5772/intechopen.93728.

Holmes, S., 1996. South African Water Quality Quidelines - Domestic Wate Use. Department of Water Affairsand Forestry. ISBN: 0-7988-5339-5.

Hove, M., Van Hille, R.P. and Lewis, A.E., 2009. The effect of different types of seeds on the oxidation and precipitation of iron. *Hydrometallurgy* 97(3-4), 180-184.

Kalombe, R.M., Ojumu, T.V., Katambwe, V.N., Nzadi, M., Bent, D., Nieuwouldt, G., Madzivire, G., Kevern, J. and Petrik, L.F., 2020. Treatment of acid mine drainage with coal fly ash in a jet loop reactor pilot plant. *Minerals Engineering* 159, 106611.

Kambole, C., Paige-Green, P., Kupolati, W.K., Ndambuki, J.M. and Adeboje, A., 2019. Comparison of technical and short-term environmental characteristics of weathered and fresh blast furnace slag aggregates for road base applications in South Africa. *Case Studies in Construction Materials* 11, 00239.

Karapinar, N., 2003. Magnetic separation of ferrihydrite from wastewater by magnetic seeding and high-gradient magnetic separation. *International Journal of Mineral Processing* 71(1-4), 45-54.

Kefeni, K.K., Mamba, B.B. and Msagati, T.A., 2017. Magnetite and cobalt ferrite nanoparticles used as seeds for acid mine drainage treatment. *Journal of Hazardous Materials* 333, 308-318.

Kurniawati, M., Azhari, N., Kadja, G., Mukti, R., Notodarmojo, S., 2021. Conversion of coal fly ash into advanced crystalline materials. *IOP Conference Series: Earth and Environmental Science* 623, 012040.

Li, L., Fan, M., Brown, R.C., Koziel, J.A. and Van Leeuwen, J.H., 2009. Production of a new wastewater treatment coagulant from fly ash with concomitant flue gas scrubbing. *Journal of Hazardous Materials* 162(2-3), 1430-1437.

Li, M.Y., Peng, Z.X., Zhang, B.W., Wang, S.K. and Wang, X.S., 2023. Morphology, mineralogical composition, and heavy metal enrichment characteristics of magnetic fractions in coal fly ash. *Environmental Earth Sciences* 82(9), 1-10.

Li, Q., Ji, B., Honaker, R., Noble, A. and Zhang, W., 2022. Partitioning behavior and mechanisms of rare earth elements during precipitation in acid mine drainage. Colloids and Surfaces A: *Physicochemical and Engineering Aspects* 641, 128563.

Linnikov, O.D., Rodina, I.V., Zakharova, G.S., Mikhalev, K.N., Baklanova, I.V., Kuznetsova, Y.V., Germov, A.Y., Goloborodskii, B.Y., Tyutyunnik, A.P., Fattakhova, Z.A., 2022. Coagulation removal of nickel (II) ions by ferric chloride: efficiency and mechanism. *Water Environment Research* 94, e10827.

Liu, Y., Wang, A. and Freemen, J.J., 2009. Raman, MIR, and NIR spectroscopic study of calcium sulphates: gypsum, bassanite, and anhydrite. 40th Annual Lunar and Planetary Science Conference, 23-27 March 2009, Woodlands, Texas. id.2128.

Lu, M., Wang, Y., Yu, J., Zhao, Q., Li, D. and Chi, R., 2023. Recycling waste with waste: Adsorption of anionic dyes in wastewater with surfactant-modified phosphogypsum. *Environmental Research* 237(1), 116963.

Manchisi, J., 2016. Development of sustainable adsorbents for wastewater treatment. PhD thesis, School of Chemical Engineering, University of Birmingham, UK.

Manchisi, J., Matinde, E., Rowson, N.A., Simmons, M.J., Simate, G.S., Ndlovu, S., Mwewa, B., 2020. Ironmaking and steelmaking slags as sustainable adsorbents for industrial effluents and

wastewater treatment: a critical review of properties, performance, challenges and opportunities. *Sustainability* 12(5), 2118.

Miranda, R., Latour, I., Hörsken, A., Jarabo, R. and Blanco, A., 2015. Enhanced Silica Removal by Polyamine-and Polyacrylamide-Polyaluminum Hybrid Coagulants. *Chemical Engineering and Technology* 38(11), 2045-2053.

Mnasri-Ghnimi, S. and Frini-Srasra, N., 2019. Removal of heavy metals from aqueous solutions by adsorption using single and mixed pillared clays. *Applied Clay Science* 179, 105151.

Mosai, A.K. and Tutu, H., 2018. Modeling of sorption and transport of cadmium, copper and chromium on an agricultural soil impacted by mining activities. *Environmental Progress and Sustainable Energy* 37(6), 2063-2072.

Mosai, A.K. and Tutu, H., 2022. Recovery of platinum (IV) from aqueous solutions using 3-aminopropyl (diethoxy) methylsilane functionalized bentonite. *Journal of Dispersion Science and Technology* 43(7), 1016-1027.

Murad, E. and Schwertmann, U., 1980. The Möessbauer spectrum of ferrihydrite and its relations to those of other iron oxides. *American Mineralogist* 65(9-10), 1044-1049.

Mwewa, B., Stopić, S., Ndlovu, S., Simate, G.S., Xakalashe, B. and Friedrich, B., 2019. Synthesis of poly-alumino-ferric sulphate coagulant from acid mine drainage by precipitation. *Metals* 9(11), 1166.

Nafai, H., Lamzougui, G., Chafik, D., Bouhaouss, A. and Bchitou, R., 2017. Performance evaluation of calcium sulphate in adsorption process of metal ions from aqueous solutions. *Journal of Materials and Evironmental Sciences* 8(3), 982-989.

Nleya, Y., 2016. Removal of toxic metals and recovery of acid from acid mine drainage using acid retardation and adsorption processes. MSc dissertation, School of Chemical and Metallurgical Engineering, University of the Witwatersrand, South Africa.

Noh, J.S. and Schwarz, J.A., 1990. Effect of HNO_3 treatment on the surface acidity of activated carbons. *Carbon* 28(5), 675-682.

Oyem, H., Oyem, I. and Ezeweali, D., 2014. Temperature, pH, electrical conductivity, total dissolved solids and chemical oxygen demand of groundwater in Boji-BojiAgbor/Owa area and immediate suburbs. *Research Journal of Environmental Sciences* 8, 444-450.

Periasamy, A., Muruganand, S. and Palaniswamy, M., 2009. Vibrational studies of Na_2SO_4, K_2SO_4, $NaHSO_4$ and $KHSO_4$ crystals. *RASĀYAN Journal of Chemistry* 2(4), 981-989.

Querol, X., Moreno, N., Umaña, J. t, Alastuey, A., Hernández, E., Lopez-Soler, A. and Plana, F., 2002. Synthesis of zeolites from coal fly ash: an overview. *International Journal of Coal Geology* 50(1-4), 413-423.

Raii, M., Minh, D.P., Sanz, F.J.E. and Nzihou, A., 2014. Lead and cadmium removal from aqueous solution using an industrial gypsum by-product. *Procedia Engineering* 83, 415-422.

Royer-Lavallée, A., Neculita, C.M. and Coudert, L., 2020. Removal and potential recovery of rare earth elements from mine water. *Journal of Industrial and Engineering Chemistry* 89, 47-57.

Sha, S., Rui, X., Xu, Y., Gao, Y., Lee, C.T. and Li, C., 2022. Enhanced precipitation performance for treating high-phosphorus wastewater using novel magnetic seeds from coal fly ash. *Journal of Environmental Management* 315, 115168.

Shabalala, A.N., Basitere, M., 2020. Interactive relationship between cementitious materials and acid mine drainage: their effects on Chromium Cr (VI) removal. *Minerals* 10(11), 932.

Simate, G.S. and Ndlovu, S., 2014. Acid mine drainage: Challenges and opportunities. *Journal of Environmental Chemical Engineering* 2(3), 1785-1803.

Sing, K.S., 1985. Reporting physisorption data for gas/solid systems with special reference to the determination of surface area and porosity (Recommendations 1984). *Pure and Applied Chemistry* 57(4), 603-619.

Sithole, N., Ntuli, F. and Okonta, F., 2020. Fixed bed column studies for decontamination of acidic mineral effluent using porous fly ash-basic oxygen furnace slag based geopolymers. *Minerals Engineering* 154, 106397.

Sithole, T., Mashifana, T., Mahlangu, D. and Tchadjie, L., 2021. Physical, chemical and geotechnical characterization of wet flue gas desulfurization gypsum and its potential application as building materials. *Buildings* 11(11), 500.

Skousen, J., Lilly, R. and Hilton, T., 1993. Special chemicals for treating acid mine drainage. *Green Lands* 23, 34-41.

Sowunmi, A.R., Folayan, C.O., Anafi, F.O., Ajayi, O.A., Omisanya, N.O., Obada, D.O. and Dodoo-Arhin, D., 2018. Dataset on the comparison of synthesized and commercial zeolites for potential solar adsorption refrigerating system. *Data in brief* 20, 90-95.

Van der Merwe, E.M., Prinsloo, L.C., Mathebula, C.L., Swart, H., Coetsee, E. and Doucet, F., 2014. Surface and bulk characterization of an ultrafine South African coal fly ash with reference to polymer applications. *Applied Surface Science* 317, 73-83.

Vunain, E., Kenneth, D. and Biswick, T., 2017. Synthesis and characterization of low-cost activated carbon prepared from Malawian baobab fruit shells by H_3PO_4 activation for removal of Cu(II) ions: equilibrium and kinetics studies. *Applied Water Science* 7, 4301-4319.

Wang, K., Li, J., McDonald, R., Browner, R., 2013. Characterisation of iron-rich precipitates from synthetic atmospheric nickel laterite leach solutions. *Minerals Engineering* 40, 1-11.

Wang, T., Cao, W., Wang, Y., Qu, C., Xu, Y., Li, H., 2023. Surface modification of quartz sand: A review of its progress and its effect on heavy metal adsorption. *Ecotoxicology and Environmental Safety* 262, 115179.

Wang, X., Wang, L., Wang, Y., Tan, R., Ke, X., Zhou, X., Geng, J., Hou, H. and Zhou, M., 2017. Calcium sulfate hemihydrate whiskers obtained from flue gas desulfurization gypsum and used for the adsorption removal of lead. *Crystals* 7(9), 270.

Wei, X. and Viadero, R.C., 2007. Synthesis of magnetite nanoparticles with ferric iron recovered from acid mine drainage: Implications for environmental engineering. *Colloids and Surfaces A: Physicochemical and Engineering Aspects* 294(1-3), 280-286.

Xu, M. and McKay, G., 2017. Removal of heavy metals, lead, cadmium, and zinc, using adsorption processes by cost-effective adsorbents. *Adsorption Processes for Water Treatment and Purification* 109-138.

Yan, L., Wang, Y., Ma, H., Han, Z., Zhang, Q. and Chen, Y., 2012. Feasibility of fly ash-based composite coagulant for coal washing wastewater treatment. *Journal of Hazardous Materials* 203-204, 221-228.

Zheng, X., Tan, Y., Li, Y. and Tian, G., 2022. Effect of metal components on NO removal performance of modified high-content iron fly ash MnCe/HIFACa. *Fuel* 321, 124025.

7 PROCESS FLOWSHEET AND ECONOMIC ANALYSIS

7.1 Introduction

The primary goal of this research, as highlighted in **Section 1.3**, **Chapter 1**, was to add value to alumina processing from CFA by generating more than one saleable product. Therefore, the results reported in **Chapter 5** and **6** showed that in addition to smelter-grade alumina, the following can also be recovered:

- Poly-ferric sulphate coagulants for wastewater treatment
- Titanium dioxide of pigment grade
- REE-concentrated solution for further oxide processing
- CFA-SSR (silica-rich) adsorbent for wastewater treatment

The final objective of this research was to construct a process flow sheet and perform an economic analysis. This chapter presents the general process units, and the results obtained from the experimental work were used to simulate the laboratory-scale process using SuperPro Designer® (version 13) (Granata and Petrides, 2022).

7.2 Process Flowsheet

The extraction and recovery of valuable resources from CFA was simulated, and the proposed process flowsheet is reported in **Figure 7.1**. The key process units are listed in **Table 7.1**. The process design was based on the optimum test results established in **Chapter 5** and **6**, including a literature survey. The process flowsheet presented in **Figure 7.1** shows magnetic separation, two-step leaching process, and the integrated purification processes to recover the valuable products listed above.

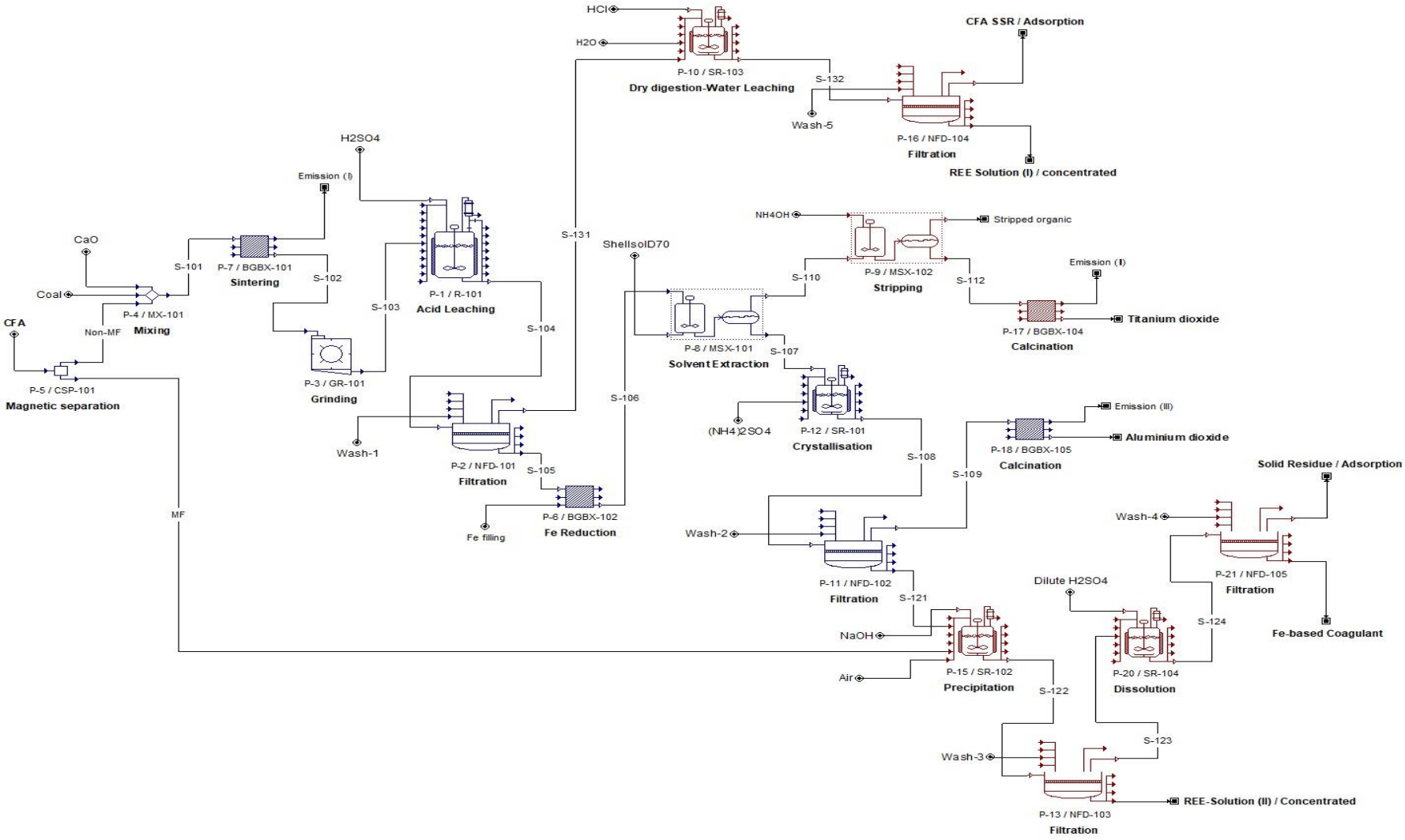

Figure 7.1: Process flowsheet for the extraction of valuable resources from CFA.

Table 7.1: Operation parameters and the equipment used in the process flowsheet

Unit Process	Equipment type	Process type	Operation parameter
Unit 1	CSP-01	Dry Magnetic separation	Intensity = 1.0T Time = 0.5 hrs
Unit 2	MX-101	Mixing	Speed = 160 rpm Time = 0.5 hrs
Unit 3	BGBX-1	Sintering	Temperature = 1000°C Time = 5 hrs
Unit 4	GR-101	Pulverising	Time = 0.5 hrs
Unit 5	R-101	Sulphuric leaching	Temperature = 80°C Time = 10 hrs Solvent = 6 M H_2SO_4
Unit 6	NFD-101	Filtration	Time = 1.0 hrs Solvent = H_2O
Unit 7	SR-103	Dry digestion	Time = 1 hr Temperature = 70°C Solvent = HCl
		Water leach	Time = 24 hrs Solvent = H_2O Temperature = 25°C
Unit 8	NFD-104	Filtration	Time = 1.0 hrs Solvent = H_2O
Unit 9	BGBX-102	Fe reduction	Temperature = 25°C Time = 1.0 hrs
Unit 10	MSX-101	Solvent extraction	Temperature = 35°C Time = 1.25 hrs Extraction stages = 3
Unit 11	MSX-102	Stripping	Temperature = 25°C Time = 0.5 hrs Stripping stages = 3
Unit 12	BGBX-104	Calcination	Temperature = 500°C Time = 5 hrs
Unit 13	SR-101	Crystallisation	Temperature = 0°C Time = 1 hr
Unit 14	NFD-102	Filtration	Time = 1.0 hrs Solvent = H_2O
Unit 15	BGBX-105	Calcination	Time = 5 hrs Temperature = 800°C
Unit 16	SR-102	Precipitation	Time = 1 hr Temperature = 25°C
Unit 17	NFD-103	Flitration	Time = 1.0 hrs Solvent = H_2O
Unit 18	SR-104	Dissolution	Time = 10 hrs Solvent = 6 M H_2SO_4 Temperature = 80°C
Unit 19	NFD-105	Filtration	Time = 1.0 hrs Solvent = H_2O

The material balance for the input and output stream is presented in **Table 7.2**. The main product (MP) of the process is Al_2O_3, while TiO_2, REE-concentrated solutions (I/II), CFA-SSR, and Fe-based coagulants can be regarded as valuable by-products. In the simulation process, it is predicted that 166 kg/batch of sintered CFA can be processed to give 55.3 kg/batch of Al_2O_3. The simulation further predicts that in the purification stage, 5.76 kg/batch of TiO_2 and 93.70 kg/batch of Fe-based coagulants can be produced. The REEs are generated as a solution (I and II) with 34.06 kg/batch. The resulting secondary solid residue (CFA-SSR) is the largest product with 147 kg/batch.

Table 7.2: Stream summary for processing CFA

Stream input	Kg/batch	Stream output	Kg/batch
Coal fly ash (CFA)	110	Aluminium dioxide	55.3
Coal	80	Titanium dioxide	5.76
$CaCO_3$	20	REE-concentrate solution (I/II)	34.06
H_2SO_4	100	Fe-based Coagulants	93.70
HCl	41	CFA- SSR/Solid residue	147.94
Fe filling	16.57	Organic phase	50.21
Shellsol/Primene JM-T	72	Emission	88.60
NH_4OH	10	Water	20.38
$(NH_4)_2SO_4$	35.38		
NaOH	11		
Air	0.01		
Water	1,245.52		
Total	**495. 96**	**Total**	**495. 96**

7.3 Estimated Costs Analysis

In this study, the simulation was performed in design mode, which means that parameters such as equipment sizing were automatically determined based on the chosen process conditions. It is also worth noting that due to potential experimental errors, there may be some deviation in the cost estimation when scaling up. Nonetheless, the costs of the reagents and utilities used in the simulation are listed in **Table 7.3**. The costs of chemicals and reagents were determined based on the purchase price from various suppliers, as described in

Table 3.1 of **Chapter 3**. Equipment purchase costs were obtained from local South African suppliers and the Matche database (Matche.com). The selling price for Al_2O_3 was set at 70.7 $/kg, and for TiO_2 it was set at 50.9 $/kg (SigmaAldrich.com, 2024). The selling price of REE concentrates is typically 30-40% lower than that of refined products. Therefore, for the purpose of this study, the REE-concentrated solution (I/II) was estimated to be 5.62 $/kg (Adamas Intelligence, 2024). The price for the adsorbents (CFA residue/solid residue) was based on the price of silica, which is 1.85 $/kg (Alibaba.com, 2024). The price of the generated coagulants was determined based on the current commercial PFS price of 1.57 $/kg (Alibaba.com, 2024).

Table 7.3: Material requirements and costs

Parameters	Costs
Utilities	
Electric power	0.1 $/kWh
Cooling water	0.05 $/MT
Natural gases	15 $/MT
Steam	12 $/MT
Chemicals	
Sulphuric acid (98%)	3.7 $/kg
Hydrochloric acid (32%)	1.5 $/kg
Calcium carbonate (99%)	4.8 $/kg
Sodium hydroxide (AR)	8.7 $/kg
Ammonium hydroxide (AR)	11.5 $kg
Ammonium sulphates (AR)	9.5 $/kg
Fe powder (fine)	41 $kg
Primary™ JM-T amine	8.4 $/kg
Shellsol D70	0.4 $/kg

A number of economic parameters were also assumed, and they are listed in **Table 7.4**. The project is estimated to run for 20 years. The process is expected to produce 48, 609 kg of Al_2O_3, per year, which is 55.3 kg per batch (assuming the number of batches per year is 904).

Table 7.4: Economic evaluation parameters

Parameter	Value
Construction period	30 months
Start-up period	4 months
Project lifetime	20yrs
Inflation	4.0%
NPV	7%
Salvage value	5%
Corporate Tax (SA)	28%

Executive Summary

SuperPro Designer can perform cost analysis by estimating the capital (CAPEX) and operating (OPEX) costs. The executive summary of the economic evaluation report is presented in **Table 7.5**. The main product (MP) is Al_2O_3 while the generated by-products are the revenue streams that contribute to the total revenue of the process. The process requires a capital investment of approximately $5 million, and the annual revenues are nearly $3.8 million, resulting in a gross margin of 4.5%. A low margin is typical of processes for commodity manufacturing, in which economic feasibility is often ensured by large production volumes (Granata and Petrides, 2022). The analysed process also exhibits a return on investment of around 12%, which, in turn, results in a payback time of close to 8 years.

Table 7.5: Executive Summary for the analysed process

Parameter	Cost	
Capital Investment Charged to this Project	5 007 630	$
Operating Cost	3 574 630	$/yr
Total Revenues	3 812 005	$/yr
Unit Processing Rate	48 609.3593	Kg MP/yr
Unit Production Cost	71.5102	$/kg MP
Unit Production Revenue	76.2525	$/kg MP
Gross Margin	6.22	%
Return On Investment (ROI)	12.18	%
Payback Time	8.21	years
IRR (After Taxes)	6.52	%
NPV (at 5.0% Interest)	678 029	$

Operating Cost Summary

In **Table 7.5**, the total annual operating cost for CFA processing was U$3,575,000. Therefore, the operating costs can be presented in a chart, as shown in **Figure 7.2**. The highest operating cost was represented by raw materials, accounting for 40% of the total cost. These materials are the chemicals and reagents (see **Table 7.3**) used to process CFA and generate saleable products. Due to the complex units involved in CFA processing, it can be observed that many chemicals and reagents are required to generate the final products. This, in turn, also affects labour costs by 31%. The extensive use of water and heat exchange systems also contributed significantly to facility-dependent expenses (24%).

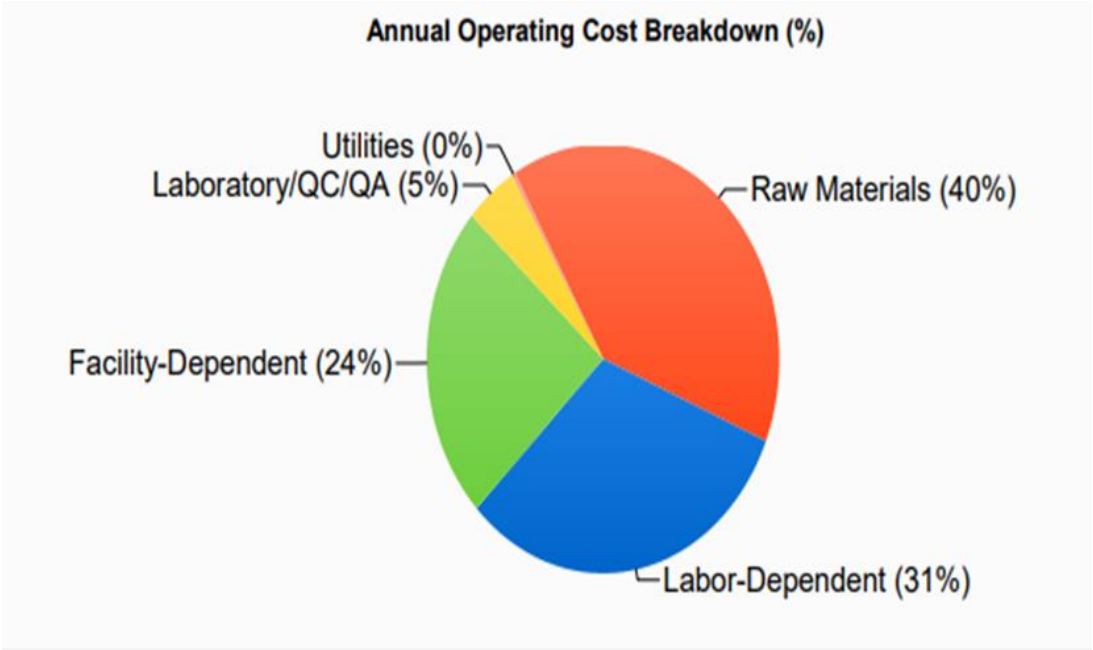

Figure 7.2: Annual operating cost summary of the itemised costs.

7.4 Summary

The purpose of this chapter was to construct a process flowsheet and estimate the cost of processing CFA using SuperPro Designer. The following are the concluding remarks:

- A process flowsheet was successfully constructed with 15 processing units, which include magnetic separation, two-step leaching processes, and an integrated purification process.

- Based on the preliminary evaluation, the production of more than one valuable resource from CFA seemed economically feasible but not particularly attractive. A possible major limitation is the complex processing units that add to the total operational costs. Since the process units are complex, the process can be improved by reducing the number of units. An alternative could be a high-pressure leaching process, which would consequently eliminate sintering, mixing/pelletisation, and grinding steps.
- The developed flowsheet also can be used to process other CFA materials and silica-rich materials such as clay minerals (i.e. kaolinite), which contains an appreciable amount of alumina worth scaling (20-30 wt%). However, the presence of other valuable elements, such as Ti and REEs, which could be turned into saleable products during processing, should also be considered to add value.

The next chapter presents the conclusion and recommendations for all the work carried out in the research study.

References

Alibaba, 2024. Available online: https://www.alibaba.com. (Accessed on 02-03-2024).

Adamas Intelligence Report, 2024, Available online: https://www.adamasintel.com/weekly-rare-earth-roundup-week-9-2024/ (Accessed on 02-03-2024).

Granata, G. and Petrides, D., 2022. Hydrometallurgical Process Design and Economics with SuperPro Designer. KU Leuven and Intelligen, Inc., Belgium 2022.

Sigmaaldrich, 2024. Chemical Costs. Available online: https://www.sigmaaldrich.com. (Accessed on 02-03-2024).

Matches, 2020. Equipment Cost Index. Available online: www.matche.com. (Accessed on 21-02-2024).

8 CONCLUSIONS AND RECOMMENDATIONS

8.1 Conclusions

A broad scope of this study was set to develop a process for the extraction and recovery of saleable products from CFA. The specific objectives outlined in **Chapter 1**, **Section 1.3** were as follows:

1. Identify the phase distribution of Al, Fe, Ti, Si and REEs in CFA.
2. Investigate the extraction of magnetic fractions using magnetic separation.
3. Investigate the optimum leaching conditions for the extraction of Al, Fe, Ti and REEs from CFA.
4. Investigate the possibility of using acid baking to recover REEs in silica residue.
5. Investigate the feasibility of purifying CFA leach solution using an intergrated of SX, seeded precipitation and crystallisation.
6. Analyse the purity of the silica-rich residue and determine its feasible application.
7. Develop a process flow sheet and perform an economic analysis.

Through a set of experimental work described in **Chapter 4** to **7**, the set objectives in this study were achieved. **Table 8.1** presents a summary of the degree of success achieved in the extraction and recovery of REEs and other values from CFA. The following conclusions were also elucidated as the major concluding remarks.

Table 8.1: Evaluation of various steps in the extraction and recovery of REEs and other values from CFA

Process	Aim/Objective	Evaluation	
Material charecterisation	Determine the distribution of REEs, Fe, Ti and Al via preliminary leaching studies and analytical techniques	√	Al – mullite and amorphous phses Ti – amorphous and Fe-rich phases Fe – amorphous , magnetite/hematite and Fe-rich phases REEs – associated with amorphous, REE-phosphate, REE-silicates phases
	Fe-oxide recovery by dry magnetic separation	√√	65.9% Fe-oxides (magnetite/haematite) recovered with amorphous, quartz, and mullite impurities
Optimisation of the sinter-H_2SO_4 leach process	Determine the optimimum conditions for alumina processing	√√	77.1% Al , 52.7% Ti, and 80.2% Fe
Intergrated Al, Ti and Fe purification	Production of smelter-grade Al_2O_3	√√	99.02 wt% Al_2O_3 smelter quality
	Synthesis of TiO_2 for wastewater treatment	××	95.03 wt% TiO_2 piment grade quality
	Synthesis of Fe-based coagulants through seeded Fe oxidation-precipitation	√√	99,9% Fe recovered. Fe-based coagulants generated and tested with efficience using brewery wastewater
Dry digestion-water leach process	Extraction of REEs from CFA-SR	√	10-30 % REEs extracted. REEs associated with Si-rich, Si-Ca-rich and discrete phases.
	Production REE-concentrate	××	66 mg/kg (High levels of Fe and Al impurities)
Charecterisation of CFA-SSR	Anaytical techniques	√√	amorphous and crystalline (quatrtz/ cristobalite, and anhydrite) phases. Mesoporous (29.236 m^2/ g) with pHpzc = 3.2
	Adsorption test (AMD solution)	√	Adsorption at pH 7, 25°C for Ni, Zn, Mg, Mn and Fe
Process flowsheet	Develop a process flowsheet and determine the economic feasibility	√√	Flowsheet with 15 unit processes: the developed process is economically feasible but not attractive.

√√ - Sussessful, √ - Partially successful,×× - Not successful

Material characterisation: The phase composition of the raw CFA used in this study was characterised using XRD, SEM-EDS, and TIMA analyses. XRD analysis showed that CFA is amorphous and contains crystalline components such as mullite, magnetite/haematite, and quartz. SEM-EDS and TIMA showed that CFA is primarily composed of Al-Si-rich phases, with additional phases rich in Ca, Si, and Fe. The REEs, Fe, and Ti were found distributed among different grains in the CFA, and were primarily associated with the Al-Si-rich phases. The REEs were dispersed within CFA, with monazite, xenotime, and zircon identified as the REE-bearing phases. These phases were also found to exist in the Al-Si grains as a solid solution and also occurred as separate discrete grains. While Ti was found in the Al-Si-rich grains, it was also quantified in some Fe-rich grains.

Since Fe was present as discrete Fe-rich (magnetite/haematite) grains and in the Al-Si-rich grains, dry magnetic separation was used to recover magnetite/haematite and reduce downstream purification costs. A maximum recovery of 65.9% Fe-oxide was achievable at 1.05 T. However, due to the agglomeration of CFA particles, both mullite and quartz were co-extracted in the CFA-MF. Nevertheless, the composition of the CFA-MF was deemed suitable for its intended use as a seeding material for Fe precipitation in this study. The non-magnetic fraction, which was concentrated with mullite and quartz (including the amorphous component), was further processed for the extraction of Al, Fe, Ti, and REEs. Among REEs, Sc, Y, La, Ce, and Nd were chosen for leaching studies due to their higher concentrations. The non-MF was also sintered for the leaching experiments to transform the mullite into a more soluble alumina phase (plagioclase/anorthite). The transformation of REEs was also monitored, and the quantified REE-phosphates and silicate (i.e. zircon) were liberated from the host grains (i.e. Al-Si), while some grains appeared to have transformed into oxides during sintering. There were also REE-phosphate grains that remained unreactive, suggesting they might have been liberated from the host grain but not reacted during sintering.

Preliminary leaching tests: The effects of acid concentration, leaching temperature, and leaching time were investigated using direct H_2SO_4 leach and sinter-H_2SO_4 leach processes. The former resulted in poor metal extraction due to the mineralogical composition of CFA, while the sinter-H_2SO_4 leach process showed much higher extraction efficiency. A maximum of 70% Al, 63% Fe, and 40% Ti extraction was observed at 6 M H_2SO_4, 70°C, 1:5 S/L ratio, and 160 rpm leaching for 10 hours. However, under the same experimental conditions, less than 20% of the selected REEs (Y, Nd, La, and Ce) were extracted, except for Sc at 35% extraction. Hydrochloric acid was further investigated as an alternative

lixiviant, and the extraction efficiency was significantly improved to more than 50% for REEs in 4 M HCl leaching for 6 hours at 70°C. The low extraction efficiency of REEs in H_2SO_4 leaching was attributed to the possible formation of calcium sulphate which precipitates with the metal sulphates in solution at high temperature and acid concentrations and the complex phase composition of CFA. Therefore, based on the results obtained it was concluded that the sinter-H_2SO_4 leach process could be used as a pre-concentration method for the REEs since they occur in trace concentrations compared to the major elements such as Al, Fe, and Ti. From the preliminary study, it was clear that calsium sulphate significantly influences the extraction of REEs and that the sinter-H_2SO_4 process is not a suitable process for REEs.

Optimisation of the sinter H_2SO_4 leach process: A full factorial design (2^4) was used to screen variables that influence aluminium extraction. Temperature and acid concentration were found to be significant, and their interactions had a negative influence. Therefore, to maximise Al dissolution, temperature was maintained at a high level, and the acid concentration was lowered. Optimisation involved the use of RSM in conjunction with CCRD. The identified significant variables were optimised, and the leaching conditions were set as follows: 82°C for leaching temperature, 10 hours for leaching time, and 6 M H_2SO_4 for acid concentration. Using confirmatory tests, the derived quadratic model fitted the experimental data very well and was therefore considered valid. Based on the optimisation process, a leach liquor with 77.1% Al, 52.7% Ti, and 80.2% Fe was generated for further purification. A sintered CFA-SR was also generated for further characterisation and processing.

Purification of CFA leach liquor: The CFA leach liquor was processed using an integrated SX, crystallisation, and oxidation-precipitation process for the potential recovery of saleable products. All the Fe(III) in the solution was first reduced to Fe(II), and Ti(IV) was selectively extracted with Primene JM-T/Shellsol D70, recovered by NH_4OH, and calcined to TiO_2. The synthesised TiO_2 was characterised as pigment-grade quality. However, characterisation as a potential photocatalyst in wastewater treatment showed low purity (95.03%) and surface properties (i.e. S_{BET} was 10.05m^2/g) compared to commercial TiO_2 (Degussa P25). Therefore, further studies were recommended to improve these properties. Nonetheless, the Al in the raffinate was directly crystallised and calcined to produce alumina that meets smelter-grade production.

Lastly, an Fe(II)-rich solution was processed using an oxidation-precipitation process at pH 5.0 to recover Fe(III) hydroxide/oxyhydroxide. To promote settling and solid-liquid separation, the extracted CFA-MF from the raw CFA was recycled as the seed material. Seeding greatly improved the filtration process, resulting in more than 99% Fe(III) recovery. Overall characterisation showed that the amorphous Fe(III) precipitates agglomerate on the CFA-MF upon seeding, leading to improved surface area. The seeded Fe(III) precipitate at Cs = 1.0 was further dissolved in dilute sulphuric acid to generate Fe-based coagulant. The generated coagulants were tested on brewery wastewater for water quality parameters and their performance was found to be efficient and comparable to that of commercial coagulants. Therefore, it was concluded that the coagulants generated in this study can be easily incorporated into mine water treatment processes to generate revenue. Overall, the study showed that Fe can be recovered by seeded oxidation-precipitation process and further used to generate Fe-based coagulants for wastewater treatment.

Processing of the sintered CFA-SR by dry digestion-water leach process: Dry digestion technique was used to investigate the extraction of REEs from sintered CFA-SR. The sintered CFA-SR was characterised as amorphous, with anhydrite and quartz as the crystalline components. Further analysis showed that the Si-Ca-S-rich particles are the major phase components with traces of Al, Fe, Ti, and REEs. Dry digestion was investigated in a sulphate and chloride system and both processes showed low REE extraction. The chloride system yielded better results, with 44.29% Nd, 45.7% La, 35% Ce, 12% Sc, and 48.1% Y. These results showed that the leaching efficiency of REEs was controlled by the solubility limit of calcium sulphate and the complex mineralogy of the residue such as the association of REEs with the Si-Ca-S-rich phase and discrete REE phases that did not transform in the sintering process.

An attempt was made to generate REE concentrate using selective oxalate precipitation. However, the purity of the product was relatively low due to high concentrations of Al and Fe. As a result, REE concentrated solution was considered as the final product for techno-economic analysis. It was concluded in this study that the dry digestion technique is not a suitable technique for the sintered CFA-SR due to the low extraction of REEs. Therefore, alternative techniques can be investigated for the extraction of REEs from sintered CFA-SR. Further mineralogical studies using EPMA and QEMSCAN can also be conducted to understand the phase composition of sintered CFA-SR and the effect on REE extraction using the dry digestion technique. Overall, from the developed process, it can be concluded that the

REEs can be selectively separated from Al, Fe, Ti, and Si. However, Sc was selectively extracted with Ti(IV) during SX, whereas the rest of the REEs remained in the solution after Fe recovery. Thus, further studies can investigate the selective stripping of Sc from Ti.

Characterisation of CFA-SSR: The generated CFA-SSR was characterised as a potential adsorbent for wastewater treatment. Chemical analysis revealed a component rich in SiO_2, CaO, and SO_3 with traces of Fe_2O_3 and TiO_2. The material was mainly amorphous, with crystalline anhydrite and quartz. The physicochemical properties showed a promising adsorbent with mesopores (11.7 nm), S_{BET} of 29.236 m^2/g, and a d_{50} of 44.76 µm. The batch test showed that CFA-SSR could be used to adsorb heavy metals such as Zn, Ni, and Fe from AMD. However, the adsorption efficiency was higher in AMD effluents (pH >5), suggesting hydrolysis and ion exchange as possible adsorption mechanisms. However, further studies can be conducted to understand the mechanism of adsorption. The overall results showed that CFA-SSR could potentially be utilised as a cost-effective adsorbent in wastewater treatment. The scope of adsorbent capacity can also be increased by functionalising CFA-SSR to include the adsorption of critical elements such as REE and PGMs reported in mine wastewater.

Preliminary economic analysis: A process flowsheet was developed based on magnetic separation, a two-step leaching process, and an integrated solvent extraction, crystallisation, and oxidation-precipitation process. The cost analysis showed a positive return on investment; however, the low margin was not appealing. Nonetheless, a pilot scale can be designed and simulated for further feasibility of CFA processing.

CFA has the potential to be a valuable resource for critical metals recovery and wastewater treatment. In this study, it was hypothesised that the extraction and recovery of multiple products from CFA could result in an economically feasible process by contributing to metal production and wastewater treatment. Therefore, this research study has contributed to scientific knowledge by providing new insights into a comprehensive strategy for producing REE-concentrated solution, smelter-grade Al_2O_3, pigment-grade TiO_2, Fe-based coagulants, and CFA-SSR for wastewater treatment. As a result, these findings have implications that are beneficial for disposal management, resource recovery, and economic growth.

8.2 Recommendations

While this study has demonstrated that a holistic approach can be an alternative for recycling CFA, there were also limitations identified. Therefore, possible future studies from this work are as follows:

- The phase composition analysis of the samples used in this study was limited to CFA, sintered CFA, and sintered CFA-SR. Further TIMA analysis could be extended to CFA-MF, coal, and sintered CFA residue after the sinter-HCl leach for a better understanding of the REE distribution.
- The mineralogical analysis of CFA could also be expanded to alternate techniques such as Electron probe micro-analyser (EPMA) and QEMSCAN for a more comprehensive understanding of REEs.
- Alternative techniques such as ultrasonic-assisted and high-pressure leaching processes could be investigated for the extraction of REEs from the sintered CFA-SR.
- The distribution of naturally occurring radioactive materials (U and Th) could also be monitored in the solids and liquid streams during processing.
- Since only batch tests were considered in the adsorption stage, the experimental test work could be expanded to include column tests. This would provide more information on the mechanisms of metal ion adsorption and the kinetics of adsorption in multiple metal solutions, such as AMD for scale-up purposes.
- Since CFA can vary in its chemical and phase composition, it is also recommended to perform thermodymanic modeling for the reactions and test the developed process flowsheet on other CFA materials.

APPENDICES

Appendix A: General Equipment

Figure A.1: (a) A riffle splitter, (b) vibrating sieve shaker, (c) laboratory pulveriser and (d) ring and puck grinding set.

Appendix B: Material Characterisation

Al content in CFA

CFA mass	=	100 g
XRF analysis	=	30 wt%
Molar mass	=	102 g/mol
Al	=	27 g/mol
n Al	=	2
Total Al_2O_3	=	30 g

Total Al $$\frac{100 * 30.52 * 27 * 2}{100 * 102} = 16.16 \text{ g} \quad \textbf{(B.1)}$$

Table B.1: Calculations of the alumina distribution in the mullite and amorphous phase

Phases	**Mullite**	**Amorphous**
XRD analysis	28.9 wt%	57.3 wt%
Total mass	28.9 g	57.3 g
Al_2O_3	$\frac{24.4 * 3 * 100}{102} = 17.52$ g	$\frac{24.4 * 3 * 100}{102} = 17.52$ g
Al	$\frac{24.4 * 3 * 100}{102} = 17.52$ g	$\frac{24.4 * 3 * 100}{102} = 17.52 - 22.04 = 8$ g
% Al_2O_3	$\frac{17 * 100}{28.9} = \mathbf{60.04}\%$	$\frac{8 * 100}{57.3} = \mathbf{39.96}\%$

Coal fly ash (CFA)	Quartz	Mullite	Magnetite	Haematite	Ettringite	Amorphous	Total
UIS_26870–629328_TUTUKA	12.8	28.5	0.9	0.4	0.5	56.9	100
UIS_26870–629329_KRIEL	8.3	32.0	0.7	0.5	0.6	57.9	100
UIS_26870–629330_MATLA	12.0	28.9	1.5	0.3	0.0	57.3	100

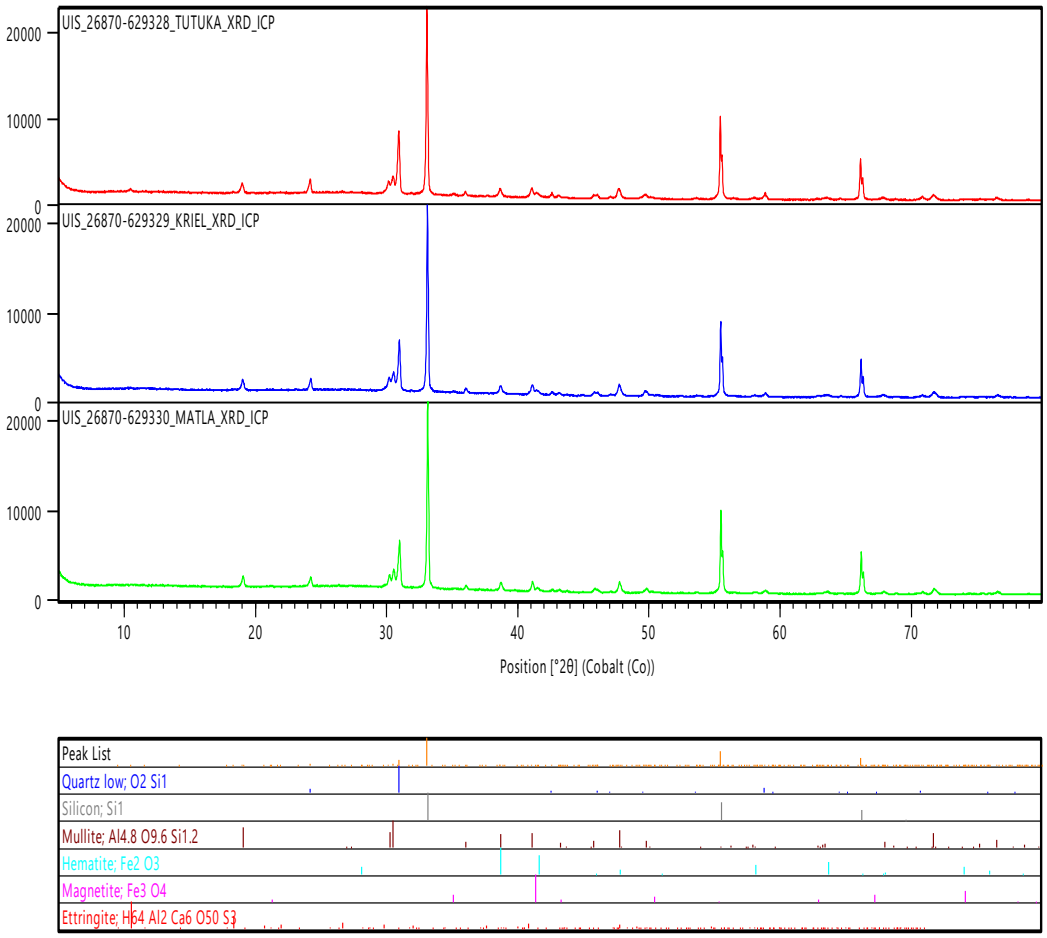

Figure B.1: Quantitative analysis and XRD spectra of different CFA materials from Tutuka, Matla amd Kriel.

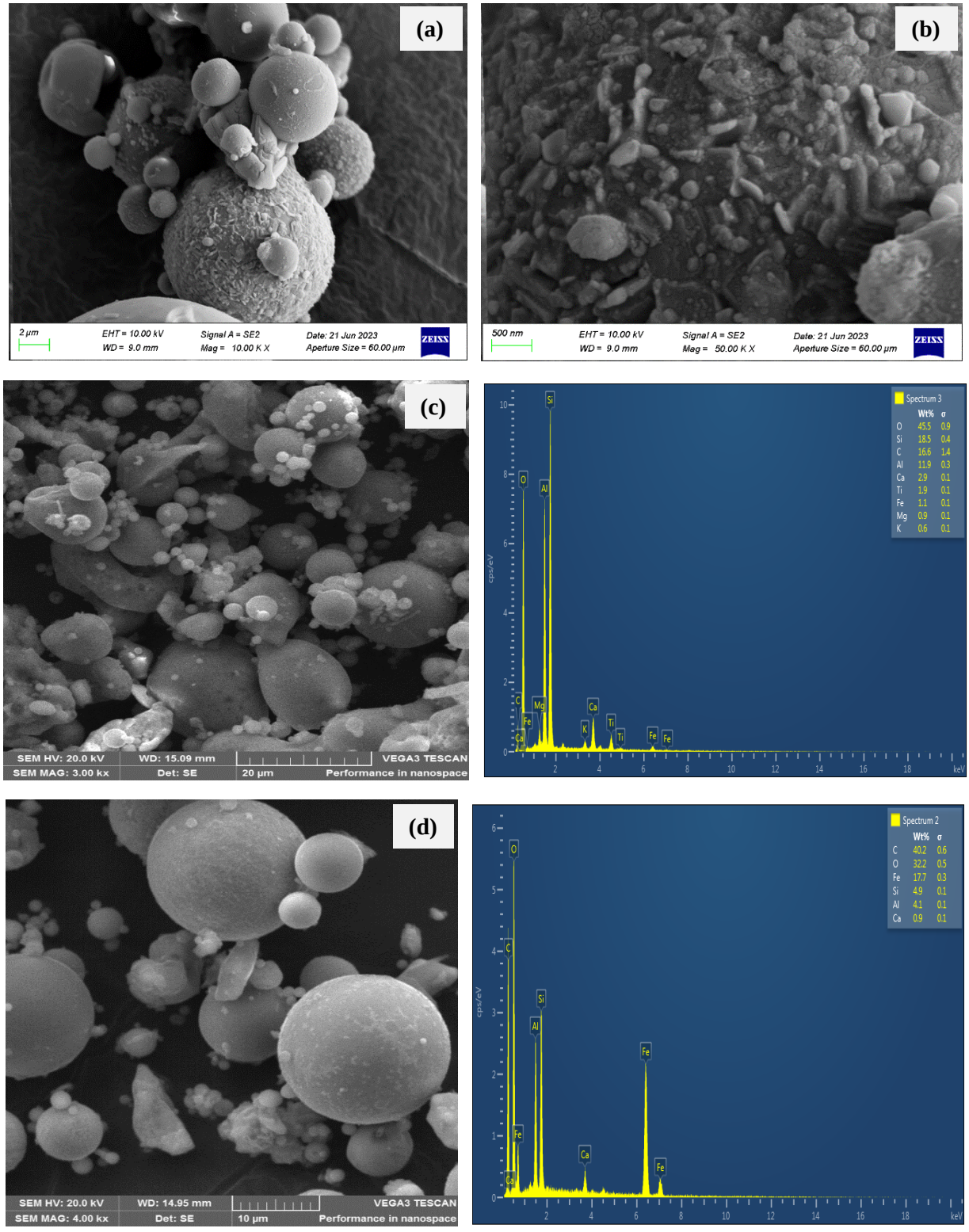

Figure B.2: (a-b) SEM-Morphology of CFA-MF and SEM-EDS analysis of (c) raw CFA and (d) CFA-MF.

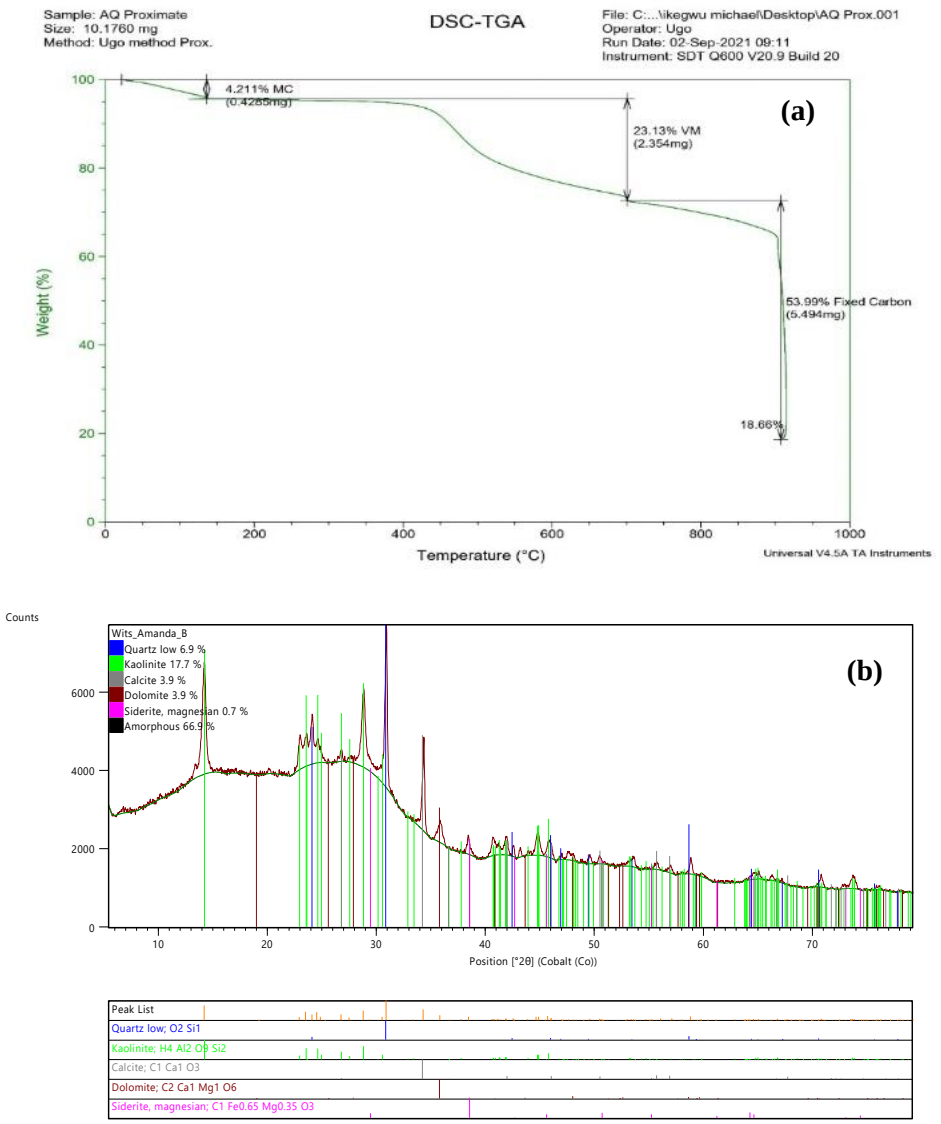

Figure B.3: Received coal analysis: (a) DSC-TGA analysis, (b) XRD spectrum, and (c) PSD analysis of pulverised coal.

Sintered –CFA	Mullite	Quartz	Anorthite	Diopsite	Microcline	Anhydrite	Amorphous
CFA_(Raw)	29.2	14.7	0.0	0.0	0.0	0.0	54.7
Sintered_CFA_(5_3_2)	0	2.4	53	5.1	2.1	0.0	37.2
Sintered_CFA_(5_4_1)	6.5	5.5	48.7	1	2.9	0.0	35.5
Sintered_CFA_(4_4_1)	0.2	3.1	56.9	3.8	2.1	0.0	33.5
CFA_Residue	1.2	2.7	0.4	0.2	1.4	23.3	62.3

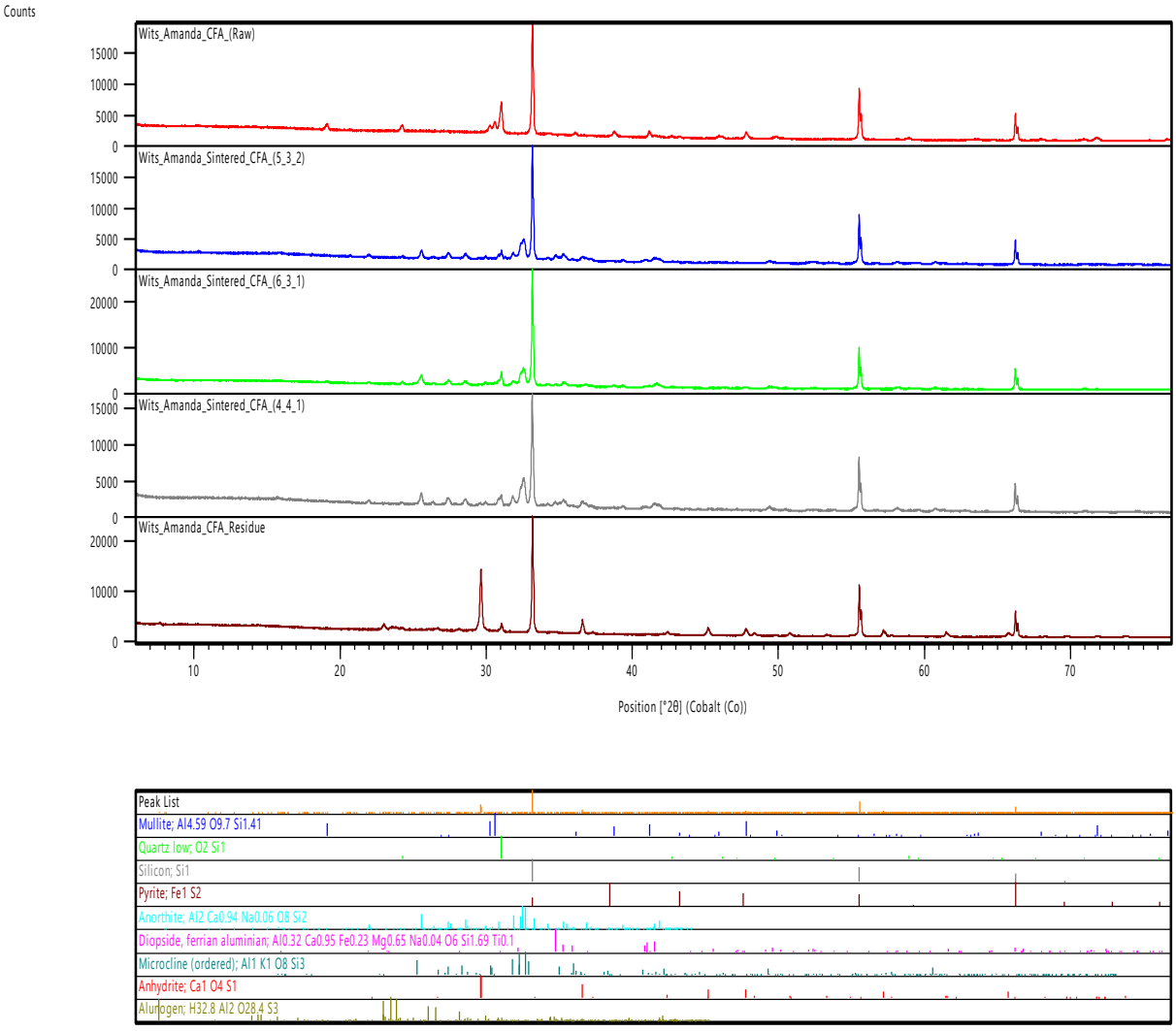

Figure B.4: Quantitative analysis and XRD spectra of (a) CFA, (b-d) sintered CFA at different ratios, and (e) analysis.

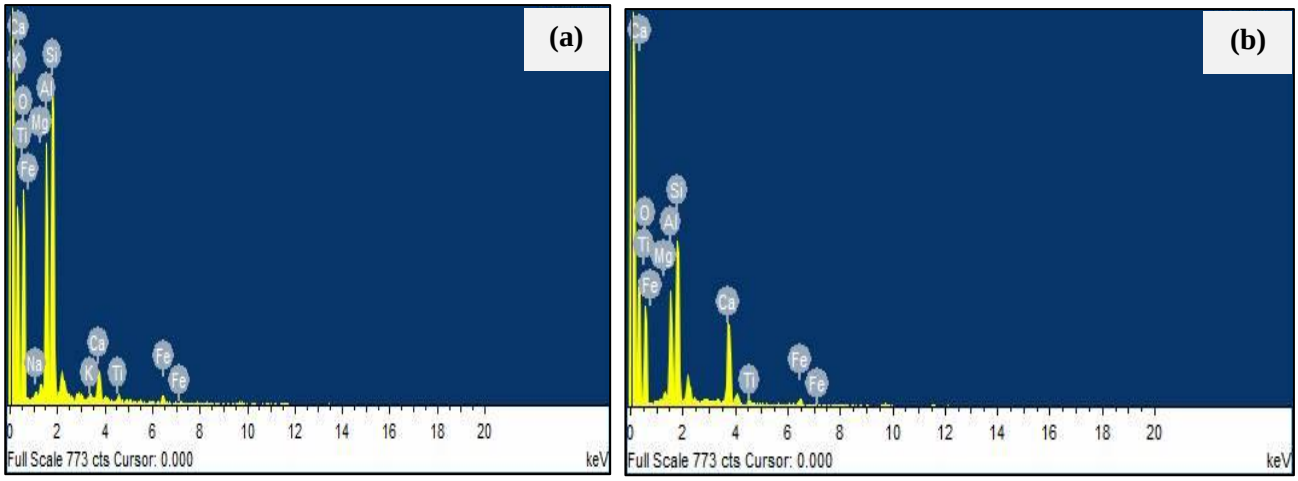

Figure B.5: EDS spectra of (a) CFA and (b) sintered-CFA analysis

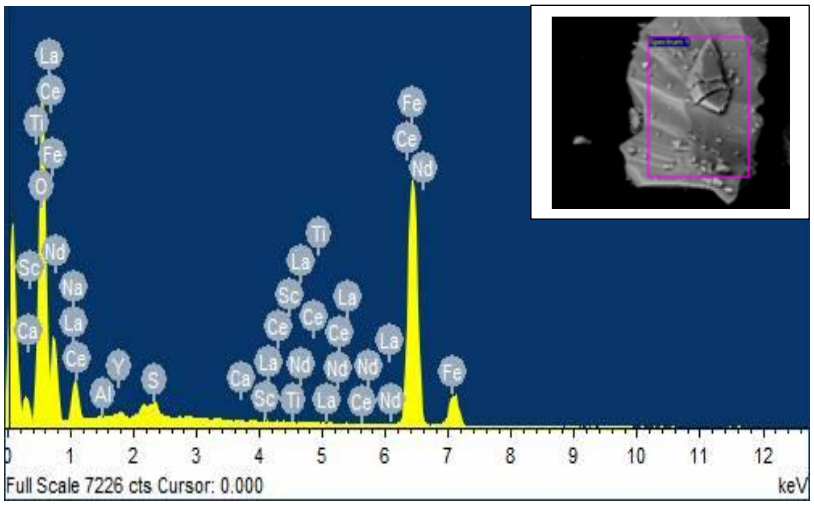

Element	O	Na	Al	S	Sc	Ti	Fe	Y	La	Ce	Nd
wt%	41.78	7.45	10.08	0.03	0.03	-0.07	41.02	-0.71	0.13	0.05	-0.23
Atomic%	57.70	8.40	10.07	0.02	0.02	-0.04	23.68	-0.21	0.03	0.01	-0.04

Figure B.6: Semi-quantitative EDS analysis of the oxalate precipitate.

Table B.2: Concentration of REEs remaining in solution after Fe recovery

mg/Kg	Sc	La	Ce	Pr	Nd	Sm	Eu	Gd
	0.26	1.53	3.32	0.14	0.48	0.07	0.01	0.09
mg/Kg	**Tb**	**Dy**	**Ho**	**Er**	**Tm**	**Yb**	**Lu**	**Y**
	0. 1	0.15	0.21	0.44	0.01	0.05	0. 1	0.21

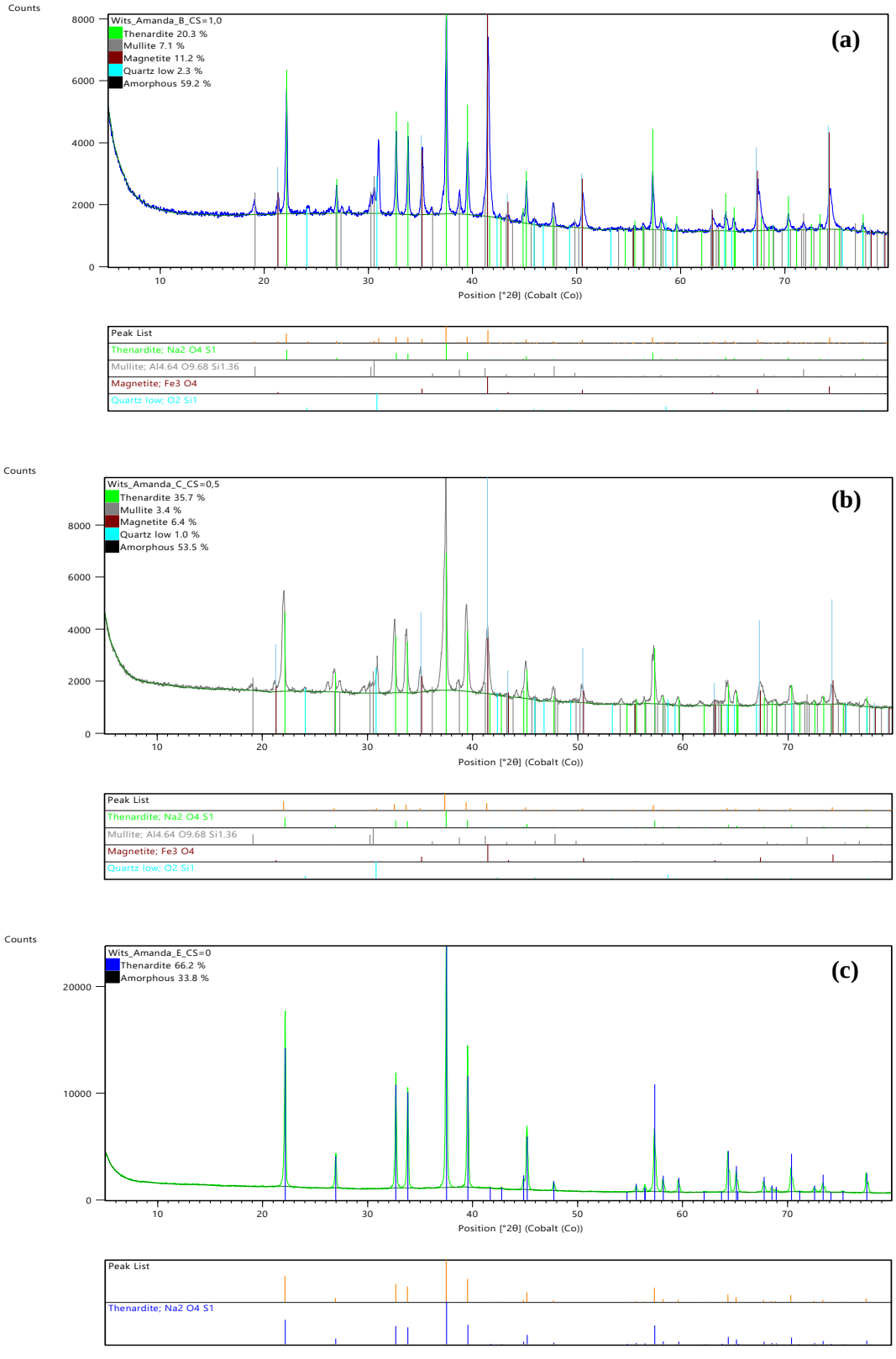

Figure B.7: XRD patterns for the Fe precipitates at (a) Cs = 0.0, (b) Cs = 0.5, and (c) Cs = 1.0.

Appendix C: Design of Experiments

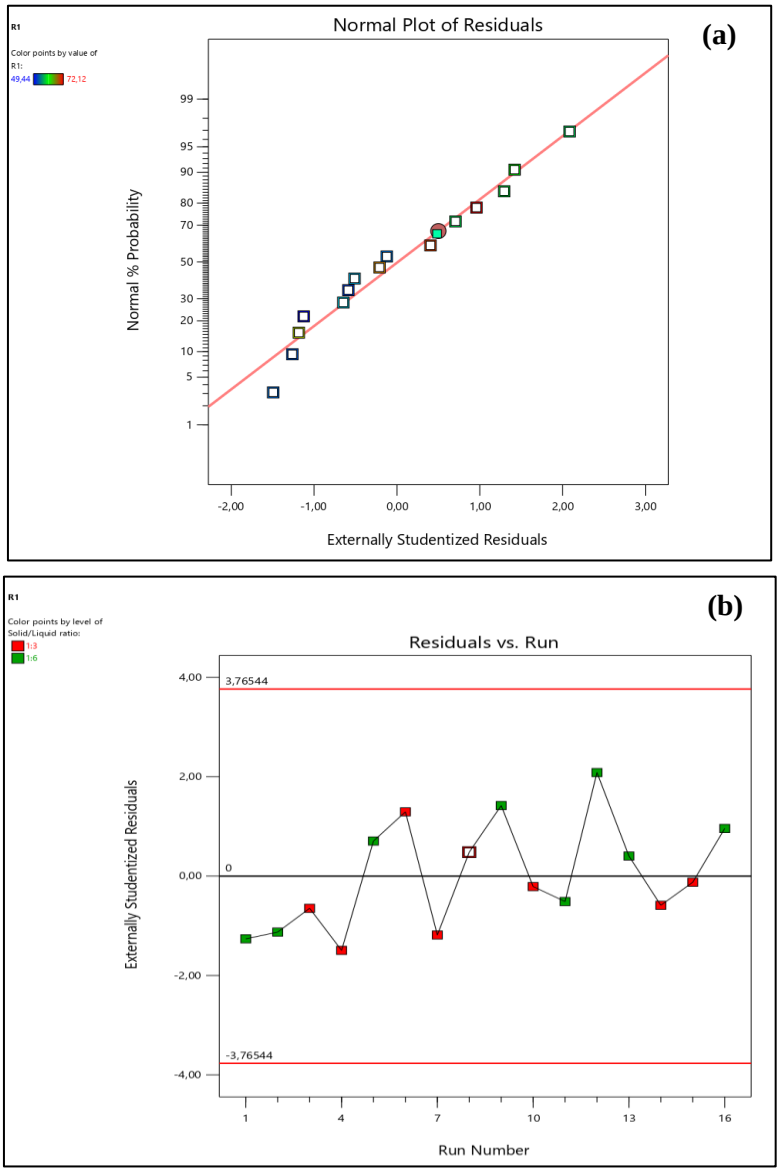

Figure C.1: (a) Normal plot of residuals and (b) Plot of residuals versus predicted extractions.

Table C.1: The Fit Statistics of the re-fitted quadratic model

Std. Dev.	0.935		**R^2**	0.9639
Mean	70.95		**Adjusted R^2**	0.9382
C.V. %	0.9775		**Predicted R^2**	0.9143
			Adeq Precision	17.9496

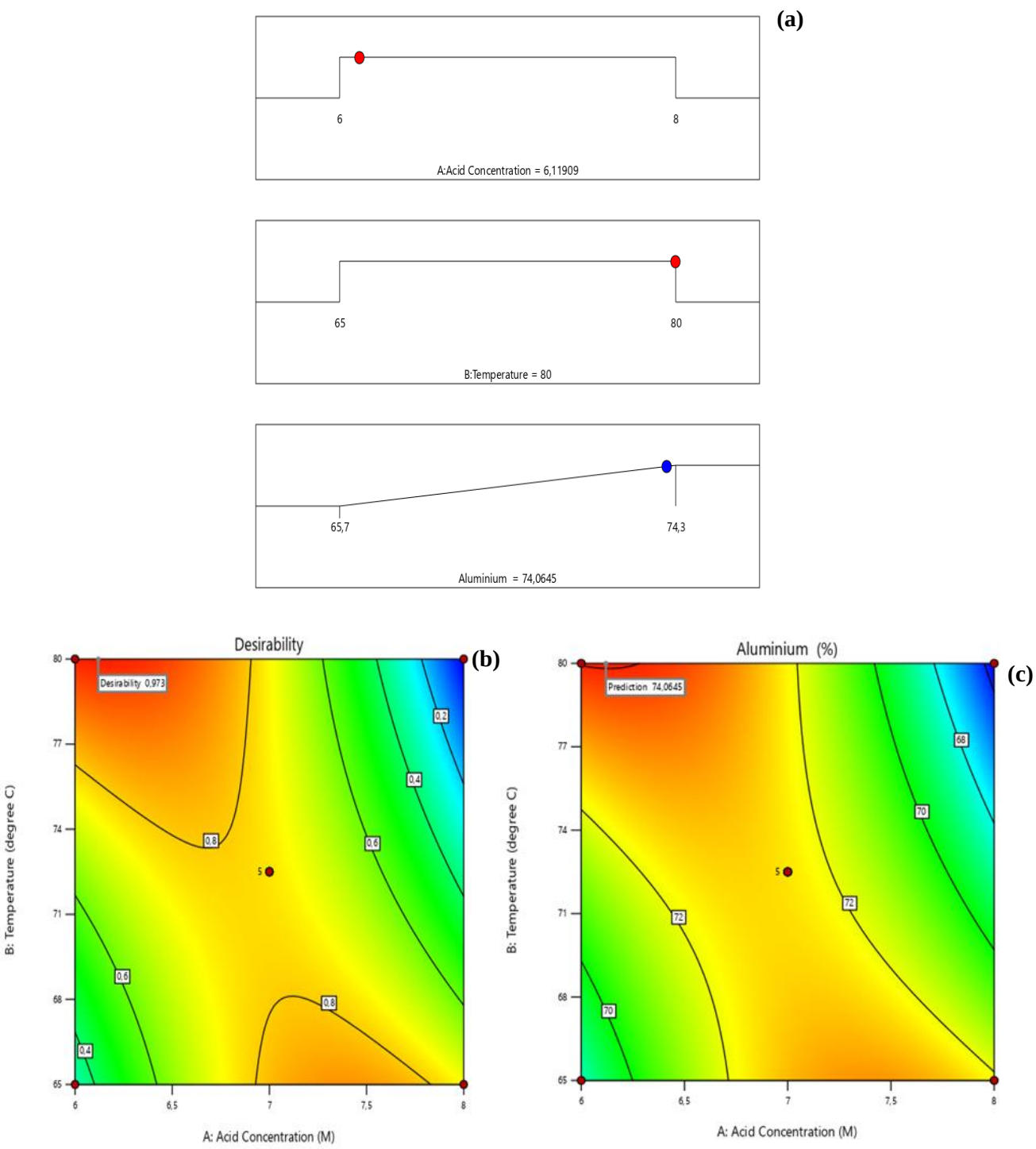

Figure C.2: (a) Numerical optimum levels, (b) Factor desirability levels, and (c) predicted aluminium extraction from sintered CFA.